Hydrodynamic Optical-Field-Ionized Plasma Waveguides for Laser Plasma Accelerators

Robert James Shalloo BSc.

Lincoln College, Oxford

Submitted in partial fulfillment of the requirements for the degree of Doctor of Philosophy in Particle Physics

October 2018

Abstract

This thesis documents the experimental development of low-density hydrodynamic optical-field-ionized (HOFI) plasma channels. Results from two experiments are presented; the first, a proof of concept experiment, performed in Oxford, demonstrating for the first time that the formation of low-density ($\sim 10^{17}$ cm^{-3}) hydrodynamic plasma channels was possible using optical-field-ionization. The second experiment, performed at Astra-Gemini TA2, aimed to demonstrate the generation of low-density axicon-formed HOFI plasma waveguides and subsequently to demonstrate high-intensity guiding in those waveguides at the highest available repetition rate.

In the Oxford experiments, short (2-4mm) HOFI plasma channels were generated in hydrogen with a spherical lens and probed with longitudinal interferometry. The channels had on-axis densities between $1.6 \times 10^{17}\,\mathrm{cm}^{-3}$ and $1 \times 10^{18}\,\mathrm{cm}^{-3}$ and matched spot sizes of order 30 µm to 60 µm. A computational investigation into the guiding properties of the measured plasma channels indicated that they would be suitable as plasma waveguides.

In the experiments at Astra-Gemini TA2, HOFI plasma channels up to 16 mm in length were generated in hydrogen using an axicon. These were probed with both longitudinal and transverse interferometry and had on-axis densities as low as $2 \times 10^{17}\,\mathrm{cm}^{-3}$. These waveguides were subsequently used to successfully guide high-intensity ($> 10^{17}$ W cm^{-2}) pulses over the full 16 mm or 14.5 Rayleigh ranges, with a maximum throughput of 60 % observed for the higher intensities. The variation in guiding with pressure and with guided beam intensity was investigated experimentally. It was found that the high-intensity guided pulse modified the HOFI plasma channel, with the result of increasing the relative throughput of the guided beam.

"I make the moves up as I go"

- T. Swift

Acknowledgements

The last four years have been an amazing experience, but one that would no doubt have ended much earlier if it weren't for the incredible people I've been lucky enough to be surrounded by, both in and out of the lab.

I am particularly indebted to my supervisors, Simon and Laura. I feel incredibly lucky to have had two mentors as supportive, approachable, patient and engaged as you both. Each of your individual supervisory styles has complimented the other and I'm only sorry that other students won't get the same great team that I got. Together, you've taught me an incredible amount of physics - both experimental and theoretical and I wouldn't be the researcher I am today without your continued effort and guidance. What's more is that you've both been extremely invested, not only in the science we've been doing together, but also in my development as a scientist. You've consistently gone above and beyond, and that has made all the difference. Thanks must also go to Roman for his support and useful discussions.

Being a PhD student in experimental laser plasma physics has an awful lot of things going for it, however, good pay, endless free weekends and sociable working hours aren't amongst them. Instead you get to tackle unique, difficult and honestly, really cool problems. Not to mention, you get to utilize (read "play with") high-power lasers which can produce some of the most extreme conditions achievable here on earth. But honestly, the best part about working in this field for the last few years has been getting to work closely with, suffer with and celebrate with the incredibly dedicated, work hard, play hard, highly entertaining group of absolute legends that are, the laser plasma accelerators group — ironic when you consider they're all physicists...

The long nights and even longer weeks at RAL, the stress of experiments that just aren't working, the elation of seeing the results start to come in, the commiseration drinks, the celebration drinks, the drinks in general actually. The bolloxed optics, the flooded laser, the demerits, the caffeine oh the caffeine. The prank wars, the botched code, the four o'clock tea, the final bet that drove this thesis to a timely completion and of course the craic! An immense thank you to: Chris A., Chris T., Jimmy, Gavin, James, Jakob, Alex P., Alex VB, Anthony, Dan and David. It's been an absolute pleasure.

One of the nicest things about doing your PhD in Physics at Oxford is that by design you're also a part of a college, which means you are prevented from spending all of your time with physicists — believe me, no one, not even physicists, want to spend all their time with other physicists... For my part, I've been lucky enough to be a member of a truly wonderful community of people at Lincoln College. A huge thank you to the Lincoln Collge MCR and Boat Club for providing a supportive, fun environment to blow off steam after a long day in the lab. For many nights in Deep Hall, several garden parties and college balls, countless dinners in hall, too many cold mornings by the river, a couple of regattas, a few snow days, 11 Emily Carrs (yes 11), one grim bus ride (thanks Jen) and three glorious signet-ring-imprinted holes in the ceiling of Downing.

In particular, a very special thanks must go to André, James, Josh, Cloé, Alistair, Jay, Kathy, Tristan and Nina. Despite not being around for days and nights on end, away at the affectionately coined "laser camp", you all made me feel immediately relaxed and at home on my return. Our times together in Bear Lane, Henry Road and beyond were what made my time at Oxford so special.

Of those not in Oxford, a special mention must go to Richy, Eoghan, Cian, Lorcan and Peter, who for some reason I can't seem to get rid of, despite moving to the UK four years ago. Wherever you go, sure there you are!

Finally, I'm more grateful than I can possibly say, to my family. To my parents Carole and Jim and to my siblings David and Hannah. Thank you for being there every step of the way with unwavering support, encouragement and love. In addition, thank you for proof reading this thesis, which I'm sure was fairly painful at best! It was touch-and-go there towards the end, but luckily there was always encouraging words from Cork and Dublin, like: "*Just pull the finger out and write it*", "*I don't know why you're making a big deal about it, its as easy as xyz*", "*Are you done yet? What's taking so long*" and "*I've always had a PHD, get a real job*". While it might seem unusual to some, this was exactly what was needed and I'm very grateful for it.

Above all, to my parents: thank you for teaching me the value of education and for affording me every opportunity to attain one, for instilling perspective and for always making all things seem possible. I couldn't have started this, much less finished it without you.

Contents

Role of the Author

Experiments in the field of Laser Driven Plasma Accelerators are rarely performed by individuals but rather require teams of experimentalists and theorists working together to ensure success. The experiments described in thesis are no exception. The work presented throughout this thesis is therefore the culmination of the work of many. To help guide the reader in identifying the work of the author, an account of his role in each of the experiments described in this thesis is given below. In addition, while data taking is again an endeavour which is rarely ever performed entirely by one person, the vast majority of analyses and plots presented in this thesis are the author's own work. In the case where a plot or set of analysis has not been generated by the author, the responsible individual is explicitly credited.

The team involved in the low-density lens-formed (hydrodynamic optical-field-ionized) HOFI plasma channel experiments performed at Oxford, discussed in chapter 3 were: R. J. Shalloo, C. Arran, L. Corner, J. Holloway, J. Jonnerby, R. Walczak, H. M. Milchberg and S. M. Hooker. The author led the experimental campaign while the theoretical and computational work was led by C. Arran. The author and L. Corner spent a significant amount of time refurbishing the Oxford TW laser system for use in the experiments. Analysis of the experimental data was performed by the author. The gas cell used in these experiments was designed and built by C. Thornton.

The experiments described in chapters 4 and 5, demonstrating optical guiding in axicon-formed HOFI plasma channels were the combined effort of: R. J. Shalloo, C. Arran, A. von Boetticher, L. Corner, G. Hine, J. Holloway, J. Jonnerby, A. Picksley, C. Thornton, R. Walczak, H. M. Milchberg and S. M. Hooker. In addition, support was provided by the staff at the Central laser Facility, UK. The experimental campaign was led by the author who was assigned the role of Target Area Operator while C. Arran was assigned the role of Deputy Target Area Operator. The experimental design was led by the author, with specific contributions including design of the main optical layout, the gas cell as well as axicon and other custom optic designs. The experimental construction, debugging and data taking involved a significant effort from every member of the team. The analysis of the experimental results was led by the author with significant input from A. Picksley and C. Arran.

The author also contributed significantly to two other large experimental campaigns not covered in this thesis. Firstly, in 2015 the author was responsible for pulse train generation for the first experimental tests of Multi-Pulse Laser Wakefield Acceleration, an experiment led by J. Cowley and C. Thornton. Secondly, in 2016 the author was responsible for measurements of the timing between Astra-Gemini TA3's North and South beams in an experiment led by J. Holloway and G. Cheung aimed at demonstrating controlled injection into a plasma wakefield via the Two-Pulse Ionization Injection technique.

List of Peer-Reviewed Publications

In addition to the work listed below, two publications are currently being written up for submission based on the work described in chapters 5 and 6.

Publications related to hydrodynamic optical-field-ionized plasma waveguides

R. J. Shalloo, C. Arran, L. Corner, J. Holloway, J. Jonnerby, R. Walczak, H. M. Milchberg and S. M. Hooker, *Phys. Rev. E* **97**, 5, pp 1-8 (2018).

"Hydrodynamic optical-field-ionized plasma channels"

DOI: 10.1103/PhysRevE.97.053203

Publications related to multi-pulse laser wakefield generation

J. Cowley, C. Thornton, C. Arran, **R. J. Shalloo**, L. Corner, G. Cheung, C. D. Gregory, S. P. D. Mangles, N. H. Matlis, D. R. Symes, R. Walczak and S. M. Hooker, *Phys. Rev. Lett.* **119**, 044802, pp 1-6 (2017).

"Excitation and control of plasma wakefields by multiple laser pulses"

DOI: 10.1103/PhysRevLett.119.044802

R. J. Shalloo and L. Corner, *Opt. Lett.* **41**, 17, pp 4068-4070 (2016).

"Secondary wavelength stabilization of unbalanced Michelson interferometers for the generation of low-jitter pulse trains"

DOI: 10.1364/OL.41.004068

R. J. Shalloo, L. Corner, C. Arran, J. Cowley, G. Cheung, C. Thornton, R. Walczak and S. M. Hooker, *Nucl. Inst & Meth. A* **829**, pp 383-385 (2016).

"Generation of laser pulse trains for tests of multi-pulse laser wakefield acceleration"

DOI: 10.1016/j.nima.2016.02.044

List of Figures

List of Tables

List of Symbols

$(\widehat{A},\ \widehat{B})$ Diffraction and refraction operators

(p, m) Radial and azimuthal indices of the Laguerre Gauss modes

(r, z) Radial and axial coordinates

(x, y, z) Cartesian coordinates

α Approach angle of axicon rays to the optical axis

α_p Parameter describing the polarization of a laser pulse

$\alpha_{1/\mathrm{e}}$ 1/e waveguide loss parameter

β Longitudinal wavenumber

χ Arbitrary phase offset

$\Delta\phi$ Phase shift incurred on a beam by passing through plasma

Δr Annular thickness of a doughnut beam

$\Delta\Phi_{\mathrm{ax}}$ Phase shift introduced by a transmissive axicon

ϵ_0 Permittivity of free space

η Refractive index

γ Cycle averaged Lorentz factor of electrons oscillating in the field of a laser

γ_A Adiabatic index

γ_k Keldysh parameter

$\hbar$	Reduced Planck constant
κ	Transverse wavenumber
Λ	Plasma parameter
λ	Wavelength of light
λ_{mfp}	Mean free path of electrons in a plasma
λ_D	Debye length
λ_f	Fringe spacing in an interferogram
λ_p	Plasma wavelength
$\mathcal{F}$	Fourier transform operator
ω	Angular frequency of light
ω_p	Plasma electron frequency
ϕ_{NL}	Nonlinear phase
ρ	Radial position coordinate in the focal region
ρ_0	Radius of first node in a Bessel focus
ρ_m	Mass density
τ	Laser pulse duration
τ_{ee}	Electron self-collision time
τ_{eq}	Equipartition time of electrons and ions
θ	Maximum approach angle of lens rays to the optical axis
φ	Angle between two interfering beams
ϑ	Base angle of an axicon
$\vec{F_p}$	Ponderomotive force

A_0 Peak value of the vector potential

a_0 Normalized vector potential

c Speed of light

D Beam diameter

E Electric field amplitude

e Elementary charge

E_A Energy per unit area in a beam

E_c Critical field required for barrier suppression ionization

E_k Energy of an ionized electron

E_l Energy per unit length

E_λ Photon energy

E_{ion} Ionization energy

E_{WB} Maximum electric field amplitude in the cold relativistic wave breaking limit

f Focal length

F_A Apparent elastic limit or rupture modulus

$f_\#$ F-number

I Laser pulse intensity

I_0 Peak laser pulse intensity

I_T Threshold laser intensity for ionization

J_0 Zero order Bessel function of the first kind

k Free space wavenumber in vacuo

k_B Boltzmann constant

k_r Radial wavevector

$k_\perp$ Perpendicular wavevector

L Length of a waveguide

L_{ch} Length of a plasma channel

$L_{1/\mathrm{e}}$ $1/e$ attenuation length in a waveguide

L_{dephase} Dephasing length

L_{deplete} Depletion length

$L_p^m(x)$ Generalized Laguerre polynomial in x

m_e Mass of the electron

m_i Mass of an ion

m_p Mass of the proton

n_{cr}^{eff} Effective critical electron density due to oblique incidence

n_0 On-axis electron density in a plasma waveguide

n_2 Nonlinear refractive index

n_e Plasma electron density

n_{cr} Critical electron density

P Pressure

P_{cr}^* Critical power for short pulses

P_g Power in a Gaussian beam

P_{cr} Critical power

R Beam radius

r_0 Initial radial point on the axicon from which all the rays hitting the optical axis at z must have originated

r_e Classical electron radius

r_L Characteristic length scale of the transverse laser intensity profile

r_s Shock front position in the Sedov-Taylor solution

r_w Radius of the wall in a truncated parabolic plasma waveguide

r_{core} Radius of the core of a grazing incidence waveguide

s Safety factor

t Time

T_e Electron temperature

T_i Ion temperature

u Transverse field amplitude of the axially propagating solution to the wave equation

U_p Ponderomotive energy

V Visibility function

v_p Phase velocity of light

w $1/e^2$ intensity spot size of a beam

w_0 $1/e^2$ intensity spot size of a beam at focus

w_m Matched spot size

x_n^0 Roots of the zeroth order Bessel function of the first kind

Z Ionic charge in units of the elementary charge

z_R Rayleigh range

z_{max} Maximum length of a Bessel focus

Chapter 1

Introduction

1.1 Motivation

Scientific research is fundamentally about solving problems and so to undertake a PhD and write a thesis in science, there has to be a good problem on which to work. For this thesis, that problem lies broadly in the field of advanced accelerator physics; here advanced does not mean more difficult, but merely distinguishes the study of conventional particle accelerator technology such as that used in the Large Hadron Collider, and novel new accelerator technology aimed at solving the problem of particle acceleration in a fundamentally different way.

A particle accelerator, as the name suggests, is simply a machine which uses electric fields to propel charged particles to high velocity or energy. While famous discovery machines, like the aforementioned Large Hadron Collider, remain the public's main reference point for such machines they are certainly not the accelerators the public interact with or directly benefit from the most. Of the roughly 40,000 particle accelerators worldwide, less than 1% are used for high energy particle physics research[1,2] such as confirming the existence of the Higgs boson[3,4]. In fact, most of them are not used for scientific research at all.

Approximately 97% of particle accelerators around the world are used in medicine (33%) and industry (64%)[1]. In medicine, accelerators are used to treat cancer[5,6] and in advanced medical imaging techniques[7]. In industry, they are used for everything from the vulcanisation of rubber[8], and the production cling film[9] to imaging of jet-engine parts[10] and production of the consumer electronics[11,12]. In fact, a 2009 study by the US Department of Energy found

that at the time, the annual market for medical and industrial accelerators exceeded $3.5 billion and was growing at a rate of more than 10% a year. Furthermore, it found that "all the products that are processed, treated or inspected by particle beams have a collective annual value of more than $500 billion"[2].

In addition to the clear economic and social benefits of medical and industrial accelerators, particle accelerators also play an increasingly large role in research over a diverse variety of fields. Originally developed as tools for discovery in particle physics, they now act as indispensable tools in material, biological and chemical science. Furthermore, they continue to be utilized by research fields outside of the core scientific subjects with roles in archaeology and art history[13] and even forensic analysis for criminal prosecution[14].

Ironic for a field which began with the discovery of the electron by British physicist J. J. Thomson*, a man who famously toasted "The electron: may it never be of any use to anybody!"[15]. In fact, when it comes to demonstrating the value of curiosity driven, or blue-skies research, one need look no further than particle accelerators and the long list of applications which they have either been responsible for, or become indispensable in.

Given their importance in science and society today it is not surprising that the development of particle accelerators has become the subject of an intense global research effort. On the one hand, new applications in research, industry and medicine are driving accelerator physicists to develop new and more advanced accelerator technology. On the other, the increasingly large role that these machines are playing globally warrants the innovation of current accelerators, which are predominantly based on technology that was fundamentally developed nearly a century ago. The field of advanced accelerator physics aims to develop these new technologies and new acceleration techniques. It aims to both produce new radiation and particle sources, and also to reduce the size and cost of particle accelerators through their innovation.

One such advanced accelerator is the Laser Plasma Accelerator (LPA). In contrast to conventional particle accelerators, in which a radio-frequency cavity is used to excite electric fields that act to propel a charged particle forward, LPAs combine a high-intensity ($> 10^{17}$ W cm^{-2}) ultrafast ($\sim$ fs) laser pulse with a plasma to generate the accelerating fields. The main advan-

*It should be noted that the term electron was actually coined by an Irishman from Co. Offaly, George Stoney. Indeed, it was once thought that the electron's name was probably the most famous thing to have ever originated in Co. Offaly — although it was later discovered that Barack Obama had an eighth cousin in Moneygall.

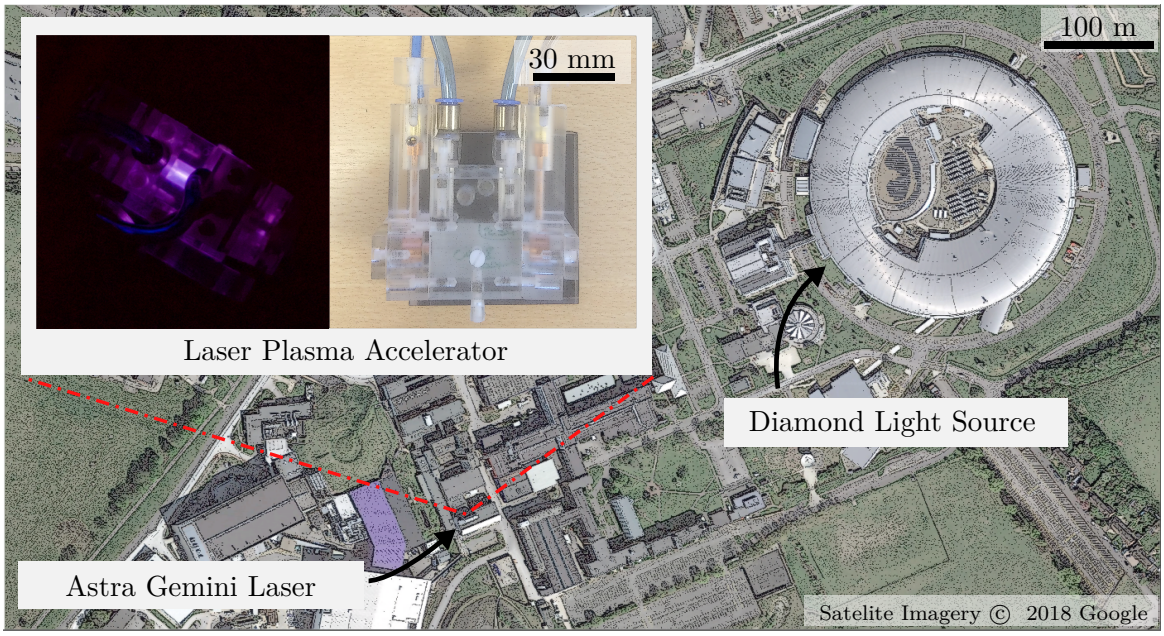

Figure 1.1: A comparison of the scale of two GeV particle accelerators. **Left**: A laser plasma accelerator developed by the Oxford Group[19] used in conjunction with the Astra-Gemini Laser System at the Central Laser Facility. **Right**: The Diamond Light Source, a synchrotron at Harwell Science and Innovation Campus in Oxfordshire.

tage LPAs have over conventional machines is that they are compact and that they produce ultrafast electron beams. A conventional machine can generate accelerating fields of order 50 MV m^{-1}[16,17], while LPAs can produce accelerating gradients three orders of magnitude higher exceeding 50 GV m^{-1}[18]. Figure 1.1 gives a sense of scale of two GeV level particle accelerators — the Diamond light source, a conventional synchrotron with a ring circumference of 561.6 m and an LPA of length 30 mm, used in conjunction with the Astra-Gemini laser system at the Central Laser Facility.

In this chapter the basic principles of LPAs will be briefly described. Scaling laws associated with LPAs will be explored and together with a look at the potential future applications of these machines a pertinent problem will be identified.

1.2 Laser Plasma Accelerators

A plasma is a quasi-neutral ionized gas consisting of positive ions and free electrons. Already being electrically broken down from neutral particles, a plasma can support extremely large electric fields without sustaining damage, making it an interesting candidate for a particle

accelerator medium. This idea of a plasma accelerator was originally put forward by Veksler[20] and further developed by Fainberg[21].

Then in 1979, the seminal paper by Tajima and Dawson[22] laid out the basic principles behind the idea of a Laser Plasma Accelerator. At the fundamental level, the Laser Plasma Accelerator relies on the ponderomotive force, F_p, which acts to push charged particles away from regions of high laser intensity:

$$\vec{F_p} = -\frac{e^2}{16\pi^2 m_e c^2}\lambda^2 \, \nabla E^2 \,, \tag{1.1}$$

where e is the elementary charge, λ is the wavelength of the driving laser, m_e is the mass of the electron and E is the amplitude of the electric field of the laser[23]†. The ponderomotive force arises from the time-averaged quiver energy associated with an electron in an oscillating electromagnetic field, known as the ponderomotive energy, U_p. The ponderomotive force is then defined as the gradient of the ponderomotive energy, $\vec{F_p} = -\nabla U_p$.

When a high-intensity laser pulse propagates through a plasma it ploughs electrons out of the way by the ponderomotive force, the ions being much heavier remain essentially stationary creating a separation of charge. Once the laser pulse has passed, the charge separation acts to pull the electrons back into the ion-rich region, where their momentum causes them to overshoot and oscillate about their initial position. As the laser pulse travels through the plasma, so too this electron density structure propagates, creating a longitudinal electron density wave which trails the driving laser pulse. This travelling electron density wave creates a set of fields, known collectively as a plasma wakefield, which can be used to accelerate charged particles to high energies.

The plasma electrons oscillate about the ion-rich core at their characteristic frequency, the plasma frequency ω_p, which depends solely on their density. The plasma frequency can be written as;

$$\omega_p = \sqrt{\frac{n_e e^2}{\epsilon_0 m_e}} \approx 56.4 \times 10^3 \sqrt{n_e \, [\mathrm{cm}^{-3}]} \,, \tag{1.2}$$

with n_e the average electron density and ϵ_0 the permittivity of free space. In addition, the

†Note that all equations presented in this thesis are given in SI units.

plasma and can sustain extremely large electric fields with one estimate, the cold non-relativistic wavebreaking limit[24], giving the order of maximum electric field as;

$$E_{WB} = \sqrt{\frac{m_e n_e c^2}{\epsilon_0}} \approx 96\sqrt{n_e\,[\mathrm{cm}^{-3}]}\,, \tag{1.3}$$

with c the speed of light *in vacuo*. For a plasma with $n_e = 10^{17}$ cm^{-3}, this corresponds to a maximum accelerating gradient of 30 GV m^{-1}.

Since their conception, LPAs have been the subject of an intense global research effort. Excellent reviews of the physics of LPAs and on their development over the last 40 years are readily available[25,26]. Throughout this time, LPAs have been, and continue to be, inseparably linked to developments in laser technology. From the beginning it had been known that intense laser pulses of order 100 fs in duration would be required to effectively drive a plasma wakefield[‡], but the technology simply did not exist[22]. Instead longer pulses were modulated to create a series of shorter pulses which could resonantly excite a plasma wakefield. This is an idea which has been revisited in recent years[27,28].

In 1985 the advent of chirped pulse amplification (CPA)[29] led to the development of high-power ultra-short laser pulses and the idea of driving strong plasma wakefields with a single short pulse was revisited[30,31]. An important breakthrough came in 2004 with the production of the first quasi-monoenergetic electron beams in a laser wakefield accelerator, achieved by three groups independently[32–34]. Shortly after this the acceleration of the first GeV electron beam from a laser wakefield accelerator[35,36] was observed, this was made possible through the use of a 33 mm long plasma waveguide which extended the laser-plasma interaction length, allowing the laser to accelerate particles for a longer distance than had been possible previously.

Today the highest reported electron energies from a laser plasma accelerator have been produced by guiding a highly intense laser pulse through a 90 mm long plasma waveguide and stand at 4.2 GeV[18]. There have been reports at conferences showing electron energy spectra extending to more than double this value, however at the time of writing this thesis, these results remain unpublished[37].

[‡]the ideal pulse duration, τ, occurs at $\omega_p \tau \approx \pi$, that is when the pulse duration is half the plasma period.

1.2.1 Challenges for Current LPAs — The Three D's

While LPAs offer synchrotron level energies over millimeter distances, they fall short of the beam quality, stability, efficiency and repetition rates obtained with conventional particle accelerators. The problems with current LPAs stem from a number of different areas including: limits to the current laser technology, electron injection mechanisms, laser guiding and controllability.

Additionally, there are three fundamental issues with the acceleration of electrons by a laser driven plasma wakefield; diffraction, depletion and dephasing.

Diffraction

In order to achieve the high intensities required for driving LPAs, laser pulses of reasonable energy ($\sim$ mJ $-$ J) must be focused down to small spot sizes (order 5-100 µm). However, once focused the laser pulses immediately start to diffract, limiting the distance over which they remain intense — and thus the acceleration length — to order the Rayleigh length. The Rayleigh length can be written as $z_R = \pi w_0^2/\lambda$, with w_0 the $1/e^2$ intensity spot size, see section 2.1. The effects of diffraction can be mitigated by use of a plasma waveguide, as was used in the first GeV electron beam experiment. The concept of a plasma waveguide will be discussed in detail in section 1.3 and 2.2.

Depletion

As the laser pulse propagates it loses energy in driving the wakefield. At some point it will no longer have the required energy to produce the high intensities necessary for driving a plasma wakefield. This situation is termed depletion and occurs over a length which scales as $L_{\text{deplete}} \sim \lambda_p^3/\lambda^2 \propto 1/n_e^{3/2}$, with λ_p the plasma wavelength. Depletion can be addressed by the staging of LPAs, of which there has already been a successful demonstration[38].

Dephasing

Dephasing is the process whereby the accelerated electrons will gain enough energy to move faster than the plasma wave and thus move from an accelerating phase of the plasma wave to a decelerating phase. It is possible for this to occur, as the plasma wave travels at the

group velocity of the laser pulse, which is lower than the velocity of light *in vacuo*. In the linear regime (section 1.2.3) this dephasing length is given as $L_{\text{dephase}} \approx \lambda_p^3/2\lambda^2 \propto 1/n_e^{3/2}$. Operation at lower densities can prolong the onset of dephasing — for example electrons in an LPA driven by an 800 nm drive pulse will dephase after 1.84 mm for a target density of $n_e = 10^{19}$ cm^{-3} compared with 1.84 m for a density of $n_e = 10^{17}$ cm^{-3}. In addition dephasing can be mitigated by longitudinal plasma density tailoring[39] — the basic idea here is that as the laser propagates through the plasma the density is raised to match the phase velocity of the plasma wakefield to the velocity of the accelerated electrons. Using this technique it is possible to accelerate electrons beyond the dephasing length.

1.2.2 Driving Laser Systems

The lasers used to drive LPAs are typically joule-level titanium sapphire (commonly denoted as Ti:sapphire) CPA systems. These are the lasers of choice due to their ability to produce petawatt levels of peak power in pulses a few tens of femtoseconds long[40]. The main drawbacks of this technology are its low wall-plug efficiency and low repetition rate. State of the art high-power Ti:sapphire systems typically operate at repetition rates of order 0.1 - 10 Hz with efficiencies much less than 0.1%[27]. The restricted repetition rate and low efficiencies are typically due to the poor thermo-optical properties of the pump lasers, commonly frequency doubled Nd:YAG systems. It should also be noted that the current laser systems used to drive LPAs have less than ideal beam quality and the improvement of this is expected to lead to benefits in the quality of accelerated electron bunches and generated radiation[41].

The problems with current laser technology have been identified within the LPA community and today there is a concerted effort towards the development of new laser driver technology looking to benchmark stable, high peak power, high average power and high wall-plug efficiency systems[42].

1.2.3 Operating Regime

The response of the plasma to the driving laser is broadly a function of the laser intensity, wavelength and focal spot size together with the plasma density[43]. It is helpful in the discussion of operating regimes to define the normalized vector potential, $a_0 = eA_0/m_e c$ where

A_0 is the peak value of the vector potential of the pulse. A practical formula for the normalized vector potential can often be quite useful:

$$a_0 \approx 8.5 \times 10^{-10} \lambda \, [\mu\text{m}] \sqrt{I_0 \, [\text{Wcm}^{-2}]} \,, \tag{1.4}$$

with I_0 the peak intensity of the pulse.

For an appropriate choice of parameters LPAs may be driven in what is known as the quasilinear regime. In this regime a near sinusoidal accelerating structure is driven which allows for nearly symmetric regions of acceleration and focusing for both electrons and positrons. As the process is quasilinear in nature, it is not as susceptible to experimental parameter fluctuations and is easier to control and tune than the nonlinear regime discussed below[43]. One of the major challenges facing LPA operation in the quasilinear regime is that by its very nature, electrons from the background plasma are not trapped by the plasma wave and so additional electron injection mechanisms must be investigated. The linear regime occurs when;

$$\frac{r_L^2}{\lambda_p^2} \gtrsim \frac{a_0^2}{2\pi\gamma} \,, \tag{1.5}$$

where $\gamma = \sqrt{1 + a_0^2/2}$ is the cycle averaged Lorentz factor of electrons oscillating in the field of the laser and r_L is the characteristic length scale of the transverse laser intensity profile[43].

By using a laser pulse with a higher a_0, LPAs may be driven in what is known as the bubble regime. In this regime a highly nonlinear plasma wake structure is driven to produce a spherical electron-free, ion cavity which propagates behind the driving laser pulse. Electrons from the plasma fall back into the wake structure and are trapped before being accelerated to high energy. The advantage of this technique is that, under ideal conditions, it can provide beams with relatively narrow band energy spectra[32–34] (order 1-10%) but as with any highly nonlinear process, fluctuations in the experimental parameters can play a large role in the resulting dynamics and thus this mechanism is hard to control. In addition, there can be large shot-to-shot fluctuations in the accelerated beam properties. Furthermore, this regime is favourable for electron acceleration, but not well-suited to the acceleration of positrons as the electron-free cavity is defocusing for positrons and thus there is only a small volume in which

they can be injected[43]. To drive the bubble regime, it is necessary to have $a_0 > 4$[44] and for

$$\frac{r_L}{\lambda_p} \lesssim \frac{\sqrt{a_0}}{\pi}. \tag{1.6}$$

It should also be noted that in this regime the laser pulse is self-guided (see section 1.3.3).

Given that many applications benefit from positron acceleration and that there is the possibility for increased control and reproducibility, it is advantageous for LPAs to operate in the quasilinear regime.

1.2.4 Electron Injection Mechanisms

The mechanism by which electrons are injected into the plasma wakefield structure has a large impact on beam quality. LPAs operating in the bubble regime are easier to realize experimentally as they self-inject electrons from the ambient plasma. However, injection can happen throughout the acceleration process rather than at one localized point which can lead to large energy spread and beam emittance issues. These effects can be mitigated by localizing the injection process.

Techniques used to localize the injection process include density transition injection[45,46], ionization injection[47–49] and colliding pulse injection[50,51]. Localization of the point of injection can lead to lower energy spreads in the accelerated beam and lower emittances. Ideally a wakefield would be driven in the quasilinear regime where it can be carefully controlled and an electron beam would be injected in a small space and in a short time into the accelerating and focusing phase of the plasma wakefield. External injection from a conventional electron source has also been investigated and in fact was the main method of electron injection employed in early LPAs. However, as electron beams from conventional sources are typically very long in comparison to the plasma wavelength (length scale of the wake structure), this method of injection is difficult to control and can lead to electrons being injected into multiple accelerating buckets[52].

Parameter	**Diamond Linac**[56]	**Low-E LPA**[55]	**Diamond Booster**[57]
Energy (GeV)	0.1	0.35	3
RMS Energy Spread	0.25 %	0.74 %	-
Normalized Emittance (mm mrad)	50π	0.05π	0.045π
Pulse Duration (ps)	1000	0.035	-
Bunch Charge (pC)	50-1500	12.8	-
Repetition Rate (Hz)	5	1[§]	5

Table 1.1: Comparison of two conventional accelerators used at the Diamond Light Source Facility with a state of the art low-energy LPA.

1.2.5 Comparison with Conventional Accelerators

Conventional accelerators, a mature technology when compared to the relative infancy of laser plasma accelerators, offer excellent beam quality, reliability and reproducibility all at high repetition rates well into the kHz and MHz regimes[53]. While today's LPAs fall short of that pedigree, there has been steady progress in their development worldwide.

Much work is currently focused on the improvement of the electron beam quality and stability. For example the EuPRAXIA project in Europe is being designed to demonstrate stable, high-quality electron beams and radiation sources capable of meeting the demands of industrial, medical and high-energy physics applications[54].

While it is important to realize that the beam quality of laser plasma accelerated electrons must be improved, it is useful to note that state of the art LPAs are already comparable to some conventional accelerators. Table 1.1 provides a comparison of the 100 MeV Linac and 3 GeV Booster synchrotron used at the beginning of the Diamond Light Source facility with beam parameters from a recently published article demonstrating ultra-low-emittance high-quality electrons beams from a laser wakefield accelerator[55].

While these parameters appear quite similar, there are some noteworthy differences, firstly the charge accelerated by LPAs is significantly lower than that produced by the conventional machine. However, in contrast, LPAs can provide much shorter bunch durations meaning that the peak current is typically higher for LPAs. Nanocoulomb-class LPAs have been developed, although currently the addition of extra charge tends to degrade the resulting beam quality[59].

Another important distinction is in the beams themselves, as discussed by Couprie[60]. While the normalized emittance of the Booster Synchrotron and the low energy LPA are

comparable on paper, the beams are actually quite different and this can make the coupling of LPA beams into secondary devices difficult. LPAs typically provide transverse beam profiles on the micrometer scale together with wide divergences on the milliradian scale. In contrast, conventional Linacs, typically provide millimeter scale transverse beam profiles together with low microradian divergences. Magnetic focusing can of course allow one to convert between the two extremes, but in the case of LPAs, the focusing device needs to be placed close to the source to catch the exiting electron beam, which can prove difficult.

One of the most challenging differences to remedy is the energy spread of LPA electron beams. The LPA described here is an exceptional example of a low-energy-spread beam, it is far more typical for the energy spread to be 5-10 %. This is particularly problematic when it comes to using an LPA electron beam as a driver for a Free Electron Laser (FEL), which is typically driven by an electron beam with an energy spread approaching 0.01%[60]. It is possible to reduce the energy spread of electron beams post-acceleration using a plasma de-chirper[61], although a reduction in energy-spread from the few percent level to levels suitable for FEL operation has not yet been demonstrated.

1.3 Plasma Waveguides for High-Intensity Laser Pulses

Diffraction is one of the fundamental problems associated with laser driven particle accelerators. A laser pulse focused down to achieve high intensity will not remain small indefinitely but rather will diffract and thus lose intensity on a length scale given by the Rayleigh Range z_R, which scales as the inverse square of the laser intensity spot size, $z_R \propto w_0^{-2}$. The higher the required intensity, the shorter the distance over which it can be maintained. This limits the acceleration distance to the same scale, unless the effect of diffraction can be mitigated.

Extension of the acceleration length of LPAs is possible through the use of plasma waveguides — either grazing-incidence waveguides with a plasma core or gradient refractive index plasma waveguides. Grazing-incidence waveguides for LPAs are a special case of step-index waveguides and take advantage of the grazing-incidence reflection at the interface of a solid dielectric material and a plasma. Gradient-index plasma waveguides have a transverse refractive index profile which is peaked on-axis, meaning that phase velocity along the optical axis is

slower than the phase velocity in the wings of the pulse. The faster wings cause the wavefront of the pulse to curve towards the axis replicating a focusing effect.

In a perfect waveguide the effects of diffraction are exactly cancelled out by the focusing effect of the waveguide. In this way it is possible to capture a pulse at focus and cause it to propagate for long distances while remaining tightly focused and thus retaining its high intensity. A plasma waveguide, being composed of a material which is already electrically broken down, will not sustain lasting damage from the passage of a high-intensity laser pulse and can thus be reliably used to guide high-intensity laser pulses. For a detailed discussion of the physics of plasma waveguides see section 2.2.

The idea of a plasma channel working as a "light pipe" originated in the 1970's in the field of thermonuclear fusion[62] where it was postulated that a creating a plasma with a density minimum on-axis and higher densities off-axis would lead to a laser pulse being trapped within this plasma channel structure allowing it to propagate for long distances. The creation of these plasma density structures has been achieved in a number of ways in the intervening decades.

1.3.1 Hydrodynamic Expansion of Laser-Heated Plasma

One of the first successful methods of creating a gradient-index plasma channel structure was through the hydrodynamic expansion of a laser-produced plasma[63–65]. A high-powered laser fired into a gas can ionize it and heat the subsequent plasma to high temperatures. This hot column of plasma will then expand radially outwards into the cold surrounding gas, driving a shockwave as it does so. After an appropriate amount of time, the high density wall of the shock together with the lower density centre, create a density structure suitable for guiding.

In the original work[63] a 100 ps laser pulse fired into Ar, Ne or Xe ionized the neutral gas and heated the plasma through inverse bremsstrahlung heating — this is a process whereby free electrons are driven by the laser field and collide with ions transferring the coherent motion of the oscillation into random, thermal motion. This inverse bremsstrahlung heated plasma then expanded and generated plasma channels which allowed for the guiding of a moderate intensity pulse ($10^{13} - 10^{14}$ W cm^{-2}) over 24 Rayleigh ranges. The two steps in this process; ionization and heating, each have different laser requirements. Ionization favours a relatively intense pulse, where as heating is better achieved by a long and not necessarily

intense pulse. The use of a high-Z gas facilitates the ionization[25,64] process due to its outer electrons being more weakly bound to the atom than that of a low-Z gas. This allows for a moderate intensity pulse to both ionize and heat the plasma, which can then become further ionized due to collisional ionization of the heated electrons with the ions.

The drawback of using high-Z gases is that they do not easily become fully ionized, and so guiding a high-intensity pulse can be problematic as there is a strong chance that such a pulse will further ionize the plasma within the channel, potentially destroying the channel structure. Additionally, ionization-induced phase modulations can distort intense pulses passing through the channel. To mitigate these effects, low-Z gases would ideally be used to form plasma channels as they are the easiest to fully ionize.

Attempts to employ low-Z gases were made by separating out the ionization and heating mechanisms, such as the ignitor-heater method[66]. Here a short high-intensity ultrafast ignitor pulse (< 100 fs) was used to form the initial plasma, while heating was achieved through the addition of a low intensity heater pulse (160 ps). By this method, fully ionized plasma channels were generated in a hydrogen target and were subsequently used to guide high-intensity pulses. Indeed one of the original breakthrough papers of 2004 describing quasi-monoenergetic electron production used this method of channel formation[33]. Variations on this technique were also investigated by other groups[67].

Other attempts to generate fully ionized plasma channels, by Gaul et al., included pre-ionizing a small fraction of a He target gas with an electrical discharge, or simply by using more energy in a longer pulse to allow avalanche ionization and inverse bremsstrahlung heating to have enough time to build up from trace field-ionized electrons[68].

The methods above all rely on inverse bremsstrahlung heating which requires high initial target densities to be efficient — this means in practice that the waveguides are limited to on-axis densities above 10^{18} cm^{-3} which is problematic for high-energy LPAs. In addition, LPAs hoping to make use of these waveguides require auxiliary laser systems to produce the picosecond heating pulses in addition to the ultrafast high-intensity pulses for driving a plasma wakefield.

In 2005, in an attempt to push down the on-axis densities of these hydrodynamically expanding plasma waveguides, Kumarappan et al. employed clustered gases[69]. In addition,

femtosecond pulses were used to mitigate the need for an auxiliary laser system.

Clustered gases, having low average density but near solid local density, can be ionized through optical-field-ionization and efficiently heated by inverse bremsstrahlung heating with femtosecond pulses. This means a single ultrafast high-intensity pulse can be used to both ionize and heat the plasma. After the femtosecond pulse has passed, the ionized clusters undergo a Coulomb explosion and form a locally uniform plasma in under 100 ps[69]. Subsequently they undergo a hydrodynamic expansion similar to the methods above. In addition, the refractive properties of clusters leads to a self-focusing effect which prolongs the optical propagation of the channel-forming pulse. With this method the on-axis density of hydrodynamic plasma waveguides was reduced to $\sim 10^{18}$ cm^{-3}

In 2015, Lemos et al.[70] attempted to mitigate the need for an auxiliary laser system by above threshold ionization heating of unclustered hydrogen and helium targets using 400 fs pulses. A second paper from the same experiment investigated the effect of the polarization of the driver pulse on the hydrodynamic expansion, showing that circularly polarized light produced a faster expansion[71]. These two papers were the first to show hydrodynamic expansion of a laser-produced plasma column which was not predominantly heated by inverse bremsstrahlung heating. The focus of the paper was the use of ultrashort pulses to generate plasma waveguides in place of the $\sim$ 100 ps systems used previously, although the authors did not seem to be aware of the work by Kumarappan et al.[69] discussed above. In these experiments the on-axis densities extended down as far as $1 - 2 \times 10^{18}$ cm^{-3} which the authors acknowledge as useful for LPAs however, the authors did not seem to have considered the application of these field-ionized plasma channels to act as low-density plasma waveguides. This will be investigated in chapter 3. Within a year of finishing this thesis another work from the same group was published demonstrating low-intensity guiding over 4 Rayleigh Ranges in the same plasma channels, formed by a lens[72].

1.3.2 Capillary Based Waveguides

Another set of methods used to generate plasma channels suitable for guiding high-intensity laser pulses is through the use of capillaries. Initial experiments made use of hollow dielectric capillaries where ionization of the inner capillary wall led to the formation of an overdense

plasma which acted in concert with the grazing-incidence reflection from the vacuum-dielectric interface to form a grazing-incidence plasma waveguide[73,74]. Ionization from the wall was not a necessary condition for guiding but acted to enhance it. The guiding in these first experiments was multi-mode.

Soon after, mono-mode guiding in hollow dielectric capillaries was demonstrated and an elongation in capillary lifetime was achieved by filling the capillary with gas[75–77]. In addition, the applicability of gas-filled capillaries to LPAs was discussed[78]. Electron acceleration in gas-filled dielectric capillaries has subsequently been demonstrated experimentally[79] and it was found that electron acceleration was observed at lower incident intensities than would be possible for a gas jet target. It was also demonstrated that the diameter of the capillary structure had an influence on the electron acceleration. One advantage of these grazing-incidence waveguides over the hydrodynamic expanding waveguides discussed above is the ability to choose the operating plasma density independent of the guiding requirements. This is possible as the guiding arises not from the plasma density profile, but due to reflection at the plasma-dielectric interface.

Capillary waveguides relying on gradient-index guiding were first developed by Zigler et al.[80] and expanded on by others[81–83]. They involved the ionization of a hollow-capillary not by a laser but instead by a slow (microsecond) electrical discharge of a few kilovolts. In these discharge-ablated capillary waveguides, the plasma ionized from the wall filled the capillary and was then heated by the continuing discharge. Thermal conduction at the capillary walls led to the formation of a temperature profile which was peaked on-axis. As the pressure throughout the capillary was uniform, this resulted in a plasma density with a minimum on-axis. The main issues with these discharge-ablated capillary waveguides is firstly, their low lifetime (typically 1000 shots) due to ablation of the wall and secondly, the fact that they form partially ionized plasmas containing impurities from the walls.

Spence & Hooker expanded upon the work of Zigler and developed a hydrogen-filled capillary discharge waveguide made from alumina (Al_2O_3)[84,85]. In this device a slow discharge, 25 kV, 300 A, 200 ns was sparked in a capillary filled with hydrogen. The hydrogen was ionized and heated by the discharge, forming a gradient-index guiding structure in a similar fashion to the Zigler capillaries, namely by developing an axially peaked temperature profile through

thermal conduction to the capillary walls. Forming the plasma from hydrogen gas rather than the capillary wall itself allowed for an increase in capillary lifetime of three orders of magnitude to 10^6 shots. The contamination of the plasma with Al and O ion impurities from the capillary walls were determined to be small at 0.3% and at this level, could in fact be useful for techniques such as ionization injection. Another advantage of using hydrogen gas was the ease with which is could be fully ionized, mitigating the effect of ionization induced refraction which can occur in partially ionized plasmas.

Since being proposed these gas-filled capillary discharge waveguides have been shown to work with a number of different target gases[84], have been shown to work at low densities with electron generation being observed for on-axis electron densities of 3.2×10^{17} cm^{-3}[86]. Developments with water cooling the structure and improvements to the discharge technology, spearheaded by the Berkeley group, have led to the demonstration of guiding of continuous wave lasers with these waveguides at kHz repetition rates[87]. There is however, no evidence of guiding high-intensity pulses at high repetition rate¶.

Another method of generating gradient-index waveguides in capillary structures is through the use of a Z-Pinch. This technique was pioneered by Hosokai et al. and while this work uses an electrical discharge in a gas filled capillary, the process of channel formation is fundamentally different to the device developed by Spence & Hooker due to the differing discharge properties. Hosokai employed a 20 kV, 4.8 kA, 15 ns Z-Pinch discharge in a helium-filled alumina capillary. The magnetic pinch effect associated with the z-pinch compressed the plasma, forming a shockwave which travelled radially inwards. Prior to reaching the axis, the converging shockwave led to the formation of an electron density profile with a minimum on-axis. These capillaries suffered from low lifetimes ($\sim 10^4$ shots), complex electrical circuitry and unstable shot-to-shot guiding due to electrical jitter.

¶Capillary Discharge Waveguides have demonstrated operation at 1 kHz for a duration of almost 3 hours with negligible erosion of the capillary wall due to the discharge. However, in these tests a CW laser was guided, not a highly-intense pulsed beam. The authors suggest in their conclusions that a sufficiently high-quality laser mode and an auxiliary pulse to extract residual wake energy through photon acceleration could allow for LPA operation at kilohertz repetition rates[87]. While extraction of wake energy has indeed been demonstrated[28], there is no experimental evidence yet, supporting the claim that this technique would be sufficient to allow kilohertz operation of a gas-filled capillary-discharge waveguide with a high-intensity pulse.

1.3.3 Self-Guiding

While many of the techniques discussed so far rely on the creation of a preformed plasma channel for guiding, this is not necessarily needed. At high-enough intensities an intensity-dependent refractive index increase is seen. This increase in the refractive index is highest on-axis, where the pulse is most intense, and leads to a focusing effect. The intensity-dependent refractive index arises from two effects **i)** a relativistic increase in the electron mass due to their quiver motion and **ii)** a reduction in electron density due to the ponderomotive expulsion of electrons[88,89].

This self-focusing effect will counteract diffraction when the laser pulse exceeds a critical power, $P_{cr}[\mathrm{GW}] = 17.4\frac{n_{cr}}{n_e}$[90]. However, the condition for self-focusing is not enough to ensure self-guiding. The guiding effect arises from the high-intensity modification of the plasma refractive index and so the leading edge of the laser pulse, which has a lower intensity, is not guided in the same manner as the rest of the pulse. This causes the leading edge of the pulse to not be guided but to diffract, albeit at a rate slower than vacuum diffraction[91]. Indeed this etching of the front of the pulse can cause the laser to develop a sharp rising edge which can lead to pulse breakup[92]. This is particularly problematic for short pulses and was one of the reasons it was originally thought that it would not be possible to self-guide ultrashort pulses $c\tau < \lambda_p$. However, it has since been demonstrated that self-guiding is indeed possible for short pulses provided that the leading edge of the pump pulse depletes quicker than it diffracts. This leads to a stricter definition of the power necessary for self-guiding of short pulses $P^*_{cr}[\mathrm{GW}] = 2.18\left(\frac{n_{cr}}{n_e}\right)^{8/5}$[44]. For channel guided laser pulses, where diffraction of the leading edge is mitigated, this condition relaxes to $P^*_{cr} \gtrsim P_{cr}$ and the self-guiding and channel guiding effects can work in tandem to keep the pulse guided.

While this guiding method offers the advantage of simplicity and robustness, it requires that the electron motion in the incident laser field to be relativistic, meaning that operation of LPAs based on self-guiding is inevitably restricted to the nonlinear-wakefield regime where there is much less control over the properties of the accelerated electron bunch. Further, operation at low-densities requires extremely high-power lasers; for example an LPA working with an 800 nm drive laser at an electron density of 10^{17} cm^{-3} requires a power 0.3 PW to self-guide or 100 PW to self-guide if it is ultrashort and the scaling by Lu et al. is followed[44].

1.4 Looking to the Future

It is an exciting time for LPAs. Energy spread aside, LPAs are fast approaching the beam quality necessary for use as injectors to synchrotron light sources and seeds for FELs. Operation in the quasilinear regime together with the successful mastering of controlled injection will likely lead to the reduction in energy spread necessary for precise scientific applications. In addition, LPAs have already been successfully used to generate antimatter[93,94], applied to medical imaging[7] and have shown promise as being suitable for a host of other applications in industry and defence[95].

One of the outstanding issues, preventing LPAs from becoming competitive alternatives for accelerator applications in industry, medicine and science, is the repetition rate and the shot-to-shot stability of the accelerated beams. It should be noted that these two issues are not independent; increased repetition rates will allow for the development of more stable and robust accelerators through the use of automatic feedback systems as has been recently demonstrated[96].

As discussed earlier, the laser technology necessary for kilohertz operation of LPAs has been identified as a pressing issue but it is not just the laser technology which is preventing high repetition rate operation. Robust plasma sources also need development to operate for extended periods at this level. Several groups have recently demonstrated kilohertz operation of MeV-scale LPAs, taking advantage of several developments in plasma source technology including near-critical density gas jets[97], micro-scale gas jets[98,99] and flowing-liquid targets[100].

It would be advantageous to develop plasma sources and associated technologies capable of multi-kilohertz operation for days without the need for source replacement. In this thesis the issue of plasma waveguide development for future high-repetition rate LPAs is investigated. Assuming a method of confining the target gas in a suitably robust way is developed, the question remains; how is a high-repetition rate plasma waveguide constructed within that gas?

1.5 The Problem: Waveguides for the Next Generation of LPAs

Current proposals for the next generation of high energy LPAs, such as the BELLA 10 GeV project and the EuPRAXIA 5 GeV project require guiding of the driving laser pulses over distances on the order of hundreds of millimeters in plasma channels with low on-axis densities of order 10^{17} W cm^{-2}[101,102].

With this in mind, it is possible to start thinking about what an ideal plasma waveguide for this next generation of laser plasma accelerators looks like. Such a waveguide should: **i)** be able to operate for extended periods at high repetition rate without damage to the waveguide structure allowing for long uninterrupted periods of operation. **ii)** It should be capable of operation at low density of order 10^{17} cm^{-3}. **iii)** It should be capable of guiding high-intensity laser pulses ($\sim 10^{17}$ W cm^{-2}) over hundreds of millimeters. **iv)** It should be compatible with wakefield acceleration in the quasilinear regime.

Currently no waveguide can meet all four of these requirements. It is possible instead, to group the current waveguiding technologies into two categories. **a)** Waveguides which can operate at low density but are susceptible to laser damage, such as the capillary based waveguides and **b)** waveguides which are effectively indestructible but cannot operate at low density, such as the hydrodynamically expanding plasma waveguides. Self guiding would also fall into category **b** with the additional constraint of not being able to operate in the quasilinear regime.

In this thesis, a new plasma waveguide capable of meeting these challenging requirements is investigated. The Hydrodynamic Optical-Field-Ionized (HOFI) plasma waveguide is an adaptation of the hydrodynamically expanding plasma waveguide discussed in section 1.3.1. Rather than collisional ionization and heating of the initial plasma with picosecond pulses, optical-field-ionization and heating with femtosecond pulses is employed. Optical-field-ionization being an atomic process, heats the ionized electrons independent of the target density. This allows for the formation of low-density initial plasma columns which can subsequently expand into low-density plasma channels. In addition, optical-field-ionization is ideally suited to femtosecond pulses and so there is no need for an auxiliary laser system to produce the plasma channel.

1.6 Thesis Outline

The contents of the remaining chapters are outlined below:

Chapter 2: Theory and Methods

A review of theory relevant to the subsequent chapters is presented here along with experimental methods pertaining to the key diagnostics. The theory relates to plasma waveguides, optical-field ionization, Sedov-Taylor blast wave theory and axicon focusing. The methods include details of the focal spot analysis techniques for both parabolas and axicons together with a detailed discussion of transverse and longitudinal interferometry.

Chapter 3: Demonstration of Low-Density Lens-Formed HOFI Plasma Channels

Results are presented here from the first proof-of-principle demonstration that optical-field-ionized plasmas can form low-density hydrodynamic plasma channels. The experiments here were performed using the Oxford group's TW laser system.

Chapter 4: Guiding In Axicon-Formed HOFI Plasma Channels: Experimental Design and Setup

The results of chapter 3 helped to bolster an application for beam time at the Astra-Gemini facility to demonstrate guiding in low-density axicon-formed HOFI plasma channels. Here design considerations for that experiment are discussed and the experimental layout that was employed is presented.

Chapter 5: Guiding In Axicon-Formed HOFI Plasma Channels: Implementation and Results

The implementation of the experiment at the Astra-Gemini facility and the key experimental parameters are discussed. The experimental results are presented, demonstrating for the first time, axicon-formation of HOFI plasma channels together with the guiding of a high-intensity pulse in those channels.

Chapter 6: Conclusions

A summary of the work described in the thesis is presented along with conclusions. Finally, the scope for future work on HOFI plasma channels is discussed.

Chapter 2

Theory and Methods

In this chapter the theory and methods relevant to subsequent chapters of the thesis are discussed. This includes a detailed look at focusing, plasma waveguides, optical-field-ionization, Sedov-Taylor blast wave theory, beam simulation, experimental beam characterization and interferometry.

2.1 Focusing of Electromagnetic Radiation

The focusing of electromagnetic radiation for the generation of high intensities is typically achieved using spherical or parabolic optics. When these optics are used in combination with Gaussian beams there are some useful relationships which act as a shorthand for determining the properties of the focused beam. While the spatial profile of beams produced by high-power Ti:sapphire laser systems are typically closer to a top-hat or super Gaussian profile, it is found that these relationships are still a good approximation.

The f-number of a focusing system is defined as $f_{\#} = f/D$, where f is the focal length of the optic and D is the diameter of the beam incident upon that optic. Knowing the $f_{\#}$ of the focusing system allows for quick estimates of parameters such as the spot size w_0, which for a Gaussian beam is the radius at which the intensity falls to $1/e^2$ of its peak value;

$$w_0 = \frac{2\sqrt{2}}{\pi}\lambda f_{\#} \approx 0.9\lambda f_{\#}\,. \tag{2.1}$$

High intensities can be achieved when a beam is focused to a small spot size, although

once focused, the beam will quickly start to expand again, causing the peak intensity to drop. The spot size of a lowest-order Gaussian beam evolves as,

$$w(z) = w_0\sqrt{1 + \left(\frac{z}{z_R}\right)^2}, \tag{2.2}$$

with z_R the distance, measured from the focus, over which the peak intensity of beam drops by a factor of two. This is defined as the Rayleigh range or Rayleigh length[103],

$$z_R = \frac{\pi w_0^2}{\lambda} \approx 2.5\lambda f_\#^2\,. \tag{2.3}$$

For example, for an 800nm beam focused to a spot size of $w_0 = 20$ µm, the Rayleigh range is 1.57 mm, leading to a total distance over which the peak intensity exceeds at least half the focal value of $2z_R = 3.14$ mm. Diffraction can therefore pose practical problems since not only is the intensity continuously varying over any finite interaction region, but assuming that the experiment requires high intensity, as is the case in many LPA experiments, the effective interaction is limited to order the Rayleigh range.

To increase the interaction length, there are several options. The easiest solution is to use a higher $f_\#$ focusing setup, although at the cost of a reduced peak intensity which varies as $I_0 \propto 1/f_\#^2$ for a fixed laser energy. A different kind of focusing optic, such as an axicon could be used (section 2.5), although this also reduces the peak intensity achievable for a given laser energy. However, one of the most common solutions is to prevent diffraction by guiding the beam.

2.2 Plasma Waveguides

In section 1.3 the need to guide highly-intense laser pulses over distances exceeding the Rayleigh length was established in the context of laser plasma accelerators. Two plasma waveguides were introduced; the grazing-incidence waveguide and the gradient refractive index plasma waveguide. In this section the theory of plasma waveguides is discussed.

2.2.1 Grazing-Incidence Waveguides

As mentioned in section 1.3, grazing-incidence waveguides are a special case of step-index waveguides and take advantage of the grazing-incidence reflection at the interface of a solid dielectric material and a plasma.

A step-index optical waveguide consists of a core of refractive index η_{core} and an outer cladding with a refractive index η_{clad}. The step-index refers to the abrupt change in refractive index at the core-cladding interface. Solving the Fresnel equations at this interface shows that for the case of $\eta_{\text{core}} > \eta_{\text{clad}}$, a ray which hits the interface at grazing-incidence will undergo total internal reflection. Indeed a full electromagnetic treatment shows that for the case of a cylindrical step-index waveguide, there exists a set of bound or lossless modes. The impact of step-index optical fibres in the telecommunications industry is well known.

In guiding high-intensity lasers it is necessary to employ a plasma or vacuum core to avoid lasting damage to the waveguide structure. Plasma has a refractive index, $\eta_{\text{plasma}} < 1$, and so for a dielectric cladding a step-index waveguide with a plasma core will have $\eta_{\text{core}} < \eta_{\text{clad}}$. This means that total-internal reflection is not possible and thus there are no truly bound modes, only quasi-bound modes. However, at grazing incidence, reflection from the plasma-dielectric interface is high and so a laser pulse can be guided a considerable distance, albeit whilst experiencing a small propagation loss.

Achieving monomode guiding in these waveguides requires matching the radius of the core region to the input spot size. It has been shown that by selecting a core radius of $r_{\text{core}} = 1.55\ w_0$, it is possible to couple 98 % of a Gaussian beam into the lowest order mode of the waveguide[104].

The transmitted energy in a grazing-incidence waveguide with a vacuum core decays exponentially with increasing waveguide length,

$$T = T_0 \exp^{-\alpha_{1/\text{e}} L}, \tag{2.4}$$

where L is the length of the waveguide and $\alpha_{1/\text{e}}$ is loss per unit length which, for the lowest

order mode, can be written as:

$$\alpha_{1/\mathrm{e}} = \frac{2.88}{k^2 r_{\mathrm{core}}^3} \frac{1+\epsilon_{\mathrm{clad}}}{\sqrt{\epsilon_{\mathrm{clad}}-1}}\,, \tag{2.5}$$

here, k is the free space wavenumber in vacuum, r_{core} is the radius of the core region and ϵ_{clad} is the relative permittivity of the cladding region[104]. For 800 nm light in a glass capillary ($\epsilon_{\mathrm{clad}} = 2.25$) of core radius 30 µm, it is found that the $1/e$ attenuation length $L_{1/\mathrm{e}} = 200$ mm. The addition of gas to the hollow capillaries and the use of high-intensity lasers, as required for experiments in plasma acceleration, increases coupling and propagation losses. The drop in transmission, shown to be of order 40 % for the addition of 20 mbar of helium, is linked with ionization of the neutral gas[75].

2.2.2 Gradient Refractive Index Plasma Waveguides

As stated in the introduction, gradient refractive index plasma waveguides have a transverse refractive index profile which is peaked on axis, meaning that the phase velocity along the optical axis is slower than the phase velocity in the wings of the pulse. The faster wings cause the wavefront of the pulse to curve towards the axis replicating a focusing effect.

The required variation of refractive index can be produced by a varying electron density profile in a plasma. The refractive index of a plasma can be written as,

$$\eta = \sqrt{1 - \frac{n_e e^2}{m_e \epsilon_0 \omega^2}}\,, \tag{2.6}$$

where n_e is the local electron density, e is the elementary charge, m_e is the mass of the electron, ϵ_0 is the permittivity of free space and ω is the laser frequency. It is useful in this case to define the critical density, the density at which electromagnetic radiation of frequency ω will not propagate within the plasma but be reflected from it (section 2.5.2);

$$n_{cr} = \frac{m_e \epsilon_0 \omega^2}{e^2}\,. \tag{2.7}$$

In the limit of $n_e/n_{\mathrm{cr}} \ll 1$ a Taylor expansion of the square root is possible and the

refractive index may be written as,

$$\eta \approx 1 - \frac{n_e}{2n_{\mathrm{cr}}}\,. \tag{2.8}$$

This condition holds for optical wavelengths and plasma densities in the range useful for LPAs (10^{17} to 10^{19} cm^{-3}). In this case the plasma is said to be highly underdense[105].

Infinite Parabolic Plasma Waveguide

As can be seen from equation 2.8, an increase in electron density will provide a reduction in refractive index and so an electron density profile with a minimum on axis can act as a gradient-index plasma waveguide. One example is the infinite parabolic plasma waveguide which has a parabolic electron density profile given by,

$$n_e(r) = n_0 + \frac{1}{w_m^4 \pi r_e} r^2\,, \tag{2.9}$$

where r is radial distance from the optical axis, r_e is the classical electron radius and w_m is the $1/e^2$ intensity spot size of the lowest order mode of the channel, known as the matched spot size.

The modes of such a plasma waveguide can be represented by a set of Laguerre-Gauss modes[106–109]

$$E(r,\phi,z) = A e^{-\frac{r^2}{w_m^2}} \left(\frac{2r^2}{w_m^2}\right)^{\frac{m}{2}} L_p^m\left(\frac{2r^2}{w_m^2}\right) e^{im\phi} e^{i\beta z}\,, \tag{2.10}$$

where A is a scaling factor and $L_p^m(x)$ is the generalized Laguerre polynomial. The modes in equation 2.10 are determined by the radial and azimuthal indices p and m, with the $m \neq 0$ modes having an intensity node on axis. The first few modes are plotted in figure 2.1.

While the matched spot size of the lowest order mode has been defined for an infinite parabolic plasma waveguide, the result is applicable for plasma channels with a wide range of transverse profiles[106].

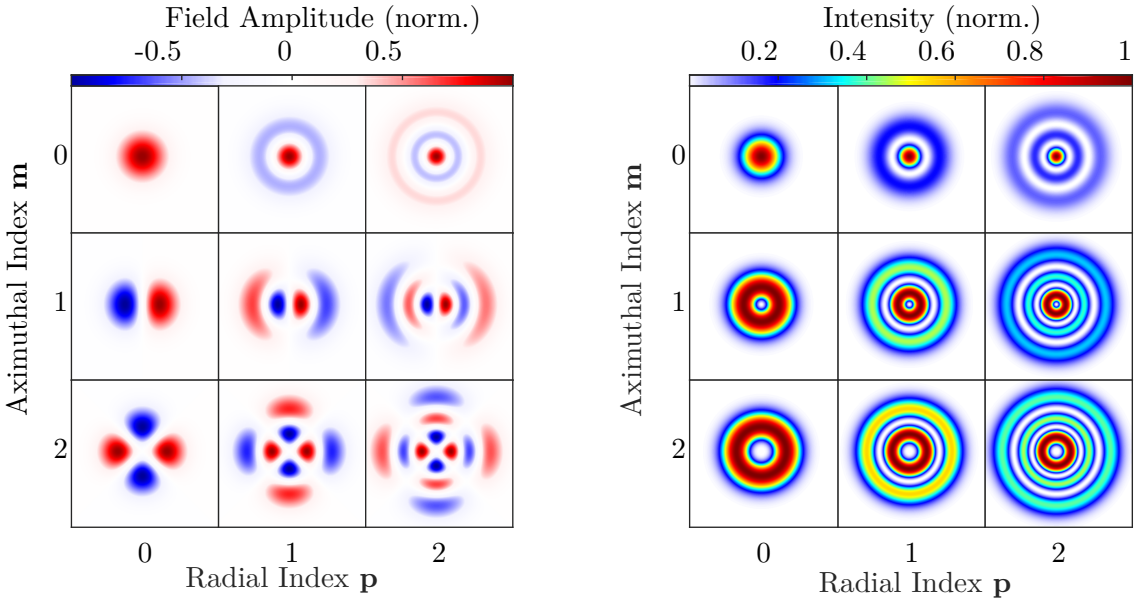

Figure 2.1: Electric field (left) and intensity profiles (right) of the first nine Laguerre-Gauss modes covering the index space $m = 0, 1, 2$; $p = 0, 1, 2$.

Truncated Parabolic Plasma Waveguides

The generation of an infinite parabolic plasma waveguide is, of course, impossible. Real plasma waveguides are better represented by a truncated parabolic plasma waveguide as depicted in figure 2.2. The mode structure of such a waveguide has been shown to be well approximated by the mode structure of the infinite parabolic plasma waveguide, albeit with a reduced number of modes. The modal cut-off is determined by the electron density difference between the axis and the wall, together with the radius of the wall[106]. Allowed modes satisfy the equation;

$$\Delta n_e = n_e(r_w) - n_e(0) \geq \frac{(2p + m + 1)^2}{\pi r_e r_w^2}\,, \tag{2.11}$$

with $n_e(0)$ the on-axis electron density, r_w the radius at which the wall of the channel peaks and $n_e(r_w)$ the electron density at the wall. Here, as above, p and m are the radial and azimuthal mode indices.

A detailed investigation into the attenuation of the modes in real graded-index plasma waveguides has been performed by Clark et al.[109], who investigated the modal structure both analytically and numerically. Solving the wave equation for the modal structure of a plasma

waveguide amounts to solving the Helmholtz equation;

$$\nabla_{\perp}^{2} u(\vec{r_{\perp}}) + \kappa^{2}(\vec{r_{\perp}}, \omega) u(\vec{r_{\perp}}) = 0\,, \tag{2.12}$$

with $\nabla_{\perp}^{2}$ the transverse Laplacian, κ the transverse wavenumber and $u(\vec{r_{\perp}})$ the amplitude of the axially propagating electric field solutions to the wave equation, $E(\vec{r_{\perp}}, z) = u(\vec{r_{\perp}}) \exp^{i\beta z} \exp^{-\alpha_{1/e} z}$. Here β is the real part of the propagation wavenumber in the plasma channel while $\alpha_{1/e}$ describes the attenuation along the waveguide due to tunneling losses of the field energy.

The transverse wavenumber can then be represented by;

$$\kappa^{2}(\vec{r_{\perp}}, \omega) = k^{2} \left(1 - \frac{n_e(\vec{r_{\perp}})}{n_{\mathrm{cr}}} - \frac{\left(\beta^{2} + \alpha_{1/\mathrm{e}}^{2}\right)}{k^{2}} \right)\,. \tag{2.13}$$

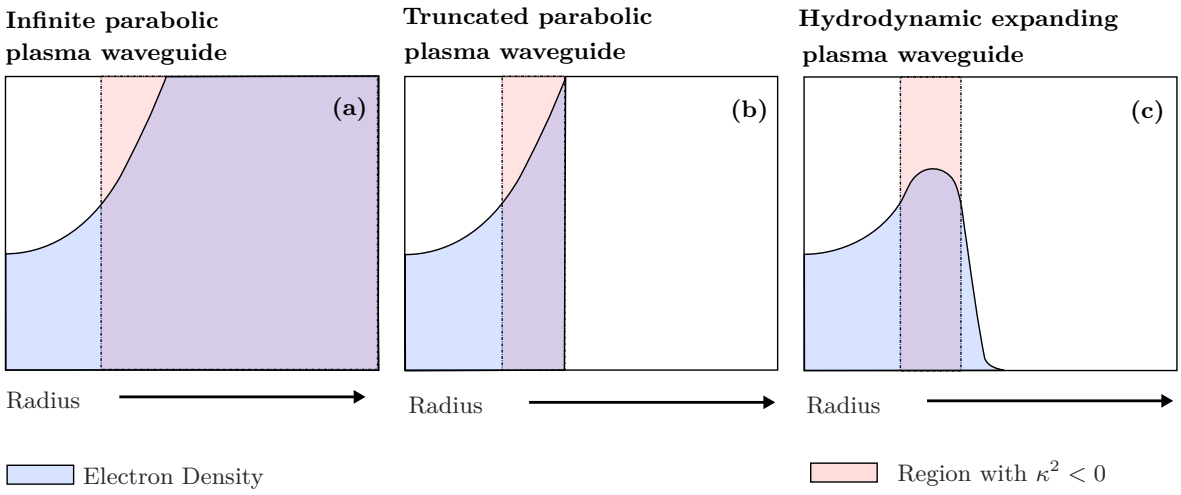

Figure 2.2: Graphic illustrating the electron density profiles of three gradient refractive index plasma waveguides. Also shown is the region, for each waveguide, in which the transverse wavenumber $\kappa^2 < 0$.

Clark groups solutions to equation 2.12 into three categories according to the behaviour of κ^2. Propagation of an electric field within the plasma structure requires that $\kappa^2 > 0$ somewhere. **Radiation modes** are described by $\kappa^2 > 0$ for all $r_{\perp}$; that is to say that there is no confinement. **Bound modes** are described by a central region of the plasma structure with $\kappa^2 > 0$ but with $\kappa^2 < 0$ for all radial position beyond some value, $r > r_w$. These modes are completely confined to the region $r < r_w$. Figure 2.2 denotes the situation for

the **quasi-bound modes** of real graded-index plasma waveguides formed by hydrodynamic expansion — in this case $\kappa^2 > 0$ for the central region of the plasma, then within the shock region the transverse wavenumber becomes imaginary, $\kappa^2 < 0$, while outside the waveguide where the electron density has dropped to zero the the transverse wavenumber becomes real again, $\kappa^2 > 0$.

The main difference between the modes of an infinite parabolic plasma waveguide and a truncated plasma waveguide are that the modes of the former are all bound modes while the truncated plasma waveguide has no bound modes — only quasi-bound or leaky modes and radiation modes. Radiation modes are not confined within the channel, while quasi-bound modes are partially confined with a non-negligible field amplitude outside r_w (due to tunneling of the field), where the radiation diverges at a shallow angle with respect to the optical axis[107].

For general electron density profiles, equation 2.12 must be solved numerically. A code has been developed by the Maryland group to perform these calculations and is described by Clark[109]. Indeed this code is employed in chapter 3 to calculate the guiding properties of experimentally generated plasma channels.

Spot Oscillations

As in the case of grazing-incidence waveguides, it is desirable to match the spot size of the beam to be guided to the matched spot size of the plasma channel to ensure maximum coupling efficiency into the lowest order mode and ideal propagation within the channel. Input beams with spot sizes $w_0 \neq w_m$ can still be guided, although will undergo spot-size oscillations[110] with the spot size of the beam at a position z along the waveguide given by;

$$w^2(z) = \frac{w_0^2}{2}\left[1 + \frac{w_m^4}{w_0^4} + \left(1 - \frac{w_m^4}{w_0^4}\right)\cos\left(\frac{4z}{k\ w_m}\right)\right]. \tag{2.14}$$

This spot size oscillation is illustrated in figure 2.3 where the propagation of a mismatched-spot in an infinite parabolic plasma waveguide has been simulated using a beam propagation code written by the author and discussed in detail in section 2.4. Plotted in panel (a) is an intensity map showing the propagation of the spot through the channel while panel (b) shows the measured $1/e^2$ spot size from the simulations together with the spot size calculated using

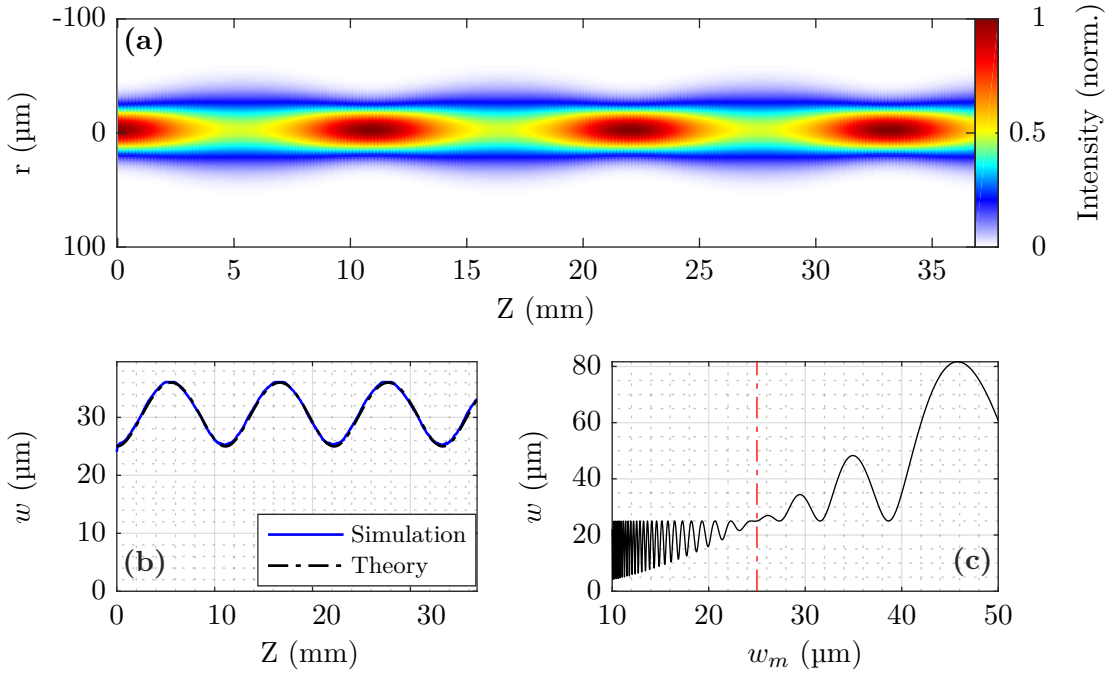

Figure 2.3: Propagation of a mismatched spot. Panel (a) shows a beam propagation simulation of the intensity variation of a beam as it undergoes mismatched propagation in an infinite parabolic plasma waveguide. Panel (b) shows the measured spot size from the same simulation together with a theory curve described by equation 2.14. Panel (c) shows how the spot size measured at the exit of the channel is affected by variations in the matched spot for a fixed input spot of $w_0 = 25\,\mu\text{m}$.

the formula in equation 2.14.

In these simulations an 800 nm beam with a spot size of $w_0 = 25\,\mu\text{m}$ was propagated 15 $z_R = 37\,\text{mm}$ in an infinite parabolic plasma channel. The channel had an on-axis density of $1 \times 10^{18}\,\text{cm}^{-3}$ and a matched spot size $w_m = 30\,\mu\text{m}$.

Panel (c) shows how the spot size measured at the end of the channel, w, would vary as a function of matched spot size, w_m for a given input spot size, $w_0 = 25\,\mu\text{m}$.

2.3 HOFI Plasma Waveguides

Introduced in chapter 1, hydrodynamic optical-field-ionized (HOFI) plasma waveguides offer a alternative mechanism for generating plasma waveguides with properties that are advantageous for LPAs. HOFI waveguides are a type of graded-index plasma waveguide which can be formed

in free space without need for an external structure. Further, these waveguides rely on a heating mechanism which operates independent of density. This leads to a plasma waveguide which has the potential to be operated at low density for extended periods without lasting damage to the plasma structure. If formed by an axicon lens, these waveguides could extend to lengths on the scale of the hundreds of millimeters necessary for future high-energy LPAs.

The formation of HOFI plasma waveguides can be subdivided into two key steps — the first is the ionization and heating of the plasma, the second is the expansion of the hot plasma into the cold surrounding gas. In this section both stages are explored theoretically.

2.3.1 Optical-Field-Ionization

The photoionization of all gaseous elements (at s.t.p) by visible to NIR wavelengths requires high-intensity sources. This is because the ionization energy E_{ion} of these elements lies in the range 10-25 eV[111] whereas the photon energy, $E_\lambda = hc/\lambda$, at visible to NIR wavelengths (390 - 2500 nm) is between 0.5 eV and 3.2 eV. A single photon alone cannot impart enough energy to ionize an electron, but rather many photons must be "stacked" to provide the required energy. As one can imagine, the cross section for this "stacking" process is small and thus high-intensities are required.

Optical-Field-Ionization (OFI) refers to the ionization of atoms or molecules by a high-intensity optical field. Mathematically, optical-field-ionization requires solving the time-dependent Schrödinger equation (TDSE) for a Hamiltonian containing terms pertaining to the atom or molecule of interest, the radiation field and the interaction between the two. The methods used to solve this complex equation determines the way in which the ionization process is viewed[112].

Optical-field-ionization is generally divided into two subcategories; i) Multi-Photon Ionization (MPI) which is historically characterized by the use of pertubative methods to solve the TDSE and ii) Tunneling Ionization (TI), historically this involved reducing the problem to that of a quantum-tunneling problem. To determine which subcategory of ionizaiton mechanism is relevant to a particular set of conditions the Keldysh parameter γ_k, is calculated. This is the square root of a scaled ratio between the ionization energy and the ponderomotive

energy[112,113] U_p,

$$\gamma_k = \sqrt{\frac{E_{\text{ion}}}{2U_p}}\,, \tag{2.15}$$

where the ponderomotive energy can be written as,

$$U_p = \frac{e^2\lambda^2\ |E|^2}{16\pi^2 m_e c^2}\,. \tag{2.16}$$

The ponderomotive energy can also helpfully be written in terms of intensity,

$$U_p[eV] = 9.3\times10^{-14}\ I[\mathrm{W\,cm^{-2}}]\ \lambda^2[\mu\mathrm{m}]\,. \tag{2.17}$$

As discussed in chapter 1, the ponderomotive energy is the cycle-averaged quiver energy of an electron in an electromagnetic field[114–116].

It should be noted that the value of intensity used in the calculation of the Keldysh parameter should be the intensity at which the ionization actually occurs, rather than the peak intensity of the laser pulse used[117].

MPI dominates for the case of $\gamma_k \gg 1$ or the case of short-wavelength, low intensity (as γ_k scales with $1/(\lambda\sqrt{I})$) while TI dominates for $\gamma_k \ll 1$ or long-wavelength, high intensity. For the experiments described in this thesis and for many other works involving the use of NIR laser systems, low-Z elements and moderate peak intensities there exists a grey area of $\gamma_k \sim 1$. Specifically, for ionization energies between 10 and 25 eV, peak intensities of order $10^{14} - 10^{15}$ $\mathrm{W\,cm^{-1}}$ and a center wavelength of 800 nm the Keldysh parameter lies in the range $0.28 < \gamma_k < 1.45$. In this regime of $\gamma_k \sim 1$ it is found that, depending upon the specific situation, the experimentally observed ionization process may be better described by MPI or TI independent of whether $\gamma_k < 1$ or $\gamma_k > 1$[117–119].

In this thesis a slightly stricter delineation of the theory of photoionization is followed. Freeman states that for highly intense laser pulses, $U_p > E_{\text{ion}} \gg \hbar\omega$, pertubative methods break down and the ionization process is best described by tunneling ionization[116].

Tunneling ionization may be investigated theoretically using the Ammosov Delone Kraĭnov or ADK model[120]. Indeed, this is a standard method of calculating the kinetic energies of such tunnel-ionized-electrons. Further, the ADK model can also be used to determine the

threshold ionization intensity of a particular ion state — this is a well defined threshold of intensity, above which ionization to this state occurs rapidly.

For very short pulses with electric fields comparable in magnitude to the atomic field of the bound electron, a third theory of photoionizaiton emerges — barrier suppression ionization (BSI). In BSI, the atomic potential is strongly distorted such that the electron is permitted to escape classically from the atom, rather than quantum mechanically tunneling out. Short pulses are necessary to ensure the validity of this theory as the electric field must ramp up in magnitude quickly to prevent excessive tunneling of electrons out of the atom on the leading edge of the pulse. In this case, "short" refers to pulses with Gaussian temporal profiles of duration less than 300 fs for the noble gases and less than 100 fs for atomic ions[121].

Ionization rates and energy spectra in the BSI regime can be calculated as an extension of the ADK model used in the TI regime[122]. This involves the addition of a classically derived term to the ionization rate at the critical field given by;

$$E_c = \frac{E_{\text{ion}}^2 \pi \epsilon_0}{e^3 Z} \,. \tag{2.18}$$

Indeed, the particle-in-cell code EPOCH[123] implements ionization in this way[124].

The critical field, E_c required for BSI, is the laser field strength which matches the electrostatic field binding the electron to the ion. This also provides a good approximation to ionization threshold intensity[115];

$$\begin{aligned} I_{\text{T}} &= \frac{c\epsilon_0}{2} \left| E_c^2 \right|^2 \,, \\ I_{\text{T}} &= (1+\alpha_p) \frac{E_{\text{ion}}^4 \pi^2 \epsilon_0^3 c}{2e^6 Z^2} \,, \end{aligned} \tag{2.19}$$

where here an additional parameter α_p has been included to account for the polarization of the driver. Linearly polarized light is denoted by $\alpha_p = 0$, while circular polarization by $\alpha_p = 1$.

For the ionization of atomic hydrogen ($E_{\text{ion}} = 13.6\,\text{eV}$) by circularly polarized light, calculations in EPOCH provide a threshold intensity of $4.0 \times 10^{14}\,\text{W cm}^{-2}$. Using equation 2.19, the same parameter is calculated to be $2.8 \times 10^{14}\,\text{W cm}^{-2}$ — the estimation differing by only 30 % from the EPOCH value.

Across all three mechanisms of ionization, it is shown that linearly and circularly polarized

drivers produce quite different electron kinetic energy spectra[114,125,126]. Typically the use of circular polarization acts to produce electrons with a higher kinetic energy. This arises physically, in the case of TI and BSI, from the drift velocity gained from motion of the free electron in the laser field.

To understand this, consider an electron ionized in the field of a laser pulse. The subsequent motion of the electron will have two components — a driven *oscillatory* component as the electron oscillates in the electromagnetic field of the pulse and a *drift* component which is obtained at the point of ionization dependent on the field in which the electron is born[114]. Once the laser pulse has passed, the driven oscillatory motion will disappear and the remaining motion will be due entirely to the drift component. In the case of linear polarization the initial velocity of this drift motion depends upon the phase in the optical cycle at the point of ionization. For circular polarization, the amplitude of the electric field remains constant throughout the ionization process and so electrons are always born with the maximum drift velocity.

2.3.2 Sedov-Taylor Blast Wave Theory

Once ionization and heating have occurred, the plasma will expand radially outwards into the cold surrounding gas, driving a radial blast wave as it does so.

The dynamics of a blast wave expansion are highly nonlinear, and thus difficult to solve. However, a standard way of modeling the expansion dynamics of a blast wave was developed independently by Sedov[127] and Taylor[128]* in the 1940's. The solution relies fundamentally on the concept of similarity — the idea that the physics involved is somewhat invariant to a change in the scale of the problem. The assumption of similarity allows for a reduction in the number of free variables and thus a reduction in the complexity of the solution.

If a cylindrical shock is assumed, as will be the case for plasma waveguides, then according to the Sedov-Taylor solution[130], the shock front position, r_s evolves in time t as;

$$r_s^4(t) = \frac{(\gamma_A + 1)^2}{\pi} \frac{E_l t^2}{\rho_m}, \tag{2.20}$$

*Interestingly, Taylor estimated the strength of the first Atomic Bomb explosion from declassified pictures of the Trinity Test released in LIFE magazine. Using dimensional analysis, Taylor estimated the strength of the explosion to be equivalent to 17 kt of TNT — incredibly close to the official value of 21 kt[129] which was still highly-classified at the time.

where γ_A is the adiabatic index of the medium, E_l is the energy per unit length contained within the blast wave at $t = 0$ and ρ_m is the mass density of the unshocked region.

The conditions required for the formation of a blast wave can be produced by laser-matter interactions. In particular, for the case of waveguide formation this is achieved through the creation of a thin, hot column of plasma. The Sedov-Taylor solution has been applied successfully to the expansion of high-density hydrodynamic plasma channels heated by inverse-bremmstrahlung[131] and optical-field-ionization[70]. Thus it has become the standard method of characterizing the temporal evolution of hydrodynamic plasma waveguides. The applicability of the Sedov-Taylor solution to low-density HOFI plasma channels will be discussed in chapter 3.

One feature of a blast wave expansion of particular importance in the formation of plasma waveguides is the generation of a shock-front. As the hot plasma expands radially outwards into the cold surrounding gas, at a speed higher than the speed of sound in the gas, plasma builds up at the plasma-gas interface. This results in a density profile in which the number density rises rapidly as the shock front is approached from the axis and falls off sharply to zero at the plasma-gas interface. This leads to the creation of structure, very like that shown in figure 2.2, which is an excellent example of a graded-index plasma waveguide.

2.4 Beam Propagation Method

In many situations it is useful to simulate the propagation of a beam within a plasma structure. This can be done using scalar diffraction theory and one method of performing these calculations is using the Beam Propagation Method (BPM). Indeed, in this thesis, the Fast-Fourier Transform Beam Propagation Method (FFT-BPM) is used to simulate the probing of HOFI plasma channels to determine whether or not a probe beam will suffer detrimental refraction from the waveguide structure in longitudinal interferometry measurements (sections 3.4.6 and 5.5.2).

Put plainly, this amounts to solving the Helmholtz equation in a split step calculation;

$$\nabla^2 E(x, y, z) + k^2 \eta^2(x, y, z) E(x, y, z) = 0\,, \tag{2.21}$$

where $E(x, y, z)$ the electric field amplitude and as before, k is the free-space wave vector and η is the refractive index of the medium through which the beam propagates. The solution is assumed to vary slowly along the propagation axis,

$$E(x, y, z) = u(x, y, z) \exp^{-ikz}, \tag{2.22}$$

and the parabolic approximation is applied,

$$\left| \frac{\partial^2 u}{\partial z^2} \right| \ll \left| 2k \frac{\partial u}{\partial z} \right| . \tag{2.23}$$

Substituting the solution into equation 2.21 and rearranging, one ends up at the parabolic wave equation;

$$\frac{\partial u}{\partial z} = -\frac{i}{2k} \nabla_\perp^2 u - \frac{ik}{2} (\eta - 1) u . \tag{2.24}$$

This can be written as sum of operators $\widehat{A}$ and $\widehat{B}$, representing diffraction or free space propagation and refraction respectively.

$$\begin{aligned} \frac{\partial u}{\partial z} &= \left(\widehat{A} + \widehat{B} \right) u , \\ \widehat{A} &= -\frac{i}{2k} \nabla_\perp^2 , \\ \widehat{B} &= -\frac{ik}{2} (\eta - 1) . \end{aligned} \tag{2.25}$$

The solution to equation 2.25 can be written as a split step operation where free space propagation and refraction are calculated independently. In particular, for the methods employed here, the procedure is to propagate the field forwards with the diffraction operator half a step $\delta z/2$, calculate the effect of refraction for the whole step δz and finally, propagate the field with the diffraction operator for a second half step;

$$u(x, y, z + \delta z) = \exp\left(\frac{\delta z}{2} \widehat{A} \right) \exp\left(\delta z \widehat{B} \right) \exp\left(\frac{\delta z}{2} \widehat{A} \right) u(x, y, z) . \tag{2.26}$$

The FFT-BPM code has already been compared to the mismatched propagation of a Gaussian beam in an infinite parabolic plasma channel (figure 2.3). Figure 2.4 demonstrates

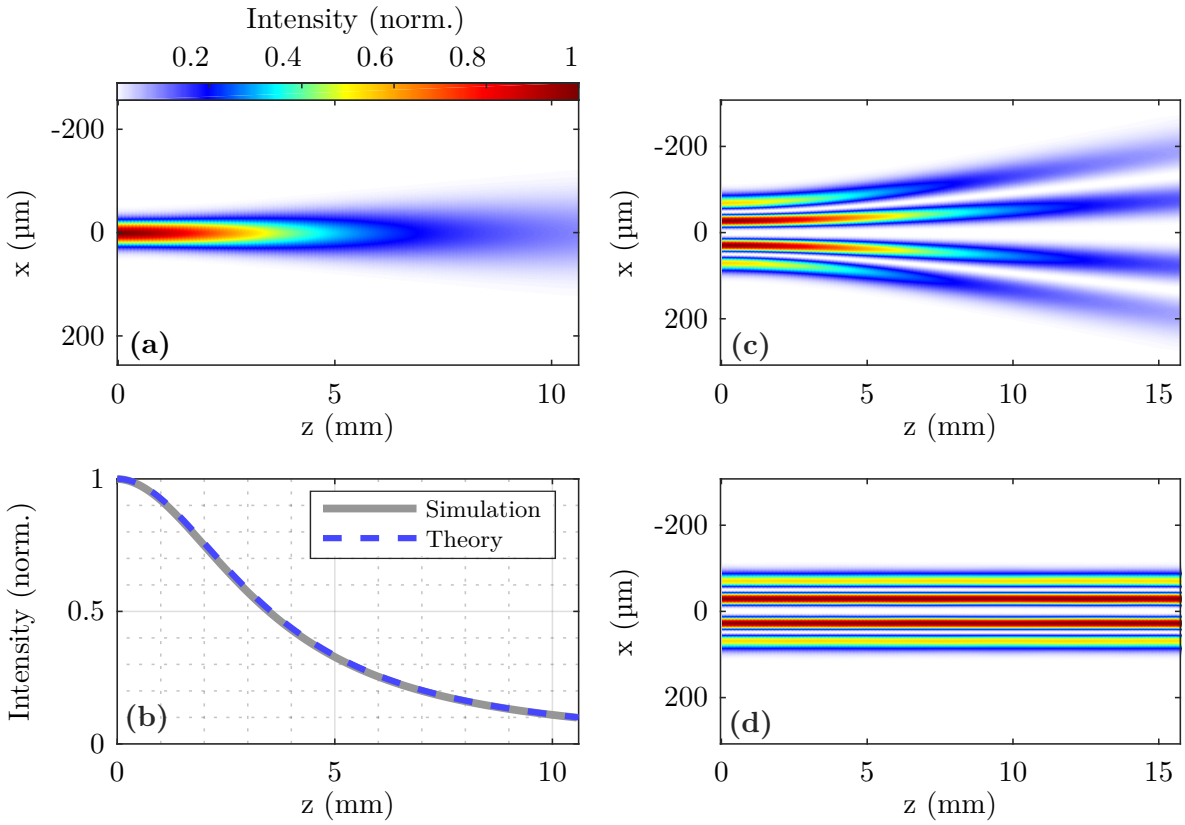

Figure 2.4: Demonstration of the FFT-BPM code. Panel (a) shows the simulated free space diffraction of a Gaussian beam focused to 30 µm. Panel (b) shows the peak-intensity of that Gaussian beam as a function of axial propagation distance z, together with an analytic expression for the diffraction of a Gaussian pulse. The remaining two panels show simulations of the propagation of a Laguerre-Gauss beam with m = 2 and p = 1. Panel (c) represents its propagation in free space while panel (d) shows its invariant propagation in a suitably matched infinite parabolic plasma waveguide. The colour scale for all three intensity maps is the same.

calculations from three other situations. Panel (a) shows the free space diffraction of a Gaussian beam focused to 30 µm over a range of $3z_R$. In panel (b) the axial intensity over the propagation distance is compared with simple Gaussian pulse theory showing excellent agreement.

Also shown is the propagation of an (p,m) = (1,2), Laguerre-Gauss mode (equation 2.10). In panel (c) the diffraction of such a mode into free space is shown while in panel (d) the matched propagation within a suitably matched infinite parabolic plasma channel is shown.

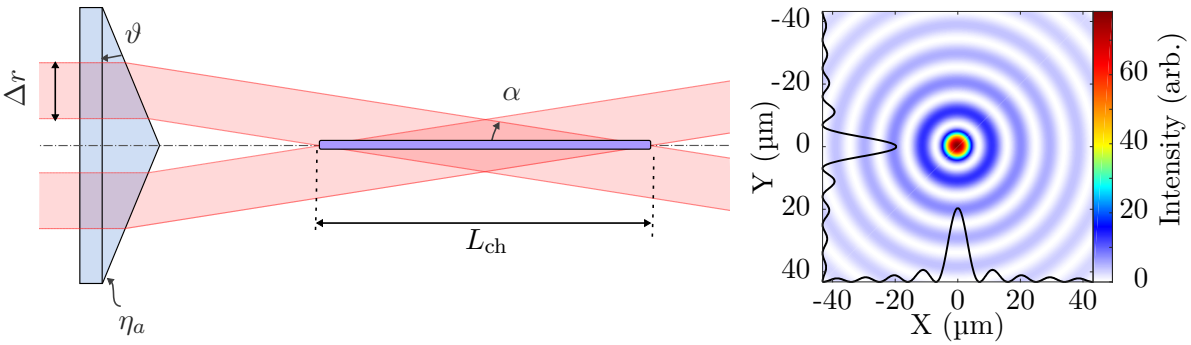

Figure 2.5: **(a)** Schematic of an axicon of base angle ϑ and refractive index η_a focusing rays from an annulus of collimated light at an approach angle of α towards the optical axis and **(b)** a simulated focal image for an 800 nm beam focused by a $\vartheta = 5°$, BK7 ($\eta = 1.5108$) axicon demonstrating the characteristic Bessel profile. The black lines indicate vertical and horizontal lineouts of the simulated focus.

2.5 Axicons for HOFI Plasma Channel Formation

As discussed in section 1.3, focusing from traditional spherical or parabolic optics limits the effective interaction length due to diffraction. This makes creating a plasma waveguide for applications with such optics both difficult and inefficient. The inefficiency in waveguide formation is a natural consequence of parabolic focusing optics as such optics are designed to focus as much optical energy as possible to a point, the focus. In contrast, for plasma waveguide formation, it is necessary to spread that optical energy into a line with a length corresponding to the desired waveguide length. In other words, rather than focusing light to a point focus, the creation of a line focus is preferred. One optic capable of forming such a line focus is an axicon lens[132]. This is a transmissive optic which has a conical surface, rather than a parabolic or a spherical one.

2.5.1 Focal Intensity Profile of an Axicon

Axicons are quite simple to understand qualitatively, a beam of monochromatic rays incident upon an axicon of refractive index η_a and base angle ϑ will enter through the back face of the optic undeviated, as shown in figure 2.5. The rays then hit the front surface where they are all refracted towards the optical axis at the same angle $\alpha(\lambda) = \arcsin\left(\eta_a(\lambda)\sin\vartheta\right) - \vartheta$.

Since all of the rays leaving the axicon approach the optical axis at the same angle, there is a direct mapping of radial beam position, r, to longitudinal position, z, where a ray crosses

the optical axis, $z(r) = r\cot\alpha$. This means that the length of the focal region can be tuned easily by either changing the size of the incoming beam or the axicon base angle. Figure 2.5 shows an axicon focusing an annular beam of thickness Δr, leading to the formation of a focal region of length $L_{\text{ch}} = \Delta r \cot\alpha$.

To understand the pseudo non-diffracting nature of the axicon, consider the radial wave vector of the beam in the focal region. At any focal position z, the radial wave vector of the beam is $k_r = k\sin\alpha$. This means that at any z position in the focal region the same interference pattern is observed. For a beam with zero angular momentum that pattern is a zero order Bessel function of the first kind, $J_0(k_r\rho)$, where ρ is the radial position in the focal region.

The phase shift introduced by an axicon can be written as;

$$\Delta\Phi_{\text{ax}} = -kr\sin\alpha\,, \tag{2.27}$$

where r is the radial distance from the center of the axicon. Gessner uses scalar diffraction theory to show that a scalar plane wave $u(r,\phi,z) = u_0(r,\phi)e^{ikz}$ transmitted through an axicon, picking up a phase shift described by $\Delta\Phi_{\text{ax}}$, produces a focal intensity profile described by;

$$I(\rho,z) = 2\pi kzI_0\alpha^2 J_0^2\left(k\alpha\rho\right)\,, \tag{2.28}$$

where ρ is the radial position in the focal region, I_0 the intensity of the beam incident upon the axicon and where the the small angle approximation has been made for α[133].

A second treatment of axicon focusing by Čižmár provides an expression for the intensity profile of an axicon focus created by a Gaussian beam;

$$I(\rho,z) = \frac{4P_g k\sin\alpha}{w_0}\frac{z}{z_{\max}}J_0^2\left(k\rho\sin\alpha\right)\mathrm{e}^{-\frac{2z^2}{z_{\max}^2}}\,, \tag{2.29}$$

with P_g and w_0 the power and beam waist of the incident Gaussian beam respectively and $z_{\max} = w_0\cot\alpha$[134].

For a Gaussian beam of the form;

$$I_{\text{Gauss}}(r) = I_0\mathrm{e}^{-\frac{2r^2}{w_0^2}}\,, \tag{2.30}$$

it can be shown by integration that the total power in the beam is related to the peak intensity by $P_g = I_0 \pi w_0^2/2$.

Substituting this into equation 2.29, making the small angle approximation for α and rearranging, it is found that;

$$I(\rho, z) = 2\pi k z I_0 \mathrm{e}^{-\frac{2(z\alpha)^2}{w_0^2}} \alpha^2 J_0^2 (k\alpha\rho) \ . \tag{2.31}$$

Looking to the exponential term, it can be seen that $z\alpha$ is the radius r, at which rays leaving the axicon arrived at the axial position z. Further $I_0 \exp\left(-2(z\alpha)^2/w_0^2\right)$ is simply the input beam profile, a Gaussian. This leads us to the more general expression,

$$I(\rho, z) = 2\pi k z I(z\alpha) \alpha^2 J_0^2 (k\alpha\rho) \ , \tag{2.32}$$

where $I(z\alpha)$ represents an arbitrary azimuthally symmetric input intensity profile with $z\alpha = r$.

While this is not a rigorous derivation of the axicon intensity profile in the focal region, the same result can be reached by considering the optical energy arriving along a small segment of the optical axis between z and $z + \delta z$. Rays reaching this point will have originated from the axicon in an annulus of inner radius $r = z\alpha$ and thickness δr. In the limit of small δr, the intensity at this radial position may be considered constant and equal to I_0. Making the same argument across all possible annuli, it can be seen that $I_0 \to I(r)$, with $r = z\alpha$.

The right panel in figure 2.6 shows the axial intensity profile for three different input profiles, shown in the left panel, each comprising the same total energy; a top hat of radius R (black), a gaussian beam (red) and an order-8 super-Gaussian beam (blue) with $w_0 = \sqrt{2}R$. It is clear, that by tailoring the input beam profile, it is possible to customize the axial intensity profile.

The calculations performed here assume a monochromatic beam, however for ultrashort pulses there is a wavelength dependence of the approach angle of rays to the optical axis α, arising from the refractive nature of the optic. Thus it would be expected that chromatic aberrations would reduce the intensity achieved in the focal plane when using ultrashort pulses. However, this could be avoided by using a reflective axicon.

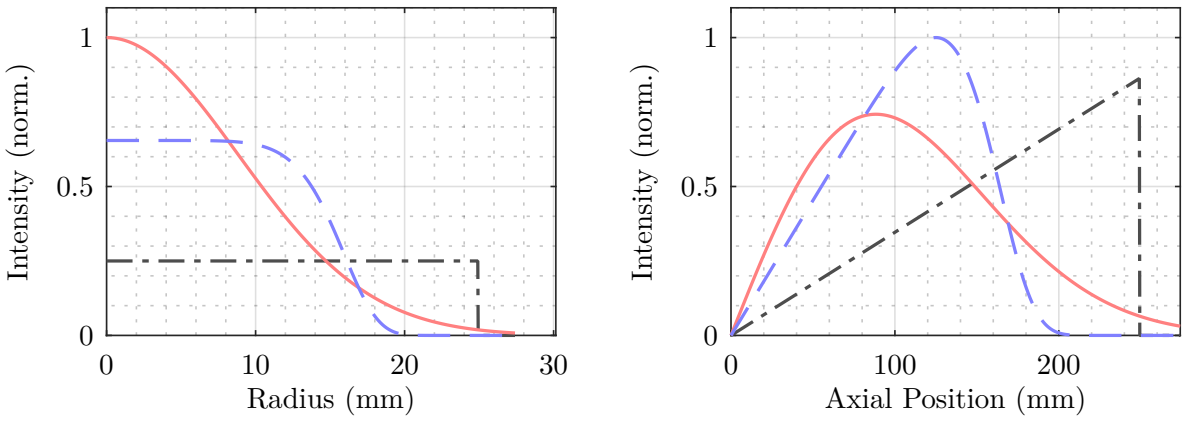

Figure 2.6: Relationship between the near field of a beam and its axial intensity profile when focused by an axicon. The left panel denotes three different near field profiles containing the same total energy; Gaussian (solid red), order-8 super-Gaussian (dashed blue) and top hat (dot-dashed black). The right panel shows the axial intensity profile that would be achieved when each of these beams is focused by the same axicon.

2.5.2 Axicon Plasma Formation

The dispersion relation for electromagnetic waves propagating in an unmagnetised plasma is a simple modification from the dispersion relation in vacuum[135], namely;

$$\omega^2 = \omega_p^2 + c^2 k^2 \,. \tag{2.33}$$

For a constant laser frequency, as the plasma density and so plasma frequency rises, the wave vector decreases. The critical density, briefly introduced in section 2.2.2, for a given laser frequency is defined as the density for which the wave vector is zero. For densities above this critical density, the wave vector is purely imaginary and thus the wave does not propagate in the plasma. In this case the plasma is said to be overdense, otherwise the plasma is said to be underdense;

$$n_{cr} = \frac{m_e \epsilon_0 \omega^2}{e^2} \,. \tag{2.34}$$

Much of the experimental work in the field of LPAs is performed using Ti:sapphire CPA laser systems which typically operate at 800 nm, corresponding to a critical density of 1.75×10^{21} cm^{-3}. Given that a substantial portion of this thesis aims to develop waveguides for LPAs operating at densities below 10^{18} cm^{-3} it may not seem prudent to focus too much

on the critical density. However, it has been shown[136,137] that when an axicon is used to focus light, the incoming rays are reflected at an effective critical density which is much lower than the nominal critical density,

$$n_{\mathrm{cr}}^{\mathrm{eff}} = n_{\mathrm{cr}} \sin^2 \alpha \,, \tag{2.35}$$

where α is the angle of incidence. This reflection of the incoming beam impedes the further absorption of laser radiation. To get an intuitive feel for why this might be, consider a plane wave of wave vector k, incident obliquely at an angle of α to a sheet of plasma of density n_e. At the interface between plasma and vacuum one may decompose the wave vector of the plane wave to find the wave vector normal to the plasma-vacuum interface, $k_\perp = k \sin \alpha$. Here the effective wave vector seen by the plasma at oblique incidence is modified from the wave vector at normal incidence by a factor of $\sin \alpha$ and so the effective critical density at oblique incidence will be modified from the critical density by a factor of $\sin^2 \alpha$ as $n_{\mathrm{cr}} \propto k^2$.

Consider a ray of 800 nm light focused by a shallow axicon approaching the optical axis at an angle of $\alpha = 2.5\ ^\circ$; here the effective critical density would be reduced by three orders of magnitude from the case above, giving $n_{cr}^{\mathrm{eff}} = 3.23 \times 10^{18}\ \mathrm{cm}^{-3}$. This large reduction in the effective critical density plays an important role in the design of axicon based systems for plasma channel formation, as will be seen in chapter 4.

2.6 Focal Spot Characterization

For the experiments described in this thesis, particularly for the results presented in chapter 5 the focal spot quality must be analyzed in detail. The techniques used to analyze the focii produced by an off-axis paraboloid and an axicon are treated separately since they require two differing approaches.

2.6.1 Paraboloid & Lens Focal Spot Analysis

While the characterization of a paraboloid focus is a standard requirement of any laser plasma experiment, it is often not performed in a standardized way, with measurement techniques not only differing between groups, but between group-members. For the case of Gaussian-like

beams, the differing methods usually provide comparable results, but for distorted beams or out-of-focus beams they can often provide results differing by a large factor.

Three of the main methods used to characterize the intensity spot size of a beam are: direct measurement, the half-maximum contour method and the D4σ method. Below these three measurement techniques will be directly compared for two different focal spots. The measurements are summarized in table 2.1.

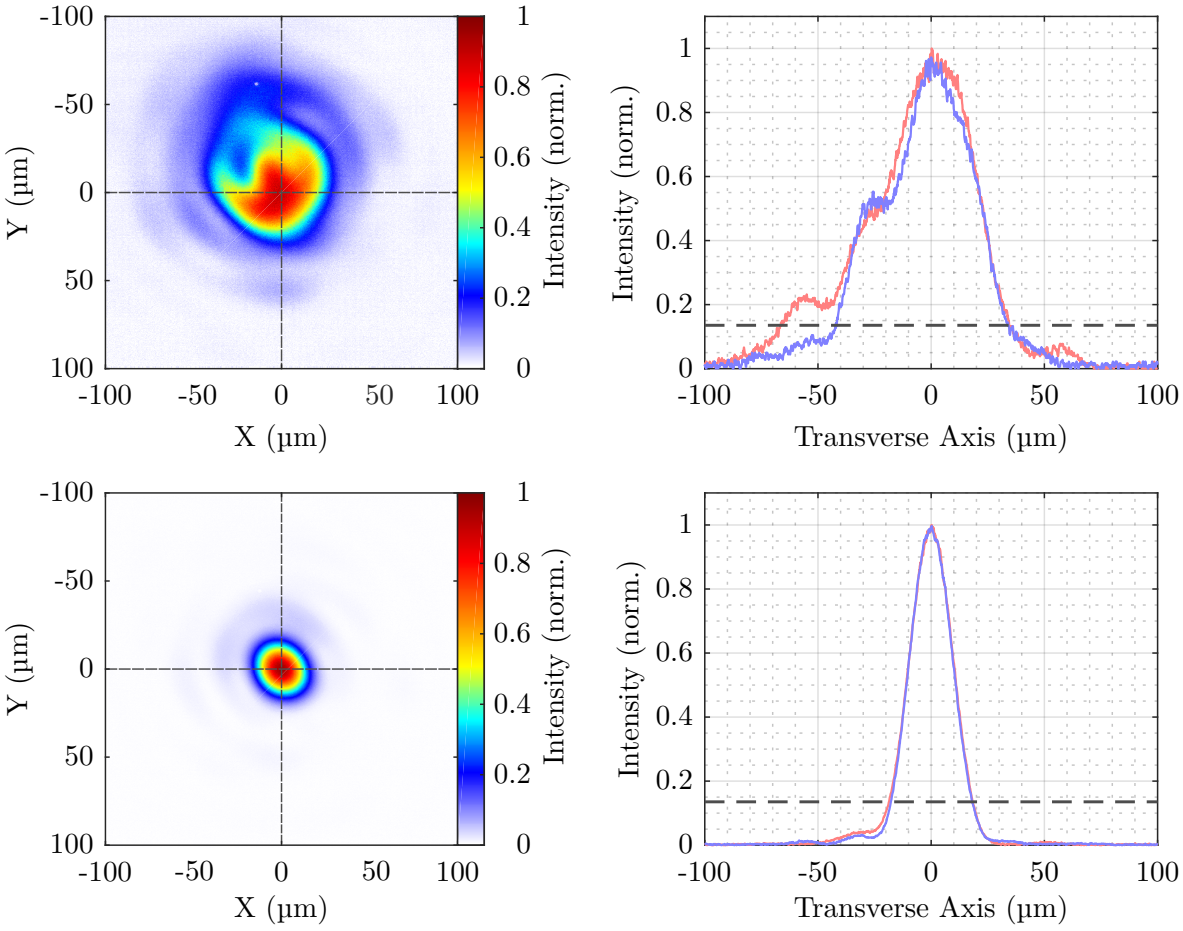

Figure 2.7: Demonstration of the direct method of measuring the $1/e^2$ intensity spot size of a beam. The two left panels show an out-of-focus spot (top) and an in-focus spot (bottom). The right panels show vertical (blue) and horizontal (red) lineouts of these spots together with a $1/e^2$ line (black). The intersection of the lineouts with the black line gives the spot size.

Direct Measurement Method

The direct measurement method is usually used to extract a focal spot size *on the fly*, although is the least accurate in terms of retrieving a realistic gauge of the spot size of a beam. This

method simply involves taking a vertical and horizontal lineout of the focal spot and finding the positive and negative radii at which the intensity of the spot drops to $1/e^2$ of the peak value. The values are averaged to provide a spot size in the vertical and the horizontal direction.

Figure 2.7 illustrates the direct measurement method. The two left panels show two spot measurements of a beam; one out-of-focus (top) and one in-focus (bottom). To the right of these spots, normalized vertical (blue) and horizontal (red) lineouts are shown together with a black dashed line representing $1/e^2$. The intersection of these lineouts with the $1/e^2$ line provides the spot size measurements.

This technique provides a good estimate of the spot size of a perfect Gaussian but can give incorrect results for non-Gaussian beams.

Half-Maximum Contour Method

Another method of measuring the spot size is the half-maximum contour method. Here, a contour is fitted to a value equal to half of the maximum intensity. An ellipse is then fitted to that contour; the major and minor axes of the fitted ellipse corresponding to the half-maximum spot size w_{HM}. To retrieve the $1/e^2$ spot size the half-maximum spot size is scaled by;

$$w = \frac{w_{\mathrm{HM}}}{\sqrt{2\ln(2)}}\,. \tag{2.36}$$

The half maximum contour method is illustrated in figure 2.8.

D4σ Method

The spot size of a beam may also be calculated using the D4σ method. The D4σ represents 4 times the standard deviation of the major and minor beam distributions. The D4σ beam diameter in the X-direction can be expressed as;

$$\mathrm{D4}\sigma = 4\sqrt{\frac{\int_{-\infty}^{\infty}\int_{-\infty}^{\infty} I(x,y)\,(x-\bar{x})^2\,dxdy}{\int_{-\infty}^{\infty}\int_{-\infty}^{\infty} I(x,y)dxdy}}\,, \tag{2.37}$$

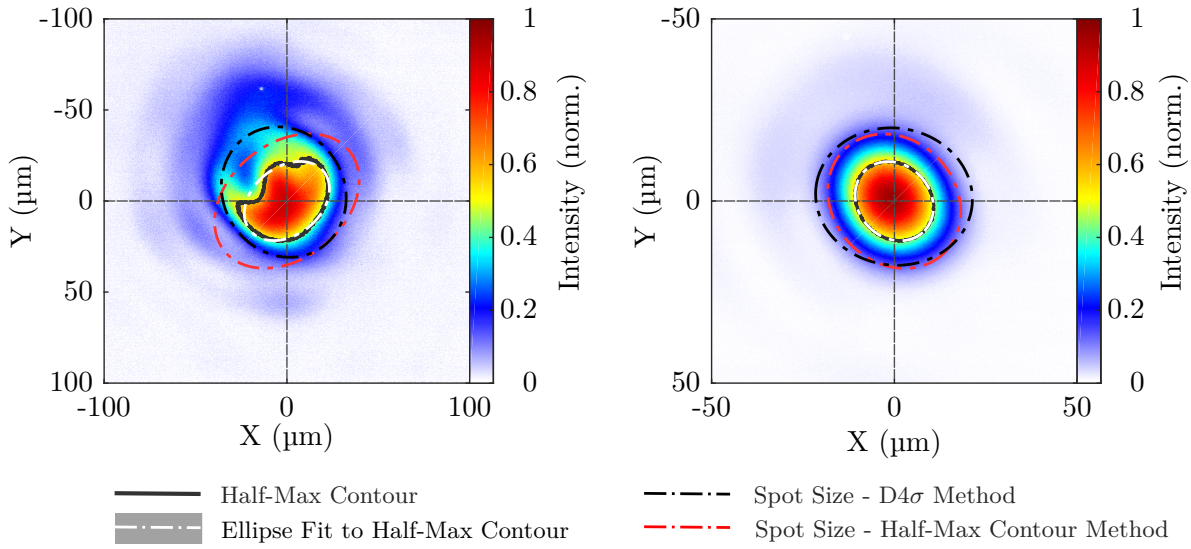

Figure 2.8: Demonstration of the half-maximum contour and D4σ methods for measuring the $1/e^2$ intensity spot size of a beam, for two different example spots.

with $\bar{x}$ the centroid position of the distribution,

$$\bar{x} = \frac{\int_{-\infty}^{\infty}\int_{-\infty}^{\infty} I(x,y)x dx dy}{\int_{-\infty}^{\infty}\int_{-\infty}^{\infty} I(x,y) dx dy} \,. \tag{2.38}$$

The D4σ measurement is a beam diameter and so to get the radius one simply divides the D4σ value by 2. For the case of Gaussian beams, it is found that half the D4σ value is equivalent to the $1/e^2$ intensity radius.

In contrast to the other methods, the D4σ measurement is meaningful for multi-modal distributions, making it an ideal choice for the characterization of focal spots from high-intensity ultrashort lasers which can often acquire severe aberrations during amplification. Indeed, the D4σ method is the ISO standard method for measuring beam diameters[138]. For these reasons, the D4σ method is used throughout this thesis.

It should be noted that when calculating the beam diameter using the D4σ method, a careful subtraction of the background is essential since in evaluating the D4σ the transverse intensity profile is weighted by a factor of x^2.

The D4σ method is shown in figure 2.8. The differing spot size measurements are summarized in table 2.1. For the in-focal spot, which is of good quality, the measurements are all in reasonable agreement, however for the out-of-focus spot, which has more energy distributed in the wings, there are large discrepancies in the measured spot size. Given the multi-modal

Measurement Method	**Spot 1: w_{maj}**	**Spot 1: w_{min}**	**Spot 2: w_{maj}**	**Spot 2: w_{min}**
Direct-Measurement	50.5 µm	37.9 µm	18.4 µm	17.9 µm
Half-Maximum Contour	43.9 µm	31.6 µm	19.7 µm	16.8 µm
D4σ Method	36.8 µm	33.1 µm	21.5 µm	18.8 µm

Table 2.1: Comparison of spot size measurement techniques for an out-of-focus spot (Spot 1) and an in-focus spot (Spot 2).

nature of the out-of-focus beam, the direct-measurement method and the half-maximum contour method cannot be trusted, rather the ISO standard D4σ method should be used.

2.6.2 Axicon Focal Spot Analysis

Analysis of an axicon focus amounts to determining the approach angle of rays to the optical axis as this will determine the location of the first Bessel zero and thus the size of the central spot. There are three ways in which this value can be extracted: by direct measurement, a fitting method and a Fourier-based method. Given the highly structured nature of a Bessel focus, determining the approach angle and so the central spot size is more straight forward than for the case of the parabola focus.

Direct Measurement

As the Bessel function contains a well defined set of roots x_n^0, such that $J_0(x_n^0) = 0$, the simplest method of determining the spatial profile of the focal spot is to directly measure the radius ρ_0 of the first root $x_1^0 = 2.4048$ occurs. The approach angle can then be extracted as;

$$\alpha = \frac{2.4048}{k\rho_0}\,. \tag{2.39}$$

This method relies on a single measure of distance within the focal profile and so is highly susceptible to measurement errors. Further, in real measurements the focal profile is unlikely to drop to zero at the locations x_n^0, but rather will reach a minimum in the vicinity of x_n^0. This can compound the measurement error.

Fitting Method

A second method to measure α is to fit the function $AJ_0^2(k\alpha\rho)$, with A a scaling constant, to vertical and horizontal lineouts of the measured profile. This method, taking account of the entire lineout, rather than a single distance measurement, provides a much more accurate measurement of α. Indeed, it has been found by the author, that for low-noise focal profiles free from excessive aberrations, an accurate value of α can usually be retrieved by this method.

Fourier Method

For noisy axicon foci measurements or axicon foci with large aberrations to the central region of the focus, it is found that a Fourier method provides the best measurement of α.

This method relies on the fact that the spacing between consecutive Bessel roots, $x_n^0 - x_{n-1}^0$ for $n > 1$, are constant to the 1% level[†]. A Fourier Transform of a Bessel profile will thus provide a peak at a frequency corresponding to the separation of Bessel roots;

$$\mathcal{F}\left[J_0(k\alpha\rho)\right](\varkappa) = \text{rect}\left(\frac{k\alpha}{2\varkappa}\right) \frac{2}{\sqrt{k^2\alpha^2 - \varkappa}}, \tag{2.40}$$

where $\varkappa$ is the spatial frequency corresponding to the spatial variable ρ and rect is the rectangle function. In this way, it is possible to extract the value of α, as the fourier transform peaks at a value of $\varkappa_p = k\alpha$.

In this thesis, the fitting and Fourier based methods are both employed due to their increased accuracy over the direct measurement.

2.6.3 Intensity Approximation by Pixel Summation

Scientific CCD (charge-coupled-device) and CMOS (complimentary-metal-oxide-semiconductor) sensors show a linear variation in output signal with optical flux up to a saturation limit. When calibrated, such sensors can provide an excellent measurement of the energy of a beam, as will be seen in chapter 5, and a reasonable estimate of the intensity profile of the beam. Making direct intensity measurements is impossible with these devices as the typical gate-time and

[†]In fact, it is found that the spacing of roots for a zero order Bessel function of the first kind is given by; $x_n^0 - x_{n-1}^0 \approx \pi$.

repetition rates of the sensors are on the scale of microseconds and milliseconds respectively. However, coupled with a pulse duration measurement, it is possible to make a reasonable estimate of the intensity profile of an incident beam.

Estimate of the Focal Intensity Produced by an Off-Axis Paraboloid

Estimating the intensity of both a paraboloid focus and an axicon focus rely on pixel summation and so a good background subtraction is essential. The easiest way to do this is to take a reference image with (no beam) under the same conditions as the data image (with beam) and subtract the reference from the data. If a background still persists due to shot-to-shot fluctuations then it can usually be removed by masking out the focal spot and fitting a second-order polynomial to the background, then subtracting this polynomial from the original image.

As the flux scales linearly with signal count, the summation of all pixel values in the background-subtracted image may be set equal to the total energy of the beam — this of course assumes that the sensor is large enough to capture the whole beam. Dividing the laser energy by the pixel summation gives a value of energy-per-pixel-count. If the pulse duration is known then dividing the energy-per-pixel-count by the pulse duration and by the area of one pixel (accounting for any magnification factor) provides an estimate of intensity-per-pixel-count. The final step is to scale the data image by the intensity-per-pixel-count value.

Estimate of the Focal Intensity Produced by an Axicon

An intensity estimate of an axicon focus is less straightforward, but can be made with some reasonable assumptions. To begin, consider the Bessel structure of an axicon focus. The intensity estimation relies on determining the energy in one ring of the focus and the idea that the energy per ring is conserved through focus — the ring itself simply shrinks and expands.

Consider an annular beam of thickness Δr incident upon an axicon which refracts rays towards the optical axis at an angle α. The number of Bessel rings, N, present in the beam immediately after the axicon is given by;

$$N = \frac{k\alpha\Delta r}{\pi}\,. \tag{2.41}$$

Thus the energy per ring may given as E_{ab}/N; where E_{ab} is the energy of the annular beam and the annulus is considered thin, such that the energy per ring can be assumed constant.

In the focal plane, the effective number of rings visible on the camera sensor, N_{eff}, can be calculated using the fitted value of α and the dimensions of the camera sensor. This is the total number of full rings and partial rings visible on the sensor. The total energy incident on the region of interest is then given by $E_{\text{eff}} = E_{ab}N_{\text{eff}}/N$.

Once E_{eff} has been calculated, the same pixel summation technique used for the parabola focus may be applied to calculate the intensity distribution in the focal plane.

2.7 Interferometry

The phase velocity of light in a medium is described by the refractive index, $\eta = c/v_p$. If a beam of light is passed through a medium with a refractive index greater than 1, it will experience a reduced phase velocity which leads to a phase delay with respect to a beam which traveled the same geometric distance in vacuum. Provided that this phase delay, or phase shift, can be measured, it is then possible to determine the refractive index of an unknown medium.

The implications of this idea for plasma experiments are clear. As there is a direct relationship between electron density and refractive index in a plasma, as described in equation 2.8, measurements of the refractive index can provide details of the electron density structure of a plasma.

One technique for measuring the phase shift incurred by light passing through a medium is interferometry. Here a beam is split into two copies which travel along separate beamlines before being recombined with a shallow angle between their phase fronts. The introduction of a shallow angle creates a set of interference fringes in which phase information about the phase can be encoded. Introducing an object of interest into one arm of the interferometer will cause the beam in that arm to incur a phase delay. Upon interfering the beam in this arm with the beam in the reference arm the fringe pattern will be modified.

The question then arises, **(1)** how is phase information about a plasma encoded into the fringe pattern, and **(2)** how is it extracted?

2.7.1 Encoding the Phase

Consider a plane wave travelling in the z direction,

$$E_{\text{probe}}(z,t) = E_0 e^{i(kz-\omega t)}\,. \tag{2.42}$$

In passing through, or probing a plasma the plane wave will acquire a phase shift $\Delta\phi$,

$$\begin{aligned}\Delta\phi(x,y) &= \frac{2\pi}{\lambda}\int[\eta(x,y,z)-1]dz \\ &= -r_e\lambda\int n_e(x,y,z)dz\,,\end{aligned} \tag{2.43}$$

where equations 2.8 and 2.7 have been used along with the substitution of the classical electron radius, given by

$$\begin{aligned}r_e &= \frac{1}{4\pi\epsilon_0}\frac{e^2}{m_e c^2} \\ &= 2.82\times10^{-15}\,\text{m}\,.\end{aligned} \tag{2.44}$$

The resulting plane wave after probing the plasma is then

$$E_{\text{probe}}(x,y,z,t) = E_0 e^{i(kz-\omega t+\Delta\phi(x,y))}\,. \tag{2.45}$$

Now consider a second plane wave, a reference wave which did not propagate through plasma, travelling in the x-z plane at an angle φ with respect to the z-axis,

$$E_{\text{ref}}(x,z,t) = E_0 e^{i(kx\sin\varphi+kz\cos\varphi-\omega t-\chi)}\,, \tag{2.46}$$

where χ is an arbitrary phase offset.

The fringe pattern arising from the interference of these plane waves can be described by

$$\begin{aligned}I(x,y,z,t) &= \frac{c\epsilon_0}{2}\left|E_{\text{probe}}(x,y,z,t)+E_{\text{ref}}(x,z,t)\right|^2 \\ I(x,y,z,t) &= \frac{c\epsilon_0}{2}\left|E_0 e^{i(kz-\omega t+\Delta\phi(x,y))}+E_0 e^{i(kx\sin\varphi+kz\cos\varphi-\omega t-\chi)}\right|^2\,.\end{aligned} \tag{2.47}$$

If the intensity distribution is observed in the x-y plane, say at $z=0$, one finds;

$$I(x,y) = c\epsilon_0 E_0^2\left[1+\cos\left(kx\sin\varphi-\Delta\phi(x,y)-\chi\right)\right]\,. \tag{2.48}$$

In the absence of a plasma, the interference pattern will consist of a set of fringes, evenly spaced by $\lambda_f = \lambda / \sin\varphi$; the addition of a plasma will distort these fringes from their original positions.

2.7.2 Decoding the Phase

Takeda et al.[139] developed a Fourier-based method of extracting the phase shift $\Delta\phi(x, y)$ from a set of interference fringes which is followed here. Consider an image containing a set of interference fringes in which phase information about a plasma $\Delta\phi(x, y)$ is encoded. Rewriting equation 2.48 more generally, it is seen that;

$$\begin{aligned} I(x,y) &= a(x,y) + b(x,y)\cos\left(kx\sin\varphi - \Delta\phi(x,y) - \chi\right) \\ &= a(x,y) + \frac{1}{2}\left(e^{ikx\sin\varphi}c(x,y) + e^{-ikx\sin\varphi}c^*(x,y)\right) , \end{aligned} \tag{2.49}$$

where the following substitution has been made;

$$c(x,y) = b(x,y)e^{-i(\Delta\phi(x,y)+\chi)} . \tag{2.50}$$

Taking a Fourier transform of equation 2.49, it is found that;

$$\mathcal{F}\left[I(x,y)\right] = A(k_x,k_y) + \frac{1}{2}\left(C(k_x - k\sin\varphi, k_y) + C^*(k_x + k\sin\varphi, k_y)\right) , \tag{2.51}$$

where capital letters denote the Fourier spectra and k_x and k_y are the horizontal and vertical frequency axes of the Fourier spectra respectively.

Adding interference fringes to an image allows for the separation, in frequency space, of information pertaining to the plasma phase shift, $\Delta\phi(x, y)$, from general background intensity fluctuations which will be present in any experimental data. This is possible as the background intensity fluctuations occur slowly when compared with the fringe frequency. The information relating to the background is centered around $(k_x, k_y) = (0, 0)$, while information relating the plasma phase shift is present in a pair of sidebands located at $(k_x, k_y) = (\pm k\sin\varphi, 0)$.

The next step is to mask the image in frequency space to remove the information about background intensity fluctuations. This done by defining a box of dimensions $K_x \times K_y$ centered

around $k \sin\varphi$ and setting all values outside this region to 0[‡].

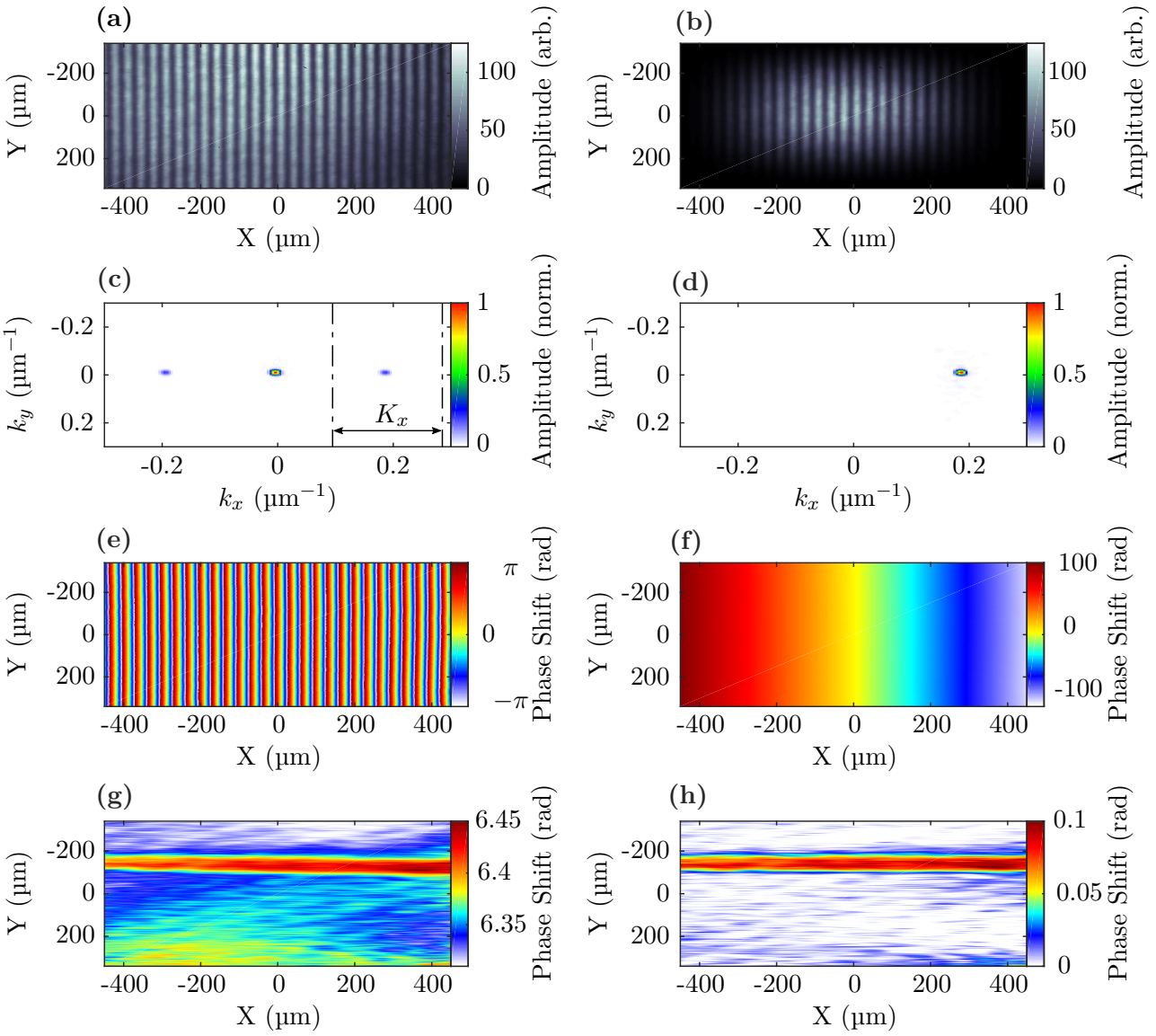

Figure 2.9: Sequence of images demonstrating the interferometric analysis technique employed in this thesis. The information plotted in the panels (a) - (h) is described in the main text.

Mathematically this can be expressed as;

$$\mathcal{F}\left[I(x,y)\right]_{\text{masked}} = \frac{1}{2}C(k_x - k\sin\varphi, k_y)\,. \tag{2.52}$$

The sideband is then shifted to the center of the Fourier transform, $\mathcal{F}\left[I(x,y)\right]^{\text{shifted}}_{\text{masked}} \rightarrow$

[‡]In masking the image, K_x should be made large enough to encompass the entire sideband for increased spatial resolution, however, it should not be made so large as to engulf the central peak of the Fourier transform. Usually $K_x = k\sin\varphi$ suffices. For vertical fringes K_y can be made as large as desired.

$C(k_x, k_y)$, and the image is subsequently inverse-Fourier transformed to retrieve,

$$\begin{aligned}\mathcal{F}^{-1}\left[\mathcal{F}\left[I(x,y)\right]^{\text{shifted}}_{\text{masked}}\right] &= \frac{1}{2}c(x,y) \\ &= \frac{1}{2}b(x,y)e^{-i(\Delta\phi(x,y)+\chi)}\,.\end{aligned} \tag{2.53}$$

The final step in the process is to extract the phase shift from the complex image described by $\mathcal{F}^{-1}\left[\mathcal{F}\left[I(x,y)\right]^{\text{shifted}}_{\text{masked}}\right]$. As $b(x,y)$ is real, this can be done by taking the argument of the image,

$$\arg\left(\mathcal{F}^{-1}\left[\mathcal{F}\left[I(x,y)\right]^{\text{shifted}}_{\text{masked}}\right]\right) = -\Delta\phi(x,y) - \chi\,. \tag{2.54}$$

In Takeda's original paper the isolated sideband was shifted back to the center as described above. If one refrained from shifting the sideband back to the center of the image, it would not invalidate the technique but merely add a linear phase gradient to the resulting image given by;

$$\arg\left(\mathcal{F}^{-1}\left[\mathcal{F}\left[I(x,y)\right]_{\text{masked}}\right]\right) = kx\sin\varphi - \Delta\phi(x,y) - \chi\,. \tag{2.55}$$

In the case of the data analyzed in this thesis, the sideband is not shifted back to the center of the Fourier transform and instead reference interferograms are employed. The reference interferogram, also not shifted back to the center of the Fourier transform, will have the same slope as the data interferogram. Subtracting the reference from the data will cause the slope terms to cancel leaving;

$$\Delta\phi(x,y) = -\arg\left(\mathcal{F}^{-1}\left[\mathcal{F}\left[I_{\text{Data}}(x,y)\right]_{\text{masked}}\right]\right) + \arg\left(\mathcal{F}^{-1}\left[\mathcal{F}\left[I_{\text{Ref}}(x,y)\right]_{\text{masked}}\right]\right)\,. \tag{2.56}$$

2.7.3 Interferometry Analysis Method

The theoretical framework for interferometry analysis has been discussed in the previous section; here the method used in this thesis is described and is summarized in figure 2.9.

- Panel **(a)** shows a raw data interferogram recorded on a camera. The phase shift incurred

is small so no fringe shift is visible by eye.

- The first step is to multiply the raw interferogram by a 2-D Hann window[§] to smooth out the hard edges of the interferogram and prevent ringing in frequency space. As this is simply a low-frequency amplitude modulation, the underlying phase profile is preserved. The result of applying the 2-D Hann window to the interferometric data is shown in panel **(b)**

- Next the image is Fourier transformed. A central peak and two sidebands are observed in panel **(c)** as expected. Here the area enclosed by the dotted lines represents the sideband to be isolated. Everything outside of the dotted black lines is to be set to zero.

- Panel **(d)** Shows the isolated sideband. The sideband is not shifted back to $k_x = 0$.

- The isolated sideband is inverse-Fourier transformed and the argument of the resulting complex image is taken. This is shown in panel **(e)**

- The function $\arg(x)$ can only return values in the range $(-\pi, \pi]$ leading to phase discontinuities as the phase wraps from π to $-\pi$ or vice-versa. Thus the image in panel **(e)** must be *phase unwrapped* to remove the sharp jumps in phase (section 2.7.4). The result of this process is seen in panel **(f)**.

- As expected from equation 2.55, there is a large phase slope in panel **(f)**. To remove this, a reference interferogram — taken with no plasma present — is analysed in parallel with the data interferogram. Then by subtracting the reference phase map from the data map, the image in panel **(g)** is obtained.

- Finally, for interferograms with very small phase shifts, like the one presented in panel **(a)**, a slowly varying background phase-shift which changes every shot is sometimes observed. This background phase shift is not due to the plasma but to variations in the phase front of the beam itself. This background phase is typically in the form of a second order polynomial and can be removed relatively easily with a background fitting procedure as described in section 2.7.5. After applying the background subtraction technique the phase map in panel **(h)** is obtained.

[§]The 2-D Hann window is given by $w(x, y) = 1/4(1 - cos(2\pi x/W)(1 - cos(2\pi y/H)$, where W and H are the width and height of the image respectively.

2.7.4 Phase Unwrapping

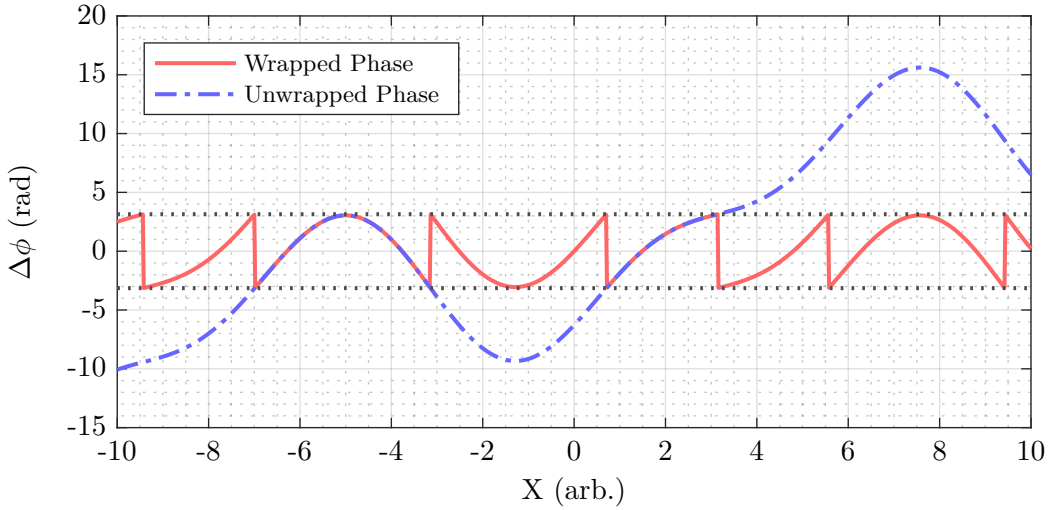

Figure 2.10: A simulated wrapped phase profile and its unwrapped counterpart.

As mentioned above, the values returned by $\arg(x)$ are constrained to lie within the range $(-\pi, \pi]$. A real phase profile $\Delta\phi(x)$ often exceeds this range and so through the process of retrieving the phase profile from an interferogram it will become wrapped. That is, it will become confined to the range $(-\pi, \pi]$ through modular division;

$$\phi_{\text{meas}}(x) = ((\Delta\phi_{\text{real}}(x) + \pi) \mod 2\pi) - \pi\,. \tag{2.57}$$

Unwrapping the phase profile in one dimension over the range $x_{\min} \leq x \leq x_{\max}$ is straightforward; track the phase from one side of the profile, say starting $x_{\min}$, to the other, $x_{\max}$, and if the value at a point x_0 jumps discontinuously from π to $-\pi$ then add 2π to $\phi(x > x_0)$. Alternatively if the phase at x_0 jumps discontinuously from $-\pi$ to π then subtract 2π from $\phi(x > x_0)$. This process is depicted in figure 2.10.

While useful to gain an understanding of the concept, the simplicity of one dimensional phase unwrapping is misleading as the problem becomes significantly more difficult in two dimensions. In the one dimensional case the starting point is irrelevant, one could just as easily have started at $x_{\max}$ and moved towards $x_{\min}$ or at a mid point and worked outwards. Aside from an unimportant offset the phase profile would not change.

However, in two dimensions the starting point and the unwrapping path followed can

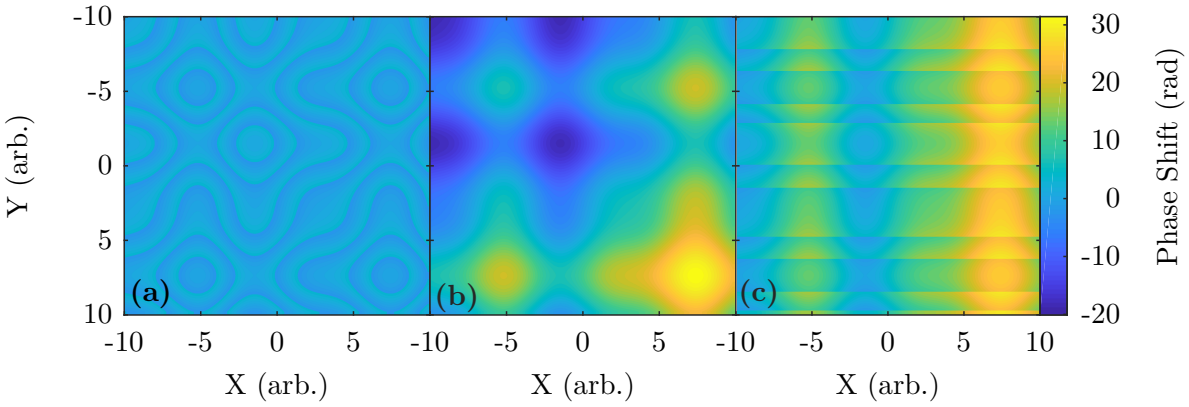

Figure 2.11: Demonstration of good and bad 2D phase unwrapping of a simulated phase map. Panel **(a)** shows a simulated wrapped phase map. In panel **(b)** this map has been correctly unwrapped using an appropriate 2D phase unwrapping routine. In panel **(c)** the image has been unwrapped row-by-row starting in the top left corner. As can be seen this does not remove all of the discontinuities in the image.

affect the resulting unwrapped phase map if care is not taken. This is illustrated in figure 2.11 which shows a 2D wrapped phase map in panel (a) that has been unwrapped correctly using an appropriate 2D phase unwrapping algorithm in panel (b), and incorrectly unwrapped by applying a 1D phase unwrapping algorithm row-by-row in panel (c).

Not only does the unwrapping path matter, but so too the treatment of any residues in the image. Residues typically arise in areas with a large local phase gradient, which cause fringes in the interferogram to bifurcate. Numerous algorithms have been developed to perform 2D phase unwrapping and to correctly treat phase residues and discontinuities. In this thesis two algorithms are employed; Goldstein unwrapping[140] implemented in *Matlab*[141] and Herráez unwrapping[142] implemented in *Python*[143].

2.7.5 Background Subtraction

As mentioned in section 2.7.3, for low-phase shift interferograms, shot-to-shot variations in the wavefront of the probe beam can add a significant background to a phase map. By viewing successive plasma-free phase maps it can be shown that the background phase typically has a second order polynomial profile. This can be removed by a polynomial subtraction.

To perform the background subtraction, it is necessary to mask out the plasma region of the image as shown in panel (a) of figure 2.12. Here the area between the dashed black lines represents the masked region. A second order polynomial is then fit to the image column by

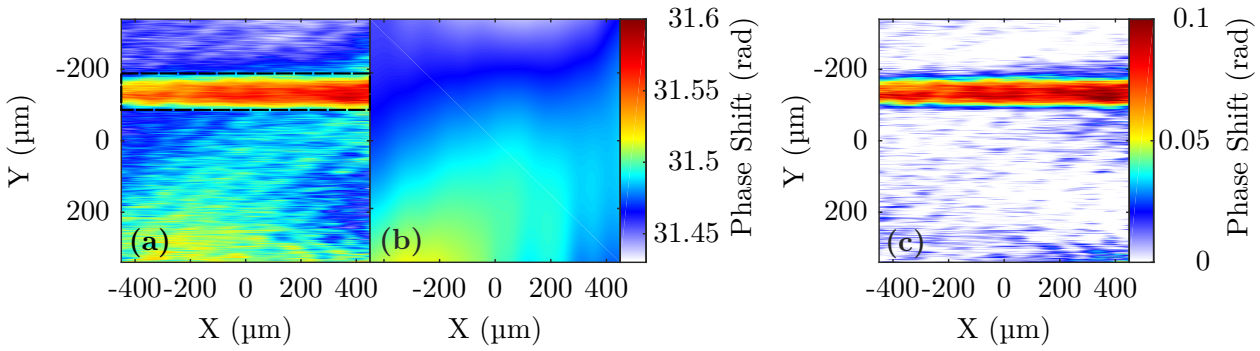

Figure 2.12: Three phase maps demonstrating the procedure by which the polynomial background subtraction operates.

column, ignoring the masked region. Each of the fitted polynomials are then placed side by side to form the columns of an image devoid of plasma as shown in panel (b) and subtracted from the original interferogram to isolate the phase shift due to the plasma, as seen in panel (c).

2.7.6 Extracting Density From Phase

As seen in equation 2.43, the measured phase profile comprises the line integrated electron density. Retrieving the electron density profile from a phase measurement requires assuming something about the variation of electron density with z. In this thesis, electron density profiles are assumed cylindrically symmetric and are probed in two ways; **(i)** longitundinally, such that the electron density profile is invarient in z, that is that the cylindrical axis of symmetry is coaxial with z and **(ii)** transversely where the variation in z is mirrored in the y axis, that is that cylindrical axis of symmetry is coaxial with x. These two scenarios are depicted in figure 2.13.

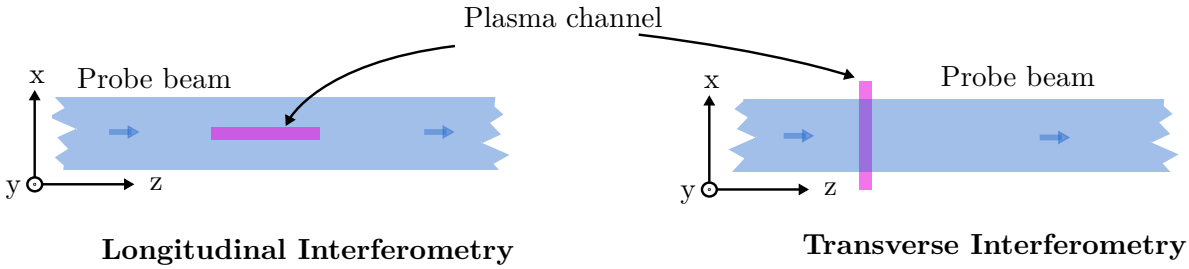

Figure 2.13: Orientation of axes for longitudinal and transverse interferometry.

Longitudinal Interferometry

If $n_e(x, y, z)$ can be reduced to $n_e(x, y)$ then the integral in equation 2.43 may replaced by a product and the equation may be easily inverted. In this case, the problem of retrieving the electron density is reduced to scaling the measured phase shift as;

$$n_e(x, y) = -\frac{\Delta\phi(x, y)}{r_e \lambda L}\,, \tag{2.58}$$

where L is the length of the plasma structure, which is assumed to be invariant along the z-axis.

Transverse Interferometry

It becomes more complex to retrieve the electron density when $n_e(x, y, z)$ is reduced to $n_e(y, z)$. In this case, the measured phase shift corresponds to a transverse projection of the electron density distribution.

Consider a cylindrically symmetric function in two dimensions characterized by $f(\rho)$, with ρ the radial displacement from the symmetry axis. The one dimensional projection of this two dimensional distribution is its Abel Transform[144];

$$f_A(y) = 2\int_y^\infty \frac{f(\rho)\rho}{\sqrt{\rho^2 - y^2}} d\rho\,. \tag{2.59}$$

The inverse Abel transform provides a method of retrieving $f(\rho)$ given $f_A(y)$. It can be written as;

$$f(\rho) = -\frac{1}{\pi}\int_\rho^\infty \frac{df_A(y)}{dy}\frac{1}{\sqrt{y^2 - \rho^2}} dy\,. \tag{2.60}$$

Specifically applied to the problem of electron density retrieval, this can be rewritten as;

$$n_e(\rho) = \frac{1}{r_e \lambda \pi}\int_\rho^\infty \frac{d\Delta\phi(y)}{dy}\frac{1}{\sqrt{y^2 - \rho^2}} dy\,. \tag{2.61}$$

Solving for the radial electron density profile at first seems relatively straight forward. However, a difficulty with directly implementing the Abel inversion from equation 2.61 arises for two reasons; firstly computation of the derivative of the phase profile can amplify any noise

present and secondly, the denominator in equation 2.61 becomes large for the lower limits of the integrand.

Numerous techniques have been developed to robustly deal with these difficulties. In the work contributing to this thesis, Abel transforms were performed using a *Python* implementation[145] of the Hansen-Law method[146]. This method relies on a recursive approach to solving the Abel Inversion problem and is applicable to noisy data which is often what is retrieved from low-signal interferograms.

It should be clear that this method relies heavily on the assumption of cylindrical symmetry. Without symmetry the standard Abel inversion density retrieval fails.

Expected Density

In many cases, it can be useful to compare measurements of the electron density with the expected density for full ionization of a particular species at a given pressure.

Consider a gas of uniform pressure P at a temperature T and with N electrons per gaseous molecule — for example diatomic hydrogen, H_2, would have $N = 2$ while argon would have $N = 18$. In this case the electron density of the fully ionized gas may be written as

$$n_e^{\text{expt.}}[\text{cm}^{-3}] = \frac{NP[\text{mbar}]}{10^4 kT}\,, \tag{2.62}$$

where k is Boltzmann's constant.

As an example, if a plasma is formed in gaseous hydrogen (N=2) at 50 mbar and at room temperature (293 K) then the expected electron density for full ionization would be $n_e^{\text{expt.}} = 2.47 \times 10^{18}\,\text{cm}^{-3}$.

2.7.7 Interferometry with Femtosecond Probe Pulses

One additional difficulty not yet addressed is the use of femtosecond probe pulses to perform interferometric measurements of a plasma. In the context of experiments in the field of LPAs, femtosecond probes are standard for two reasons. Firstly, the evolution of plasma structures can occur on the femtosecond timescale and secondly use of a femtosecond probe removes the need for an auxillary probing laser system. A leakage taken from behind a mirror in the early

stages of amplification can often suffice as a reliable and synchronized probe.

The analysis in the above sections assumed a harmonic plane wave. If instead the interference of two pulses of light of duration τ is considered the interference pattern generated described in equation 2.48 is modified[147];

$$I(x,y) = c\epsilon_0 E_0^2 \left[1 + V(x)\cos\left(kx\sin\varphi - \Delta\phi(x,y)\right)\right] , \tag{2.63}$$

with $V(x)$ a function that describes the visibility of the fringes, given as,

$$V(x) = e^{-\frac{\ln(2)\sin^2\varphi}{c^2\tau^2}\left(x-\frac{d}{\sin\varphi}\right)^2} , \tag{2.64}$$

with d the path difference between the pulses.

This describes mathematically what is quite intuitive from an experimental point of view. As d becomes large, $V(x) \to 0$, that is, if the path difference between the pulses is very large, then the pulses will not interfere. Even if the pulses are perfectly overlapped, $d = 0$, the interference term in equation 2.63 will still vanish for large values of x. Indeed the amplitude of the interference term will drop by a factor of $1/e$ at a position;

$$x_{\text{int}} = \pm\sqrt{\frac{1}{\ln(2)}}\frac{c\tau}{\sin\varphi} . \tag{2.65}$$

For ultrashort pulses the interference region $(-x_{\text{int}}, x_{\text{int}})$ can become too small to observe features of interest. In this case, placing a bandpass filter into the interferometer can help to stretch the pulses and widen the interference region.

2.7.8 The Folded Wavefront Interferometer

In practice there are many different implementations of the interferometer, although a subclass of these schemes particularly conducive to interferometry with femtosecond probe pulses and scenarios where access to the interaction region is restricted, is the folded-wavefront interferometer. The folded-wavefront interferometer differs from other implementations in that the beam is split and recombined *after* passage through the object of interest — this removes the need for long reference and probe arms in which it can be difficult to match the optical

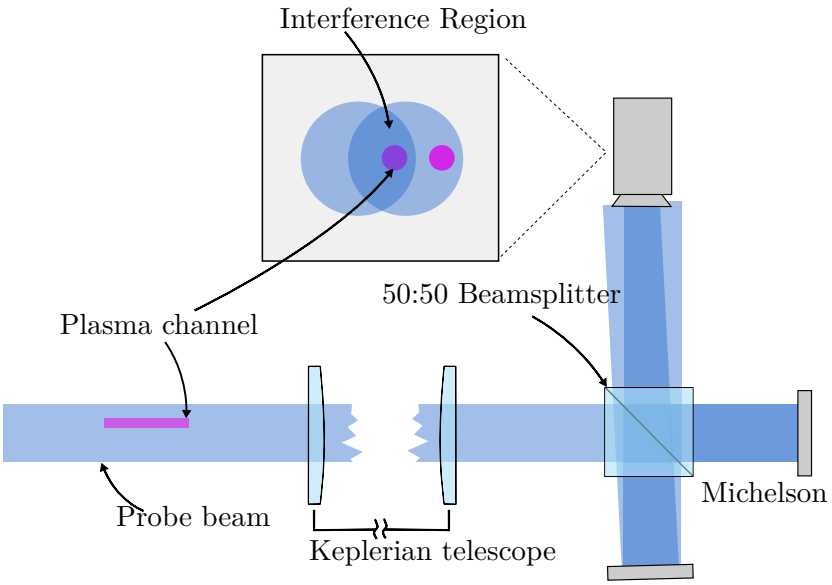

Figure 2.14: Schematic of a folded wavefront interferometer in a Michelson configuration performing longitudinal interferometry on a plasma structure. The inset shows an example of the kind of image expected on the CCD.

path length to the required micron length scale consistent with femtosecond pulse durations. The price that must be paid for this convenience is that the probe beam must be much larger than the plasma object of interest such that a large unperturbed part of the beam which has not interacted with the plasma may be used as the reference for the region of the beam which has passed through the plasma.

The basic layout of one implementation of the folded-wavefront interferometer is shown in figure 2.14. A collimated probe beam is passed through a region of plasma such that the plasma only sits on one side of the beam. The downstream end of the plasma structure is then imaged onto a camera. However, before allowing the beam to hit the camera, it is split in a Michelson interferometer and one of the arms is adjusted to cause the second image of the probe beam to become offset from the first.

As shown in the figure, this is done in such a way as to cause a region of no plasma from one of the beams to overlap with a region of plasma from the copy of the beam. In doing so, a small angle is introduced between the wavefronts of the two arms which leads to the formation of interference fringes.

Chapter 3

Demonstration of Low-Density Lens-Formed HOFI Plasma Channels

3.1 Introduction

In this chapter results are presented from the first proof of concept experiment to demonstrate the formation of hydrodynamic optical-field-ionized (HOFI) plasma channels with on-axis electron densities below $1 \times 10^{18}\,\mathrm{cm}^{-3}$. The experiment was performed in early 2017 using the Laser Plasma Accelerator Group's TW laser system. This system was restored to full operation by the author over the course of six months after a long period of downtime.

3.1.1 Motivation

As discussed in section 1.5, a plasma waveguide for the next generation of laser plasma accelerators would have several desirable properties: **a)** it would be capable of operation with low on-axis densities of order 10^{17} cm^{-3}; **b)** it would have a length of order hundreds of millimeters; **c)** it would be capable of multi-kHz operation; and **d)** it would be capable of operation at those high repetition rates for extended periods.

Plasma waveguides for high-intensity lasers currently fall into two categories, as described

in section 1.5: **i)** waveguides which can operate at low axial density but which are not suited to operation at high repetition rate, and **ii)** waveguides which can operate at high repetition rates for indefinite periods, but are restricted to high-axial density. Here the aim is to bridge that gap by demonstrating, for the first time, the generation of a plasma channel which can operate as a low-axial density waveguide and has the potential to operate for an extended period of time at high repetition rates in the multi-kHz regime.

At the start of this experimental campaign, simulations of the formation of HOFI plasma channels were proving difficult to implement due to the many different timescales at play: ionization and heating on femtosecond timescales, isotropization on picosecond timescales and thermalization and shock propagation/channel expansion on nanosecond timescales[148]. Several particle-in-cell and fluid codes were tested by other group members and finding consistency in the results was non-trivial due to a suite of bugs discovered in the codes.

The idea behind this first proof of concept experiment was to create a short HOFI plasma channel in hydrogen with low-axial density as a proof of concept and to compare its expansion dynamics with both analytic theory and simulations to determine whether they could be relied upon to predict sensible results.

3.1.2 Objectives

The objectives of the experiment were as follows:

- Provide the first experimental demonstration of the formation of HOFI plasma channels at low-density.
- Characterize the expansion dynamics and compare with analytic theory and simulations.
- Investigate the effect of the laser polarization on the expansion dynamics.
- Assess the suitability of these plasma channels to act as waveguides for future experimental work.

3.1.3 Overview of Chapter

Section 3.2 outlines the laser system used in these experiments while the experimental layout specific to this experiment is described in section 3.3. Section 3.4 gives details on the experimental results and analysis techniques employed and finally in section 3.5, conclusions are drawn.

3.2 Oxford TW Laser System

The Oxford laser system is a TW class Ti:sapphire chirped pulse amplification (CPA) laser system consisting of an oscillator (shared with a second laser system), a pulse stretcher, a regenerative amplifier, a multi-pass amplifier and a pulse compressor. In addition there is a probe beam which is split off from the main beam after the multi-pass amplifier and compressed separately.

The system produces three output beams divided across the two target areas. The beam delivered to the laser machining target area is a sub 100 fs, 0.5 mJ, 15 mm diameter, 800 nm centre-wavelength pulse operating at a repetition rate of between 990 Hz and 1 kHz. In the primary target area the main beam delivers a 50 fs, 30 mJ, 40 mm diameter, 800 nm centre-wavelength pulse operating at up to 10 Hz*. The probe beam consists of a sub 100 fs, $\sim$ 1 mJ, 3 mm diameter, 400 nm centre-wavelength pulse, synchronized to the main drive beam. All beams are horizontally polarized, that is the E-field oscillates parallel to the optical table surface and is p-polarised for most optical components in the system.

3.2.1 Detailed System Description

The system starts with an oscillator (*Spectra Physics Mai Tai SP*) producing compressed 800 nm centre-wavelength pulses with a bandwidth of 55 nm. The oscillator outputs a train of 35 fs pulses at a repetition rate of 84 MHz, with a mean power of 600 mW. The 3 mm diameter beam is evenly split between the Oxford TW laser system and another laser system (used for experiments in high-harmonic generation) which will not be discussed here.

*The output of the laser system at the time of writing this thesis is greatly improved, see section 3.2.2. However the parameters discussed here are relevant to the experiments described in this chapter.

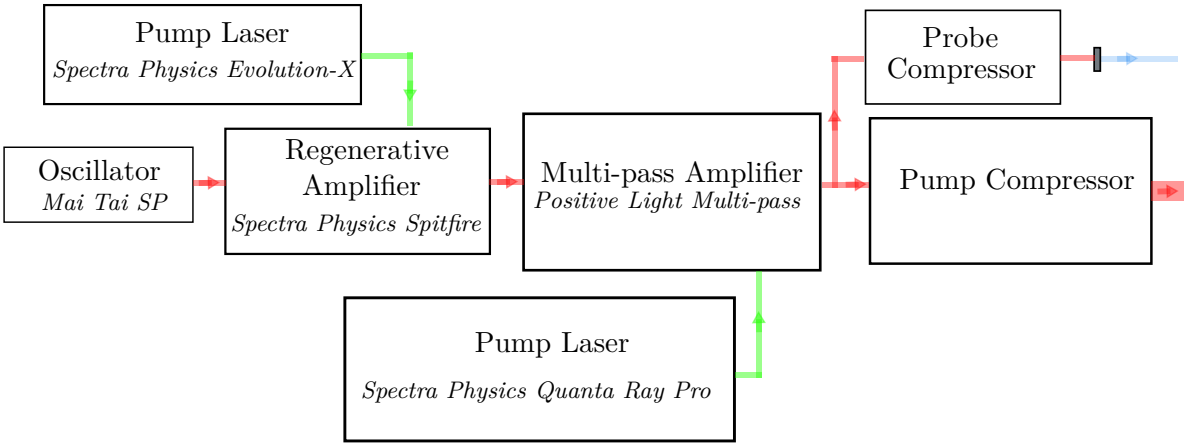

Figure 3.1: Simple schematic of the Oxford TW laser system layout.

The oscillator beam, once split, is directed to a regenerative amplifier (*Spectra Physics Spitfire*). Before amplification the pulse is stretched in a single grating pulse stretcher to approximately 115 ps, it is then injected into the regenerative cavity at a repetition rate of 1 kHz, controlled via a Pockels cell. In the cavity, the pulse passes several times through a Ti:sapphire crystal pumped at 1 kHz by a diode-pumped Nd:YLF laser (*Spectra Physics Evolution-X*) producing 11 W of 527 nm radiation in 112 ns FWHM pulses. The seed pulse is then switched out of the cavity by a second Pockels cell and passed out of the amplifier. At this point in the laser chain, the repetition rate of the seed beam has been down-converted from 84 MHz to 1 kHz and typically has an energy of 1.4 mJ per pulse.

The seed beam then enters a multi-pass amplifier (*Positive Light*). This amplifier is pumped by a flash-lamp-pumped Nd:YAG laser (*Spectra Physics Quanta Ray Pro*) producing frequency doubled 532 nm, 9.2 ns FWHM pulses at 10 Hz with an average pulse energy of 848 mJ per pulse. As the Nd:YAG laser runs at 10 Hz, the repetition rate of the seed beam must be again down converted. To achieve this a pulse slicer is used; a combination of two polarizing beam splitters and a Pockels cell. In addition to down converting the repetition rate, this pulse slicer also acts to reduce the amplitude of any pre-pulses produced by the regenerative amplifier.

The repetition rate of the seed beam can be down-converted to 10 Hz, 5 Hz or single shot using the pulse slicer. The repetition rate is adjusted by a control system, developed by the author, consisting of a *LabView* script which controls a pulse generator (*Berkeley Nucleonics Corporation Model 555*) connected to a MOSFET gate. By opening and closing the MOSFET gate the signals to open the pulse slicer are allowed through or blocked allowing for seed pulses

to be let through to the amplifier or blocked. The choice of repetition rate is decided by mode of operation required: 10 Hz is the maximum repetition rate the system can operate at; the 5 Hz operation allows for the production of an early trigger, more than 100 ms before a shot is fired, to allow for arming of diagnostics and pulsing of gas into the target cell. The single shot capability is particularly useful for data taking runs and was used extensively in the experiments described in this chapter.

The pulses which pass through the pulse slicer propagate through the four passes of the multi-pass amplifier, each time passing through the Ti:sapphire crystal pumped evenly on both sides by the Nd:YAG laser. The energy of the laser pulse leaving the multi-pass amplifier is typically in the range of 170-200 mJ and the diameter of the beam is approximately 6 mm.

After the multi-pass amplifier, the pulse is split at a ratio of 99:1. The more energetic beam is enlarged in a Galilean telescope to a diameter of 40 mm and passed to the pump compressor while the remaining beam is directed to a separate probe compressor. The pump compressor consists of two parallel, gold coated, 1500 lines per millimeter, sinusoidal gratings operating at an angle of incidence (measured with respect to the grating normal) of 55° and separated by 368 mm (measured normal to gratings). The pump compressor operates at atmosphere. The probe compressor, designed and built by the author, consists of a pair of parallel, gold coated, 1200 lines per millimeter diffraction gratings arranged to add almost identical amounts of second and third order dispersion to the probe pulse as that added to the main Ti:sapphire laser pulse by the main compressor. To achieve this the gratings were set up with an input angle of 30.9° and separated by 521.5 mm.

Finally the probe beam passes through a type I second harmonic generating crystal, a 500 µm thick piece of Lithium Triborate, LiB_3O_5, to frequency double it. The resulting probe beam operates at a wavelength of 400 nm.

3.2.2 Condition and Stability

The system described here is more than fifteen years old and as such does not perform as reliably as one would expect a modern system to perform. The main issues include poor stability and degraded optical components.

In terms of stability, the main beam has energy fluctuations of around 15 % rms and

peak to peak energy fluctuations exceeding 55 %. These fluctuations largely originate in the multi-pass amplifier and are thought to be due to the poor stability and reduced peak energy of the Nd:YAG pump laser. For Ti:sapphire systems — designed to operate their amplifiers in saturation — a degradation in peak pump energy causes a decrease in output energy and makes the overall stability of the system much more susceptible to variations in the peak pump energy[149,150]. The Nd:YAG laser, whose peak energy is currently 15 % reduced from its design energy of 1 J, regularly performs with 4 % rms and 22 % peak to peak fluctuations. Efforts have been made to improve the stability of the Nd:YAG laser, including cleaning and realignment of the optical cavities, replacing of the flashlamps and replacement of damaged optics within the laser itself as well as along the beam path to the Ti:sapphire crystal. While these measures helped to raise the peak energy of the Nd:YAG laser to its current value of 848 mJ, the stability remained unchanged.

Due to the age of the system, several of the components required replacement, the most important of these being the compressor gratings, which not only had severe burn marks and holes, but had also become milky with age; the milkiness most likely being due to contact with aerosols or dust in the air rather than oxidization of the gold itself, as gold is a very unreactive metal[151]. The gratings, along with other aged components such as a slightly damaged Ti:sapphire crystal in the multi-pass amplifier, produce an elliptical and structured near field spatial profile which ultimately affected the ability to focus to a diffraction limited spot.

In addition to the near-field exhibiting unwanted structure, the energy of the system was below specification. The degraded gratings in particular led to a poor total compressor efficiency of 25 % or an average individual grating efficiency of 71 %. Since performing the experiments described in this chapter, the gratings have been replaced and the total compressor efficiency is now 78 %, that is 94 % on average diffracted into the first order of each grating.

3.3 Experimental Setup and Parameters

Figure 3.2 shows the experimental layout used in the creation and diagnosis of the first low-density HOFI plasma channels. An 800 nm pump beam delivered an average energy of

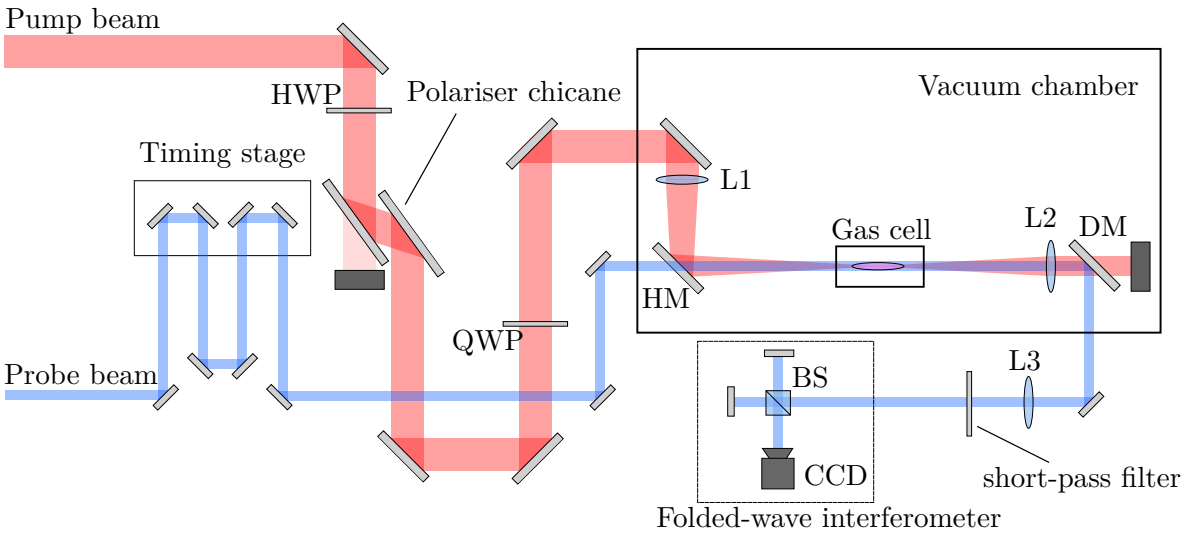

Figure 3.2: Experimental Layout: HWP (half-wave-plate), QWP (quarter-wave-plate), HM (holey mirror), L1 (lens with 500 mm focal length), L2 (lens with 270 mm focal length), L3 (lens with 1000 mm focal length), DM (400 nm reflecting, 800 nm transmitting dichroic mirror), BS (50:50 non-polarizing beam splitting cube), CCD (charge coupled device).

(26.7 ± 2.9) mJ on target in a (56.7 ± 3.4) fs FWHM pulse. The energy of the pump beam was controlled by a combination of a half-wave-plate and polariser chicane, while the ellipticity of the polarisation was controlled by a quarter-wave-plate. The pump beam was passed into the vacuum chamber through a 3 mm thick magnesium fluoride, MgF_2, window (c-cut to minimize birefringence) and focused using an uncoated, plano-convex, 500 mm focal length transmissive lens, L1, via a high-reflecting holey mirror to the centre of a gas cell. Folding the focus using this holey mirror allowed for the collinear injection of a 400 nm probe beam. The delay between the pump and probe was controlled via a four-pass delay stage.

3.3.1 Imaging the Interaction Point

Rays from the interaction point (IP) were magnified and imaged onto an 8-bit CCD (*Point Grey FL2G-13S2M-C*) outside the vacuum chamber using a Keplerian telescope consisting of two 50.8 mm diameter uncoated lenses, L2 and L3, of focal lengths 270 mm and 1000 mm respectively. Lens L2 was a bi-convex, while L3 was plano-convex. An 800 nm transmitting 400 nm reflecting dichroic mirror, DM, placed after the first lens in the telescope allowed for most of the pump light to be dumped post IP. The beams then exited the chamber, passed through L3, through a short-pass filter and into a folded-wave interferometer in a Michelson

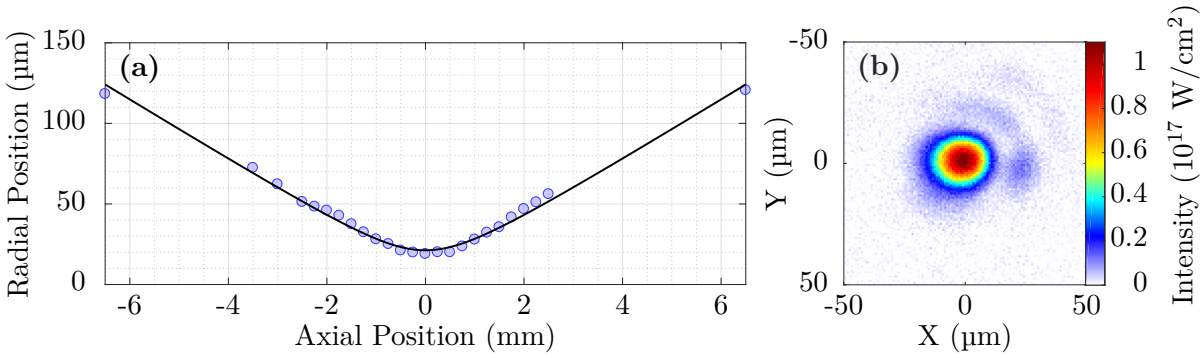

Figure 3.3: (a) Focal scan data showing the longitudinal variation in beam radius as measured with the $D4\sigma$ method. The scatter data represents individual measurements while the black line, a fit of equation 2.2 to the data. (b) An image of the focal spot with an approximate intensity distribution calculated using a pixel summation method.

configuration, consisting of a 50.8 mm uncoated non-polarising beam splitting cube. The CCD sensor was covered with two more removable short-pass filters to prevent unwanted pump light from interfering with the diagnostic.

By removing or inserting the short-pass filters it was possible to use the CCD to image the pump or probe beam respectively, although, due to chromatic aberrations associated with singlet plano-convex and bi-convex lenses, the image plane for the 800 nm and 400 nm beams were 12 mm from each other. The lens L2 was mounted on a motorised translation stage to allow for small changes to the image plane to account for this. Respective calibrations of the CCD at both 400 nm and 800 nm showed no measurable change in the calibrated pixel size with imaging position over the motion of the stage. Calibrations of the CCD were performed by back-lighting a standard 1951 USAF resolution target placed at focus with collimated 400 nm and 800 nm radiation. The calibration was found to be (0.83 ± 0.01) µm per pixel at both 400 nm and at 800 nm. The USAF target was also used to measure the resolution of the imaging system; this was found to be (7.0 ± 0.8) µm at 400 nm and (9.8 ± 1.1) µm at 800 nm.

3.3.2 Pump Beam Focus

By removing the short-pass filters it was possible to image the focal spot and make a measurement of the focal profile of the pump beam. Figure 3.3 shows a focal scan of the pump beam and an image of the focal spot; the measured spot size is $(16.5 \pm 0.2) \times (20.5 \pm 0.2)$ µm while the Rayleigh range, obtained from a fit of equation 2.2 to the focal scan data, comes to 1.06 mm. Analysis of the measured focal spot profiles was performed using the ISO-standard D4σ

method[138] (section 2.6.1). The focal spot has an $M^2 \approx 2$ and shows some evidence of coma as well as some structure in the wings, all of which is not unexpected as the near field spatial profile is structured, as described in section 3.2.2, and a central elliptical portion of the beam has been removed from reflection off the holey mirror prior to IP.

The focal spot data was recorded outside the vacuum chamber. The reliability of focal spot data taken using the camera outside the chamber was confirmed by taking consecutive scans with an in-chamber focal camera and the out-of-chamber camera at atmosphere and then pumping down the vacuum chamber and ensuring that no distortion in the pulse arose during the pump down as viewed on the out-of-chamber camera. The focal spot data shown here was taken while the chamber was up to air using a low-power setting of the laser. Pumping down the chamber did not affect the focal spot, nor did the spot change substantially at high-power due to nonlinear effects in the transmissive lens or vacuum window.

Using a pixel summation method, it was possible to estimate the intensity of the pulse at high-power (section 2.6.3); this gives a peak intensity of $1.1 \times 10^{17}\,\mathrm{W\,cm^{-2}}$. This method does not account for spatio-temporal couplings[152] or chromatic aberrations but provides a reasonable estimate of the intensity, which can be quite useful during the experimental setup. This estimate is in good agreement with a back of the envelope calculation of the expected peak intensity of a Gaussian pulse using the measured energy, spot size and pulse duration, $(0.88 \times 10^{17} \pm 0.18 \times 10^{17})\,\mathrm{W\,cm^{-2}}$. The same pixel counting method was used to determine the peak intensity at a distance of 1 mm and 2 mm from focus and found it to be in agreement with Gaussian theory. By these estimates, it would be expected that the peak intensity at a distance of 2 mm either side of focus would be $2.2 \times 10^{16}\,\mathrm{W\,cm^{-2}}$, approximately 160 times the ionization threshold for atomic hydrogen, assuming a simple barrier suppression model for the ionization and linear polarization as described in section 2.3.1. Thus it is expected that full ionization out to a large radius is achieved over the full length of the gas cell.

3.3.3 Pump Pulse Duration

The duration of the pump pulse was measured outside the vacuum chamber, after the polariser chicane shown in figure 3.2, on a single-shot autocorrelator (SSA). The SSA was custom built by previous group members, based upon a design that in theory allowed for the detection of

pulse-front tilt (PFT)[153].

After the SSA, the pulse passed through three transmissive optics; the zero order quarter-wave-plate of negligible thickness, a 3 mm thick MgF_2 window and the transmissive lens approximately 4 mm thick, made of fused silica. Together, the material after the SSA added approximately 240 fs^2 of GDD which would cause a 50 fs transform limited pulse outside the chamber to stretch to at most 52 fs on target.

Figure 3.4 shows an example autocorrelation taken using the SSA. The panel on the right shows the image visible on the CCD, while the panel on the left shows a lineout taken along the black line indicated in the right panel. The SSA shown here, optimized for maximum pulse compression by adjusting the compressor gratings, has a full width half maximum of 87.2 fs. To find the FWHM temporal duration of the pulse this number must be deconvoluted by assuming a temporal pulse shape. In this case a $sech^2$ pulse shape was assumed, giving a FWHM deconvolution factor of 0.65 and thus a FWHM pulse duration of 56.7 fs. The error in the pulse duration, 3.4 fs was extracted from the error in the fit of the data together with the error due to the finite pixel size (2.63 fs per pixel).

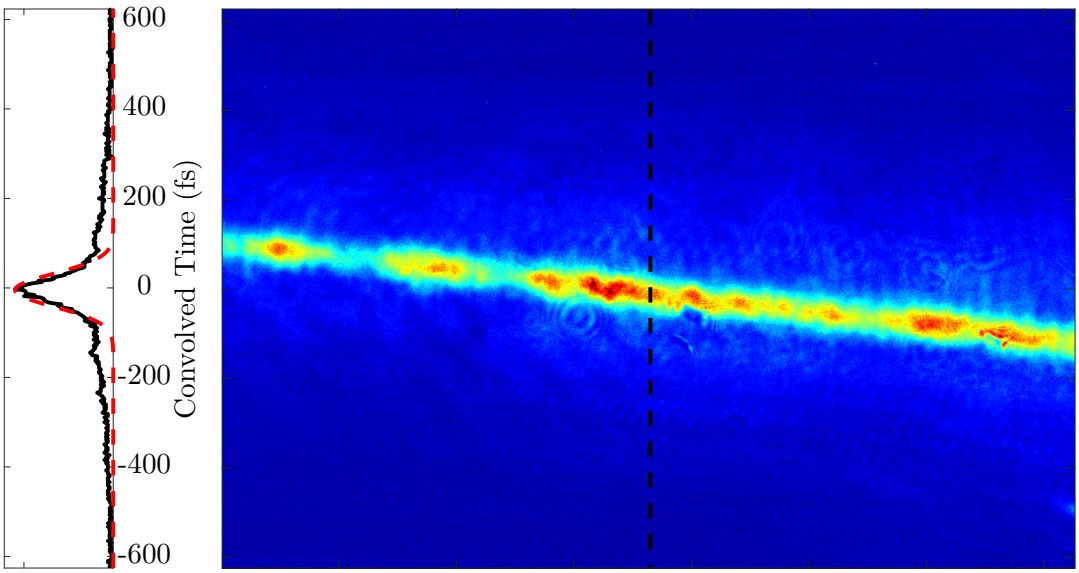

Figure 3.4: Raw data taken from the SSA (right pane) and a lineout (left pane) which is taken along the black line shown in the raw data. The red dashed line shows a Gaussian function fitted to the lineout.

It can be seen from the lineout and from the SSA image that there are significant wings on the autocorrelation. These are believed to arise, in part at least, from amplified spontaneous emission[154] in the multi-pass amplifier which has high-gain, showing an amplification in pulse energy by a factor of ~ 200. Other contributing factors could include the deteriorated pulse compression gratings, misalignment or pre/post pulses not removed by the pulse slicer in the multi-pass. Although attempts were made to remove these wings from the autocorrelation, it was not possible in the time frame of the experiment to address the issue fully. Wings in a pulse will reduce the peak intensity in the focus of the beam, though this was not thought to be problematic since the laser pulse was only required to field-ionize hydrogen, and the peak intensity was substantially above the threshold for this.

The tilt in the SSA in figure 3.4 suggests that there is some degree of PFT present. While the SSA should have been capable of quantitatively analyzing the PFT, crucial information relating to the crystal used and other design specifications could not be located (as the SSA is more than eight years old) and so a figure for the PFT could not reliably be extracted. It is however known that the SSA was designed to measure ultrashort pulses below 50 fs and given that the SSA calibration was performed by the author there is no concern with the measured value of pulse duration. In addition, the PFT if present, did not appear to be a significant issue as the threshold laser energy required for ionization of hydrogen was found to be approximately equal to the expected value.

3.3.4 Measuring the Polarization of the Pump Pulse

The polarization of the pump pulse was measured both outside the vacuum chamber and at the IP, in both cases using a setup similar to that shown in figure 3.5 (a). A polarizing beam splitter (*ThorLabs CM1-PBS252*) was placed at the location at which the polarization was to be measured and photodiodes (*ThorLabs DET10A*) were placed at each of the outputs. By monitoring the photodiode signal as a function of quarter-wave-plate position it was possible to determine the angle necessary to produce the required ellipticity. Figure 3.5 (b) shows that the measured signal varies with waveplate angle as expected. The data shows that circular polarization occurs for a quarter-wave-plate angle of 41.1° while linear polarization occurs for an angle of 356.1°. The blue data represents the photodiode signal at the vertical polarization

output of the polarizing beamsplitter while the red data represents the horizontal polarization output.

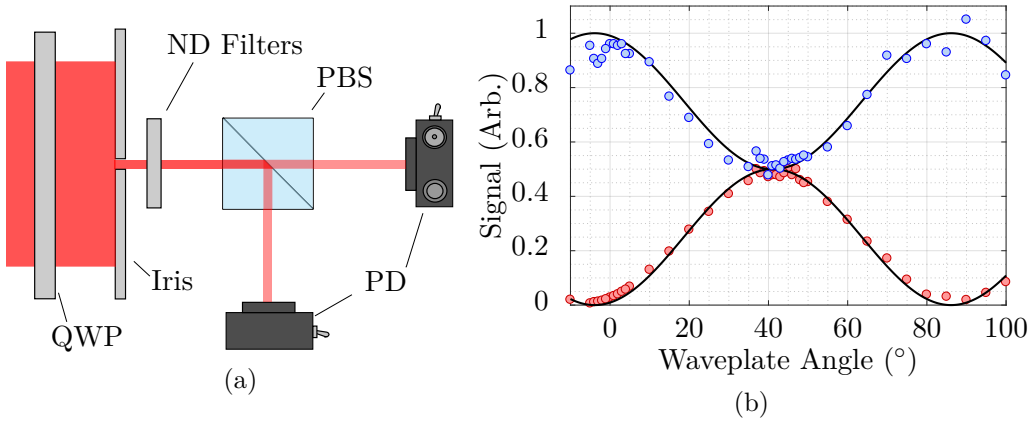

Figure 3.5: (a) Setup used to determine the angle of waveplate required to induce circular polarization; PD (photodiode), PBS (polarizing beam splitter) , QWP (quarter-wave-plate). (b) Scaled photodiode signal (circles) fitted to a squared sinusoid (black lines). The blue data represents the photodiode signal at the vertical polarization output of the PBS, while the red data represents the horizontal polarization output.

3.3.5 Measuring Energy of Pump Pulse

The energy of the pulse on target was measured in situ (just after the holey mirror) at high power in air using a pyroelectric energy meter (*Gentec QE25SP-S-MB-D0*). To ensure that the energy meter did not burn it was placed $\sim$ 300 mm upstream of the focus and subjected to 500 consecutive shots to provide an accurate measurement of both the average pulse energy as well as the associated rms and peak to peak errors.

3.3.6 Interferometry Diagnostic

The phase gained by the probe beam passing through the laser formed plasma was measured using a longitudinal folded-wave interferometer (section 2.7.8) consisting of a Michelson interferometer and a CCD. Upon splitting the probe pulse in two, interference fringes were introduced to the output of the Michelson by spatially off-setting the two beams to introduce an angle between the wavefronts of the two pulses. The spacing of the fringes could be adjusted by changing this spatial offset subject to two caveats; i) the area of the probe beam containing

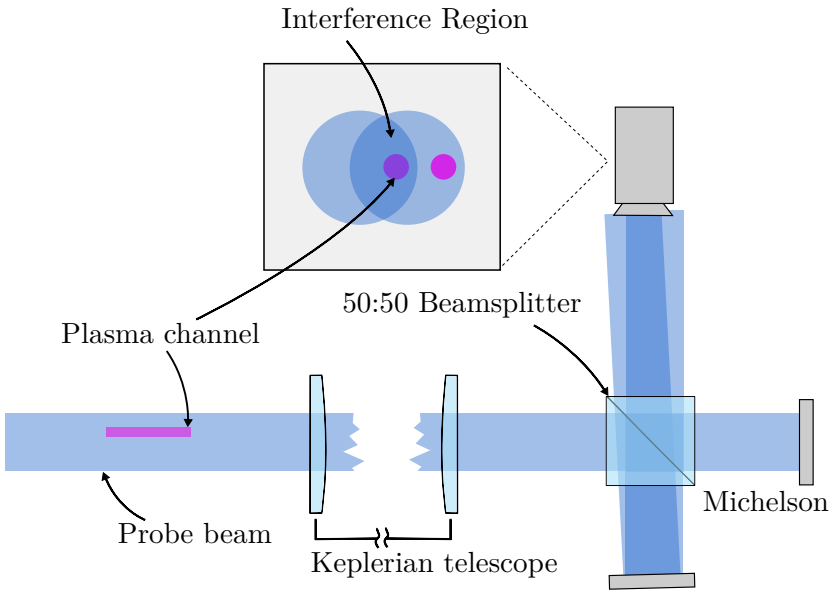

Figure 3.6: Schematic of the folded wavefront interferometer used to perform the longitudinal interferometry measurements in this chapter. The inset shows an example of the kind of image expected on the CCD.

light which had passed through plasma must be spatially overlapped with a part of the probe beam which didn't see any plasma and ii) the area of interference, dictated by the angle between the phase fronts and the transform limited pulse duration, must cover the entire area of interest.

As the wavefront of the probe beam was not perfectly flat and free from deformations, reference interferograms were taken with the pump and probe beams firing but without any gas in the cell. During the data analysis these reference shots were grouped by shot conditions, analysed and their extracted phase profiles averaged before being subtracted from the phase profiles retrieved from shots containing gas in the cell. In this way, systematic errors resulting from non-ideal probe beam quality could be mitigated. Reference shots were re-taken after any adjustment to the probe beam optical system.

Figure 3.7 (a) and (b) gives examples of the raw CCD image showing the interferogram of a reference and data shot respectively. Clearly visible is the outline of the downstream pinhole of the gas cell (section 3.3.9). The image of the pinhole was duplicated in the Michelson interferometer and partially overlapped with itself to produce the reference wavefront from a region of the probe beam with no plasma. The fringe spacing was then adjusted to be smaller than the smallest feature that was to be observed.

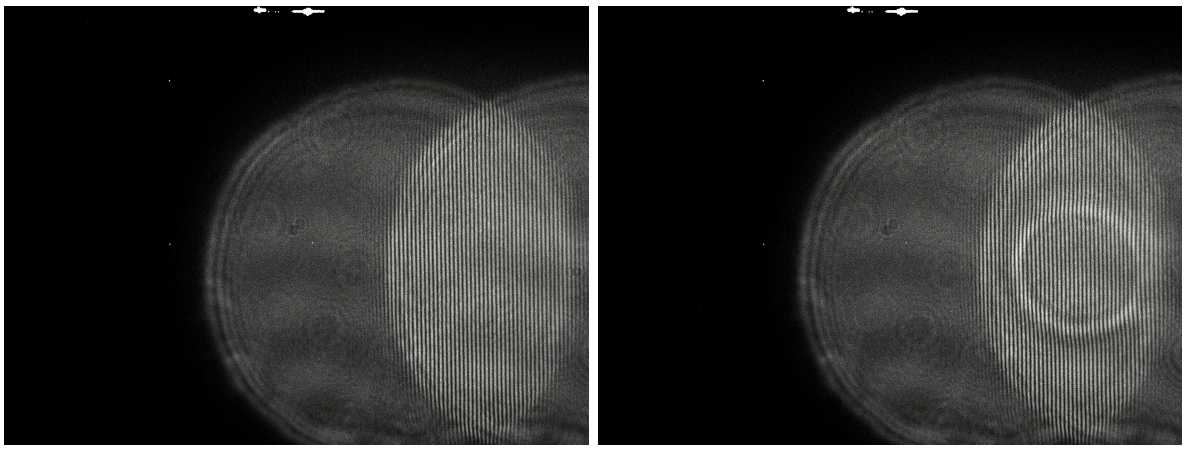

Figure 3.7: Sample raw CCD images of a reference (a) and data (b) interferogram obtained from the folded wavefront interferometer.

3.3.7 Optimizing the Image Plane of the Interferometry Diagnostic

Using standard alignment techniques it was possible to set the image plane of the interferometry diagnostic accurate to within a millimeter. To ensure good quality imaging of the plasma structures generated, it was necessary to further optimize the image plane by scanning it longitudinally using the imaging stage (the motorized translation stage upon which L2 was placed). Optimization of the image plane was achieved by monitoring the plasma structure as seen by the interferometry camera. The timing stage was driven to the end of its motion (corresponding to a large pump probe separation with the probe arriving after the pump) and the cell filled with between 30 and 60 mbar of hydrogen. The standard alignment procedure was good enough that the imprint of the plasma upon the probe could be seen on the interferometry diagnostic immediately using an online interferogram analysis code developed by the author based upon the analysis techniques discussed in section 2.7.3. As the imaging stage position was varied, the peak density read out by the online diagnostic increased and decreased, and in addition, features of the plasma structure sharpened and blurred out. The optimal image plane was taken to be the plane at which the features of the plasma channel were sharpest and the peak density extracted was highest.

The validity of this method for finding the optimal image plane was confirmed by beam propagation simulations using a FFT-BPM code developed by the author (section 2.4). The results of the simulation are shown in figure 3.8; panel (e) shows a 2 mm long sample plasma channel, while panel (d) shows the phase profile of a 400 nm probe beam as it is passed over

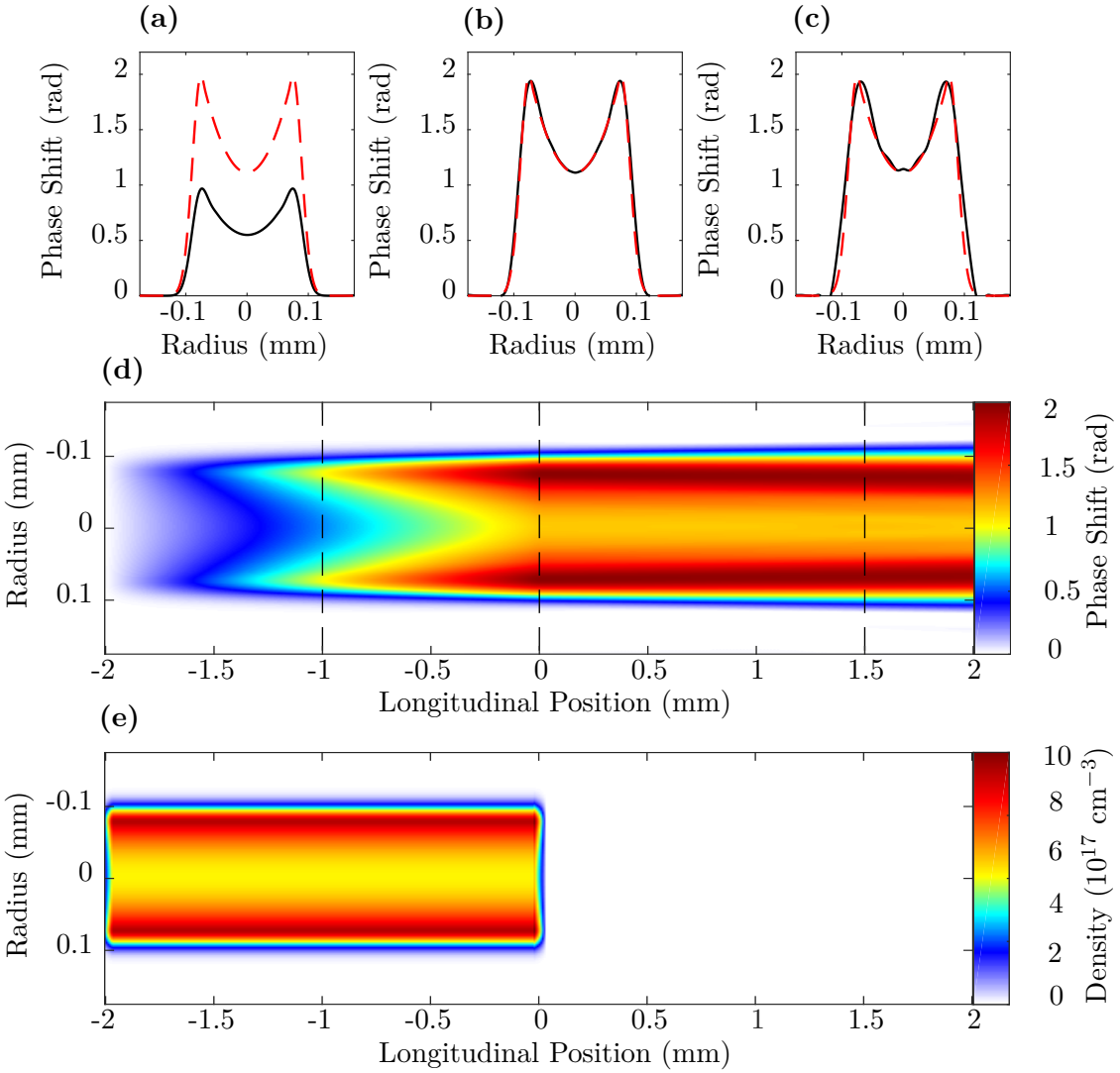

Figure 3.8: Simulation results confirming the experimental method used to determine the object plane of the imaging system. The simulated phase shift seen by the probe beam (black line) compared to the expected total phase shift (red dashed), for a 2 mm long plasma channel, with the object plane located: (a) 1 mm upstream of the end of the channel; (b) at the end of the plasma channel; and (c) 1 mm downstream of the end of the channel. A heat map of the accumulated phase shift throughout the propagation is given in (d) while (e) shows a heat map of the electron density profile of the plasma channel used in the simulations.

the plasma channel. Lineouts of this phase profile taken at the middle of, end of, and after the plasma channel are shown in panels (a) through (c). As the probe beam passes through the channel the phase imprinted upon the beam by the plasma increases linearly until the end of the channel is reached. At this point, the features imprinted upon the probe start to diffract

causing a very slight blurring of the channel features. This shows that the correct location of the object plane could be found reliably by adjusting the cell/optics position to yield the deepest and sharpest retrieved electron density profile.

The experiment as compared to the simulations, showed a slightly stronger blurring of the features as the imaging stage was moved downstream of the plasma channel. This was attributed to minor misalignment between the channel axis and the probe axis. However, the misalignment was deemed to be small and did not cause concern in the subsequent plasma channel measurements.

3.3.8 Pump Probe Timing

The relative timing between the pump and probe pulse was controlled by moving the 4-pass delay stage on the probe line. The overlap of the two pulses was found using a plasma blowout technique in which the gas cell was filled with hydrogen to around 200 mbar and the relative timing between the pump and probe scanned while the spatial profile of the probe beam was monitored for changes resulting from high levels of refraction around a plasma structure. If the probe pulse arrived at IP before the pump it saw unionized gas and passed through effectively unchanged. However, when the probe arrived behind the pump it saw a large amplitude localized phase shift from the plasma which caused a small portion of the beam to refract leaving a clear hole in the observed spatial profile of the probe pulse. The technique can identify the relative timing between the two pulses to within a pulse duration, or the accuracy of the timing stage.

3.3.9 Gas Cell

Both the gas cell and gas delivery system used in the experiments described here were designed and developed by previous members of the Laser Plasma Accelerators group[155,156]. Cell lengths of 1.95 mm and 4.20 mm were employed and in both cases 750 µm diameter pinholes were used. Hydrogen gas was fed to the cell from a central reservoir located approximately 2 m from IP, outside the chamber. The gas was pulsed in to the gas cell approximately 150 ms before a laser shot was fired to allow sufficient time for the cell to fill. The fill time was determined empirically.

The gas cell was mounted on a 6-axis Hexapod (*Physik Instrumente M-824*) to allow for the accurate alignment of the cell to the optical axis, and focal position of the beam.

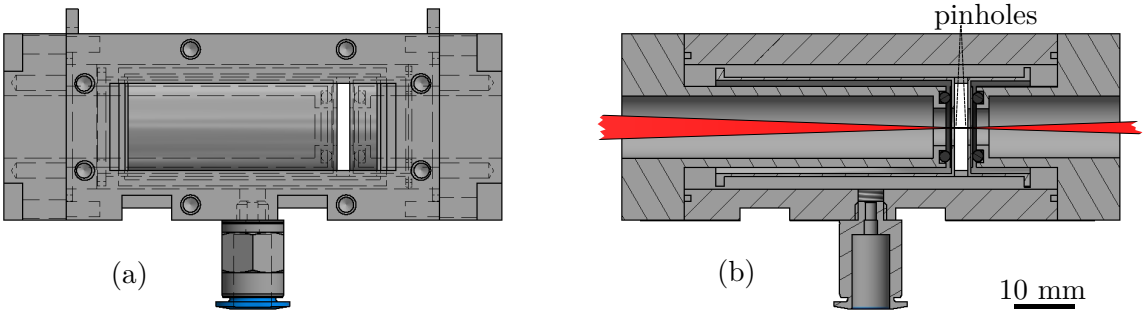

Figure 3.9: Gas cell used in Oxford plasma channel experiments (a) full view (b) section.

3.3.10 Determination of Gas Cell Length

For longitudinal interferometry it is important to determine the length of the gas cell accurately since the phase shift seen by the probe beam is proportional to the length of the cell. The cell length was measured in two ways: i) it was measured using a vernier calipers; and ii) the length was deduced from a pressure scan of the gas cell.

The pressure scan technique for deducing the gas cell length relies on the assumption that the pressure in the cell is uniform. In this case, the phase shift acquired by the probe passing through the cell may be reduced to

$$\phi = -\frac{\lambda e^2}{4\pi c^2 m_e \epsilon_0} \int_0^L n_e(z) dz \approx A n_e L \,. \tag{3.1}$$

It is assumed, based on previous work with the gas cell[155][156], that the pressure in the cell is close to that recorded by a pressure transducer placed near to the gas cell. This pressure allows for a calculation of the density of plasma expected from the full ionization of hydrogen gas, see section 2.7.6. By plotting the measured phase shift versus expected plasma density for a range of different fill pressures of the cell it is possible to extract the slope, Γ, of the data which can be related to the cell length by

$$L = \frac{1}{A}\Gamma = \frac{4\pi c^2 m_e \epsilon_0}{\lambda e^2}\Gamma \,. \tag{3.2}$$

It would be expected that any density ramps would be the same length for both the short and the long cell and thus to have a larger impact in the operation of the short cell, however, it was found that there was no substantial difference in the results obtained with the short and long cells. In addition, the cell length extracted from the pressure scan was very similar to the measured length and thus it was determined that the density ramps did not play a large role in the operation of the gas cell or the measurement of the plasma density.

3.4 Results & Discussion

3.4.1 Plasma Channel Formation

Figure 3.10 shows the extracted electron density profiles measured from single shots of a circularly polarised channel-forming pulse of energy $(26.7 \pm 2.9)\,\mathrm{mJ}$ and an initial cell pressure of 50 mbar. The initial plasma formed comprises an approximately cylindrical region of diameter 72 µm and peak electron density $n_\mathrm{e}(0) \approx 2.4 \times 10^{18}\,\mathrm{cm}^{-3}$, corresponding to full ionization of the hydrogen gas. After the initial ionization, hydrodynamic expansion of the plasma is observed. During the course of this expansion a clear high density shock-front emerges at the plasma-gas interface leaving behind it a core of lower density plasma.

The initial plasma formation, while approximately cylindrical, is slightly asymmetric and contains some fine structure. However, during the expansion the fine structure disappears and a more symmetric plasma distribution evolves. It was observed during the course of the experiments that while the energy of the laser fluctuated with an rms spread of 2.9 mJ, the shape and density of the plasma profiles obtained did not vary significantly. Small changes in the size of the phase feature were observed and could be attributed to the varying size of the initial plasma column ionized by a laser of fluctuating intensity.

To mitigate the effects of this shot-to-shot jitter in the pulse energy, the electron density profiles were averaged over between 5-10 shots and this subsequent electron density profile was rotationally averaged about its centre to produce a 1-D lineout of the average electron density for a range of different times.

Figure 3.11 (a) shows averaged lineouts of the temporal evolution of a plasma channel formed in an initial cell pressure of 50 mbar of hydrogen. For this pressure, at $t = 3.9$ ns the

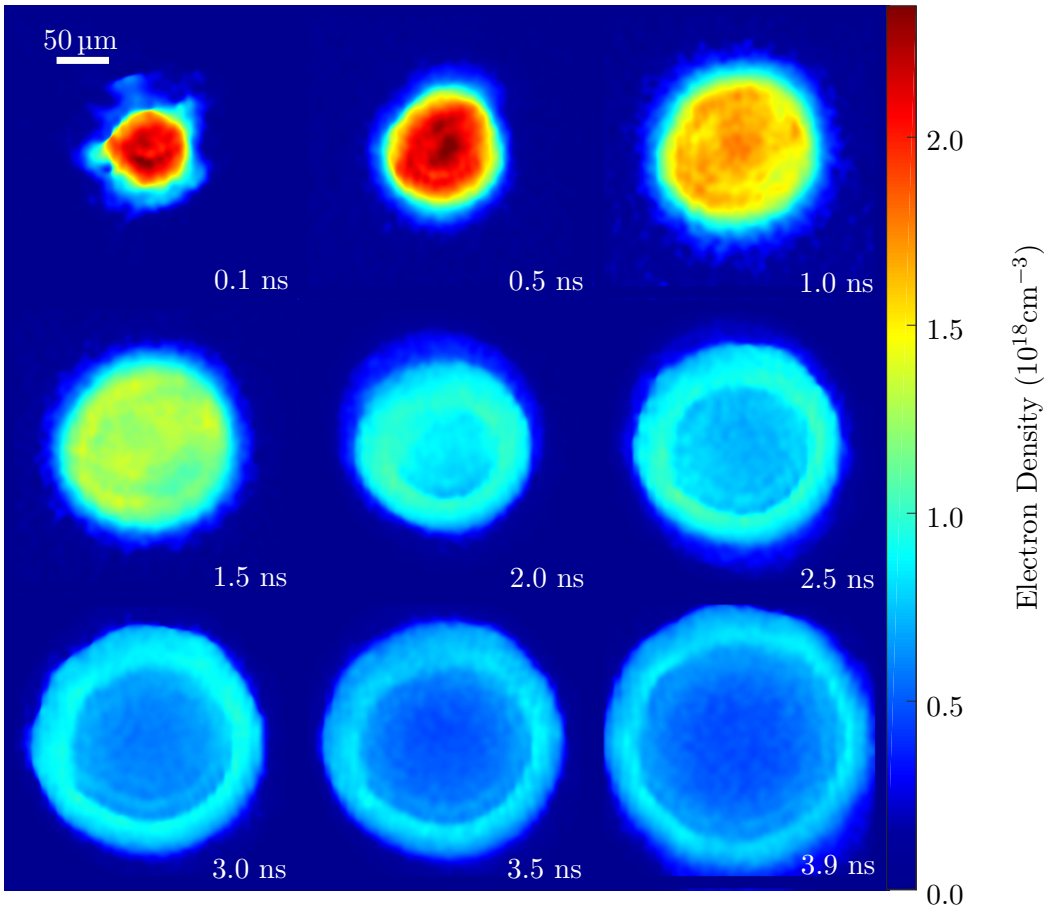

Figure 3.10: Single-shot data showing measured transverse electron density profiles at times t after the arrival of a channel-forming pulse focused into 50 mbar of hydrogen gas. Each profile is obtained from analysis of a single interferogram and is shown in a square of side 280 µm. The delay t is indicated for each plot.

plasma column has driven a cylindrical shock wave, with an electron density peak at $r \sim 92\,\mu$m; the electron density increases from $n_e(0) \sim 5 \times 10^{17}\,\mathrm{cm}^{-3}$ to approximately $7.9 \times 10^{17}\,\mathrm{cm}^{-3}$ at the peak of the shock front. Figure 3.11 (b) shows the evolution of the plasma channel at $t = 3.9\,$ns for a range of differing initial cell pressures, demonstrating plasma channels with on-axis densities below $n_e(0) = 2 \times 10^{17}\,\mathrm{cm}^{-3}$ for an initial cell fill pressure of 25 mbar. The lowest on-axis electron density recorded in these experiments (during a scan of fill pressures)

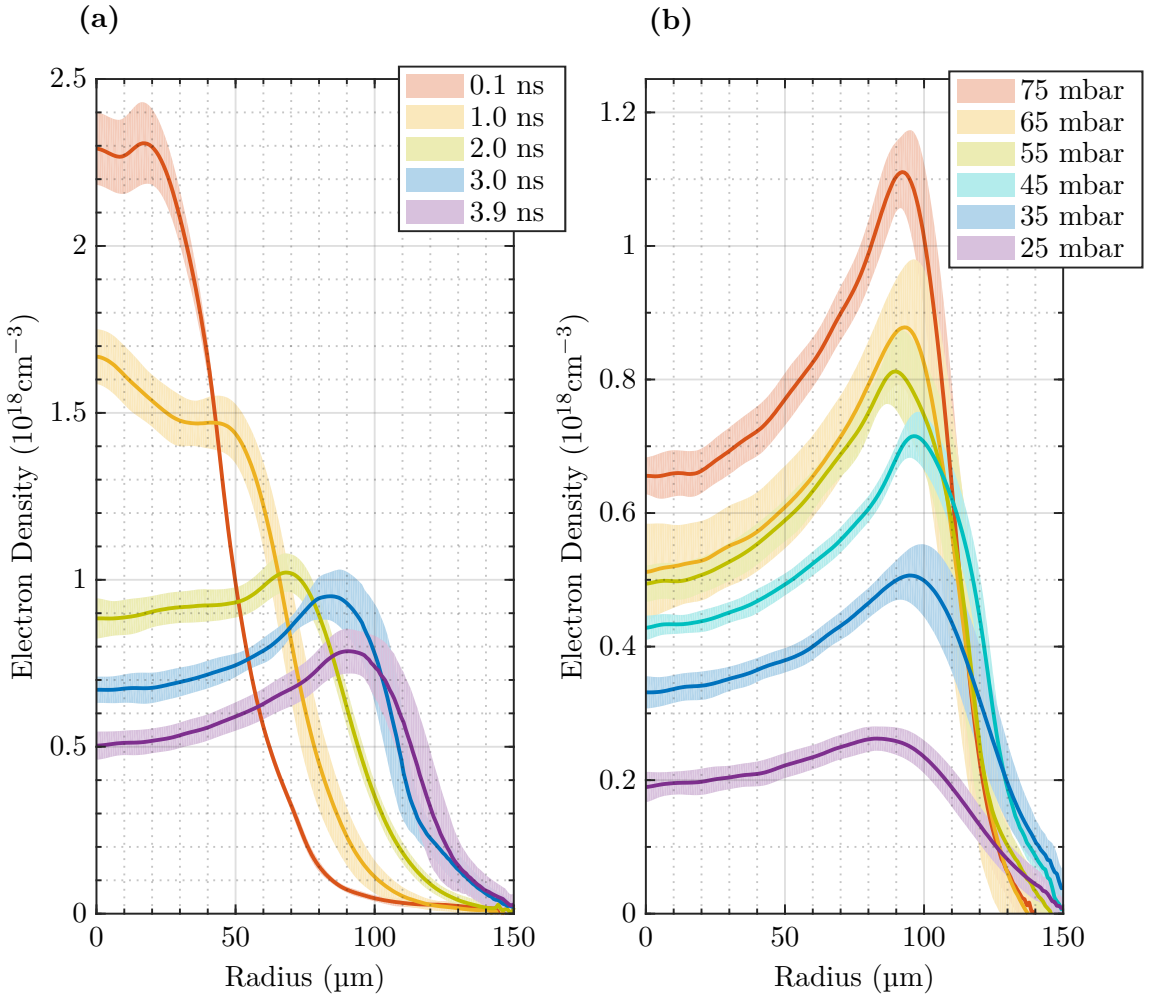

Figure 3.11: Measured transverse electron density profiles for hydrogen plasma after OFI by a circularly polarized pulse. The solid lines show the mean rotationally averaged profile for 5-10 shots while the associated coloured band shows the rms error in the measurement. (a) shows the temporal evolution of a plasma channel from an initial fill pressure of 50 mbar while (b) shows the electron density profile 3.9 ns after ionization for a range of different cell fill pressures.

was $n_e(0) \sim 1.6 \times 10^{17}\,\mathrm{cm}^{-3}$, as can be seen in figure 3.13.

3.4.2 Expected Guiding Properties

The rotationally-averaged electron density profiles at $t = 3.9$ ns can be used to calculate the lowest-order modes of the measured HOFI plasma channels by solving the Helmholtz equation, equation 2.12. A "leaky mode" code, developed by the Maryland group[109], was used to perform the calculation by assuming an electric field of the form $E(\vec{r_\perp}, z) = u(\vec{r_\perp})e^{i\beta z}e^{-\alpha_{1/e}z}$ where z is the position along the waveguide axis and $\vec{r_\perp}$ is the position vector perpendicular

to the laser propagation direction. The 1/e attenuation length for the *power* of the guided mode is then given by $L_{1/e} = 1/(2\alpha_{1/e})$.

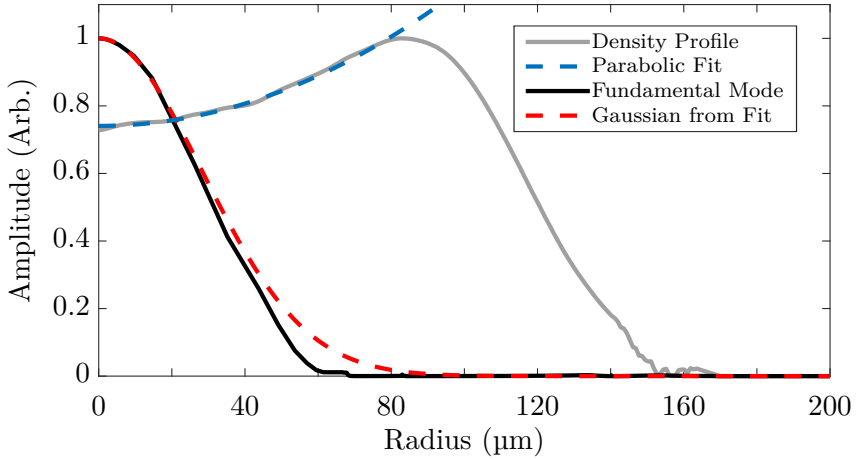

Figure 3.12: The lowest order mode (black) of a measured plasma channel (gray) calculated by providing the plasma channel's electron density lineout as an input to a leaky mode solver. A parabolic fit to the central region of the channel is shown by the dashed blue line, and the dashed red line shows the calculated lowest order mode for this parabolic channel.

For $P = 25\,\text{mbar}$ ($n_e(0) \approx 1.9 \times 10^{17}\,\text{cm}^{-3}$ at $t = 3.9\,\text{ns}$) the measured channel has a calculated lowest-order mode with a $1/e^2$ intensity spot size of $w_m = 50.1\,\mu\text{m}$, and an attenuation length of $L_{1/e} = 178\,\text{mm}$. Figure 3.12 shows the density profile for this case, along with the intensity profile of the lowest order mode. For batch analysis of the data, it was more convenient to calculate the matched spot size of the channels by fitting a second order polynomial to the central region of the density profile — in other words approximating the central portion of the plasma channel to an infinite parabolic plasma waveguide. From this parabolic fit, it is possible to extract an approximate matched spot size from equation 2.9.

Figure 3.12 shows the parabolic fit to the central region of the density profile and in addition it shows a Gaussian (the lowest order mode of the infinite parabolic plasma waveguide) with a spot size of $w_m = 56.6\,\mu\text{m}$ calculated from the parabolic fit. The leaky mode solver provides a fundamental mode with a non-Gaussian profile that is in relatively good agreement with the simple parabolic estimate and thus it is concluded that it was acceptable to use the parabolic estimate to perform a batch analysis of the pressure scan data to get a sense of the variation of matched spot size with on-axis density. This data is shown in figure 3.13.

The top panel shows the on-axis density, $n_e(0)$ versus the fill pressure. Here on-axis densities ranging from $\sim 1.6 \times 10^{17}$ cm^{-3} to $\sim 1.0 \times 10^{18}$ cm^{-3} are observed, demonstrating on-axis densities almost an order of magnitude lower than has previously been demonstrated for hydrodynamic plasma channels[72,137]. The lower panel shows the matched spot size as a function of on-axis density demonstrating a clear trend to larger matched spot sizes at lower densities. At lower densities the mean free path, $\lambda_{\mathrm{mfp}} \propto 1/n_e$[157], of the plasma electrons is larger and so the shock front — the width of which scales with the mean free path[158,159] — becomes thicker. With a thicker shock front the parabolic profile at the channel centre becomes shallower, leading to a larger matched spot size. This is advantageous, as the ideal matched spot size for quasilinear wakefield generation also increases as the density is dropped[43]. This can be shown clearly by taking equation 1.5 from the discussion in section 1.2.3 and replacing the characteristic length scale of the transverse laser intensity profile with the matched spot size:

$$w_m^2 \gtrsim \frac{a_0^2}{2\pi\gamma}\lambda_p^2 \propto \frac{1}{n_e}\,. \tag{3.3}$$

3.4.3 Comparison with Sedov-Taylor Blast Wave Theory and Simulations

The hydrodynamic expansion was compared with Sedov-Taylor blast wave theory discussed in section 2.3.2. According to the Sedov-Taylor solution[130], the position of the shock front as a function of time $r_s(\tau)$ in cylindrical coordinates is:

$$r_s^4(t) = \frac{(\gamma_A + 1)^2}{\pi}\frac{E_l t^2}{\rho_m}\,, \tag{3.4}$$

where γ_A is the adiabatic index of the medium, E_l is the energy per unit length contained within the plasma and ρ_m is the mass density in the unshocked region which, in this case, is simply given as the product of the number density of particles in the neutral gas times the mass of the hydrogen molecule $\rho_m = n_g M_{H_2}$, approximately equal to (in the case of full ionization) the product of the initial plasma density and the mass of the hydrogen ion $n_0 m_p$. For a cylindrical column of plasma, the energy per unit length may be approximated

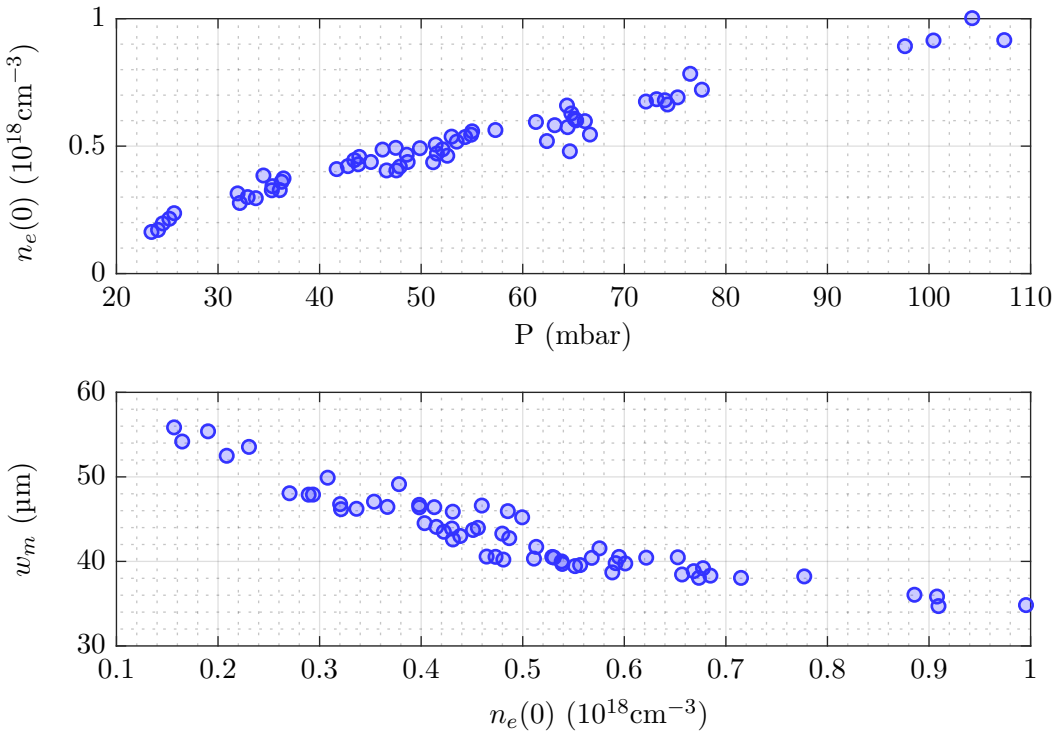

Figure 3.13: (Top) Measured variation with cell pressure of the on-axis density of the plasma channels extracted from a parabolic fit to the central region of each channel's electron density profile as measured at $t = 3.9$ ns. (Bottom) Variation with on-axis density of the matched spot size of the lowest order mode, as deduced from parabolic fits to the measured plasma channels.

by $E_l = (n_0 E_k)\pi r_0^2$, where n_0 is the initial electron density in the plasma column, E_k is the average energy of the ionized electrons and r_0 is the radius of the initial column.

The Sedov-Taylor solution assumes that the energy is deposited at time $t = 0$ in an infinitesimally small region of space. This is clearly unrealistic. To reflect this, one can view the initial plasma column — formed at laboratory time $t' = 0$ — as a plasma column which started expanding at $t = 0$ from an idealized column of $r_s = 0$.

$$r_s(t') = (\gamma_A + 1)^{\frac{1}{2}} \left(\frac{E_k}{m_p}\right)^{\frac{1}{4}} \left(r_0 \left(t' + t_0\right)\right)^{\frac{1}{2}} . \tag{3.5}$$

This time difference between the idealized time t and laboratory time t' is given as $t_0 = t - t'$. By requiring that the plasma column radius at $t' = 0$ is r_0, the time difference t_0 can be

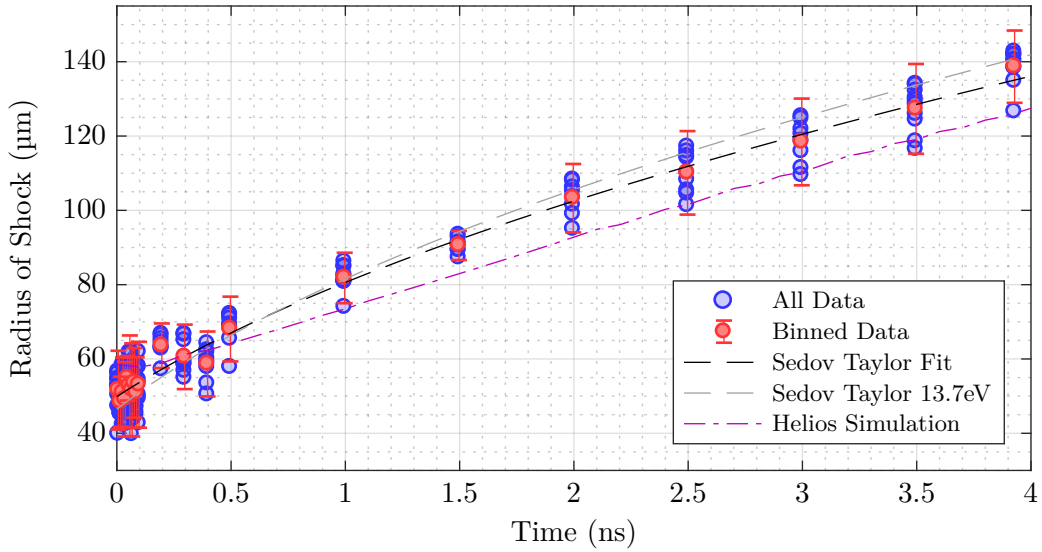

Figure 3.14: Comparison of measured, calculated and simulated temporal evolution of the shock front. Blue circles show the average of the major and minor axes of an ellipse fitted to a half-max contour of the measured electron density profiles; the same data binned by time interval is shown as red circles. The gray dashed line shows a fit of the data to the Sedov-Taylor solution assuming an electron energy of 13.7 eV while the black dashed line shows a fit to the data allowing the electron energy to vary. The dashed purple line shows the results of a HELIOS simulation.

expressed in terms of the initial radius of the plasma column as:

$$t_0 = \sqrt{\frac{m_p}{E_k}} \frac{1}{(\gamma_A + 1)} r_0 \,. \tag{3.6}$$

Experimentally the shock radius is defined to be the half-width at half maximum (HWHM) of the measured electron density profile. The expansion of the shock front observed in the laboratory, for the case of circularly polarized pump light, is plotted in figure 3.14. The Sedov-Taylor solution was fitted to the experimental data in two ways; first using r_0 as a free parameter and assuming an initial electron energy $\langle E_k \rangle = 13.7$ eV as calculated from EPOCH[123] simulations of the ionization of hydrogen with circular polarization†; and secondly by treating both r_0 and E_k as free parameters. In both cases $\gamma_A = 5/3$ was used, corresponding to a fully ionized plasma. The EPOCH simulations calculated the energy of the ionized electrons using the ADK model[120] with the Posthumus strong-field correction[122] corresponding to Barrier Suppression Ionization[124].

†EPOCH simulations courtesy of Mr. Chris Arran[160].

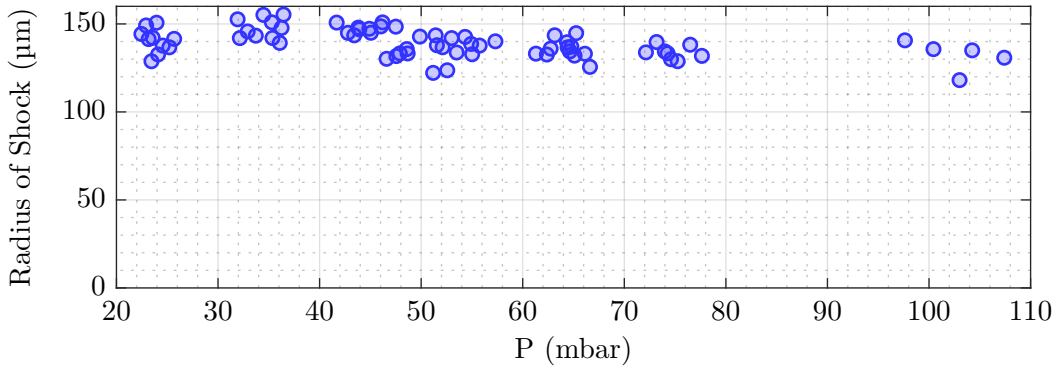

Figure 3.15: Variation of shock front position with pressure at $t = 3.9$ ns.

Fixing the electron energy at 13.7 eV, an initial plasma column radius equivalent to $r_0 = (46.5 \pm 0.7)$ μm was found to best fit the experimental data. However, allowing both r_0 and E_k to vary, it was found that an initial radius of (49.9 ± 1.0) μm and an electron energy of (9.5 ± 0.8) eV provided the best fit. The error in these parameters being given as the 95 % confidence interval provided by *MatLab*'s curve fitting tool. Figure 3.14 shows the *energy-fixed* fit in gray and the *energy-variable* fit in black; while the electron energy between the two cases differ by ~ 30 % of the simulated value, it is clear that both lines constitute a good fit of the data. This insensitivity to the initial electron energy arises from the $E_k^{\frac{1}{4}}$ term in equation 3.5 and demonstrates that while the Sedov-Taylor solution is a useful tool in modeling the shock expansion, it is difficult to extract accurate values for the electron energy from the rate of shock expansion.

HELIOS fluid code simulations, performed by Mr. Chris Arran[160], were also run to model the expansion dynamics. They assumed an initial electron temperature $k_B T_e = (2/3)\langle E_k \rangle = 9.1$ eV and an initial transverse electron density profile described by a 10th order super-Gaussian chosen to match the measured profile of the initial plasma column.

It can be seen in figure 3.14 that both the HELIOS simulations and the Sedov-Taylor solution are in good agreement with the experimental data, demonstrating that the essential physics of HOFI channel formation is captured by the models of OFI-heating of the initial plasma column and its subsequent expansion as a Sedov-Taylor blast wave.

Another prediction of the Sedov-Taylor solution, as demonstrated in equation 3.5, is that the expansion dynamics of the plasma column should remain independent of density. An

expansion is observed which, as can be seen in figure 3.15, appears to be relatively insensitive to density over the timescales and pressure ranges used in this experiment, although the shock radius does start to exhibit a minor downward trend in shock position with increasing pressure.

3.4.4 Plasma Dynamics: Charge Separation and Cold Ions

It is clear that while the Sedov-Taylor solution provides a reasonable set of analytic equations describing the experimentally observed expansion of the OFI-heated plasma column, it has a few shortfalls. Namely, that it neglects to explicitly consider the cold plasma ions or charge separation. The Sedov-Taylor solution ignores these and considers the expansion of a fluid containing a certain amount of energy per unit length into a surrounding fluid (the neutral gas). These are potential issues as it is known that optical-field-ionized electrons and ions are not born in thermal equilibrium. To investigate one can consider some general timescales.

The electrons generated from barrier suppression ionization are initially born at $t = 0$ with a non-isotropic, non-Maxwellian energy distribution of average energy $\langle E_k \rangle$. They isotropize and attain a Maxwellian energy distribution on the electron self-collision timescale[148];

$$\tau_{ee} = \frac{2.7 \times 10^5}{n_e \ln(\Lambda)} T_e^{3/2}, \tag{3.7}$$

with Λ the plasma parameter, $\Lambda = (4/3)\pi n_e \lambda_D^3 = (4/3)\pi n_e \sqrt{\epsilon_0 k_B T_e / (n_e e^2)}^3$ and λ_D the Debye length. For an initial electron density of $n_e = 10^{18}$ cm^{-3} with $\langle E_k \rangle = 10$ eV, it is found that $\tau_{ee} \sim 2.7$ ps. The ions remain at room temperature on this timescale. Thus within several picoseconds (much shorter than the expansion timescale), the electron and ion populations have attained Maxwellian energy distributions separated in mean energy by approximately the energy of the electrons. These two species will thermalize over the equipartition time[148],

$$\tau_{eq} = \frac{5.87 \times 10^6 \; m_e m_i}{m_p^2 n_e Z_i^2 \ln(\Lambda)} \left(\frac{m_p T_e}{m_e} + \frac{m_p T_i}{m_i} \right)^{3/2}, \tag{3.8}$$

with m_i the ionic mass, m_p the mass of a proton, Z_i the ionic charge and T_i the ionic temperature. In the case described above, $\tau_{eq} \sim 2.5$ ns.

The plasma expansion into the cold surrounding gas and the thermalization of the electrons and ions occur on similar timescales complicating the dynamics at play. It is difficult to

assess theoretically the effect that this thermalization process has on the expansion dynamics, however it could be further investigated experimentally by choosing a different species as the plasma source. For example a singly ionized nitrogen plasma would have an electron population with an initial energy very similar to that of hydrogen but the thermalization time for such a plasma would be an order of magnitude higher than that of hydrogen.

The dynamics could be further complicated through collisional ionization of neutral atoms in the surrounding gas by hot electrons streaming radially outwards. The timescale for this collisional ionization, derived by Lotz[161], is calculated for the conditions here to be 0.2 ns. This effect was included in the HELIOS simulations discussed earlier.

Ignoring charge separation in the dynamics, as fluid based codes and theories do, is somewhat counter-intuitive. At first glance it seems perfectly reasonable; both the electron and ion Debye lengths are much smaller than 1 µm compared to the typical dimensions of the plasma, ~ 50 µm. However, insight may be gained by considering the physical mechanism by which the plasma expands. At early times, the plasma column consists of cold ions and hot electrons. The electrons thermal velocity will be $\sim 42.8\sqrt{T_e/T_i}$ times the ions thermal velocity, rendering the ions essential stationary at early times and still much slower than the electrons after thermalization. Therefore, it is expected that the electrons will stream radially outwards much faster than the ions, creating a charge separation which generates strong electric fields that acts to reign the electrons back in. In this way, the electrons will drag the ions radially outwards at a speed determined by the electron temperature and the ion mass. In other words, charge separation is responsible for the expansion of the ions in the plasma column. The process is similar to ambipolar diffusion, which is defined as the simultaneous diffusion of electrons and ions in the presence of their own space charge fields[162]. However, the presence of a shock front and indeed the results shown in figure 3.14 suggest that the dynamics can be accurately modeled by employing a fluid model in which the dynamics are driven by a pressure differential rather than by charge separation.

3.4.5 Effect of the Ellipticity of the Laser Pulse on Expansion Dynamics

In theory, an advantage in the use of optical-field-ionization to generate plasma channels is that the energy of the initial electron population may be tuned by adjusting the polarization of the

ionizing pulse. To investigate the effect this had on the channel formation, timing scans were performed for both circular and linear polarization, keeping all other experimental parameters fixed. The expansion in circular polarization, shown in figure 3.14 has already been discussed. Its counterpart, the expansion of a plasma channel generated using a pump pulse with linear polarization is shown in figure 3.16. Similar analysis was performed to that used in the case of circular polarization. The *energy-fixed* fit (with a mean electron energy fixed to 1.6 eV, corresponding to that calculated from EPOCH simulations performed by Mr. Chris Arran[160]) leads to a much slower expansion than that which is observed. The *energy-variable* fit closely follows the experimental data with an initial radius of $(47.7 \pm 1.0)\,\mu m$ and an electron energy of $(7.8 \pm 0.6)\,eV$.

While the experimental results described in this chapter provide different estimates of the energy in the initial plasma, as would be expected for plasmas ionized by pulses of differing ellipticity (section 2.3.1) there is clear disagreement between the energy in the plasma estimated for the case of linear polarization as compared to the EPOCH simulations. One possible reason for this discrepancy are the approximations made in EPOCH's calculation of the average electron energy.

As discussed in section 2.3.1 EPOCH calculates the electron energy spectrum based on the ADK model of tunnel ionization with a correction for the case of strong-fields[120,122,124]. The simulations performed assumed an atomic hydrogen target which in the ADK model, produces hot electrons and cold ions as there is no direct mechanism to transfer energy from the radiation field to the atomic core[163]. However, this experiment makes use of diatomic hydrogen molecules. Optical-field-ionization for single atoms is an extremely complex process, the addition of molecular dynamics further increases the complexity and like the optical field-ionization of atoms, it has become a rich field in its own right — an excellent review on the topic can be found here[164]. Investigating, in detail, the ionization dynamics at play is beyond the scope of this thesis, however it should be noted that the basic assumption that the ions are born cold no longer holds in the case of field-ionization of diatomic molecules.

In particular, for the case of the ionization of H_2 by highly-intense femtosecond pulses, it is possible for the molecule to be completely stripped of electrons before it has had time to dissociate. This leads to a Coulomb explosion of the ionic core and thus to ions with an

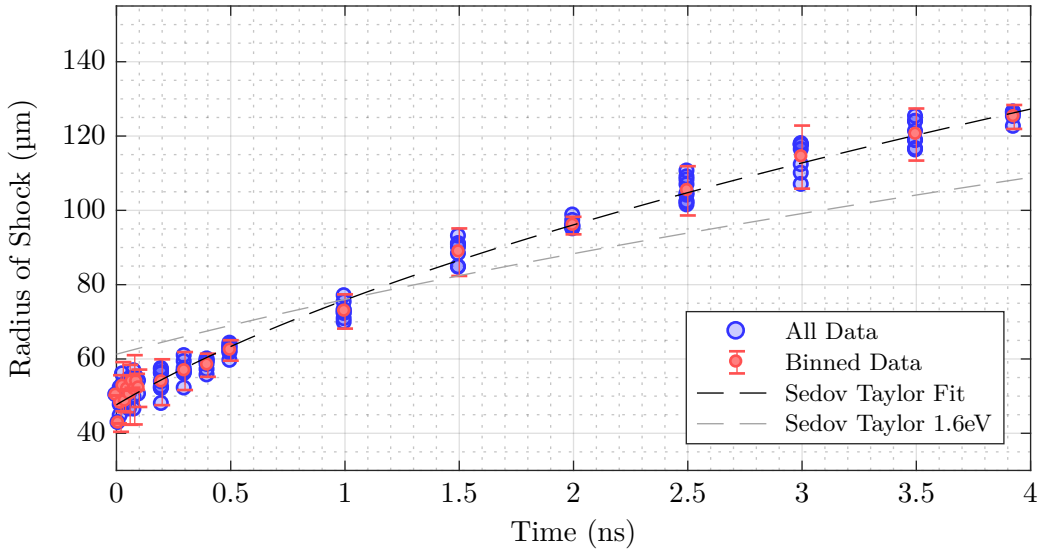

Figure 3.16: Comparison of measured and calculated temporal evolution of the shock front. Blue circles show the average of the major and minor axes of an ellipse fitted to a half-max contour of the measured electron density profiles; the same data binned by time interval is shown as red circles. The gray dashed line shows a fit of the data to the Sedov-Taylor solution assuming an electron energy of 1.6 eV while the black dashed line shows a fit to the data allowing the electron energy to vary.

energy comparable to that of the liberated electrons[165]. Alternatively, for the case of linear polarization there is the possibility for rescattering[166] of the first liberated electron with the ionic core which can produce protons with several electronvolts of kinetic energy[167].

The production of these energetic ions will of course affect both the linear and circular polarization cases mentioned above and may indeed reduce the effects of polarization on expansion dynamics. Thus understanding the complex dynamics at play will form the focus of future work.

3.4.6 Investigating Potential Probe Refraction

One natural concern with longitudinal probing of a relatively long plasma channel structure is unwanted refraction of the probe beam as this can lead to systematic errors in the channel measurements. Beam propagation simulations were performed, using the FFT-BPM code developed by the author (section 2.4), to determine the degree of probe refraction in the case of the experiments described here and ultimately to assess its potential impact upon the results. The beam propagation simulations follow the technique described in section 2.4.

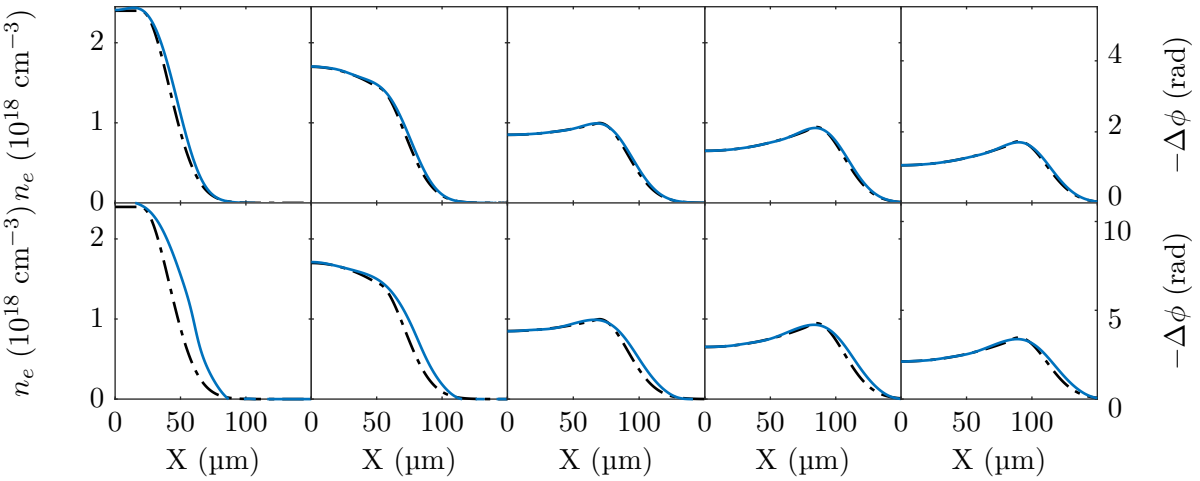

Figure 3.17: Beam propagation simulations showing the electron density/phase profile extracted from a probe beam (blue) after propagating 2 mm (top) and 4 mm (bottom) in a plasma channel with the electron density profile given by the black curve.

Figure 3.17 shows the results of these calculations for an example plasma channel formed in 50 mbar of H_2 where the black dashed line represents the inputted electron density profile and the blue line corresponds to the electron density profile extracted from the phase of a 400 nm probe beam passed through the plasma. The simulations were run for the case of the two gas cell lengths used in this experiment (2 mm and 4 mm) and show, as would be expected, that the longer cell exhibits more probe refraction. For the 4 mm long cell probe refraction broadens the retrieved electron density profile at earlier times, although the peak electron density is extracted correctly; further, the extracted electron density profile is close to the true profile at later times. For the 2 mm long cell the extracted electron density profile is close to the true profile for all times.

The results from these simulations were taken into account in the analysis of the experimental data; for timing scans, data from the 2 mm and 4 mm cells were combined to examine the whole expansion in detail. The 2 mm cell was used to look at the plasma at earlier times without concern for significant probe refraction while the 4 mm cell was used to examine plasma at later times when the longer cell provided a stronger signal and probe refraction was no longer a concern.

3.5 Conclusions & Outlook

In this chapter results have been presented from a proof of concept experiment to demonstrate the formation of low-density HOFI plasma channels using a lens. The laser used in these experiments, the Oxford TW laser system, was reviewed in detail and the layout of the experiment was described together with information about the key parameters of the setup and how they were characterized. The results clearly demonstrate the ability of this technique to generate plasma channels with on-axis densities in the range $1.6 \times 10^{17}\,\mathrm{cm}^{-3} < n_e(0) < 1 \times 10^{18}\,\mathrm{cm}^{-3}$, almost an order of magnitude lower than previously demonstrated[70,72].

An investigation into the expected guiding properties of the lowest-order modes of these channels has shown matched spot sizes of order a few tens of microns and $1/e$ attenuation lengths of order hundreds of millimeters. The guiding properties were investigated with both a leaky mode solver[109] and with a simple approximation of the measured channels to an infinite parabolic waveguide. The two analyses produced similar results.

The expansion of HOFI plasma channels was investigated for the case of hydrogen and found to agree well with Sedov-Taylor theory. Both linear and circular polarization were investigated and it was found that the inferred temperature of the plasma ionized by circular polarization was larger than that ionized by linear polarization, as expected. However, it was also noted, that the linearly polarized driver did produce a hotter shock than expected. This higher than expected plasma temperature for a linear polarized driver is thought to be due to an oversimplified view of the ionization process; further investigation will be required to fully understand the complex dynamics at play and this will form the basis of future work.

Low-density HOFI plasma channels hold promise for applications as waveguides for the next generation of laser plasma accelerators. Here their ability to operate with low on-axis density and with promising waveguiding characteristics was demonstrated for the first time. In addition, as these plasma channels are formed without an external structure, they are limited in repetition rate only by the recombination time of the plasma itself, meaning operation in the multi-kHz regime is a very reasonable prospect. Indeed with further work, channels of this type would appear to be an ideal basis for multi-GeV laser-plasma accelerator stages capable of long-term operation at high pulse repetition rates.

Chapter 4

Guiding In Axicon-Formed HOFI Plasma Channels: Experimental Design and Setup

4.1 Introduction

Over the next two chapters an experiment aimed at providing the first demonstration of axicon-formed HOFI plasma channels and optical guiding in those structures will be described. The work is separated into two chapters; this chapter describes the challenges associated with this work compared with the experiments described in the previous chapter, the process of designing the experiment to overcome these challenges and the resulting experimental setup employed. Chapter 5 details the implementation of the experimental setup and the results obtained. The experiments described here were performed on the Astra-Gemini TA2 system within the Central Laser Facility in three experimental periods totalling 19 weeks, over the course of six months starting in February 2018, with planning commencing mid 2017.

4.1.1 Motivation

In the last chapter it was successfully demonstrated for the first time that the formation of low-density ($\sim 10^{17}$ cm^{-3}) HOFI plasma channels was possible using a lens to focus the

channel-forming beam; an important step towards establishing the viability of HOFI plasma channels as waveguides for the next generation of LPAs.

Lenses (or paraboloids for that matter) are excellent optics with which to explore the fundamental aspects of plasma channel formation and dynamics but are not well suited to the generation of very long plasma channels (100's of millimeters). This is because lenses are designed to localize a maximum amount of optical energy at a specific point in space, the focus. This makes long channel formation with lenses an inefficient use of energy. Assuming the same energy per unit length of channel as found in the experiments reported in chapter 3, $\sim 6.7\,\mathrm{mJ\,mm^{-1}}$, it is found that joule levels of energy would be required to form plasma channels fitting specifications for the next generation of high energy LPAs as laid out in section 1.5. Furthermore, achieving ionization over such long distances would necessitate very high focal intensities and this would facilitate nonlinear laser plasma interactions near the focus which could destroy the pulse or adversely affect the ionization/channel formation dynamics

Instead it is desirable to form long plasma channels using an optic such as an axicon which can shape the incident optical energy into a line focus (section 2.5). Using such optics should allow for a much more efficient use of energy and the generation of very long plasma channels.

As was discussed in section 1.3.1, axicons have been used extensively to form inverse-bremsstrahlung-heated hydrodynamic plasma channels. There is however no evidence, to the authors knowledge, of optical-field ionized hydrodynamic plasma channels formed with an axicon; nor have axicons been employed with femtosecond beams to form plasma channels*.

4.1.2 Objectives

The objectives outlined for the experiment were as follows:

- Demonstration of long low-density HOFI plasma channels efficiently formed by an axicon.
- Demonstration of high-intensity ($> 10^{17}\ \mathrm{W\,cm^{-2}}$) guiding in those plasma structures.
- Demonstration of both channel formation and guiding at the highest available repetition rate of 5 Hz.

*For example the femtosecond inverse-bremsstrahlung heating of clusters by Kumarappan et al. used a lens for channel formation[69]; in this case self-guiding through the cluster medium elongated the plasma channel allowing for guiding lengths exceeding the Rayleigh range.

4.2 Challenges

While a change of focusing optic may appear innocuous at first, it turns out that the change from a lens to an axicon brings a number of challenges to the fore which make not only plasma channel formation more difficult, but the diagnosis of those channels more difficult too.

As discussed in section 2.5.2, there is a reduced critical density[136,137] for axicon formed plasmas which depends upon the approach angle of rays to the optical axis, α; $n_{\mathrm{cr}}^{\mathrm{eff}} = n_{\mathrm{cr}} \sin^2 \alpha$. Further, the $1/e^2$ size† of the central Bessel peak of an axicon also depends on approach angle, $w_{\mathrm{ax}} = 1.75/\left(k \sin \alpha\right)$. Assuming that the initial density of the plasma is close to $n_{\mathrm{cr}}^{\mathrm{eff}}(\alpha)$ and that the plasma is only ionized within the central peak of the Bessel profile, it is then possible to calculate the energy per unit length of ionized plasma as done in section 3.4.3. It is found that the maximum energy per unit length which can be coupled into the plasma is independent of the axicon approach angle and instead depends only on the kinetic energy of the liberated electrons E_k and the laser wavelength λ used;

$$E_{l_{\mathrm{ax}}} = \frac{3 E_k \pi n_{cr}}{k} \propto \frac{E_k}{\lambda} \,. \tag{4.1}$$

For the case of circularly polarized light, the peak of the electron kinetic energy spectra scales with the ponderomotive energy[121], equation 2.16, and thus scales as λ^2. If it is assumed that the intensity at the time of ionization is fixed by the ionization threshold, as is the case in the barrier suppression ionization model (section 2.3.1), then it can be shown that, for a given plasma species, the energy per unit length which can be coupled into the plasma channel scales only with wavelength of the channel-forming laser.

$$E_{l_{\mathrm{ax}}} \propto \lambda \,. \tag{4.2}$$

This is in direct contrast to a lens in which the energy per unit length at focus can be tuned easily by increasing the plasma density for a fixed focal spot size. This is not possible with an axicon due to the reduced $n_{\mathrm{cr}}^{\mathrm{eff}}$. In the case of an axicon, an increase in density is completely cancelled out from an energy perspective by a necessary decrease in the spot size. This places

†Here $1/e^2$ is used for familiarity — when considering ionization by a Bessel beam it can be useful to define the maximum-ionization spot size $w_{\mathrm{ion}} = 1.69/(k \sin \alpha)$ the maximum radius out to which ionization can occur without ionizing with the Bessel's first ring.

tighter constraints on plasma channel formation and thus necessitates careful planning.

In addition to the tight constraints on plasma channel formation, there are also difficulties with probing the channels and making measurements of the electron density profile. As an example consider the parameters used for the results demonstrated in figure 3.11 (a). An initial fill pressure of 50 mbar of fully ionized H_2 would necessitate a minimum approach angle of $\alpha = 0.034$ rad and thus a maximum central Bessel spot size ($1/e^2$) of 6.6 µm in comparison to the plasma column shown in figure 3.11 (a) which has a radius of ~ 50 µm. One can expect that given how much thinner the initial column of plasma is, it will cause a longitudinal probe to be much more susceptible to diffraction at early times. Furthermore the expansion of this column will likely be quite different to that shown in figure 3.11 (a).

Guiding in a HOFI plasma channel is one of the main experimental objectives. As this necessitates the plasma channel strongly affecting the propagation of a pulse travelling collinear with the axis of the channel, longitudinal interferometry is not possible. An alternative method of probing is to use transverse interferometry. This allows for probing of small sections of arbitrarily long plasma channels at the cost of a smaller measured phase shift. For example, it would be order 100 mrad (assuming a truncated parabolic channel with on axis density of $1 \times 10^{17}\,\mathrm{cm}^{-3}$ and a matched spot size of 20 µm).

4.3 Experimental Design

Facility experiments, such as those performed at Astra-Gemini, typically require a much more complete design phase than those that can be performed in a local lab, such as the experiments described in chapter 3. This is mainly due to the time constraints placed on experiments. The Oxford group was awarded 12 weeks to pursue experiments related to guiding of high-intensity beams in axicon-formed HOFI plasma channels and to achieve the goals outlined above. Thus having a detailed plan, together with several contingency options, should something not work as expected, was essential to success. In this section, the design considerations that were explored for the Astra-Gemini TA2 2018 run are discussed. This includes design parameters relating to the focusing geometry, optics and cell design among others.

While the goal of guiding in an axicon-formed HOFI plasma channel is clear, there are a

few constraints that must be placed on the design to achieve this goal. These can be divided into two categories, restrictions on the focusing and restrictions on the cell.

Focusing Constraints

- The intensity of the channel-forming beam in the focal region must exceed a threshold value determined by the target species in order to field-ionize the neutral gas
- The focal region of the channel-forming beam must have a minimum transverse dimension so that the energy per unit length of the axicon-generated plasma is sufficient to drive a shock wave to radii greater than the desired matched spot size of the channel.
- The interaction of the channel-forming pulse with the plasma at a point should not detrimentally affect plasma formation further downstream. This would mainly occur by refraction of the focusing axicon beam due to plasma formation at a density above the effective critical density $n_{\mathrm{cr}}^{\mathrm{eff}}$.

Gas Cell Constraints

- The gas cell must provide a uniform body a gas and be capable of holding pressure up to a few hundred mbar.
- The cell must allow for the coupling of the guided (and probe) beam into and out of the plasma channel without significant wavefront distortion.
- The cell should be robust so as to allow for extended periods of operation under vacuum at 5 Hz

Before discussing the experimental design in detail it is useful to explore the laser system used in these experiments.

4.3.1 The Astra-Gemini Laser System

The Astra-Gemini laser system is a PW class Ti:sapphire chirped pulse amplification laser system at the Central Laser Facility, UK. The system provides high-energy ultrafast beams to two target areas; TA2 and TA3.

The difference in the two target areas is predominantly the power available on target; TA2 providing up to 12.5 TW (500 mJ in 40 fs) and TA3, a dual beam system providing two independently controlled 0.5 PW beams (15 J in 30 fs) for an impressive 1 PW on target in total. The system consists of four amplification stages with the beams for the two target areas being split after the third amplifier. This amplifier outputs uncompressed pulses of approximately 900 mJ at 10 Hz. Half of the pulses generated are sent to TA2 where they are compressed before being directed to the TA2 target chamber, while the other half seed TA3's final amplification stage.

The experiments described in this chapter were performed in TA2. In addition to the main TW class pulse, TA2 also provides a probe beam (taken from a leak in the second amplifier). This pulse is passed into a separate probe compressor, also contained in the target area and compressed. At the output of the probe compressor the beam is approximately 0.9 mJ.

4.3.2 Choice of Axicon

Axicon Intensity and Ionization

In section 2.5 it was shown that the focal intensity profile of a top-hat beam focused by an axicon could be written as:

$$I(\rho, z) = \frac{4\pi^2}{\lambda} z I_0 \alpha^2 J_0^2 \left(\frac{2\pi}{\lambda} \alpha \rho \right) . \tag{4.3}$$

Here there is a one-to-one mapping between longitudinal position z and r_0 the initial radial point on the axicon from which all the rays hitting the optical axis at z must have originated; $z = r_0/\alpha$. For the purposes of experimental design, its turns out to be useful to keep the explicit dependence on r_0. Equally it is more useful to represent the intensity incident upon the axicon, I_0, as the energy per unit area, E_A, incident upon the axicon and the pulse duration τ, such that $I_0 = E_A/\tau$. In this case the peak axial intensity of the focal region can be stated as:

$$I_{max}(\rho = 0, z = r_0/\alpha) = \frac{4\pi^2}{\lambda} \frac{E_A}{\tau} r_0 \alpha \, . \tag{4.4}$$

If it is assumed that the wavelength and pulse duration of the channel-forming laser are

fixed, the remaining variables which determine the peak intensity are; E_A, r_0 and α.

The radius at which the first Bessel zero occurs is,

$$\rho_0 = \frac{2.4048\lambda}{2\pi\alpha}\,. \tag{4.5}$$

Which may be taken as a measure of the "spot size" of the axicon focus. It is clear that while the peak intensity of the focal profile increases linearly with the axicon approach angle α, the spot size of the focal profile of an axicon is inversely proportional to it.

Fluid simulations, performed by Mr. Chris Arran[160], benchmarked against the experimental results of chapter 3, were used to simulate the expansion of an axicon formed OFI-heated plasma column. These indicate that to achieve a channel in hydrogen with a matched spot size of at least w_m after a time t, it is necessary to ionize an initial plasma column greater than ρ_i in radius,

$$\rho_i > \frac{w_m^2}{3.6\times 10^4 t}\,. \tag{4.6}$$

Efficient Use of Energy

To incorporate the requirement given by equation 4.6 into the experimental design, the radius of ionization, ρ_i, must be related to the axicon approach angle, α. This could be done very easily by choosing α such that $\rho_0(\alpha) > \rho_i$ and increasing the incident pulse energy until ionization occurred. But this is energy inefficient, and also leads to further problems with nonlinear phase in the axicon, as discussed below.

Equation 4.3 may be rearranged to solve for energy per unit area incident upon the axicon and minimized with respect to axicon approach angle α:

$$\frac{\partial}{\partial\alpha}E_A = \frac{\partial}{\partial\alpha}\left(\frac{I_T\lambda\tau}{4\pi^2 z\alpha^2 J_0^2\left(\frac{2\pi}{\lambda}\alpha\rho_i\right)}\right) = 0\,, \tag{4.7}$$

where I_T is the threshold intensity required to ionize the target species and the intensity profile has been fixed such that $I(\rho_i, z) = I_T$.

Solving equation 4.7 leads to the transcendental equation $xJ_1(x) - J_0(x) = 0$, with $x = 2\pi\rho_i\alpha/\lambda$. This equation can be solved numerically and while it has an infinite number of

roots, it has only one root with $x < 2.4048$, or one root with a value less than the first root of J_0. This root is chosen as ionization is desired only within the central peak of the Bessel focus. Solving for this first root it is found that the most efficient use of energy occurs when the radius of ionization is given by:

$$\rho_i = 0.256\lambda/(2\pi\alpha) = 0.522\rho_0 \,. \tag{4.8}$$

Constraints of Approach Angle α

We can combine equations 4.8 and 4.6 to determine an upper bound on α;

$$\alpha < 7192\frac{\lambda t}{w_m^2} \,. \tag{4.9}$$

Based on geometric and engineering constraints, a maximum delay of $t = 5\,\text{ns}$ was assumed between the channel-forming and guided beams at the interaction point[‡]. Thus equation 4.9 is reduced to $\alpha \lesssim 3.6 \times 10^{-5}\lambda/w_m^2$. For example, for an 800 nm channel-forming beam, matched spot sizes of 15 µm and 25 µm require a maximum limit on the axicon approach angle of 7.3° and 2.6° respectively.

As discussed in section 2.5.2, the lower limit that is placed on α is determined not only by the intensity achievable in the focal profile for a limited energy per unit area incident upon the axicon but it is also determined by the effective critical density of the plasma formed by the axicon (equation 2.35).

Channels with on-axis densities below 1×10^{18} cm^3 are desired in this demonstration and thus it seems sensible to place a minimum bound on the initial electron density to 1×10^{18} cm^3. This corresponds to a lower bound of $\alpha_{min} = 1.37$ °.

Determining values for E_A and r_0

For a chosen value of α, two variables remain: E_A and r_0. It is known that the on-axis intensity increases linearly with distance z from the axicon and so it is possible to tune E_A and r_0

[‡]Constraints on the target chamber geometry in TA2 meant that the channel-forming and guided beams could only be split within the chamber. Thus all of the necessary delay between the channel-forming and guided beams also had to be placed under vacuum which increased the complexity of the design.

subject to meeting a requirement placed on the intensity at $z = r_0/\alpha$. It may then be assumed that all later points in the axicon focus will also meet this minimum intensity threshold[§].

Assuming a safety factor s in the threshold value for ionization, it is found that:

$$I(\rho_i = 0.522\rho_0, z = r_0/\alpha) = sI_T = I_{max}(z = r_0/\alpha)J_0^2\,(1.255)\ , \tag{4.10}$$

and so

$$E_A r_0 = \frac{sI_T}{J_0^2\,(1.255)}\frac{\lambda\tau}{4\pi^2\alpha}\,. \tag{4.11}$$

It is unsurprising that there is an inverse relationship between the energy per unit area incident upon the axicon and the initial radius of the axicon from which the rays at the start of the plasma channel (ionized region) come from. It may be useful at this stage to consider some limits. In the limit that the start of the plasma channel is brought towards the tip of the axicon, the energy per unit area necessary to ensure a sufficiently high focal intensity to ionize the target species ramps up significantly, approaching infinity as $r_0 \to 0$. Equally, as the start of the plasma channel is pushed away from the axicon focus, it is found that the energy per unit area required to gain a high focal intensity reduces substantially. This can be explained geometrically. Consider the energy in the focal region $z(r_0)$ to $z(r_0 + \delta r)$ coming from an annulus of inner radius r_0 and outer radius $r_0 + \delta r$. The area of this annulus is $\pi(2\delta r\ r_0 + (\delta r)^2)$ and so the total energy in the focal region $z(r_0)$ to $z(r_0 + \delta r)$ increases linearly with the value of r_0 for a fixed value of E_A.

Looking specifically to the experiment at hand, limits can be placed on the values of E_A and r_0. The Astra-Gemini TA2 beam is nominally 55 mm in diameter, although to avoid edge-effects near the outer diameter of the beam a 50 mm diameter axicon will be assumed. A channel of length L_{ch} corresponds to an annulus thickness of $\delta r = \alpha L_{ch}$ and thus the maximum value of initial radius is $r_0[mm] = 25 - L_{ch}[mm]\alpha$. Equally a constraint can be placed on the maximum energy that can possibly get into the channel-forming beam which is of order[¶] 550 mJ, corresponding to an approximate upper limit for E_A of 0.23 $\mathrm{mJ\,mm^{-2}}$.

[§]Note that this assumes a top-hat spatial profile for the beam. While no beam is truly top-hat, together with a safety factor, this estimate will be sufficient for the purposes of this design.

[¶]This was the energy post compression reported during the design phase. As will be seen in section 5.2.2, the measured value of energy post compression was closer to 420 mJ.

4.3.3 Nonlinear Phase

As with all high-power ultrafast beams, nonlinear phase acquired in passing through transmissive optics can lead to a large deformation in the wavefront. This can detrimentally affect the Bessel focus which results from the mutual interference of converging conical wavefronts. The nonlinear phase acquired by a pulse passing through a material is given by:

$$\phi_{\mathrm{NL}} \approx \frac{2\pi}{\lambda} n_2 I T \,, \tag{4.12}$$

where n_2 is the nonlinear refractive index of the material in question (typically order $1 - 4 \times 10^{-16}$ cm^2 W^{-1} for common optical components), I is the local intensity incident upon the optic and T is the local thickness of the optic. The nonlinear phase gained by a pulse passing through an axicon can thus be written as;

$$\phi_{\mathrm{NL}} \approx \frac{2\pi}{\lambda} n_2 \frac{E_A}{\tau} \left(t_s + \left(\frac{D_{\mathrm{ax}}}{2} - r_0 \right) \tan\left(\frac{\alpha}{\eta - 1} \right) \right) \,, \tag{4.13}$$

where t_s is the axicon substrate thickness, D_{ax} is the axicon diameter and η is the refractive index of the axicon. Here it has been assumed that the axicon base angle ϑ is small, so that $\alpha = \arcsin(\eta \sin\vartheta) - \vartheta \approx (\eta - 1)\vartheta$.

In most cases, it is desirable to keep $\phi_{\mathrm{NL}} < 1$. Applying this condition it is found that:

$$r_0 > \left(t_s - \frac{\lambda\tau}{2\pi n_2 E_A} \right) \cot\left(\frac{\alpha}{\eta - 1} \right) + \frac{D_{\mathrm{ax}}}{2} \,. \tag{4.14}$$

4.3.4 Exploring the Available Parameter Space

By combining the restrictions discussed in sections 4.3.3 and 4.3.2, and the Astra-Gemini TA2 laser system specifications, it is possible to determine an available parameter space. The experimental constraints assumed here are: a UVFS axicon with substrate thickness $t_s = 3$mm, diameter $D_{\mathrm{ax}} = 50$mm, refractive index $\eta(800nm) = 1.45$ and nonlinear refractive index $n_2 = 2.6 \times 10^{-16}\,\mathrm{cm}^2\,\mathrm{W}^{-1}$. It is assumed that the target species is hydrogen which has an ionization threshold of $I_T = 4 \times 10^{14}\,\mathrm{W\,cm}^{-2}$, for circularly polarized light, according to the ADK model. A short pulse option of $\tau = 40$fs and a long pulse option $\tau = 150\,$fs are considered. The

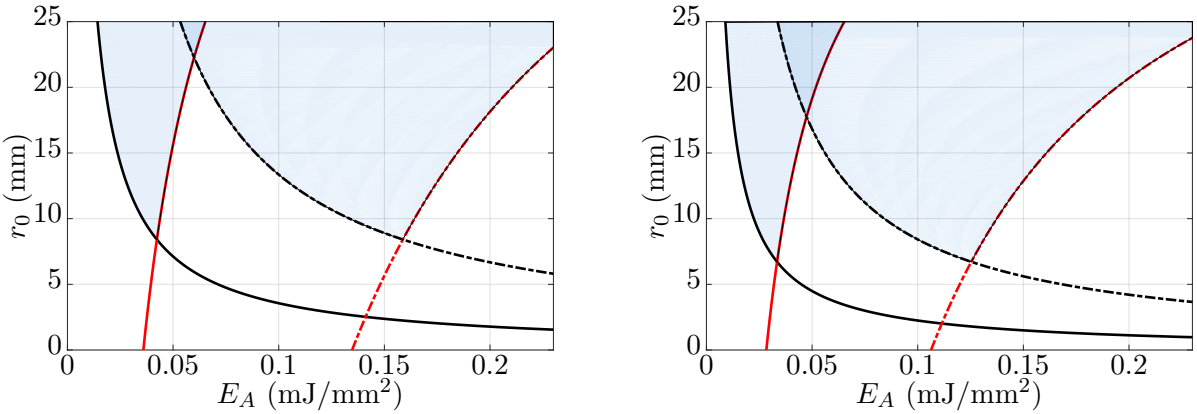

Figure 4.1: Operable parameter space, shaded blue, for the 2.5 ° approach angle axicon (left) and the 4.0 ° approach angle axicon (right) Above the black lines the combinations of r_0 and E_A are capable of reaching the ionization threshold of H_2 with a safety factor $s = 2$ while above the red lines the combinations of r_0 and E_A provide a B-integral less than 1. The solid lines correspond to the short pulse case while the dashed lines represent the long pulse case.

maximum value of E_A is set to $0.23\,\mathrm{mJ\,mm^{-2}}$.

This information can be used to plot out the available parameter space for a given axicon as has been done in figure 4.1. The available parameter space, the blue shaded region, shows the combinations of r_0 and E_A for which the value of $\phi_{\mathrm{NL}} < 1$ and which also allow for ionization of the initial plasma column out to a minimum radius of $\rho_i = 0.522\rho_0$, assuming a safety factor of s=2. For reasons developed in section 4.3.5, two different axicons of approach angle $\alpha = 2.5°$ and $\alpha = 4.0°$ are explored.

It should be noted that the gas cell has yet to be considered, which may introduce further constraints, and any nonlinear phase introduced prior to the target chamber has also been ignored.

4.3.5 Experimental Geometry

Separating Channel-Forming and Guided beams

One of the desired experimental results was the demonstration of high-intensity guiding in an axicon-formed HOFI plasma channel. As TA2 provides only one high-intensity beam it is necessary to separate this beam into a channel-forming and guided beam.

Given the collimated intensity of the TA2 beam, $\sim 6 \times 10^{11}\ \mathrm{W\,cm^{-2}}$ at full power, a standard plate beamsplitter would not work due to the nonlinear phase that would be accrued

in passing through it, which would degrade the laser wavefront. Two alternative optics capable of separating a high intensity beam are pellicle beamsplitters and apodizers.

Pellicles offer an exceptionally thin beamsplitting optic, typically of order 5 µm thick and hence the B-Integral they introduce is negligible. However, these optics are also notoriously delicate and are not typically very flat. Standard large "laser quality" pellicles will usually have their reflected wavefront error quoted to no smaller than one wavelength per inch of surface at 633 nm.

A hole drilled in a mirror provides a robust method of apodizing a beam by simply reflecting a certain portion of it. While robust, these optics can introduce diffraction rings in the intensity profile due to diffraction from the hard edge of the hole. This can cause optics further downstream to be damaged. In addition, their accurate alignment can be difficult.

For the purposes of the experiment described here a holey mirror was chosen as the separating optic for the following reasons: **i)** For a large approach angle of $\alpha = 4.0°$, the creation of a 50 mm long plasma channel requires an annulus thickness of only $\delta r = 3.5$ mm. Thus splitting a whole copy of the beam is an inefficient use of energy and further **ii)** splitting a whole copy of the beam requires lowering the maximum energy per unit area in the beam by the pellicle split ratio thus reducing the size of the available parameter space. **iii)** Achieving the required intensity on target requires a good focus and this becomes more difficult with poor wavefront quality. The flatness of a holey mirror can be an order of magnitude better than that of a pellicle.

From a flexibility, reliability and efficiency viewpoint, the holey mirror is a superior option and so was chosen as the separating method. During the design phase, beam propagation calculations were performed using the FFT-BPM code described in section 2.4 to ensure that diffraction effects could be ignored for the case of the experiments described in this chapter.

Recombining Channel-Forming and Guided Beams

For the same reasons that the two beams are separated by a holey mirror, so they are recombined by a holey mirror. As both beams will be combined after they've hit their respective focusing optics, there is a restriction on the approach angles of each beam to the optical axis. Namely, both beams must approach the optical axis at different angles to ensure that one can pass

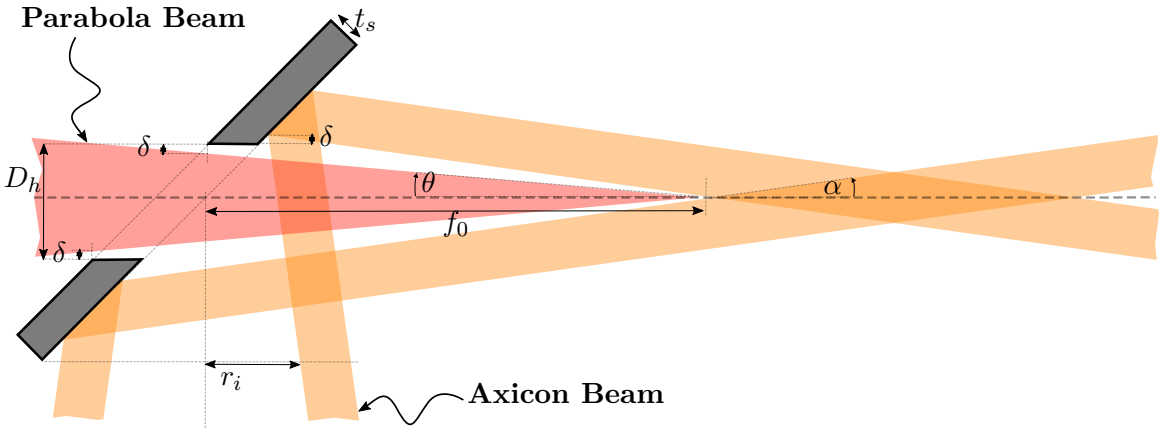

Figure 4.2: Schematic showing the axicon and guided beam approaching the optical axis.

through a holey mirror and the other be reflected by it while still arriving to focus at the same point. The maximum approach angle to the optical axis for the guided (paraboloid focused) beam is $\theta = 1/2f_{\#}$.

It makes sense to ensure that the guided beam has a smaller approach angle than the channel-forming beam as the channel-forming beam is already an annulus. Thus reflecting it from a holey mirror results in no loss of energy in the channel-forming beam and furthermore the guided beam does not get distorted either. However, it is important to consider the distance at which a holey mirror must be placed and the diameter of hole needed in order to successful couple the two beams with reliability. The channel-forming and guided beams approach the optical axis at angles of α and θ respectively, thus the difference between the inner radius of the annular beam and the outer radius of the guided beam is $\Delta = f_0(\alpha - \theta)$, where f_0 is the distance to focus. The coupling of the beams is easier further from focus when their angular separation leads to a large physical separation.

It is important to also take into account the thickness of the substrate through which the hole is made and the angle at which the holey mirror is placed as these ultimately place a tighter restriction on the cone of rays approaching the optical axis which can both fit through and fit around the hole. In addition, coupling the two beams reliably means introducing a reasonable tolerance on the dimensions of the coupling optic. This not only aids alignment but also accounts for the fact that most holey mirrors are not flat right to the edge of the optic but have a clear aperture, usually equal to 90-95 % of the total diameter. For example, for a

50.8 mm diameter optic, a 1.27 - 2.54 mm gap is expected on the inner and outer parts of the mirror where the surface quality cannot be guaranteed.

It is assumed for simplicity that the optic chosen to couple the beams operates at an angle of incidence of 45 ° and that it has a hole of diameter D_h cut at 45 ° to its normal. The mirror will be assumed to have a thickness of t and a diameter of D_m. It will further be required that the minimum tolerance δ between the channel-forming beam and the edge of the hole is equal to the minimum tolerance between the guided beam and the edge of the hole. This setup is shown graphically in figure 4.2.

It can be shown for this case that the axial distance f_0, between the front face of the mirror and the focus of the guided beam is given as;

$$f_0 = \frac{\sqrt{2}\sin\left(\frac{\pi}{4}+\alpha\right)\left(2\delta+\delta\tan\theta+\sqrt{2}t\tan\theta\right)}{\sin\alpha+\sin\alpha\tan\theta-\sqrt{2}\sin\left(\frac{\pi}{4}+\alpha\right)\tan\theta}\,, \tag{4.15}$$

and that the required hole diameter is then;

$$D_h = \frac{2\left((f_0+\sqrt{2}t)\tan\theta+\delta\right)}{1-\tan^2\theta}\,. \tag{4.16}$$

Until now α and θ have been treated as free parameters, however, it is possible at this stage to start to put constraints on the allowable values.

Constraint 1: The first constraint relates to fitting the axicon into the beam line before the coupling holey mirror. Rays traced backwards from the focus are found to have an inner radius of r_i at the entrance to the holey mirror system, as seen in figure 4.2. Rays leaving the axicon starting from a radius r_0 will only fit through the system if $r_0 > r_i$.

Constraint 2: The second constraint is that the waveguide created by the channel-forming beam should be capable of guiding the guided beam after a reasonable amount of time. This time is again taken to be 5 ns, as this can reasonably be expected to fit into the TA2 chamber. Since the focal spot of a paraboloid beam of maximum approach angle θ is given by $w_0 = \sqrt{2}\lambda/(\pi\theta)$. Combining this with equation 4.9, it is found that $\alpha < 222\ \theta^2$.

Constraint 3: The third constraint is a lower bound placed on the density as discussed in section 4.3.2 which leads to a minimum value for the axicon approach angle $\alpha_{min} = 1.37°$.

Figure 4.3 shows the (α, θ) parameter space for the case of a mirror of diameter 50.8 mm

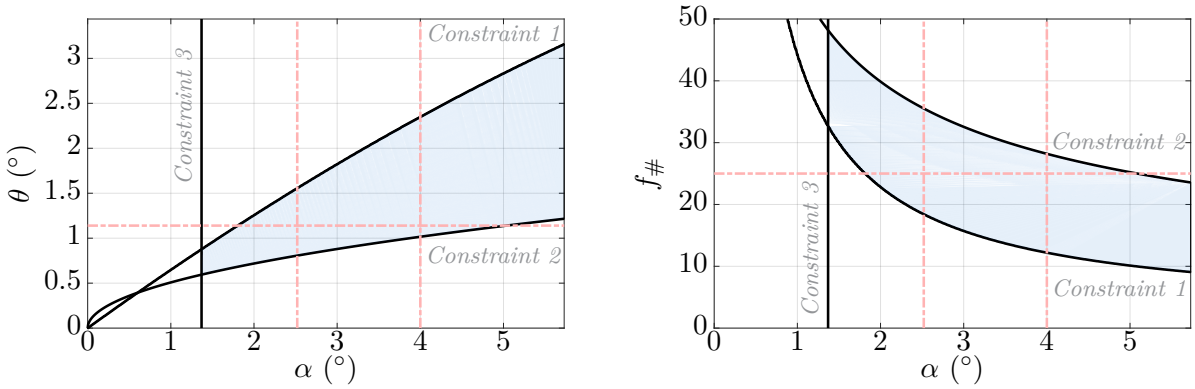

Figure 4.3: **Left:** Available (α, θ) parameter space (blue shaded region) with 3 constraints applied. The constraints are represented by the solid black lines while the intersections of the dashed red lines represent two particular combinations of axicon approach angle and guided beam approach angle that are allowed. **Right:** Same as shown in the left plot but with the guided beam approach angle converted to a focusing optic f-number.

and thickness $t = 6$ mm. In other words, it shows combinations of paraboloids and axicons that work well together. A tolerance of $\delta = 3$ mm has been selected and the radius from the optical axis at which rays leave the axicon has been chosen as $r_0 = 18$mm. Also shown is the same parameter space, but using the conversion $f_{\#} = 1/(2\theta)$ to provide a more intuitive map.

Two operating points are chosen in this parameter space, denoted by the intersections of the dashed red lines. These points correspond to two different axicon designs which will guide the same f/25 guided beam. The axicons of choice have approach angles of 2.5° and 4.0°. Any combination of approach angles can be chosen but keeping at least one of the approach angles fixed, in this case that of the guided beam, allows for fewer items to be changed should the need to change the setup arise.

For the case of the 2.5° approach angle the holey mirror must be placed 275 mm from focus and requires a hole of approximately 17.4 mm in diameter. In the case of the 4.0° approach angle the holey mirror must be placed 134 mm from focus and requires a hole of approximately 11.8 mm in diameter.

The choice of coupling optic affects the choice of splitting optic and thus the focal length of paraboloid used. In the analysis here, the radius at which rays leave the axicon was chosen to be $r_0 = 18$ mm. If the same logic of a 95 % clear aperture is applied to the separating optic, this leads to a hole of radius $r_s = 15.6$ mm. Rounding down to $r_s = 15$ mm or a diameter of $D_s = 30$ mm, it is found that a paraboloid of focal length 750 mm would be required to focus

this beam at f/25.

Counter Propagating Geometries

A short note on counter propagating geometries: It is seen here that there are tight constraints on the $f_{\#}$ which can be guided by a particular axicon. Unfortunately a counter propagating geometry cannot alleviate these constraints since the spot size at the output of the channel should match that of the input in which case, if the beam needs to be extracted, the same analysis as above applies.

Further, counter propagating geometries introduce a time delay, between the point at which ionization of the channel occurs and the point at which the guided beam passes, which varies linearly with position. This delay must be kept short compared to the timescale of channel evolution, assumed to be ∼100 ps. This limits the maximum channel length in the counter propagating geometry to less than 15 mm.

Exotic focusing schemes, in which the group velocity of the focusing beam is manipulated to mitigate this effect may be possible, but are beyond the scope of this thesis[168].

4.3.6 Gas Cell

Plasma Source Selection

It is clear that the design of the experimental layout is far from trivial. Indeed the same is true for the gas cell. In fact, the gas cell design is one of the most challenging aspects of this project. This begs the question; why wasn't an alternative plasma source considered?

To the author's knowledge, every previous experiment generating axicon formed plasma channels for guiding high intensity lasers has used either gas jets[66,69,70,137,169] or has filled the interaction chamber to a suitable backing pressure with the desired target species[64,68,131].

For the work described in this chapter it was decided that a gas cell target would be used rather than a gas jet. It was desired that channels be generated with lengths approaching 50 mm. As mentioned in section 1.5, channels of order hundreds of millimeters long must eventually be developed to meet the demands of the next generation of LPAs. Experiments with elongated gas jets[137] demonstrated operation up to only 16 mm and the scaling of such

technology is non-trivial, while the scaling of gas cells, once a basic design has been established, is more straight forward. Indeed cells up to 90 mm in length have been used in laser plasma electron acceleration experiments[170].

Back filling the chamber was not considered as the guided pulse would ionize the background gas well before the entrance to the plasma waveguide and could easily be destroyed by nonlinear effects integrated over the focusing distance. Further there were safety concerns with backfilling the chamber with hydrogen and there was not enough time to put in place new systems at the facility to mitigate the increased risk.

Plan B: A Backup Option for Medium-Length Plasma Channels

LPA experiments employing gas cell sources have previously operated in the nonlinear regime. Here the laser pulse is focused at the entrance to the gas cell and through relativistic self-focusing it propagates to the end of the cell[170]. As the pulse is focused to the entrance of the cell, this allows for the use of a small gas cell aperture to couple the laser pulse into the cell without allowing too much gas to escape. This is critical for maintaining a quasi-uniform pressure in the cell.

For the case of beams guided with an axicon plasma channel, such as the experiments described here, the guided beam will have to be focused at the entrance to the plasma channel to be coupled in correctly, but of course the beam forming the end of the channel will still be quite large at this point, having a diameter of $D_{\mathrm{ax}} = 2L_{ch}\alpha$ where L_{ch} is the length of the required channel. For $L_{ch} = 50$ mm channel and $\alpha = 4°$, $D_{\mathrm{ax}} = 7$ mm. This would not be an acceptable aperture size as it would create very long density ramps at the front of the gas cell which would hamper the coupling of the guided beam.

To determine the maximum acceptable pinhole size, *OpenFOAM* simulations were performed by Mr. Alexander von Boetticher. The simulations used the 2D compressible flow solver *SonicFOAM* and looked at the effect that a variation in the front pinhole diameter would have on the axial pressure profile for a fill pressure of 100 mbar of hydrogen. A cell geometry modelled on the Astra-Gemini TA2 2018 gas cell was used for the simulations and the back pinhole was kept fixed at 0.75 mm (this had no effect on channel beam coupling and so was kept smaller or equal to the front pinhole in size).

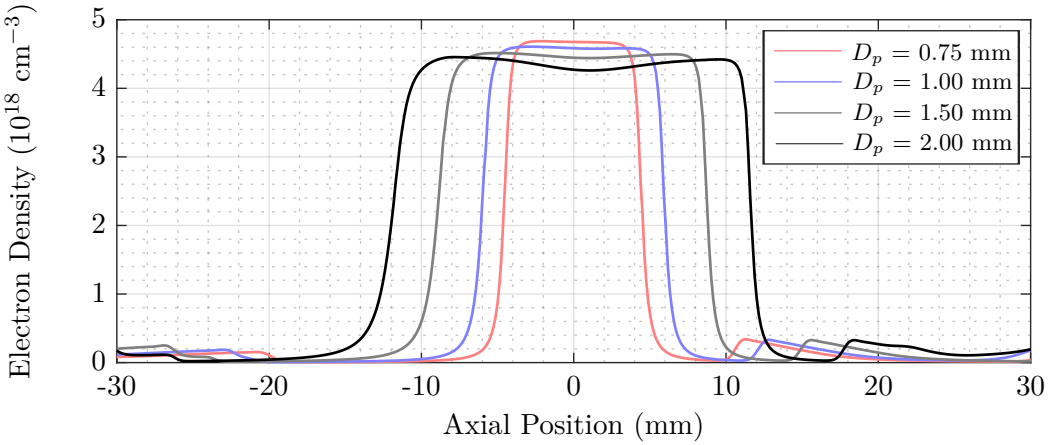

Figure 4.4: *OpenFOAM* simulations showing variation in axial electron density profile due to changes in the front pinhole diameter. Four different front pinholes are simulated; D_p = 0.75, 1.00, 1.50 and 2.00 mm. For $\alpha = 2.5°$, these correspond to channel lengths of L_{ch} = 8.5, 11.4, 17.0 and 22.7 mm.

Figure 4.4 shows the calculated axial electron density profiles (assuming full ionization of the hydrogen fill) for four different front pinhole diameters; 0.75 mm, 1.00 mm, 1.50 mm, 2.00 mm. As would be expected, the length of the density ramp increases with increasing pinhole size reaching a width at half-maximum of 570 µm for the largest pinhole diameter. In addition, there is a small drop in the axial density with increasing pinhole size but the pressure remains approximately uniform within the cell.

If the pinhole size is set to 1.50 mm, twice that of the back pinhole, then the maximum achievable channel length is restricted to 17 mm for the 2.5° axicon and 10.8 mm for the 4° axicon. In addition the ramp length is reduced to 420 µm. While not capable of providing the desired 50 mm long channels, a conventional gas cell of this style could still produce a medium-length channel which would constitute a demonstration of the concept of axicon formed HOFI plasma channels and thus makes for a good backup option.

Plan A: A Gas Cell for Production of Long Plasma Channels

Designing a cell for a long plasma channel requires re-engineering of the mechanism by which light from the axicon is coupled into the cell. After much investigation of possible schemes, a design was chosen which involved replacing the front pinhole of a conventional gas cell with a thin window as shown in figure 4.5. That is, instead of constructing the front pinhole from

a metal, it was constructed from fused silica, BK7 or some other material which could be polished to form an optically flat, transparent thin window.

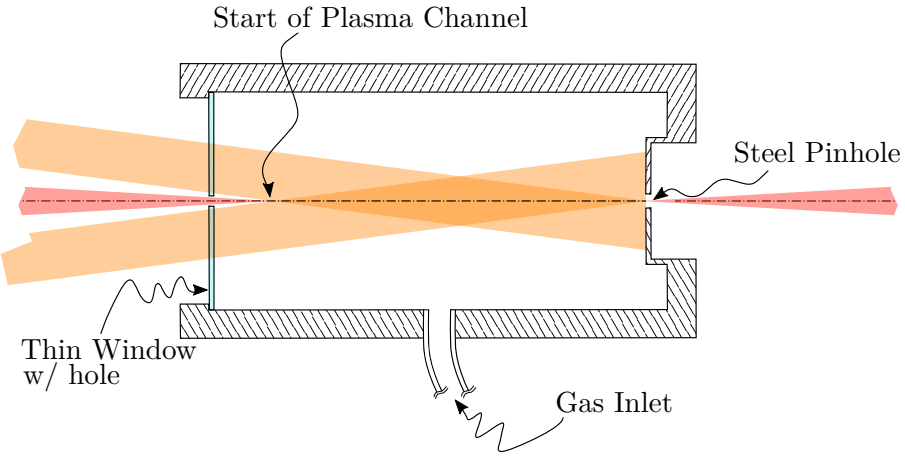

Figure 4.5: A modification to a conventional gas cell design in which the front metal pinhole has been replaced by a transmissive, thin, polished window with a hole.

In this design the axicon beam, being much less intense than the guided beam, is permitted to travel through very thin windows even when close to the start of its focus. A analysis similar to that in section 4.3.3 can be followed to determine just how close to the start of the focus the window can be placed. Figure 4.6 shows the same parameter space as in figure 4.1 but rather than using the nonlinear phase restriction given by equation 4.14, a new restriction on allowable combinations of r_0 and E_A is defined. In this case, not only is the nonlinear phase accrual in the axicon taken into consideration, but also the nonlinear phase acquired in passing through a thin window of thickness t_w placed a distance f_w from the beginning of the axicon focus;

$$r_0 > \frac{\frac{\lambda\tau}{2\pi n_2 E_A} - t_s - \frac{D_{\text{ax}}}{2}\tan\left(\frac{\alpha}{\eta-1}\right) - \frac{L_{ch}t_w}{2f_w+L_{ch}}}{\frac{2t_w}{2f_w\alpha+L_{ch}\alpha} - \tan\left(\frac{\alpha}{\eta-1}\right)}. \tag{4.17}$$

Clearly the introduction of a gas cell window adds non-negligible amounts of nonlinear phase to the pulse acting to reduce the available parameter space. However, for the case shown in figure 4.6 ($f_w = 5$ mm and $t_w = 250$ µm) it is seen that, in the case of both axicons and both long and short pulse options, there is still parameter space available which could acceptably be used for operation.

It should be pointed out that the parameter space calculations for this section have been

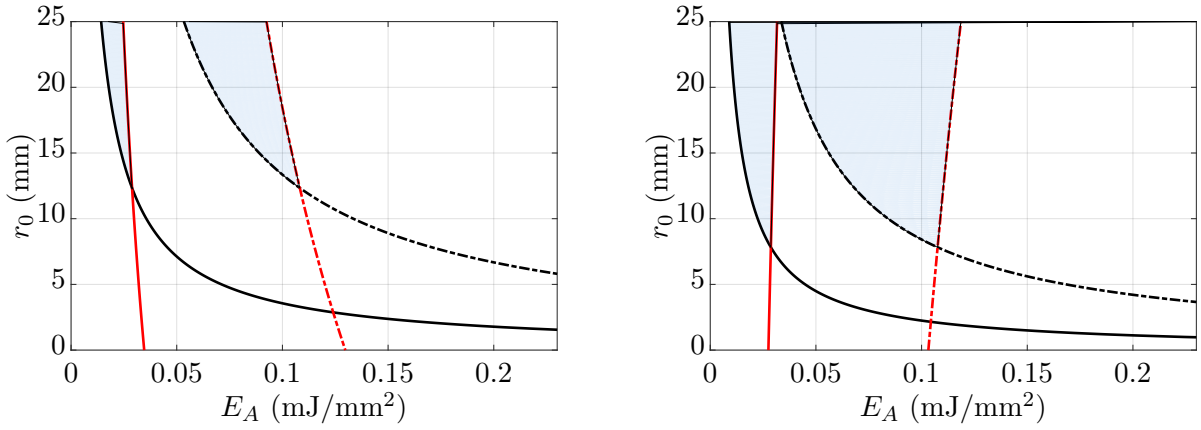

Figure 4.6: Operable parameter space, shaded blue, for the 2.5 ° approach angle axicon (left) and the 4.0 ° approach angle axicon (right) Above the black lines the combinations of r_0 and E_A are capable of reaching the ionization threshold with a safety factor $s = 2$ while above the red lines the combinations of r_0 and E_A provide a B-integral less than 1 for the case of a windowed gas cell and a transmissive axicon. The solid lines correspond to the short pulse case while the dashed lines represent the long pulse case.

made with deliberately tight constraints. It should be recalled that a safety factor of 2 has been included on the required intensity necessary to ionize H_2 and that the nonlinear phase acquired by the axicon pulse has been kept below 1. Both of these constraints are rather tight to allow for acceptable experimental operation with a healthy margin of error.

One issue with using an ultra thin window pertains to the ability of the window to withstand the pressure differential between the cell and vacuum, typically of order a few hundred mbar. Using a semi-empirical formula distributed by *Crystran*[‖], a UK based optics supplier, it is possible to estimate the maximum operating pressure of such a window. For a clamped circular window the maximum allowable pressure difference is;

$$P = \frac{5.3 F_A t_w^2}{D^2 s_w}, \tag{4.18}$$

where F_A is the apparent elastic limit or rupture modulus of the window material, D is the unclamped diameter of the window and s_w is a safety factor. It should be noted that the rupture modulus is so named for a reason. Thus in many standard applications a safety factor of 4 is used; this is not only to prevent rupture, but also to avoid plastic deformation in the window. For the cases here a safety factor 50% greater than standard is used to help mitigate

[‖]https://www.crystran.co.uk/

any significant deformation in the window which would act to deform the axicon focus.

For a 250 µm thick window of Fused Silica with an unclamped diameter of 10 mm and a safety factor of 6 it is found that the maximum pressure allowable in the cell is 304 mbar.

4.4 Experimental Setup

Taking the experimental design constraints, considerations and objectives into account the experimental setup detailed below was developed and built at TA2. A broad overview of the interaction region is shown in figure 4.7. A channel-forming beam was setup to form a HOFI plasma channel which would guide a second high-intensity pulse (the guided beam). The HOFI channel was then probed with both longitudinal and transverse interferometry.

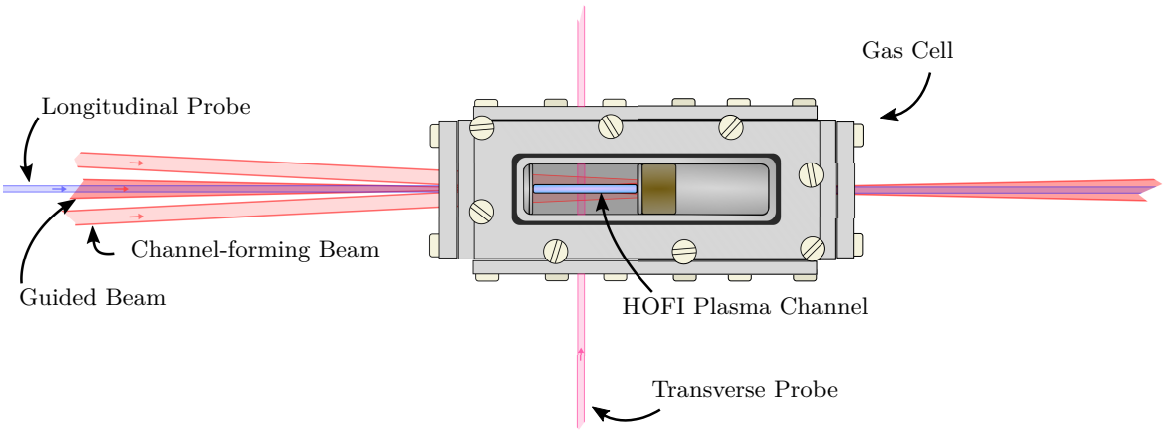

Figure 4.7: Schematic of the interaction region showing the formation of, guiding in and probing of a HOFI plasma channel.

The Astra-Gemini TA2 laser system, described in section 4.3.1, provided a high energy beam and a probe beam to the target area. The main beam entered the target area uncompressed and was passed into the target chamber via a dual grating vacuum compressor. The probe beam, also entering the area stretched, was compressed at air and passed onto an optical table (the probe table) prior to the vacuum chamber for manipulation.

4.4.1 Probe Table Layout

The probe beam in TA2 exhibited substantial pointing drift over the course of the day and so an automatic pointing stabilizer was installed on the probe table. This pointing stabilization

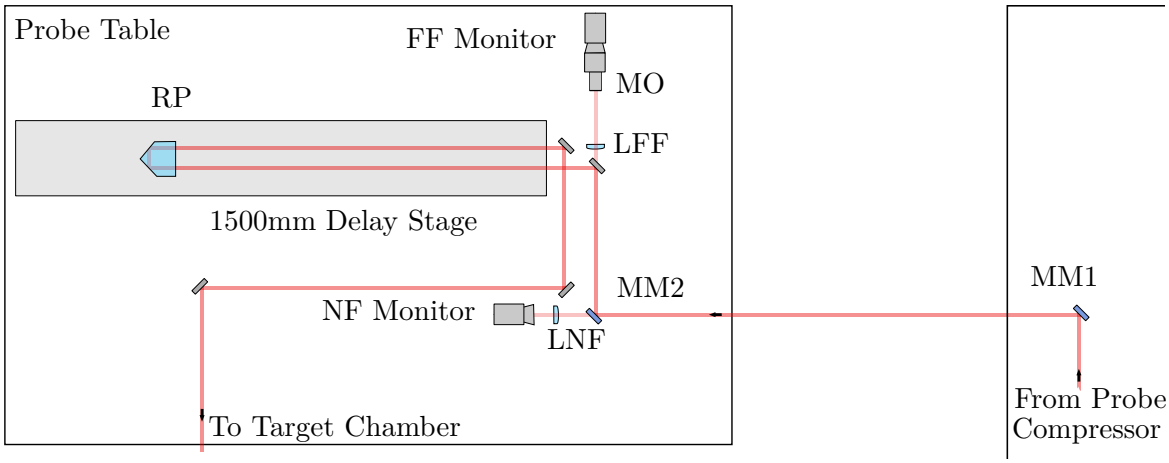

Figure 4.8: **Experimental layout on Probe Table:** MM1 (motorized mirror 1), MM2 (motorized mirror 2), LNF (plano-convex lens $f = 150$ mm), LFF (plano-convex lens $f = 75$ mm), MO (10X microscope objective), RP (retro-reflecting prism).

system was found to be essential to maintaining alignment over the course of the day and throughout long data sets. The stabilization system was left running for long periods of time, even when shots weren't being taken, to keep the system well aligned.

The stabilization system consisted of two motorized mirrors, a set of near/far field monitors and a *LabView* script written by previous group members, Dr. Kevin O'Keefe and Dr. David Llyod, and adapted for use at TA2 by the author. For the near-field monitor a leak was taken through the back of the second motorized mirror in the setup and slowly focused with a 150 mm lens, LNF, to a CCD placed approximately 75 mm upstream of the focal point. The beam had to be weakly focused to fit it onto the CCD, while this does not constitute a true near-field measurement, it was a sufficiently good approximation for the purposes of establishing a beam position monitor. For the far-field monitor, a leak was taken after the second motorized mirror. The leakage beam was focused with a 75 mm focal length lens, LFF, onto the object plane of a 10X microscope objective attached to a CCD.

After the pointing stabilizer, a 1500 mm long delay stage was also installed on the probe table. A 50 mm diameter retro-reflecting prism mounted on top of the delay stage allowed for the probe arrival time at the interaction point, IP, to be varied by up to 10 ns without major changes in the probe pointing. The beam was then directed into the target chamber.

4.4.2 Chamber Layout

Figure 4.9 shows a scaled drawing of the experimental layout used in the vacuum chamber. The 750 × 1000 mm breadboard in the TA2 vacuum chamber provided quite a small space to install the necessary optics required to create and manipulate the four beamlines used in this experiment as can be seen in figure 4.10.

The 800 nm drive beam, nominally a 55 mm diameter, 420 mJ, 40 fs beam arrived into the chamber from the top right as shown by the large black arrow in figure 4.9. It was apodized into a channel-forming and guided beam by taking the reflection and transmission respectively of a holey mirror, HM1. The holey mirror was a 101.6 mm diameter dielectric coated mirror with a 30 mm hole cut through the center of the reflecting face at 45 ° to the mirror normal (*Rainbow Research Optics*).

Channel-Forming Beam

The channel-forming beam was passed through a quarter-wave-plate, QWP, to control its ellipticity before being sent to a 300 mm retro-reflecting delay stage, DS1. It was then passed through a 5.6 ° base angle, UVFS, AR coated, transmissive axicon, AX, with a 10 mm diameter center hole (*Doric Lenses*). The axicon was mounted on a 25 mm motorized translation stage to allow for extra control over the longitudinal positioning of the focal region of the axicon. After the axicon, the beam was aligned to the interaction region via two final turning mirrors, the second of which was a holey mirror, HM2, used to couple the channel-forming and guided beamlines to the interaction axis. This second holey mirror was a 50.8 mm diameter, 6 mm thick dielectric coated mirror with an 18 mm diameter hole cut through the center of the reflecting face at 45 ° to the mirror normal (*Rainbow Research Optics*).

Guided Beam

The guided beam, transmitted by HM1, now 30 mm in diameter, was passed into a 500 mm retro-reflecting delay stage, DS2, and was subsequently focused by a 76.2 mm diameter 750 mm focal length, silver coated, off-axis paraboloid, OAP, (off-axis angle of 11 °). A removable beam block (RB), specifically a flip mount with a beam block attached, was installed before

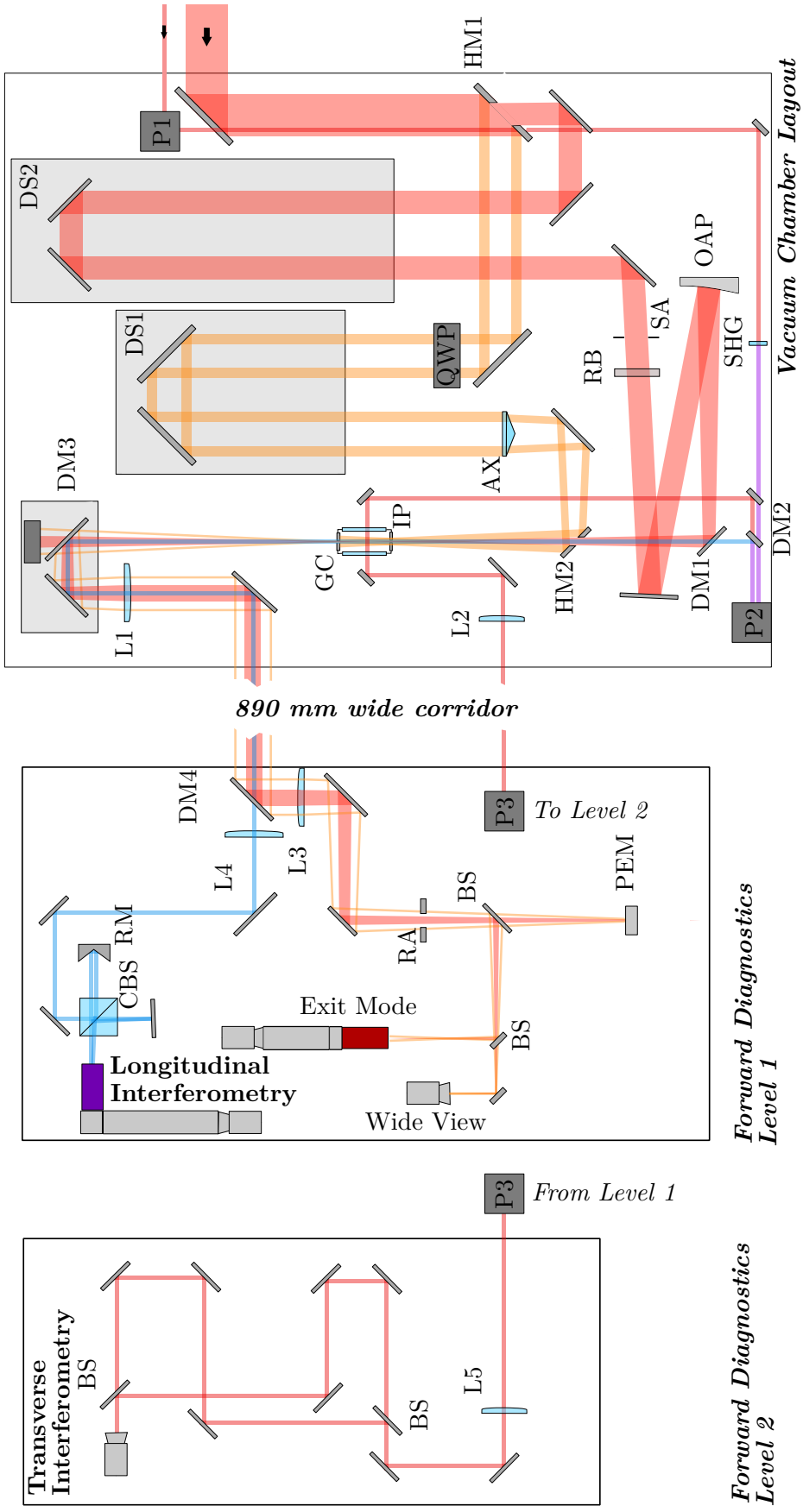

Figure 4.9: **Experimental layout in vacuum chamber:** HM1 (holey mirror), OAP (750 mm focal length off-axis paraboloid), RB (removable beam block), SA (serrated aperture), DM1 (800:400 R:T dichroic), HM2 (holey mirror), IP (interaction point), GC (gas cell), DM3 (400:800 R:T dichroic), L1 (achromatic lens $f = 500$ mm), QWP (quarter-wave-plate), AX (axicon), P1 (downward, turning periscope), SHG (second harmonic generating crystal), P2 (upward, non-turning periscope), DM2 (400:800 R:T dichroic), L2 (plano-convex lens $f = 250$ mm).
Experimental layout in forward diagnostics setup: DM4 (800:400 R:T dichroic), L3 (achromatic lens $f = 750$ mm), BS (50:50 plate beamsplitter), RA (removable aperture), PEM (Pyroelectric Energy meter), L4 (achromatic lens $f = 750$ mm), CBS (cubed 50:50 beamsplitter), RM (roof-mirror), P3 (upward, non-turning periscope), L5 (plano-convex lens $f = 1500$ mm)

the paraboloid and allowed the guided beam to be blocked remotely when not conducting guiding experiments. In addition, a 30 mm diameter serrated aperture was installed in the guided beam to disperse diffraction rings at the edges of the beam which could damage optics downstream. Approximately half way to focus, the guided beam was folded onto the interaction axis by a 50.8 mm diameter, 800 nm reflecting 400 mm transmitting, high damage threshold dichroic mirror DM1 (*Manx Precision Optics*). A second option for a lower intensity guided beam was to replace DM1 with a 3 ° optical quality fused silica wedge. After DM1 the beam was passed through HM2 en route to IP.

Probe Beams

The 800 nm probe beam was periscoped down below the optical mounts of the main beams by a turning periscope, P1, to allow for easier manipulation of the probe beam within the target chamber. It was directed around the edge of the breadboard before being passed through a 15 x 15 x 0.5 mm, type I, Beta Barium Borate (BBO) second harmonic generating crystal to generate a 400 nm beam which propagated colinearly with the 800 nm source. Both beams were periscoped back up to the height of the main beam by a non-turning periscope, P2, before being separated by a 650 nm long pass dichroic mirror DM2. The 400 nm beam was passed through the back of DM1 and aligned colinearly with the channel-forming and guided beams. The 800 nm beam, transmitted through DM2, was directed down a beamline parallel to the interaction axis before being passed through the gas cell to probe the interaction transversely.

Imaging the Interaction Region

Two mirrors on the opposite side of the gas cell directed this transverse probe out of the chamber, with a 50.8 mm diameter, 250 mm focal length plano-convex lens being used to collect image rays from the interaction region and collimate them prior to sending them out of the chamber.

Post IP, on the longitudinal line, the channel-forming beam, guided beam and 400 nm probe beam all propagated colinearly. Rays from the interaction region were collimated by a 76.2 mm diameter, 500 mm focal length achromatic lens which was placed in the beam after a 50 mm long retro-reflecting imaging stage which allowed for the object plane for the forward

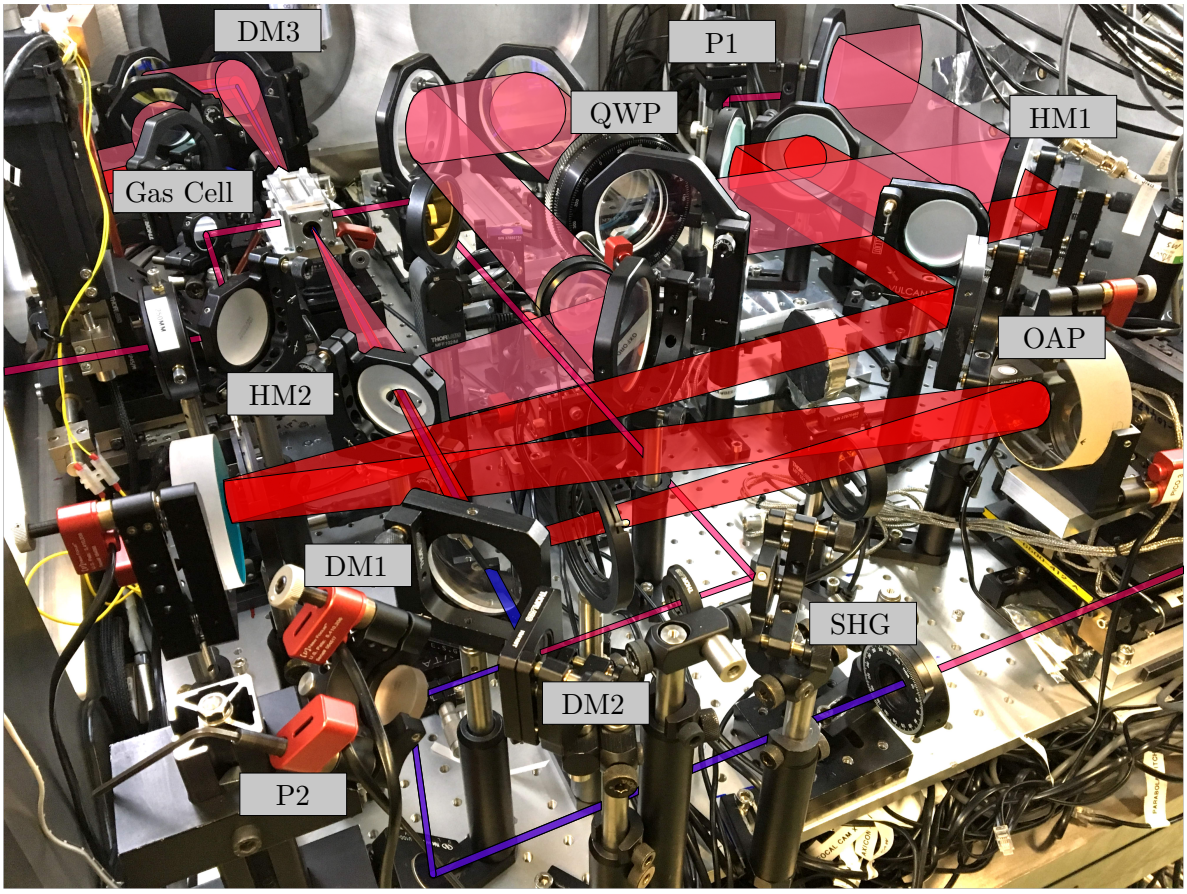

Figure 4.10: A photograph of the Astra-Gemini TA2 vacuum chamber taken during the experiment. Several optics are identified and the beams superimposed to help orient the reader.

diagnostics to be varied. The first optic in the imaging stage was a 76.2 mm diameter wedged 800 nm transmitting 400 mm reflecting high-damage-threshold dichroic mirror, DM3 (*Manx Precision Optics*). This enabled most of the pump light to be dumped before the beams left the chamber, while retaining the probe light.

4.4.3 Forward Diagnostics Layout

The forward diagnostic setup was split into two levels: an upper level used for the 800 nm transverse probe and a lower level used to diagnose the 400 nm probe and the channel-forming/guided beams. Upon exiting the chamber all beams propagated across an 890 mm corridor before arriving at the forward diagnostics table.

The channel-forming beam, guided beam and 400 nm probe beam left the chamber through an uncoated UVFS window and were split apart by wavelength using a 76.2 mm diameter 400 nm transmitting 800 mm reflecting dichroic mirror DM4 (*Manx Precision Optics*).

Longitudinal Probe Diagnostic

The 400 nm probe beam was then passed through a 76.2 mm diameter, 750 mm focal length achromatic lens, L4, which acted as the second lens in a Keplerian telescope used to image the interaction region onto the probe diagnostic camera**. The probe was passed into a folded wavefront interferometer in a Michelson configuration, with one of the mirrors of the Michelson having been replaced with an UV enhanced aluminium roof-mirror to spatially offset the beams in the two arms thus allowing for a very fine fringe spacing to be obtained in a compact interferometer. The 400 nm rays imaged from the interaction region propagated through this setup and came to a focus in the image plane at the output of the folded wavefront interferometer. A 5X infinity-corrected microscope objective (*Mitutoyo M-Plan APO*) together with a 200 mm tube lens (*Mitutoyo MT-L/1X*) were used to magnify this image onto the CMOS sensor of a camera (*Allied Vision Mako G-503B POE*). A 450 nm short-pass filter (OD4) was installed into the microscope objective setup to cut out any remaining 800 nm light which managed to make it through DM3 and DM4.

Channel-Forming and Guided Beam Diagnostics

The 800 nm rays reflected from DM4 were passed through a 76.2 mm diameter, 750 mm focal length achromatic lens, L3, which imaged the rays onto the 800 nm diagnostics. The beam was passed through a removable aperture, RA, which blocked the axicon beam while the guided beam was transmitted; together with the removable guided beam block in the chamber (RB), this setup allowed for independent viewing of the channel-forming beam or guided beam. The beam was then split by a 50:50 plate beamsplitter, with the transmitted beam being passed onto a pyroelectric energy meter (*Gentec QE25LP-S-MB*). This allowed for energy measurements of the transmitted guided beam. The reflected beam was passed to a second

**All imaging of the interaction region was performed using pairs of lenses in a Keplerian telescope configuration.

50:50 plate beamsplitter which allowed for the focus of either beam to be viewed on a high and low magnification camera simultaneously.

The beam transmitted through this 50:50 splitter passed directly onto the CCD of the low magnification wideview camera (*Allied Vision Stingray F033BF*). The reflected beam was passed into a high magnification exit mode camera consisting of a 10X infinity-corrected microscope objective (*Mitutoyo M Plan APO*), a 200 mm focal length tube lens (*Mitutoyo MT-L/1X*) and a camera with a CMOS sensor (*Allied Vision Mako G-503B POE*). The relevant calibration, resolution and magnification measurements[††] for these and the other cameras mentioned in this chapter are given in table 4.1. For full power shots neutral-density filters were placed before the cameras to prevent burning of the CMOS/CCD sensors.

Transverse Probe Diagnostic

The 800 nm transverse interferometry probe beam exited the chamber through an uncoated UVFS window and was transported to the upper level of the forward diagnostics table via a non-turning periscope, P3. Here it passed through a 50.8 mm diameter, 1500 mm focal length achromatic lens, L5, used to image the interaction region onto the CMOS sensor of the transverse probe diagnostic camera (*Allied Vision Mako G-503B POE*). After L5, the 800 nm probe beam was passed into a folded wavefront interferometer in a novel Mach-Zhender configuration. The splitting and recombining of the beams was performed with 800 nm 50:50 plate beamsplitters. A Mach-Zhender configuration was chosen as space was not limited on the upper level of the forward diagnostics table and such a configuration offered increased control over fringe spacing, angle and object position on the camera. To increase the visibility and extent of the fringes viewed on the CMOS sensor, a 10 nm FWHM bandpass filter, centered around 810 nm, was attached to the front of the camera.

Vacuum Focus Camera

Not shown in the experimental layout is an in-chamber focal camera which was suspended from the chamber roof due to space restrictions. The channel-forming and guided beam could be directed towards the vacuum focal camera by a mirror attached to motorized flip mount placed

[††]The cameras were calibrated by imaging a 1951 USAF resolution test chart.

Diagnostic Camera	**Calibration**	**Resolution**	M_{Exp}	M_{Meas}
Exit Mode	0.13 ± 0.02 µm/pixel	7.8 ± 0.9 µm	15	18.3
Wide View	6.65 ± 0.14 µm/pixel	19.7 ± 2.5 µm	1.5	1.49
Transverse Interferometry	0.369 ± 0.004 µm/pixel	8.7 ± 0.9 µm	6	5.96
Longitudinal Interferometry	0.291 ± 0.002 µm/pixel	7.8 ± 0.9 µm	7.5	7.55
Vacuum Focus Camera	0.517 ± 0.011 µm/pixel	2.2 ± 0.3 µm	20	19.15

Table 4.1: Calibrations for the five main diagnostic cameras used. Shown is each cameras measured calibration and resolution together with the measured and expected magnification M_{Meas} and M_{Exp} respectively. All calibrations were performed using a 1951 USAF Resolution Test Chart placed at the diagnostics object plane.

just prior to IP. The vacuum focal camera consisted of a 20X infinity-corrected microscope objective (*Mitutoyo M Plan APO*), a 200 mm tube lens (*Mitutoyo MT-1*) and a CCD camera (*Allied Vision Stingray F033BF*).

Chapter 5

Guiding In Axicon-Formed HOFI Plasma Channels: Implementation and Results

5.1 Channel-Forming and Guided Beam Focii

HOFI plasma channels represent an all-optical method of creating plasma waveguides, as such, beam characterization is paramount to interpreting any experimental results. In this section both the guided (paraboloid-focused) beam and the channel-forming (axicon-focused) beam are characterized.

5.1.1 Guided Beam

An example focal scan of the guided beam in the absence of a waveguide structure is shown in figure 5.1 (a). The intensity map shown has been produced by averaging horizontal and vertical lineouts of the guided beam taken at a number of longitudinal positions within ± 6 mm of the focus. Superimposed onto the intensity map are D4σ measurements of the $1/e^2$ intensity spot size of the guided beam together with a fit $w(z)$ from equation 2.2, from which the Rayleigh range can be extracted. Panel (b) shows the beam at focus; the colorscale for both plots is the same.

For the data here, the measured spot size at focus was found to be $(22.4 \pm 3.4)\,\mu m$ with an approximate peak intensity at full power of $6.25 \times 10^{17}\,W\,cm^{-2}$ calculated using the pixel summation method discussed in section 2.6.3 (note that all intensities quoted in this chapter are calculated by this method). The Rayleigh range was found to be $(1.1 \pm 0.4)\,mm$, consistent with the $f_{\#}/25$ focusing setup (expected Rayleigh range $z_R^{exp.} = 1.25\,mm$), while the spot size was a factor of 1.24 times diffraction limit.

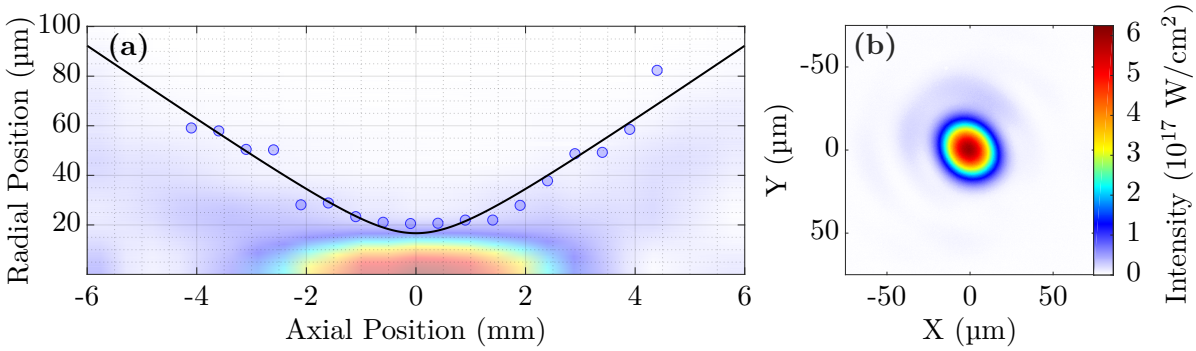

Figure 5.1: (a) Intensity map of the transverse profile of the input guided beam in the focal region. Measurements of the spot size are superimposed together with a fit to equation 2.2. (b) Shows the transverse intensity profile of the focal spot.

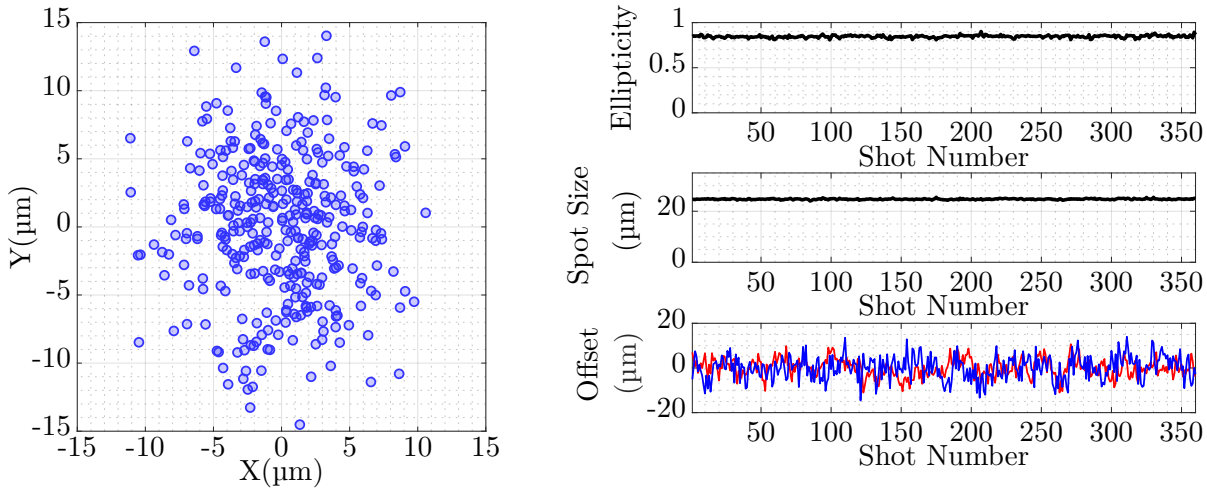

Figure 5.2: Stability of the guided beam. The left panel shows the location of the center of the spot for 360 consecutive shots. The top two panels on the right show the ellipticity and $1/e^2$ spot size for all shots. The bottom right panel shows the transverse offset from the average center position for all shots — the X-offset is shown in red and the Y-offset is shown in blue.

Not only is the quality of the focus important, so too is the stability of the center position of the spot. To determine the pointing stability of the spot, a sequence of 360 consecutive

shots were taken. Figure 5.2 shows the collected data. The main panel on the left shows the center-of-mass for each shot, while the three panels on the right show the ellipticity of the beam (measured as the minor axis spot size divided by the major axis spot size), the spot size and the spatial offset from the mean position. The plot showing the spatial offset, shows both the X-offset (red) and the Y-offset(blue). The spot size and ellipticity remained very stable with negligible variation (standard deviation of $< 2\%$) while the measured offset showed a shot-to-shot jitter with a standard deviation of 2.4 µm in the X-direction and 3.2 µm in the Y-direction for a total transverse jitter of 3.1 µm. The transverse jitter equated to an angular pointing jitter with a standard deviation of 4.1 µrad

5.1.2 Channel-Forming Beam

A representative near field profile of the TA2 pulsed beam is shown in figure 5.3 (a). An approximate scaling has been added to the horizontal and vertical axes in the absence of an accurately calibrated image. A dashed annulus has also been superimposed onto the near field profile indicating approximately the portion of the beam that was used in these experiments to attempt long HOFI channel formation. The profile exhibits a clear asymmetry with much of the energy concentrated in the upper half of the image.

Figure 5.3 (b) shows a typical focal image of the channel-forming beam taken at the front of the gas cell. Axicon focii are highly susceptible to both the phase front and spatial profile of the near field of the incident beam. For this reason, the axicon was aligned and optimized using an 808 nm CW diode which traveled colinearly with the main TA2 pulsed beam. The CW beam, having an excellent near field profile allowed for an accurate optimization of the axicon focus without distraction or confusion being introduced by features in the pulsed beam focus caused by a structured near field or spatio-temporal couplings. Lineouts of the Bessel focus taken in the vertical and horizontal directions (black lines) agree well will the expected Bessel profile for the given axicon parameters (dashed red lines), with better visibility of the Bessel zeros seen in the horizontal lineout. The peak intensity at full power was estimated as $5.25 \times 10^{15}\,\mathrm{W\,cm^{-2}}$, a factor of more than 10 above the hydrogen ionization threshold. The results presented in this chapter pertain to data taken with a fused silica axicon with an approach angle $\alpha = 2.5°$.

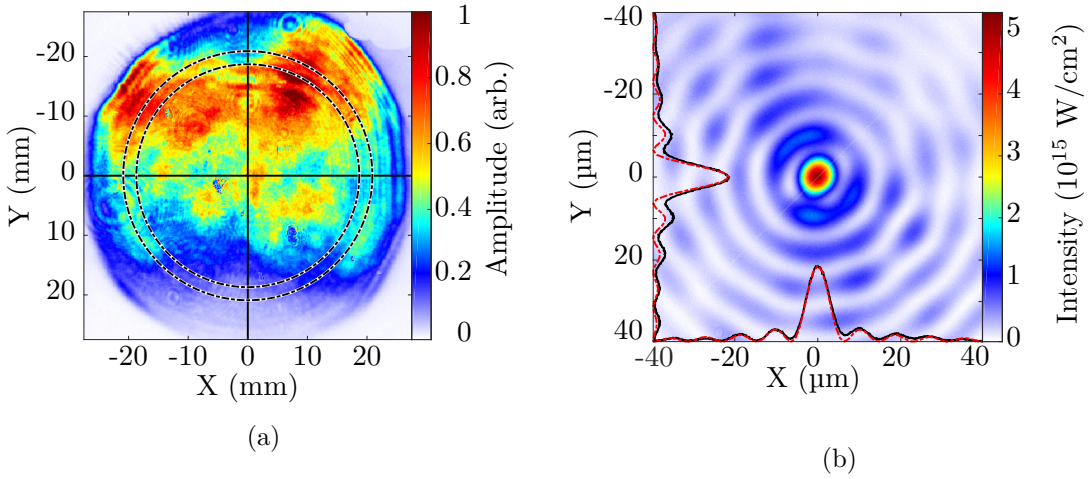

(a) (b)

Figure 5.3: (a) Near field of the Astra-Gemini beam taken after the third amplifier. The dotted annulus represent the portion of the beam that would be needed to form a 50 mm long axicon focus. (b) Axicon focus taken at the front pinhole of the gas cell. Horizontal and vertical lineouts through the center of the focus are plotted in black; the red dotted line shows the ideal focal profile for the given axicon parameters (normalized in amplitude to the measured lineout).

The longitudinal profile of the axicon focus is extremely important. Figure 5.4 shows a focal scan of the channel-forming beam taken over a 60 mm range along the axicon focus. The pseudo-non-diffracting nature of the Bessel beam is apparent; it is seen that the profile and intensity of the beam do not vary very much in this range. The focal quality, viewed as the visibility of the Bessel zeros, is better for the horizontal slice, a point which will become important in later sections.

A stability analysis, similar to the one performed for the guided beam above, showed that the axicon focal position had a total transverse jitter of 1.1 µm (0.8 µm in the X-direction and 1.2 µm in the Y-direction). This corresponds to an angular jitter of standard deviation 2.4 µrad.

5.1.3 Focal Optimization

A deformable mirror was employed to aid in the optimization of the focii of the channel-forming and guided beams. This mirror was located post compression but prior to apodizing the beam which meant that the wavefront could not be optimized independently for both beams.

As a starting point, the wavefront of the beam (prior to apodization) was viewed on a

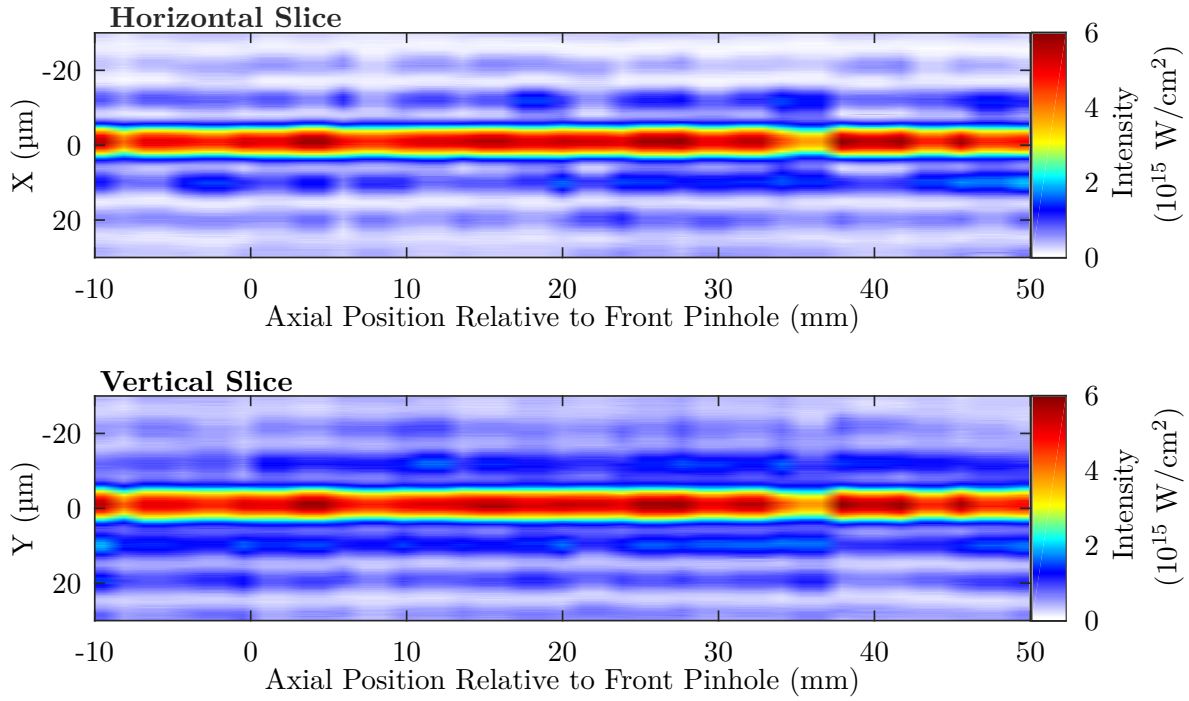

Figure 5.4: Results of a focal scan of the guided beam taken over a 60 mm range. The top panel shows a 2D horizontal slice of the data while the bottom panel shows the vertical slice. The zero point longitudinally represents the location of the front pinhole of the gas cell.

wavefront sensor (*Imagine Optic HASO 32*) and flattened using the deformable mirror and a commercial closed-loop optimization algorithm. The resulting wavefront was found to have an rms variation of 0.47 rad (0.075λ).

Next the beams were aligned and optimized using their respective focusing optics to remove any remaining aberrations. For the parabola this involved the standard 5-axis alignment (pitch, yaw, X, Y, Z) while for the axicon a 2-axis alignment was sufficient to optimize the focus (pitch, yaw), while the transverse axes (X, Y) allowed for accurate positioning of the focus. In contrast to the parabola, the axis of the axicon could be translated relatively large distances in the transverse plane of the focus without seriously deteriorating the focal profile. This was helpful when coupling the guided beam into the plasma channel; rather than moving the parabola focus to the waveguide, it turned out to be far simpler to move the waveguide to the parabola focus.

The final round of optimization involved a set of open-loop corrections made to the adaptive

optic; adding successive Zernike polynomials to the phase front to correct for any remaining aberrations. It was found during this process that while the parabola focus could withstand minor changes to the phase front without any obvious degradation in its focal profile, the axicon was quite responsive to the same changes.

5.2 Beam Parameters: Pulse Duration, Energy & Polarization

5.2.1 Pulse Duration

A holey mirror was installed as the last optic in the grating compressor vacuum chamber to allow for an accurate pulse duration measurement. This optic had a 5 mm diameter hole drilled at 45° to the normal of its front face and was placed in the beamline such that the hole resided off center of the main beam. The beam transmitted through the holey mirror was reduced in intensity by reflection off a glass wedge before being passed out of the compressor vacuum chamber through a thin window. It was then passed into a commerical SPIDER* (*APE Compact LX Spider*) which allowed for characterization of the temporal profile of the pulse[171].

Figure 5.5 shows the FWHM pulse duration measurements made over the course of the experiment using the SPIDER, the average FWHM pulse duration used was (44.3 ± 3.6) fs. The compression of the pulse was achieved using TA2's main dual grating compressor and was optimized by an acousto-optic programmable dispersive filter (*Fastlite Dazzler*)[172] installed in the laser front-end.

5.2.2 Pulse Energy

Measurements of the pulse energy were made using a pyroelectric energy meter (*Gentec QE50SP-S-MB-D0*) which could be placed in the beam-path prior to the TA2 vacuum compressor. Throughput measurements made at a medium power setting of the laser in air provided calibrations between energy measured before the compressor and energy delivered on target for both the channel-forming and guided beams. It was found that 15 % of the energy present

*Spectral Phase Interferometry for Direct Electric-field Reconstruction.

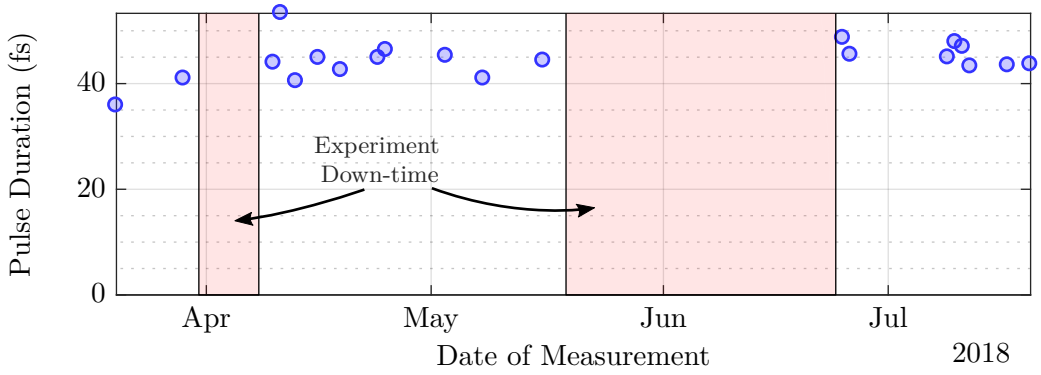

Figure 5.5: SPIDER measurements made of the FWHM pulse duration of the main beam over the course of the experiment.

in the beam prior to the vacuum compressor chamber reached the interaction point (IP) in the channel-forming beam, while 22 % of it ended up in the guided beam focus, for a total throughput to IP of 37 %.

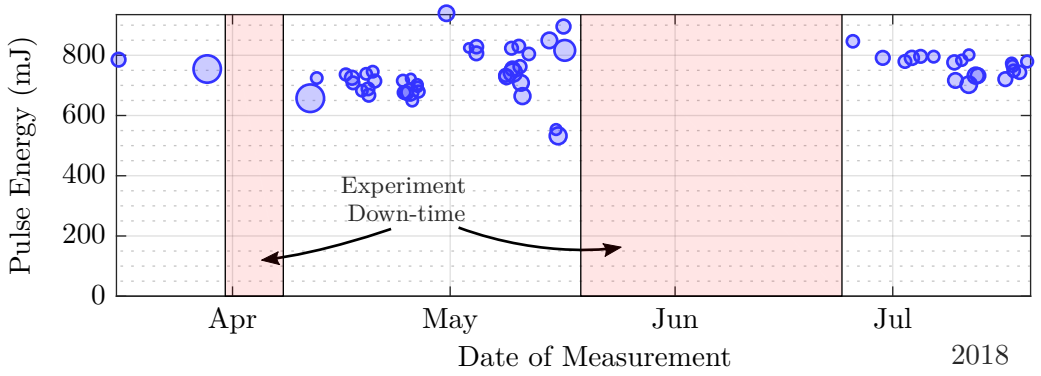

Figure 5.6: Measurements made over the course of the experiment of the energy of the main beam prior to the vacuum compressor. The center of each marker gives the average energy of 100 consecutive shots, while the size of the marker denotes the RMS spread in the energy values for that measurement.

This low throughput was the result of the cumulative effect of many sources of loss. The throughput of the TA2 compressor (measured as energy throughput from before the compressor chamber to just after HM1 in the TA2 vacuum chamber) was measured to be 56 %. Subsequent to this, the main source of loss in the channel-forming beamline post HM1 was the intentional clipping of the aperture of the beam en-route to IP. The 55 mm diameter beam was not only focused by a 50 mm diameter axicon, but some of the axicon beam was also transmitted through the hole in HM2. In fact, 39 % of the energy in the channel-forming beam was lost

between the axicon and IP. While this appears wasteful, it is important to remember that as only a thin annulus of the beam is required to form a long plasma channel, it was always intended that much of the channel-forming beam would not be used.

The energy present in the main beam prior to the vacuum compressor varied daily, as seen in figure 5.6, with the average value being 761 mJ at full power. Thus the typical on target energy for the channel-forming beam was 114 mJ while for the guided beam 167 mJ was achieved on target. The rms stability of the main pulse was typically 3 % while the peak to peak fluctuations in pulse energy were typically 15%.

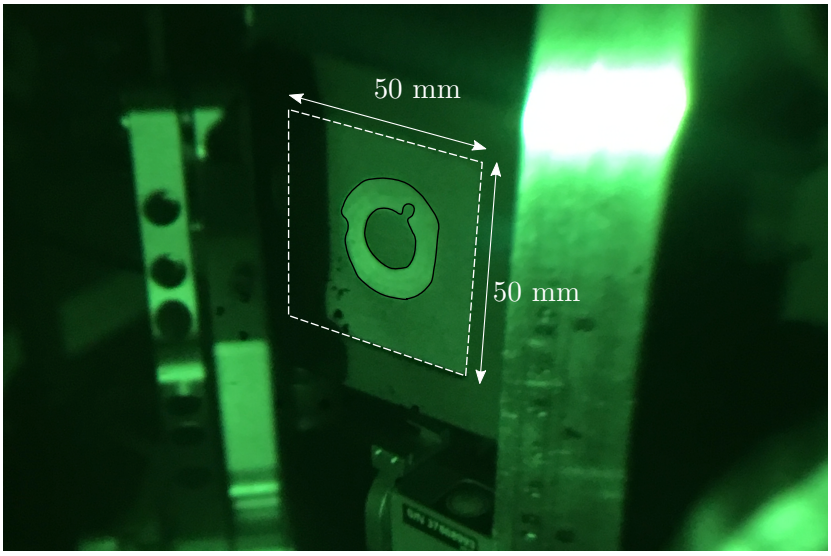

Figure 5.7: A Photograph, taken through an IR viewer, of the near field of the CW beam incident upon an energy meter placed just after HM2. The clear aperture of the energy meter is outlined in white, while the beam profile is outlined in black.

A key figure of interest when discussing laser-formed plasma channels is the energy per unit length of focus necessary to form a suitable waveguide. Mesauring this value directly is tricky, but an estimate may be deduced from the above measurements together with the photograph of the beam near field shown in figure 5.7. The figure shows a photograph taken through an infra-red (IR) viewer of the energy meter placed just after HM2. The dimensions of the clear aperture of the energy meter, outlined in white, are known and can be used to calibrate the spatial scale of the photograph. Outlined in black is the near field profile of the focusing CW beam (which runs colinear with the pulsed beam). Using the *ImageJ* image analysis software suite, it is possible to extract the area of the region confined by the black outline. Together with a measurement of energy recorded before the vacuum compressor and the throughput

measurements discussed above, the average energy per unit area of the channel-forming beam at this point in the chamber can be found. Finally, combining the energy per unit area, together with the distance to focus and the approach angle of rays to the optical axis it is possible to extract the energy per unit length of axicon focus. At full power, the average energy per longitudinal millimeter of axicon focus was 0.84 mJ, with channel formation and guiding observed for energies as low as 0.5 $\mathrm{mJ\,mm^{-1}}$. This is more than an order of magnitude lower than the energies required of OFI-heated plasma waveguide formation with lenses[72,173], and only a factor of five above the values returned from simulations[173].

5.2.3 Polarization of the Channel-Forming Beam

The TA2 beam is p-polarized for the optics in the main vacuum chamber. A quarter-wave-plate was introduced into the channel-forming beam line to produce an elliptically polarized pulse to increase the amount of OFI-heating (section 2.3.1). To align the axes of the quarter-wave-plate the setup shown in figure 5.8 was employed. The setup shows the key optical components used in the calibration and for simplicity treats all other optics in the beamline as a set of black boxes. As none of the optics "contained" within these black boxes are birefringent, they cannot change the ellipticity of the beam, but can only change the orientation of the linear polarization. To calibrate the quarter-wave plate, it was first removed from the optical setup

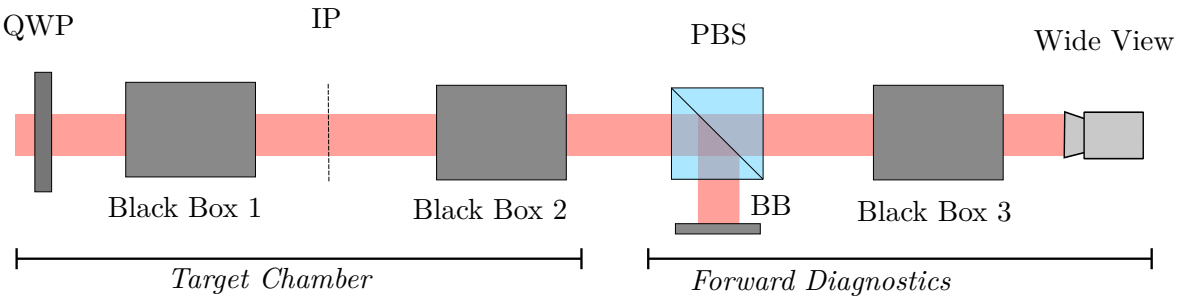

Figure 5.8: Optical setup employed in the calibration of the quarter-wave-plate (QWP): IP (interaction point), PBS (polarizing beam-splitter cube), BB (beam block).

and a cubed polarizing beamsplitter installed on the forward diagnostics table. The beam profile was monitored on the wide view camera and the beamsplitter rotated until the signal was extinguished, meaning that the beam cubes axes were aligned with the polarization of the beam.

The quarter-wave-plate was then reinstalled and rotated until the signal on the wideview camera was entirely extinguished again, meaning the the polarization after the quarter-wave-plate must be linear. Thus for this angle of rotation, the ordinary or extraordinary axis of the quarter-wave-plate was aligned with the laser polarization. A deviation from this angle of rotation by 45 ° would then produce either left- or right-handed circularly polarized light. As H_2 has no inherent chirality, it would not be expected that the handedness of the circularly polarized light would affect the ionization process and thus knowing the handedness wasn't critical.

5.3 Channel-Forming, Guided and Probe Beam Timing

The timing between the four beams: guided beam, channel-forming beam, transverse probe and longitudinal probe, were controlled via a set of retro-reflecting delay stages. Three stages were used: a 1500 mm stage on the probe beam line, a 300 mm stage on the channel-forming beam line, and a 500 mm stage on the guided beam line.

The timing between the channel-forming and guided beams was controlled using a combination of the 300 and 500 mm stages, both of which resided in the vacuum chamber after the beams had been split from the main TA2 beam. Together they could delay the time of arrival of the guided beam with to respect to the channel-forming beam by between 0.75 ns and 6.08 ns.

The timing between the channel-forming beam and the probe was mainly controlled using the 1500 mm delay stage which offered a 10 ns range of motion. In practice, the transverse probe could achieve this 10 ns delay but the longitudinal probe, which arrived at IP before the transverse probe, could not. The longitudinal probe was capable of approximately 9.5 ns delay.

Synchronization of the beams was achieved using the plasma blowout technique described in section 3.3.8. Both the channel-forming and guided beams could be timed relative to the transverse probe beam by looking for plasma blowout. In the initial stages of the experiment the gross timing between pumps and probes was achieved via a long delay line situated in the probe compressor. Once the gross timing was fixed, daily changes in the blowout position remained of order 1 mm.

5.4 Gas Cell

In the interests of guiding over distance approaching 50 mm, tests were performed using a long, windowed gas cell (section 4.3.6). The finalized cell design can be seen in figure 5.9. A 250 µm thick, 12.7 mm diameter Fused Silica window (*Mark Optics*) was used in place of a front pinhole; the window had a 600 µm diameter hole machined into it using the Oxford TW laser machining rig.

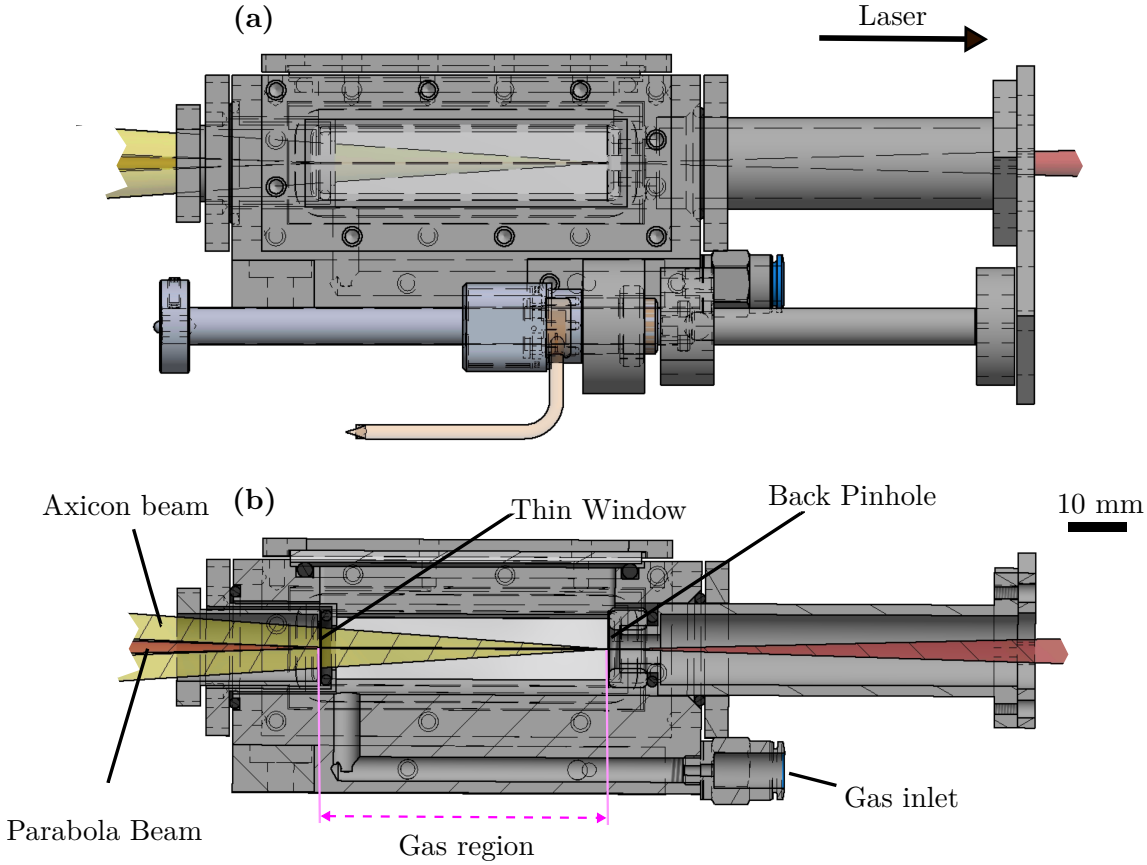

Figure 5.9: Gas cell used in TA2 plasma channel experiments (a) full view (b) section view.

The cell was designed such that the channel-forming beam could pass through the window to form an axicon focus beginning 6.8 mm upstream of the front window and ending at the back pinhole. The guided beam, being more intense, would pass through the hole in the window to focus at the beginning of the axicon-formed channel.

It was found that it was possible to form a long plasma column with this arrangement, as shown in figure 5.10 where a plasma column is seen to extend over ∼36 mm of the cell. Several hundred shots were taken showing similar plasma columns. However, plasma channel

formation and guiding were not observed for the long gas cells. The reason for this is that the plasma column did not start in the predicted location but approximately 7.2 mm downstream of it (a total of 14 mm downstream of the window). Scanning the cell and or the axicon did not help to move the axicon focus further upstream with respect to the cell. This meant that the plasma column itself could not be probed; given the tight geometric constraints within the chamber, it was not possible to probe the plasma further downstream. The increased distance from the front window also prevented coupling of the guided beam into the plasma column and thus guiding was not observed. It is possible that HOFI channels were being produced with the long cell, but due to the constraints above, measurements of any such channels were not possible.

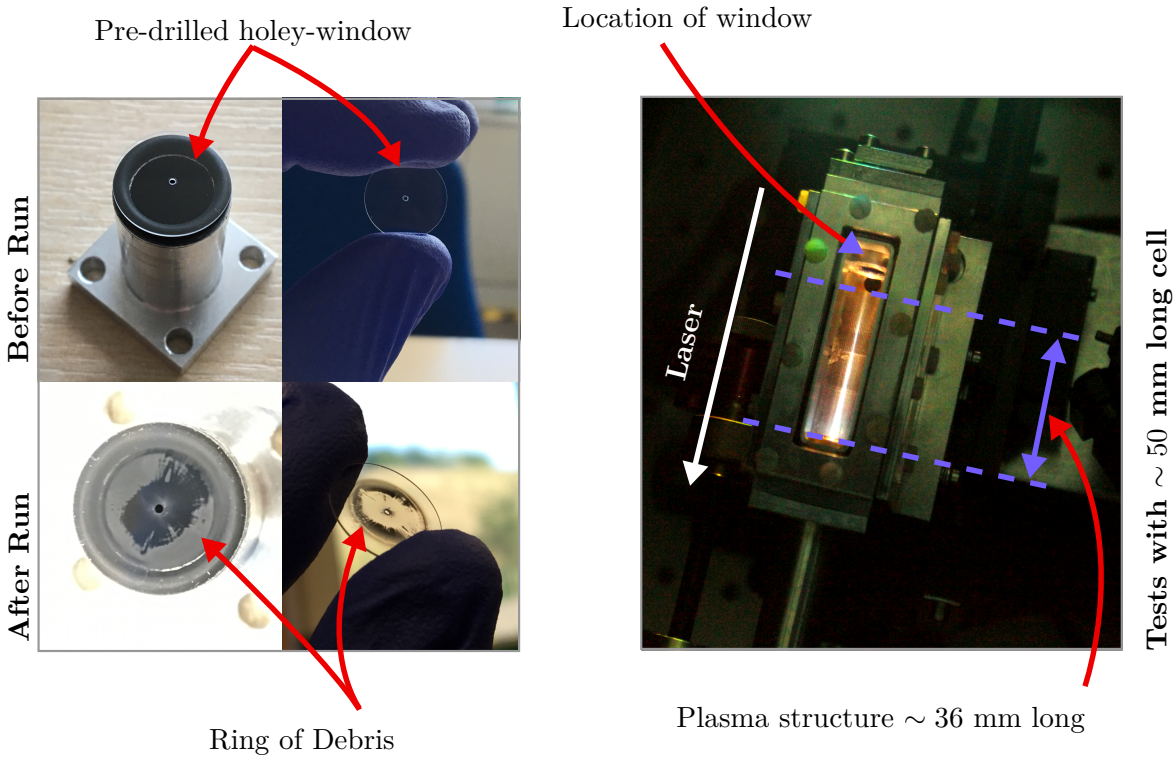

Figure 5.10: Tests performed using a long, windowed gas cell demonstrated appreciable damage to the front window but showed that long plasma columns could be generated for hundreds of shots. The left 4 panels show the holey window prior to the run and after the run while the right hand panel shows plasma formation in a long cell.

The left panel of figure 5.10 shows a set of photographs taken before and after the run. After the run, appreciable damage is seen on the window in an annular pattern near to where the o-ring seal was formed. Additionally, damage is seen at radii close to the pre-drilled hole,

which may explain the longitudinally delayed onset of plasma formation. In between this small region of damage surrounding the hole and outer ring of damage, the window is clear and it appears that the passage of the Bessel beam did not significantly damage this region.

It is postulated that the outer ring of damage arose from ionization of the metal holder by the incident axicon beam, while the inner ring of damage arose from debris/roughness left on the surface of the window after machining the hole.

It was not possible to solve these issues of damage on the timescale of the experimental campaign, however the design of a long gas cell remains an active area of work within the group. In place of a long, windowed gas cell, a shorter cell of 16 mm in length was employed for the guiding results described in this chapter. This cell had a 1.5 mm diameter front pinhole to couple in the channel-forming beam and a 750 µm back pinhole. The pinholes were constructed from both steel and inconel. Figure 5.11 shows a photograph of the TA2 gas cell in action and the formation of a 16 mm HOFI plasma channel.

5.5 Interferometry Diagnostics

5.5.1 Transverse Interferometer

In the gas cell, information about the plasma was imprinted upon the transverse probe pulse. The plane of the plasma structure was imaged through a folded wavefront interferometer in a novel Mach-Zhender configuration onto a camera. A detailed schematic of the folded wavefront interferometer is shown in figure 5.12.

One of the most difficult aspects of the experiment was accurately measuring the phase profile of the axicon-formed plasma channels. The channels were by design low-density, in addition they are small in transverse extent. This combination of small and low density plasma features leads to a very low phase shift imparted upon the probe beam. For parameters relevant to this experiment, the maximum predicted phase shifts of the transverse probe beam were of the order of 100 mrad to 300 mrad. In order to measure the transverse profile of the plasma channel it would be necessary to resolve changes in phase about an order of magnitude smaller than this. Clearly this is a challenge.

The transverse interferometer designed and built for the TA2 experiments underwent a

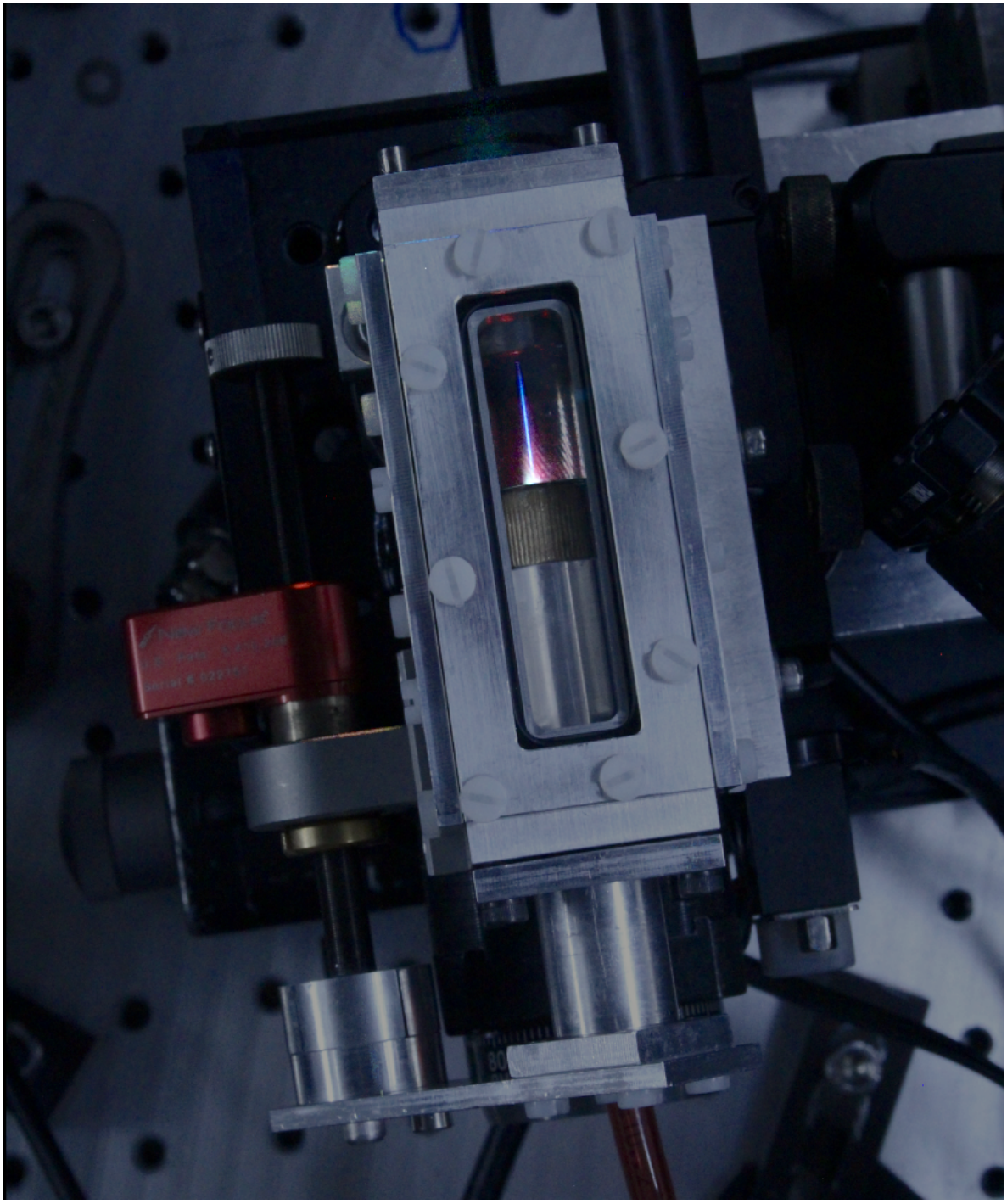

Figure 5.11: Photograph of a 16 mm long HOFI plasma channel formed in hydrogen during experiments at TA2. The laser travels from top of the image to bottom. The photograph was taken with a triggered *Canon* SLR camera with filtering placed in front of the lens to protect the camera's sensor from scattered 800 nm light. The image shown here is a composite of an image without plasma and with the chamber lights on, together with a second image taken with plasma and with the chamber lights off.

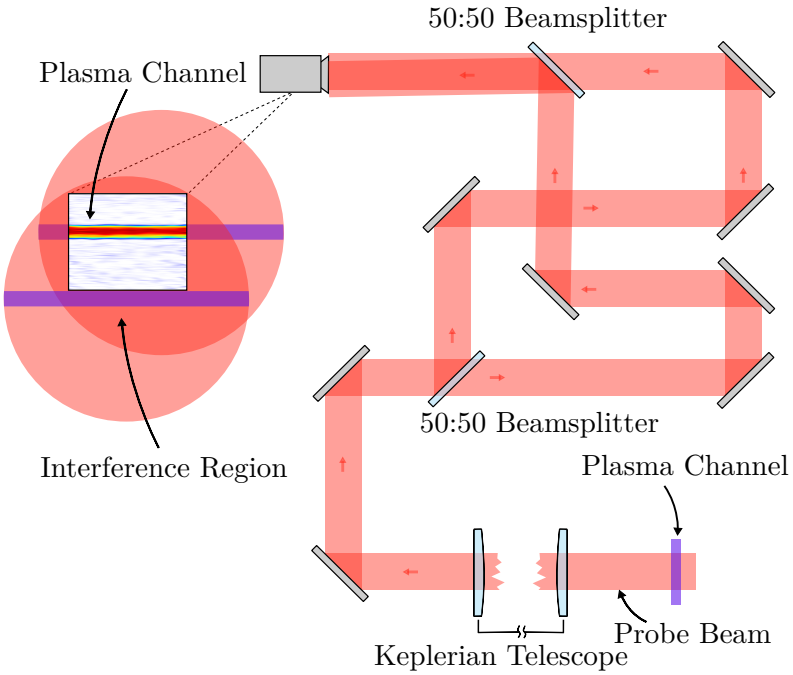

Figure 5.12: Schematic of a folded wavefront interferometer in a novel Mach-Zhender configuration performing transverse interferometry on a plasma structure. Also shown is an example of the beam overlap at the CMOS sensor plane and where the recorded images fit within this.

number of iterations to ensure it was capable of measuring milliradian level phase shifts. Some of the key efforts made are explored below.

Probe Pointing Stabilization

As mentioned section 4.4.1, the probe beam was susceptible to jitter and drift; the movement of the beam included a short term jitter, a long term slow drift and an intermittent fast drift. The source of this drift was discovered to be in the main laser area, not the target area. Due to time and access constraints it was not possible to fix the drift at the source, and instead it had to be corrected in TA2 using an active pointing stabilizer.

Stabilization of the probe beam was found to be critical to achieving the required phase resolution in the interferograms over the course of a data run. Without the pointing stabilization, the probe would quickly drift away from optimum alignment and while it would still be visible on the camera, the fringe quality (visibility and straightness) would strongly deteriorate making precision measurements impossible.

Improvements to Probe Wavefront

While the pointing stabilization system accounted for the long term and intermittent drifts of the probe, it was unable to account for the jitter of the beam. During initial experiments there hadn't been much concern with the beam jitter as the probe was much larger than the plasma. However, it quickly became apparent that the jitter was affecting the quality of the fringes - some shots provided very low noise phase maps, while others didn't. It was reasoned that one cause for this could be variations in the local wavefront of the probe.

Indeed, upon inspecting the path of the probe into the target area, and within the probe compressor, it was discovered that the probe was too large to fit cleanly through the clear aperture of the beamline. Clipping of the beam en-route to the target area and within the probe compressor had a detrimental effect on the beam quality. Since the clipping occurred many meters before the interaction point or interferometer, these clips on the outside of the beam had space to propagate in towards the center of beam and cause variations in the wavefront.

To mitigate these effects, and improve the quality of the probe wavefront, a 10 mm diameter serrated aperture was installed on the probe beamline in the laser area. This smoothed out the hard edges in the probe to prevent diffraction rings propagating to the center of the beam; the cost of the improvements was a reduction in probe energy which dropped from just under a millijoule to (0.35 ± 0.02) mJ. However, the reduced size of the probe beam allowed it to propagate to the target area and through the probe compressor without clipping, leading to a much higher quality beam, higher quality fringes, and an increased proportion of interference patterns yielding low noise phase maps.

Reference Management

The manner in which references were taken had a large impact on the retrieved phase profiles. During the early stages of the experiment, a batch of ten reference shots would be taken with pump and probe, but no gas in the cell. Subsequently, ten data shots (with gas) would be taken. The phase of the reference shots would be averaged and subtracted from each of the data phase maps in turn. However, it was noticed that while the first two or three data shots had low background phase noise, subsequent shots became steadily worse.

The solution to this problem was to change the way in which references were taken. The experimental control code was set up such that when the laser was fired, the system would actually take two probe shots; a probe only reference shot, with no gas and no pump laser and 400 ms later a data shot consisting of pump, probe and gas. The time between the reference and data shots was to allow a full 300 ms for the gas cell to fill (determined empirically). During the analysis each data shot would be paired with its own specific reference shot, taken less than half a second before it. This approach was found to yield phase maps with much lower noise.

Fringe Size Optimization

The phase resolution is governed by how accurately the location of a fringe can be determined. This depends not only on the size of pixels in the camera, but also on the bit depth of those pixels. In all cases, smaller pixels and higher bit depth act to increase the phase and spatial resolution. This was the reasoning behind the choice of interferometer camera, an *Allied Vision Mako G-503B POE* with a pixel size of 2.2 µm and depth of 12 bits. In addition, resolution can be improved by increasing the fringe spacing, though to the detriment of the spatial resolution.

For the experiments performed here, the fringe spacing played an important role; several different fringe spacings were used and empirically optimized to achieve the most repeatable, stable and sharp phase features. It was found that a fringe spacing of approximately 200 µm, measured in the plane of the CMOS sensor (33.6 µm in the object plane), was the optimum for these experiments.

Cleanliness

In addition to the measures noted above, achieving the maximum phase resolution required that the standard techniques used to set up the interferometer were performed with extra care and attention. For example, the cleanliness of optics was imperative; dust spots or other debris on windows and mirrors led to diffraction patterns which embedded themselves in the phase profile of the beam and ultimately became difficult to distinguish from low phase shift signals of plasma. In this regard the gas cell windows were particularly problematic. On a daily basis anywhere up to several thousand shots could be taken; the outer Bessel rings of

the axicon focus would ablate the back pinhole of the gas cell slightly on each shot such that after a day of runs the windows would start to develop a coating of debris. To prevent this build up of debris from scrambling the phase front of the beam, the windows of the gas cell were removed every day or two for cleaning.

Resulting Phase Maps

Combining the efforts described above, it was possible to make accurate measurements on the phase profiles of the HOFI plasma channels. An interferogram from an exemplary data shot is shown in figure 5.13. Also shown is the phase map extracted after analysis of the interferogram and subtraction of its associated reference shot. The standard deviation of the noise in the analysed phase maps could be as low as 5 mrad for good data shots, as is the case for the image shown here, but for bad shots it could approach 20 mrad detrimentally affecting the accurate retrieval of the phase profiles. A post selection of data based upon the standard deviation in the phase for a region containing no plasma ensured that only the best data shots were used.

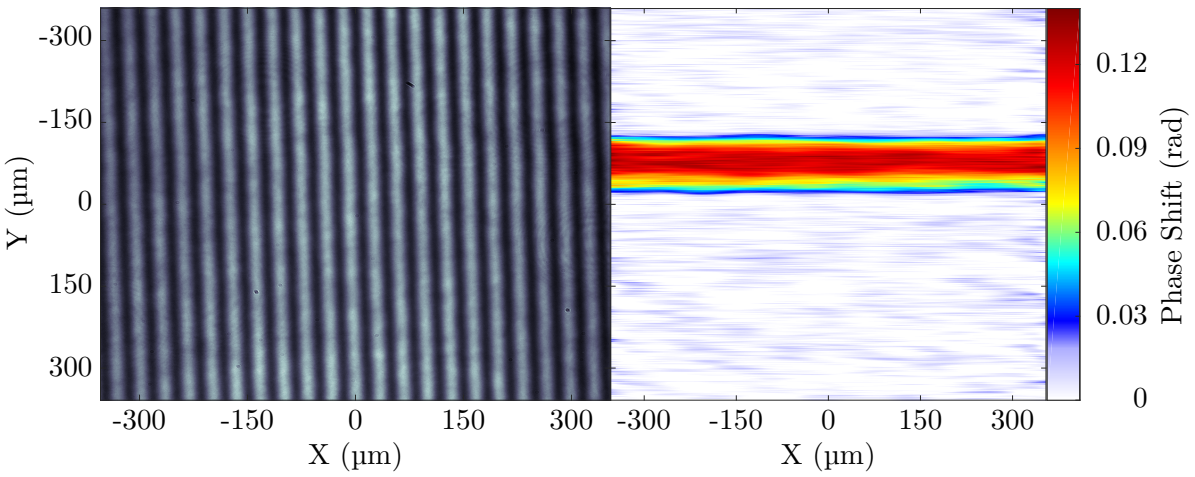

Figure 5.13: Fringe pattern (left) recorded on the transverse interferometer from an exemplary data shot and its analyzed phase map (right) showing a column of plasma. In the image shown, H_2 was used at a backing pressure of 100 mbar and probed 2.5 ns after ionization.

5.5.2 Longitudinal Interferometer

In chapter 3 the issues described above pertaining to the transverse interferometer were avoided by probing the plasma longitudinally, allowing the probe beam to travel through a significant amount of plasma many times the size of its transverse extent. This technique was extremely successful, but had its own drawbacks. The requirements on the alignment of the system were demanding, even a small misalignment between the pump and probe would cause phase information imprinted on the probe to be averaged transversely. Further there was also the issue of probe refraction at higher densities.

Probe refraction was expected to be worse for the experiments described in this chapter over those discussed in chapter 3. This was mainly due to the smaller initial plasma column expected from the axicon, ∼15 µm compared with that formed by the lens, ∼100 µm. While probe refraction was a concern for small delays, preventing detailed timing scans, it was expected that at later delays a longitudinal interferometer would be able to retrieve the density profiles and thus a longitudinal interferometry system was installed at TA2 as a backup to the main transverse interferometer. Beam propagation simulations similar to those performed in section 3.4.6 were performed again for the TA2 experimental parameters to confirm this.

The longitudinal interferometry setup employed in this experiment was very similar to the setup used in the Oxford experiments, described in section 3.3.6. The main difference was the replacement of one of the mirrors in the Michelson setup with a roof-mirror, which allowed the interferometer to achieve a very small fringe spacing within the geometrical constraints of the forward diagnostics table. A schematic of the setup is shown in figure 5.14.

5.6 Diagnosis of Plasma Channels

The plasma structures were diagnosed with both longitudinal and transverse interferometry. Both diagnostics were set up at the beginning of the experimental campaign, and data was taken with both — although rarely simultaneously, due to the differing arrival times to the interaction region. Effort focused on the transverse diagnostic for much of the experimental campaign due to the desire to probe long plasma channels while performing guiding runs. However, due to the difficulties that will be explored below, effort shifted towards data taking

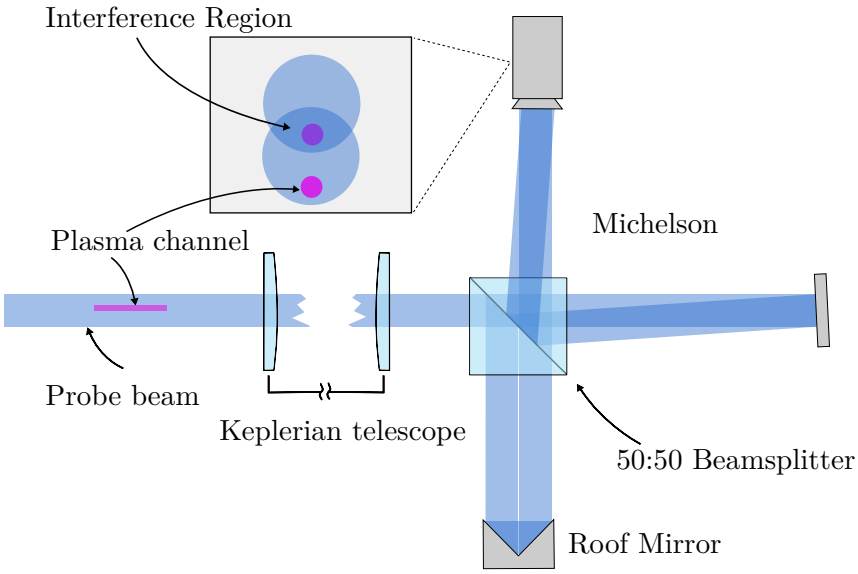

Figure 5.14: Schematic of a folded wavefront interferometer in a novel Michelson configuration performing longitudinal interferometry on a plasma structure. Also shown is a schematic diagram of the beam overlap in the CMOS sensor plane.

with the longitudinal interferometer towards the end of the experimental campaign.

Longitudinal Interferometry

Using the longitudinal interferometry diagnostic, repeatable and clear axicon-formed plasma channels were observed for the case of a hydrogen gas target. Due to probe refraction effects it was difficult to reliably extract phase profiles for the channels at early times, however, it was possible to probe the channels after about 1 ns of evolution. The longitudinal interferometry data was taken with a reduced cell length, between 2 mm and 4 mm.

Figure 5.15 shows an example fringe pattern and retrieved density profile from the longitudinal interferometry measurements. In this case, a HOFI plasma channel was formed in 80 mbar of hydrogen and probed 1.5 ns after ionization. A channel is clearly visible, with an on-axis density of $9.5 \times 10^{17}\,\mathrm{cm}^{-3}$. The plasma channel in this case exhibits a clear rotational asymmetry, with a large lobe of plasma visible to bottom of the feature. However, close to the center, the channel remains approximately rotationally symmetric.

The asymmetry evident in figure 5.15 was observed in both the longitudinal and transverse phase maps, particularly at early times. It is thought to arise from the asymmetry in the axicon focus due to a non-uniform near field profile of the channel-forming beam, as seen in

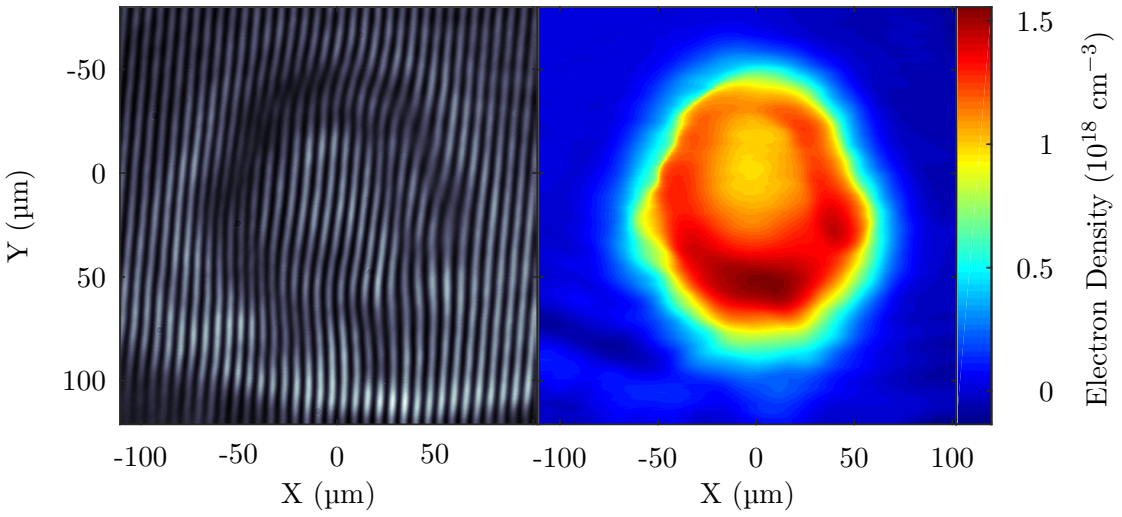

Figure 5.15: Fringe pattern recorded on the longitudinal interferometer from a typical data shot together with its analyzed density map showing a plasma channel. In the image shown, H_2 was used at a backing pressure of 80 mbar and probed 1.5 ns after ionization in a cell of length 4 mm.

figure 5.4. Indeed, looking back to figure 5.4, it can be seen that the axicon focus is asymmetric with reduced quality in the vertical dimension. It is believed that this poor quality causes extra ionization in the vertical dimension producing an asymmetric plasma column which subsequently expands asymmetrically.

This asymmetry in the initial plasma column causes a number of issues with accurate density retrieval from the transverse phase maps. However, for the longitudinal interferograms, transverse asymmetry does not pose a problem.

At later times the profile starts to become more symmetric although still maintains a degree asymmetry. This can be seen in figure 5.16 in which a HOFI plasma channel was formed in 80 mbar of hydrogen and probed 2.5 ns after ionization. The on-axis density at this later stage in the expansion has dropped to $6.6 \times 10^{17}\,\mathrm{cm}^{-3}$.

To investigate the HOFI channels further with the longitudinal interferometry diagnostic, scans were performed to determine the variation of on-axis density and matched spot size with pressure. Figures 5.17 shows the results of two such scans, taken at 1.5 ns and 2.5 ns respectively. The top panel in the figure shows the on-axis density of the plasma channel as a function of pressure while the lower panel shows the calculated matched spot size as a function of pressure.

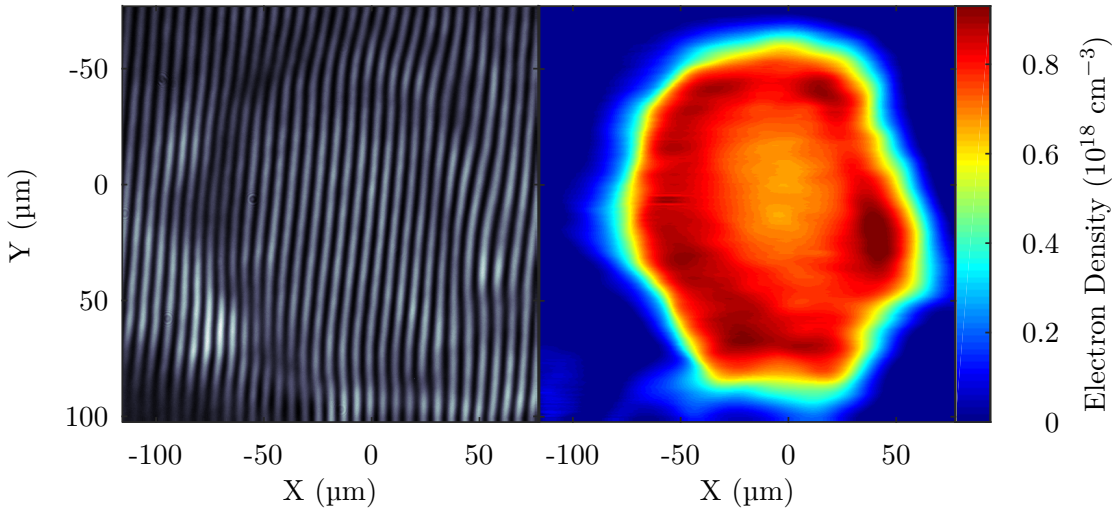

Figure 5.16: Fringe pattern recorded on the longitudinal interferometer from a typical data shot together with its analyzed density map showing a plasma channel. In the image shown, H_2 was used at a backing pressure of 80 mbar and probed 2.5 ns after ionization in a cell of length 4 mm.

The matched spots were calculated by rotationally averaging the density profile in a similar way to the analysis performed in chapter 3. While the density profiles were asymmetric far from the center of the channel, they were found to be quite symmetric close to the center of the channel, allowing for the rotational averaging technique to be used.

On-axis densities as low as $4 \times 10^{17}\,\mathrm{cm}^{-3}$ were found for a delay of 1.5 ns, with this extending down to less than $2 \times 10^{17}\,\mathrm{cm}^{-3}$ at 2.5 ns.

Transverse Interferometry

A significant amount of time was spent attempting to improve the transverse interferometry results and to ensure that they were as good as they could be. The efforts made in this regard certainly improved the ability of the diagnostic to produce low noise phase maps of the HOFI plasma channels. However, the observed asymmetry in the data caused problems in converting the measured phase maps into electron density profiles. At first it was thought that the asymmetry was simply a result of poor alignment or resolution. However, after seeing the same asymmetric feature repeatedly, day after day even after improving the optical setup and alignment procedures, it was accepted that the feature was likely real. In fact, it was this asymmetric data that prompted the group to revisit the longitudinal interferometry diagnostic

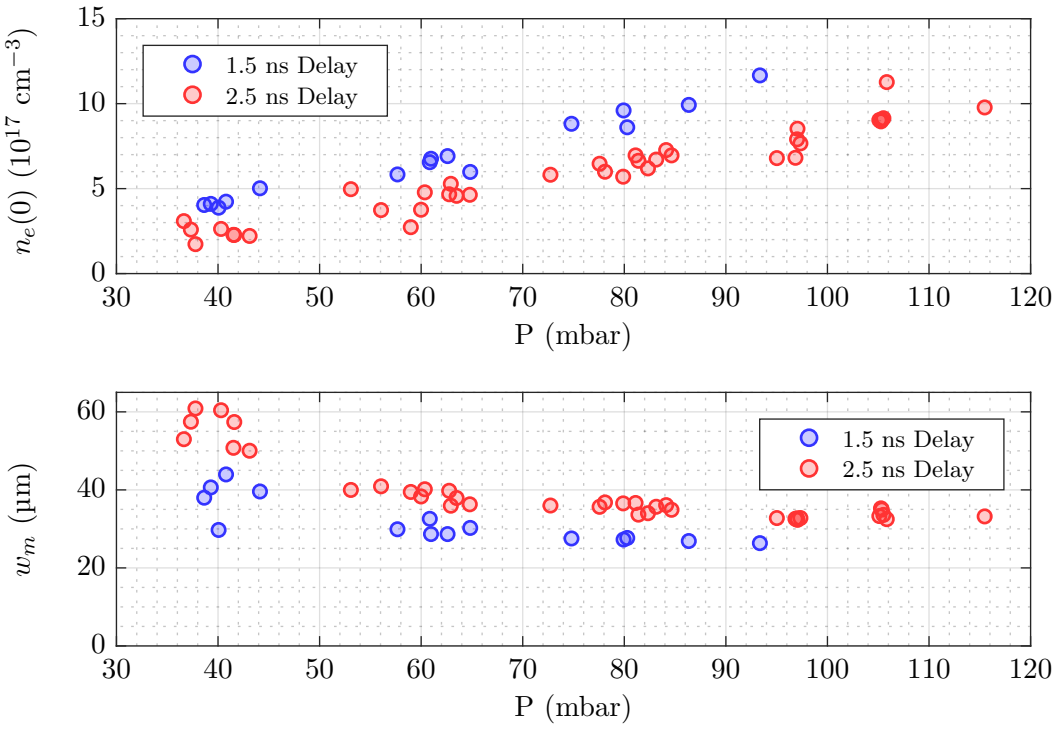

Figure 5.17: (Top) Measured variation with cell pressure of the on-axis density of the plasma channels measured 1.5 ns and 2.5 ns after ionization. (Bottom) Variation with pressure of the matched spot size of the lowest order mode, as deduced from parabolic fits to the electron density profile of the measured plasma channels. The cell length for these scans was 4 mm.

which until that point had been overlooked in the attempts to improve the transverse.

Figure 5.18 shows a comparison of two interferograms, one transverse and one longitudinal, taken under the same experimental conditions which both demonstrate the same asymmetry. For this comparison, a longitudinally averaged transverse phase lineout $\phi(y)$ from the transverse interferometer was compared with the $\phi(y)$ calculated by integrating, in the X-direction, the transverse phase map $\phi(x, y)$ obtained from the longitudinal interferometer. The good agreement in the shape of the phase profiles demonstrates that the two interferometers were set up well, and that the asymmetry in $\phi(y)$ was confirmed by the longitudinal diagnostic.

As discussed in section 2.7.6, an Abel inversion is required to extract an electron density from transverse phase maps. However, as was noted, it is imperative that the feature being inverted be symmetric. Several methods were explored to attempt to extract a reliable density profile from the asymmetric transverse data; good progress is being made in this direction,

but it is too early to report the outcome of that investigation in this thesis.

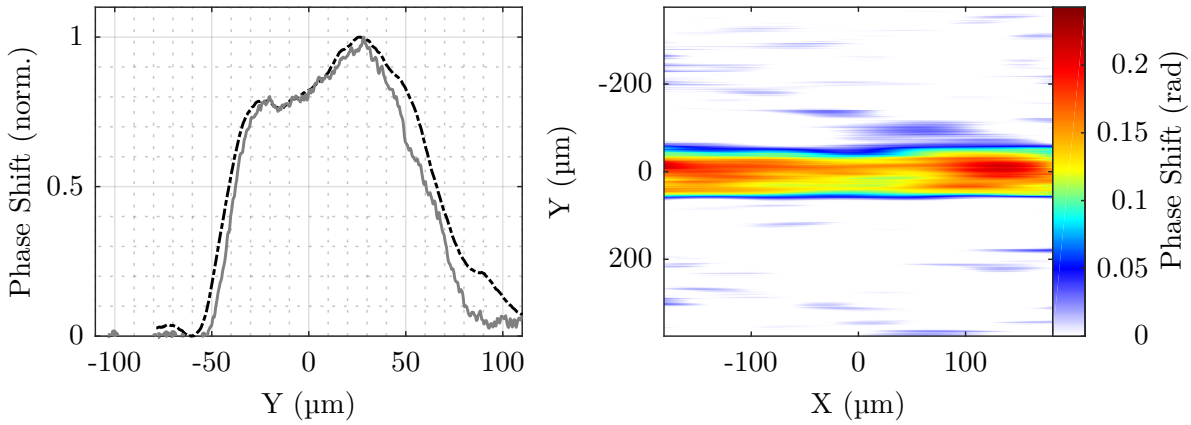

Figure 5.18: The left panel shows a longitudinally averaged phase lineout from the transverse interferometer (gray line) together with a phase lineout from the longitudinal interferometer (black dashed) which has been projected horizontally to simulate the effect of probing the plasma transversely. The two phase lineouts were taken under the same experimental conditions and both exhibit the same asymmetry. The transverse phase map from which the transverse lineout was retrieved is shown in the right hand panel.

5.7 High-Intensity, High-Repetition Rate Guiding

Figure 5.19 demonstrates the guiding of a high-intensity pulse over 16 mm or $\sim 14.5 z_R$ in a HOFI plasma channel. Panel (a) shows the focus of the unguided beam (measured with the gas cell removed); the peak intensity of the beam is $4.0 \times 10^{17}\,\mathrm{W\,cm^{-2}}$ ($a_0 = 0.43$). As the beam propagates away from focus it diffracts; 16 mm downstream of the focus the unguided beam has expanded to be larger than the camera chip, an estimate from Gaussian theory approximates the beam radius to 244 µm. The unguided beam is seen in panel (b). The intensity of a Gaussian beam $\sim 14.5 z_R$ back from focus would be approximately 211 times less intense (the value varies between 114 and 523 for $z_R = (1.1 \pm 0.4)$ mm); applying the pixel summation method, an average intensity hitting the sensor of $0.027 \times 10^{17}\,\mathrm{W\,cm^{-2}}$ is calculated, a reduction in intensity of a factor of ~ 150, i.e. within the expected range.

Figure 5.19 panel (c) shows a beam which has been coupled into the HOFI plasma channel and guided over 16 mm or $\sim 14.5 z_R$. The peak intensity of the guided beam is $1.76 \times 10^{17}\,\mathrm{W\,cm^{-2}}$ ($a_0 = 0.29$) and the spot appears very similar in both shape and size to the input beam (a detailed study of spot sizes will follow in the next sections.). The total

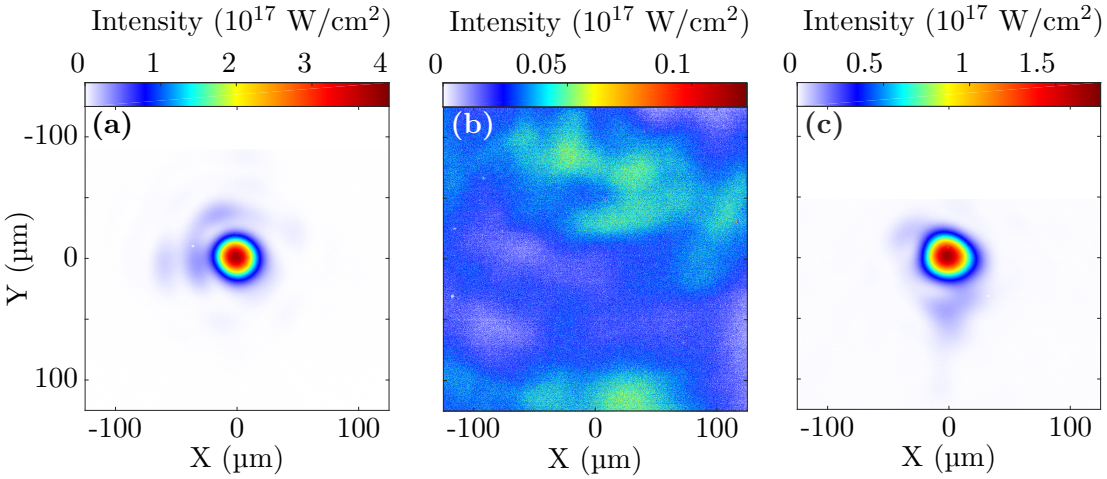

Figure 5.19: Demonstration of High-Intensity Guiding in a 16 mm HOFI plasma channel. The three panels show (a) the unguided beam at focus (b) the unguided beam 16 mm back from focus and (c) the guided beam after 16 mm of propagation in a HOFI plasma channel.

energy throughput in this case was determined to be 56 %.

The HOFI plasma channel used for this demonstration was formed in hydrogen. The high-intensity guided beam was delayed by $\tau = 1.5$ ns with respect to the channel-forming beam. The guided beam was injected into a plasma channel with an on-axis density of $\sim 6.5 \times 10^{17}\,\mathrm{cm}^{-3}$ as determined by longitudinal interferometry measurements (see section 5.6).

One of the main objectives of the experiment as detailed in section 4.1.2 was "Demonstration of both channel formation and guiding at the highest available repetition rate of 5 Hz". The motivation for this objective was not only to demonstrate high repetition rate[†] operation but also to show stability and repeatability at these high repetition rates. As the field of LPAs strives towards operation at higher repetition rates and towards use in applications, stability and repeatability are of paramount importance. Its important to present not just, the one 'exemplary' shot, but rather to present as much data as is possible. With this in mind, figure 5.20 (c) shows a waterfall plot of every single shot in a 485 shot run demonstrating the high-intensity, high-repetition rate operation of a HOFI plasma waveguide. Here, the transverse intensity profile of each transmitted beam was centered, horizontal and vertical lineouts were taken, and their average plotted along the Y-axis. The resulting waterfall map shows that the HOFI plasma channel can reliably guide the high-intensity beam.

[†]While 5 Hz operation would not be considered a high-repetition rate in many fields, it is considered high in the field of LPAs where typically systems operate from 0.01-10 Hz.

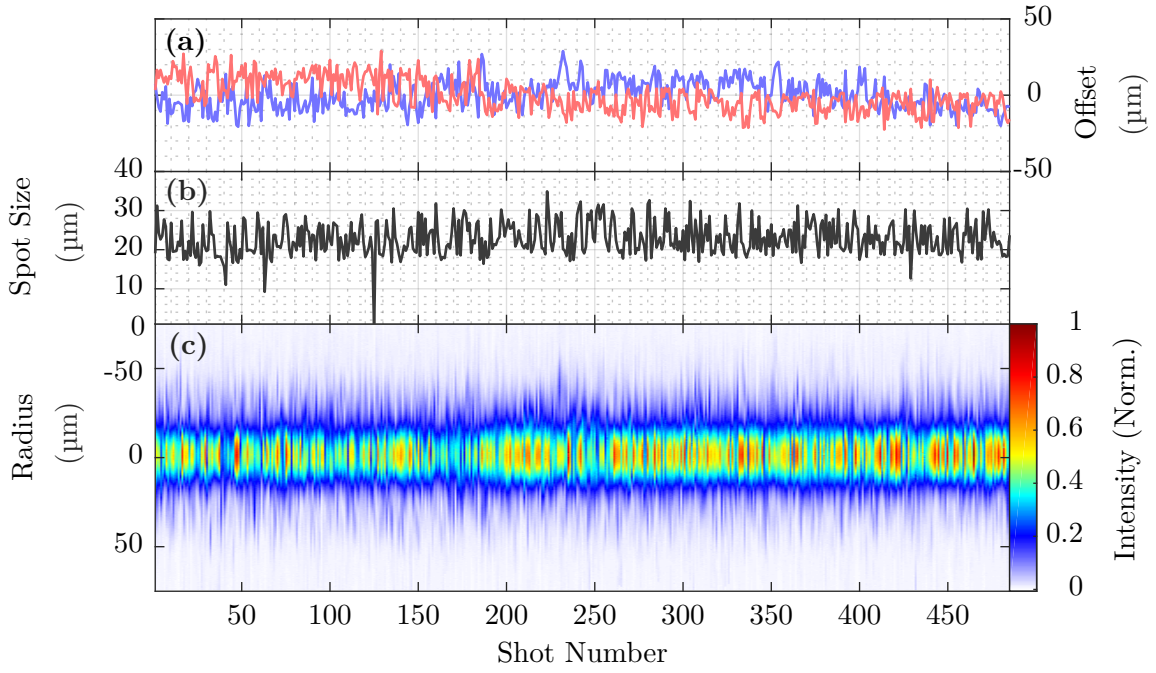

Figure 5.20: Results of a guiding stability run. In this run 485 consecutive shots were taken under the same experimental conditions to investigate the stability and repeatability of the guiding. Panel (a) shows the transverse jitter in the X-direction (red) and Y-direction (blue). Panel (b) shows the measured $1/e^2$ intensity spot size of the beam for each shot (average of major and minor axes of the D4σ measurement). Panel (c) shows a waterfall plot containing 485 lineouts (averaged along the horizontal and vertical directions of the spot profile) of the guided beam demonstrating the ability of HOFI plasma channels to guide high-intensity pulse repeatably. The data was recorded at a repetition rate of 5 Hz.

The data was taken at 5 Hz in a burst mode to help mitigate the gas load on the chamber; $\sim$ 12 shots were taken consecutively at 5 Hz, with the gas in free-flow, before the laser was shuttered and the gas was switched off. This allowed residual gas in the chamber to be pumped out. For this run, the set pressure was 80 mbar corresponding to an approximate on-axis density of $9 \times 10^{17}\,\mathrm{cm}^{-3}$.

The other sub-panels in figure 5.20 show the jitter and spot size of the beam and give an indication of the stability of the guiding. The standard deviation of the X- and Y-jitter are 10.5 µm and 9.5 µm respectively which is approximately a factor of 3 more than the guided beam alone. The spot size averaged over all shots was 22.75 µm approximately equal to the input spot size, however, whereas the unguided spot showed a shot-to-shot standard deviation

in spot size of $< 2\%$, in the guided case a variation of closer to 20 % is seen. This is thought to be due variations in coupling arising from both pointing fluctuations and ionization of neutral gas en-route to the waveguide entrance. It could also be compounded by small variations in the matched spot size due to fluctuations in the axicon-ionized column or its subsequent expansion.

5.7.1 Effect of Cell Fill-Pressure on the Guided Beam

As was observed in experiments with a lens in Oxford, section 3.4.2, and as was seen in section 5.6, there is general trend with increasing pressure and with decreasing temporal delay towards the formation of waveguides with smaller matched spot sizes. Keeping the temporal delay between the channel-forming and the guided beam fixed, it would be expected that changing the pressure would result in a resonance in peak intensity when the spot size of the guided beam matched the optimal matched spot of the channel. This is because waveguides with matched spots different than the guided beam would suffer from poor coupling into the fundamental mode of the channel.

To investigate this effect, cell fill-pressure pressure scans were performed. In these scans the fill-pressure of the cell was varied while monitoring the guided spot. Figure 5.21 and 5.22 show the results for pressure scans at a temporal delay between the channel-forming and guided beams of 1.5 ns and 2.5 ns respectively. Similar to figure 5.20, these scans have been presented as waterfall plots (panel (c)), however, in this case the x-axis of the waterfall plot has been converted to pressure and shots taken at the same pressure have been binned together. Above each of these waterfall plots are two line plots showing data points pertaining to (a) peak intensity of the guided beam and (b) the guided spot size. A Lorentzian curve has been fitted to the peak intensity data, the peak of which represents the optimum guiding pressure. A Lorentzian was chosen as the fitting function to attempt to capture the resonant behaviour in the peak intensity.

It can be seen that the optimum fill pressure, for a delay $\tau = 1.5$ ns, is 76 mbar; while for $\tau = 2.5$ ns the optimum pressure has shifted to 110 mbar. This is consistent with the expected behaviour of the channels. For a fixed guided spot size, it would be expected that later delays would require a higher pressure to produce a similar matched spot to channels formed at earlier

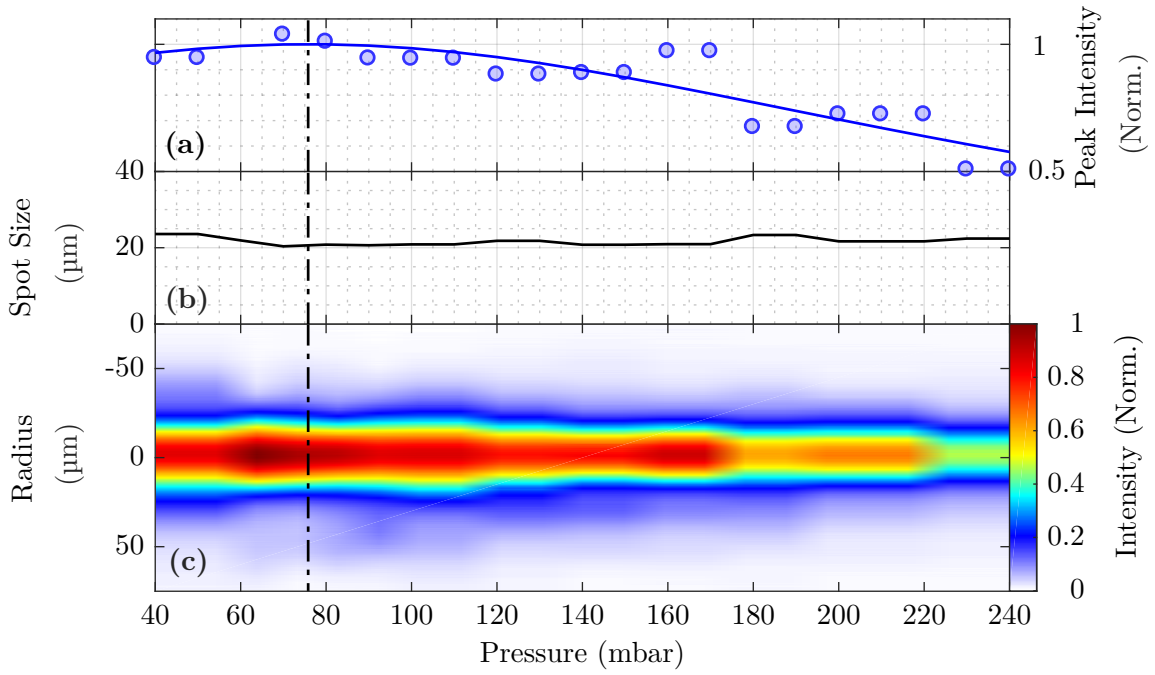

Figure 5.21: Variation of guided beam parameters with pressure at $\tau = 1.5$ ns. The results have been binned by pressure. The scatter data in panel (a) shows the peak intensity of the guided beam measured at the exit of the HOFI plasma channel, the solid blue line is a Lorentzian curve fit to the scatter data, showing a resonance in guided intensity at 76 mbar. Panel (b) shows the $1/e^2$ intensity spot size (averaged along major and minor axes of the D4σ measurement) of the guided beam at the exit of the channel while panel (c) shows a waterfall plot of the guided beam profile as a function of pressure.

delays. At 1.5 ns, no significant trend in the measured spot size is observed, whereas for 2.5 ns the guided beam spot size is minimized around the resonance location.

5.7.2 Energy Throughput

Using the pixel summation method described in section 2.6.3 it was possible to estimate not only the peak intensity of the guided spot but also the energy throughput. Further, at high-intensity it was possible to benchmark this pixel summation method against energy measurements made using the pyroelectric energy meter PEM, seen in figure 5.23. For these measurements, the cell was removed and the imaging stage driven to image the focus of the beam where a reference energy measurement was made (using both the pyroelectric energy meter and the pixel summation method). The cell was then driven back in and the imaging

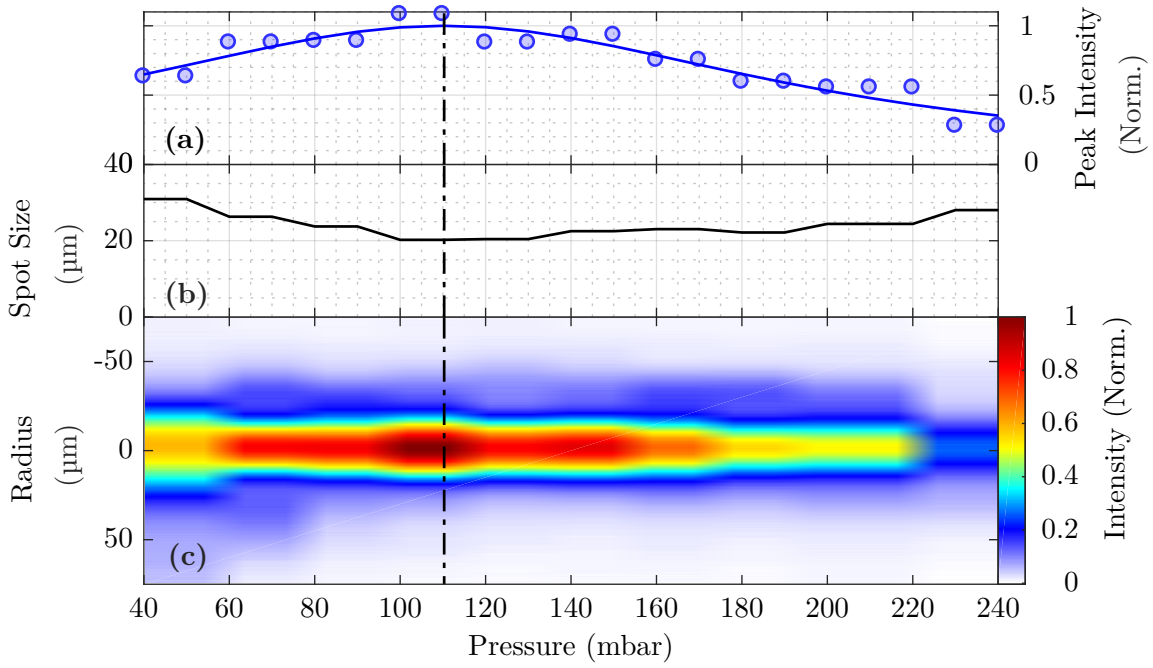

Figure 5.22: Variation of guided beam parameters with pressure at $\tau = 2.5\,\text{ns}$. The results have been binned by pressure. The scatter data in panel (a) shows the peak intensity of the guided beam measured at the exit of the HOFI plasma channel, the solid blue line is a Lorentzian curve fit to the scatter data, showing a resonance in guided intensity at 110 mbar. Panel (b) shows the $1/e^2$ intensity spot size (averaged along major and minor axes of the D4σ measurement) of the guided beam at the exit of the channel while panel (c) shows a waterfall plot of the guided beam profile as a function of pressure.

stage set to image the back of the plasma channel where the energy of the guided spot could be measured. Figure 5.23 shows the energy throughput, measured by both the pixel summation method and using the pyroelectric energy meter, for a pressure scan at 1.5 ns. Measured pressure data for the individual shots is not available for this run due to a pressure monitor failure, instead the shots are grouped together by pressure set point.

It is seen that the two measurements of energy throughput are in excellent agreement. While it was possible to measure the energy throughput at high-intensity with either the pyroelectric energy meter or the pixel summation method, measurements of energy throughput at low-intensity could only be measured with the pixel summation method as the energy leaving the chamber was too low to register on the pyroelectric energy meter.

Looking at total energy throughput of the guided beam as a function of pressure, figure

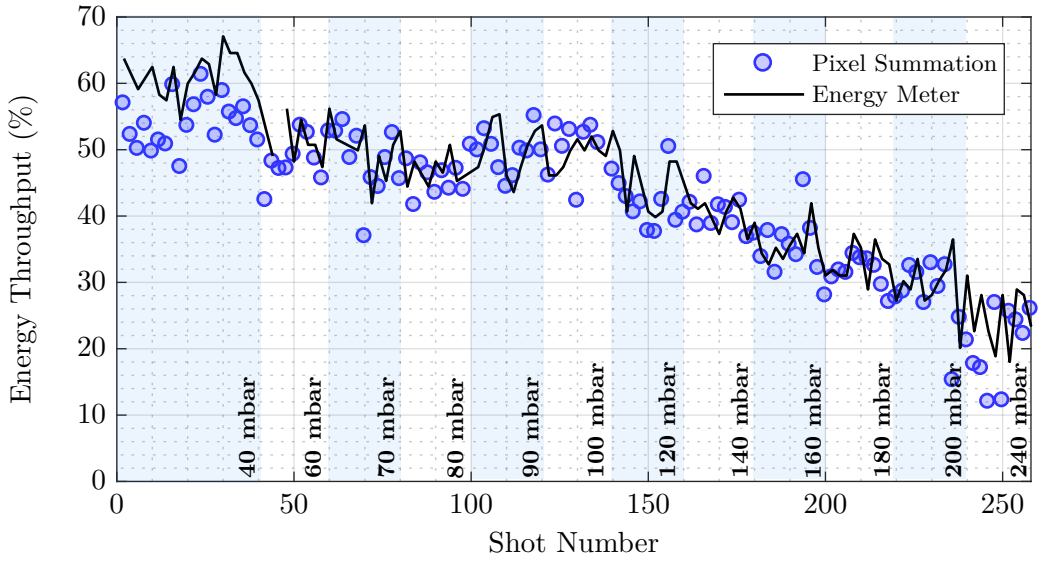

Figure 5.23: Guided energy throughput of the HOFI plasma channels as a function of shot number for a pressure scan in the range of $40 - 240$ mbar. The y-axis represents the energy throughput as the fraction of energy leaving the waveguide to energy incident upon the waveguide. The measurements were made at high-intensity using both a pixel summation method (scatter data) and a pyroelectric energy meter (black line). Shots taken at the same pressure set point are grouped together by the blue and white coloured bands.

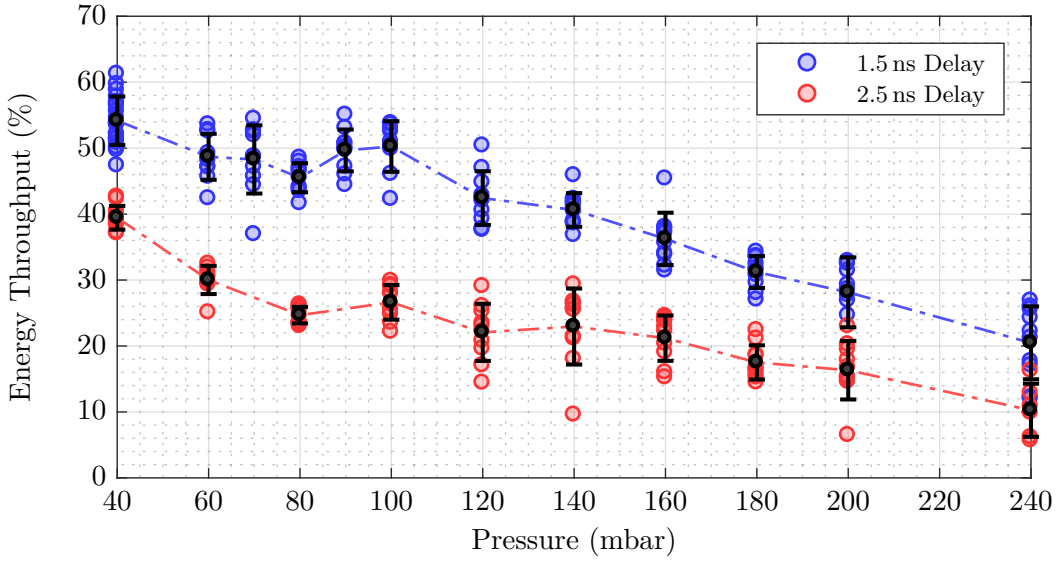

Figure 5.24: Guided energy throughput at high-intensity of the HOFI plasma channels as a function of pressure for two different temporal delays between the channel-forming and guided beam; 1.5 ns (blue data) and 2.5 ns (red data).

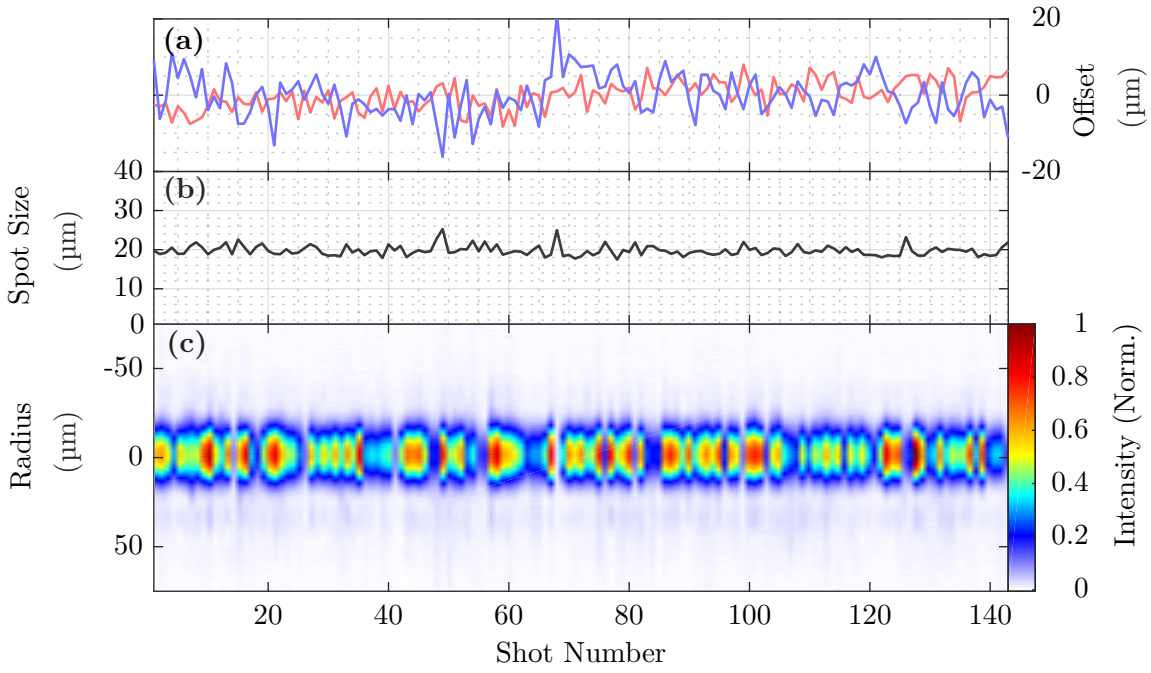

Figure 5.25: Results of a guiding stability run recorded at low-intensity. In this run 143 consecutive shots were taken under the same experimental conditions. Panel (a) shows the transverse jitter in the X-direction (red) and Y-direction (blue). Panel (b) shows the measured spot size of the beam for each shot (average of major and minor spot size). Panel (c) shows a waterfall plot containing a 143 lineouts (averaged along the horizontal and vertical directions of the spot profile) of the guided beam demonstrating the ability of HOFI plasma channels to guide low-intensity pulses. The data for this run was taken at an average repetition rate of 0.06 Hz in a cell of length 16 mm at a fill pressure of 140 mbar.

5.24, for the two temporal delays discussed above; 1.5 ns and 2.5 ns, it is seen that there is a general trend towards lower throughput at higher pressures. As the density increases, the matched spot size decreases and it is postulated that this leads to a larger fraction of the input beam being coupled into much higher order modes which have large losses. In addition, effects such as ionization induced refraction at the waveguide entrance, have a larger impact at higher fill pressures.

5.8 Comparison with Low-Intensity Guiding

The dynamics of guiding high- and low-intensity beams in hydrodynamic plasma waveguides can be quite different. For high-intensity beams, effects such as ionization induced refraction, wake-generation and self-focusing can modify the propagation and coupling of the beam significantly. For the case of the experiments described here, wake generation is expected to be relatively small (for LPAs), of order $10\,\mathrm{GV\,m^{-1}}$ for $a_0 \sim 0.5$ and the densities employed here. This corresponds to a 12 % peak density modulation and so the small change in refractive index induced by this modulation is not expected to greatly affect the guiding characteristics. There is also not expected to be a significant effect on beam dynamics due to self focusing as the peak power of the guided beam is $\sim 4\,\mathrm{TW}$ while the lower limit on the critical power (occurring for channels with the highest on-axis density of $\sim 10^{18}$ $\mathrm{cm^{-3}}$) is $\sim 30\,\mathrm{TW}$.

Thus it would be expected that the most significant cause for a change in guided beam dynamics would be due to ionization induced refraction, and indeed as shall be seen this is the case. There are two main ways in which ionization induced refraction can significantly affect the guided beam;

- The first, is during the coupling of the guided beam into the plasma waveguide; it has been shown previously that neutral gas near the entrance of a plasma waveguide can cause ionization induced refraction which leads to poor coupling into a plasma waveguide[174,175].

- The second area in which ionization induced refraction could modify the propagation of the guided beam is due to ionization during propagation within the plasma waveguide itself; this ionization can occur within the plasma channel if it is formed of a partially ionized plasma or the ionization could occur in the region of neutral gas outside the plasma waveguide from leakage fields of the guided pulse. As was discussed in section 2.2, hydrodynamic plasma channels form leaky waveguides; strictly speaking there are no bound modes, but rather only radiation and quasi-bound modes exist.

To investigate the effect of further ionization by the high-intensity guided beam, a set of data was taken with a low-intensity guided beam. The low-intensity guided beam was created by replacing the last guided beam mirror before IP, DM1, with a 3° optical quality fused silica

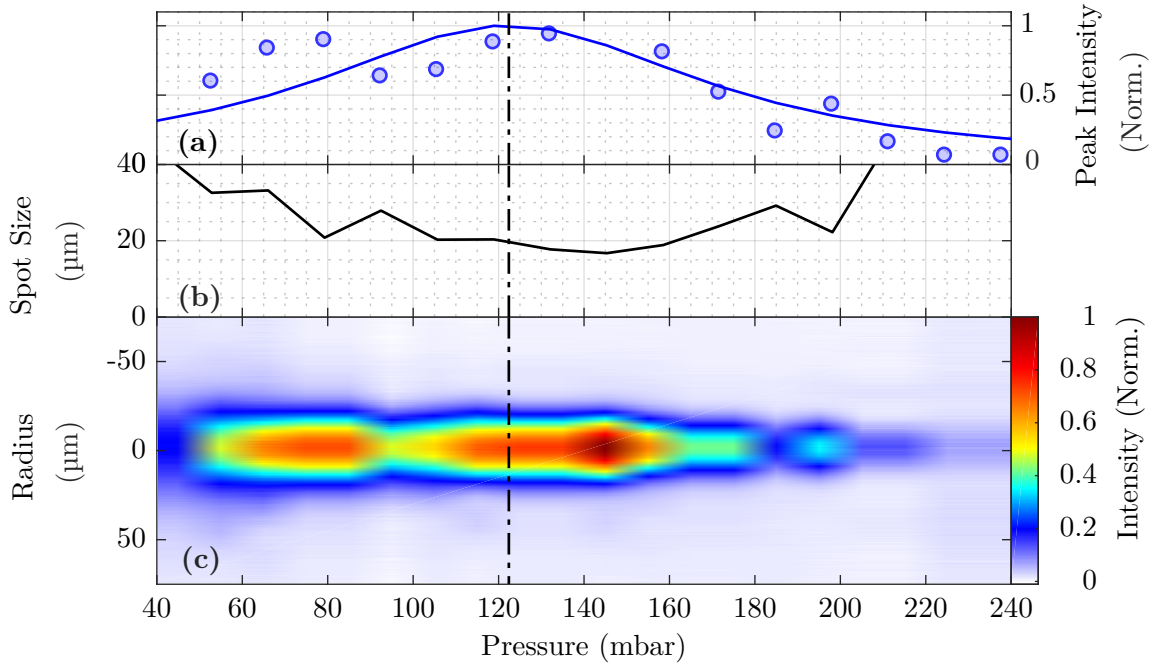

Figure 5.26: Variation of guided beam parameters with pressure at $\tau = 1.5\,\text{ns}$. The results shown in this figure were generated by guiding a low-intensity pulse and have been binned by pressure. The scatter data in panel (a) shows the peak intensity of the guided beam measured at the exit of the HOFI plasma channel, the solid blue line represents a Lorentzian curve fit to the scatter data demonstrating a resonance in guided intensity at 122.2 mbar. Panel (b) shows the spot size of the guided beam at the exit of the channel while panel (c) shows a waterfall plot of the guided beam profile as a function of pressure.

wedge. Aside from a reduction in energy, there was no change observed in the parameters of the unguided spot. At an angle of incidence of 45°, the reflectance of 800 nm p-polarized light is 0.0066[‡] and thus the peak of the low-intensity guided beam is estimated as $2.6 \times 10^{15}\,\text{W}\,\text{cm}^{-2}$. As this is still above the ionization threshold of hydrogen by approximately a factor of 6.5 it would be expected that the beam would not only ionize any partially ionized plasma in the channel, it would also ionize any residual neutral hydrogen within approximately 3 z_R of the waveguide entrance; this in contrast to the 10 z_R that would be expected for the high-intensity beam. Thus while the effect of poor coupling and ionization of partially ionized species within the waveguide may perhaps be slightly mitigated, it will remain an issue.

[‡]This is easily calculated using the Fresnel equations; in particular $R_p = (\tan(\theta_i - \theta_t)/\tan(\theta_i + \theta_t))^2$, where R_p is the reflectance of p-polarization, θ_i is the angle of incidence onto the material and θ_t is the angle of the transmitted beam, calculated using Snell's Law[176].

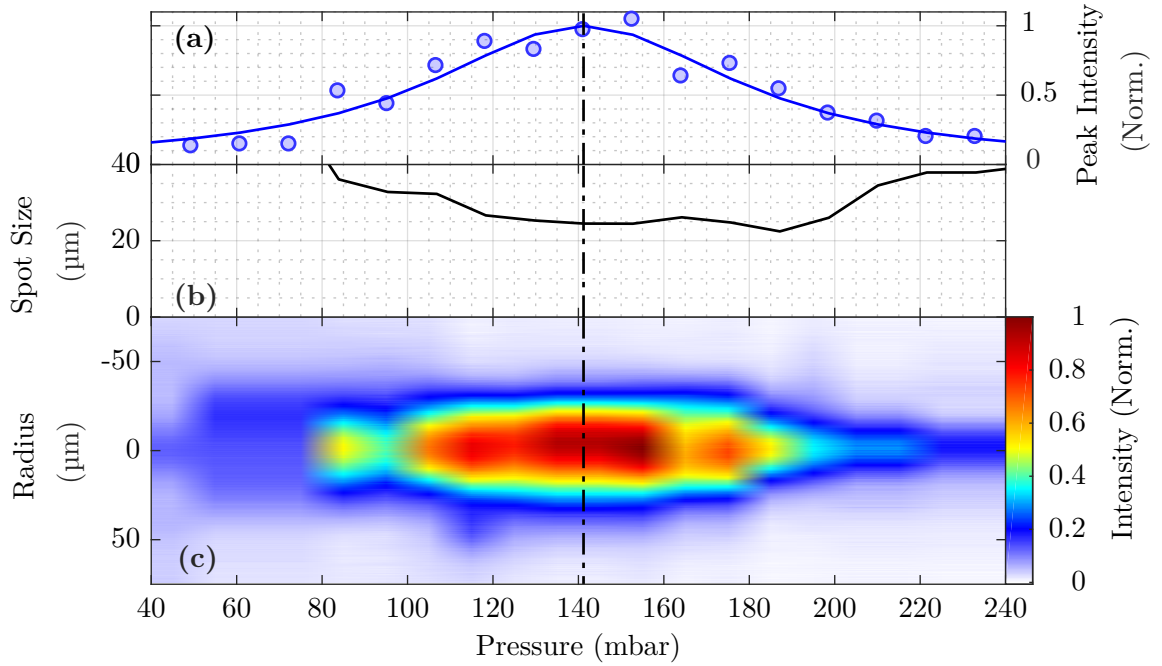

Figure 5.27: Variation of guided beam parameters with pressure at $\tau = 2.5\,\text{ns}$. The results shown in this figure were generated by guiding a low-intensity pulse and have been binned by pressure. The scatter data in panel (a) shows the peak intensity of the guided beam measured at the exit of the HOFI plasma channel, the solid blue line represents a Lorentzian curve fit to the scatter data demonstrating a resonance in guided intensity at 141.4 mbar. Panel (b) shows the spot size of the guided beam at the exit of the channel while panel (c) shows a waterfall plot of the guided beam profile as a function of pressure.

The real advantage of this regime of guided beam intensity is that ionization transversely outside the waveguide structure is eliminated. For the case of the low-intensity beam, the intensity will have dropped below the ionization threshold within a radius of $\omega_0 \approx 22\,\mu\text{m}$.

In the case of the low-intensity beam, consistent guiding was again observed in a 16 mm HOFI plasma channel, as can be seen in figure 5.25.

Scans in which the cell pressure was varied and the guided beam leaving the plasma channel was monitored were performed at $\tau = 1.5\,\text{ns}$ and $\tau = 2.5\,\text{ns}$. The results of these scans can be seen in figures 5.26 and 5.27. As with the high-intensity beam, there is evidence of a move towards higher optimum guided pressures at longer delay times. However, there are two key properties of these scans worth pointing out explicitly.

Firstly, there is a tighter resonance around the optimum guiding conditions; that is that

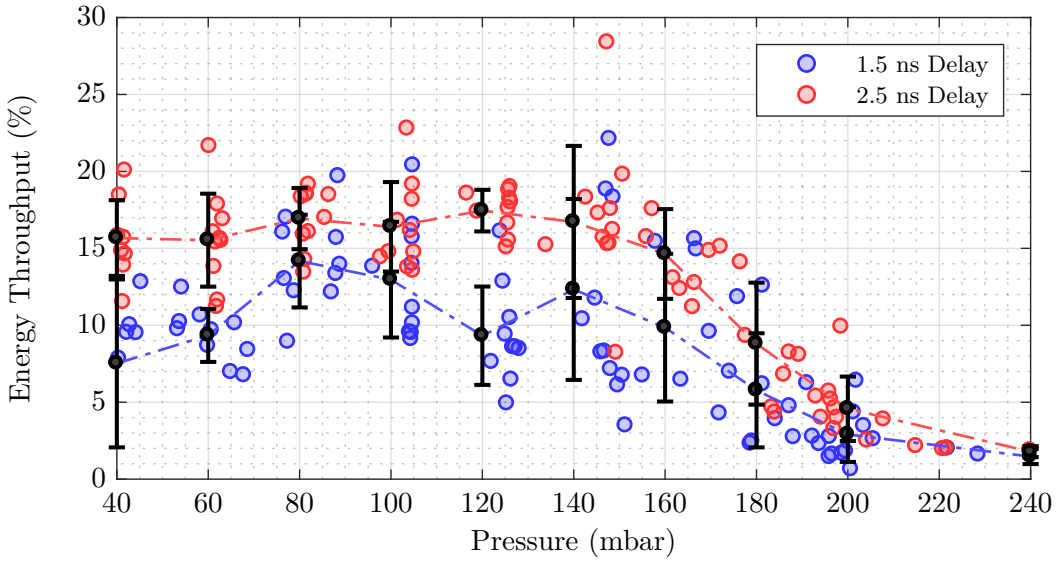

Figure 5.28: Guided energy throughput at low-intensity of the HOFI plasma channels as a function of pressure for two different temporal delays between the channel-forming and guided beam; 1.5 ns (blue data) and 2.5 ns (red data).

at lower intensity, the guided beam appears to be more sensitive to the cell fill pressure and thus to the channel parameters. Secondly, use of a lower intensity guided beam has increased the optimum cell pressure. In the case of data taken at 1.5 ns, the optimum guiding pressure has been raised from 76 mbar to 122 mbar, while at 2.5 ns it has been raised from 110 mbar to 141 mbar. Both of these results would indicate that either the higher intensity beam is modifying the transverse profile of the plasma channel in some way or that the coupling into the waveguide is significantly changed at higher intensities due to increased ionization-induced refraction. Indeed both effects could be playing a role.

Figure 5.28 shows the energy throughput for the pressure scans taken with the low-intensity guided beam at 1.5 ns and 2.5 ns. Immediately obvious is the reduced energy throughput compared to the throughput measurements with a high-intensity guided beam. Compared to the measurements at the optimum guiding conditions with the high-intensity beam showing 40 % - 60 % throughput, at low intensity maximum throughputs range from 15 % - 25 %. This could again be attributed to a difference in coupling between high- and low-intensity, to channel modification by the high-intensity pulse or both.

Guided Beam	X-Jitter	Y-Jitter	Spot Size	ΔE Throughput
High-Intensity	10.5 µm	9.5 µm	(22.8 ± 4.2) µm	19 %
Low-Intensity	3.6 µm	5.6 µm	(19.8 ± 1.3) µm	45 %

Table 5.1: Comparison of guided beam parameters for two stability runs, one with a low-intensity guided beam and one with a high-intensity guided beam.

5.8.1 A Note On Stability

As was presented earlier, figure 5.25 shows every shot from a 143 shot guiding stability run, in which the experimental parameters were kept the same and were optimal for the guiding of the low-intensity beam. This stability run differs from the high-intensity stability run presented earlier, figure 5.20, in two ways; firstly, for the guiding of a low-intensity beam the optimal fill pressure was 140 mbar rather than 80 mbar and secondly, this scan was not performed at 5 Hz but rather in a shot-on-demand fashion with an average repetition rate of 0.06 Hz.

Comparing the stability of the two runs it is found that; the jitter in transverse position of the beam (standard deviation of X- and Y-positions) is much lower for low-intensity beam, indeed the X-jitter is approximately the same as the unguided beam, while the Y-jitter is slightly larger (it is recalled that the X- and Y-jitter on the unguided beam was 3.2 µm and 3.1 µm respectively). Further, the spot size also remains more stable for the low-intensity case, with a standard deviation of 6.6 % approximately a factor of 3 higher than the unguided case, though a factor of 2.8 lower than the high-intensity guided case.

It is interesting to note, that while the low-intensity guided beam has reduced jitter and reduced variation in spot size over the course of the stability runs, the energy throughput and the stability in that throughput are poorer than the high-intensity beam. Not only does the high-intensity beam have a throughput more than twice that of the low-intensity beam, it reduces the variation in that energy throughput a factor of 2.3, from 45 % to 19 %. These results are summarized in table 5.1 and are clearly evident in figure 5.29. In this figure, both the high-intensity and low-intensity stability scans are shown, with their x-axes having the same scale, and importantly, with the shot-to-shot energy variation removed by normalizing the intensity profile of each spot in the waterfall plot. Panel (a) shows the high-intensity guided run, comprising 485 shots, while panel (b) shows the low-intensity guided run, comprising 143 shots. Panel (c) shows the variation in peak intensity as a function of shot number for both

runs.

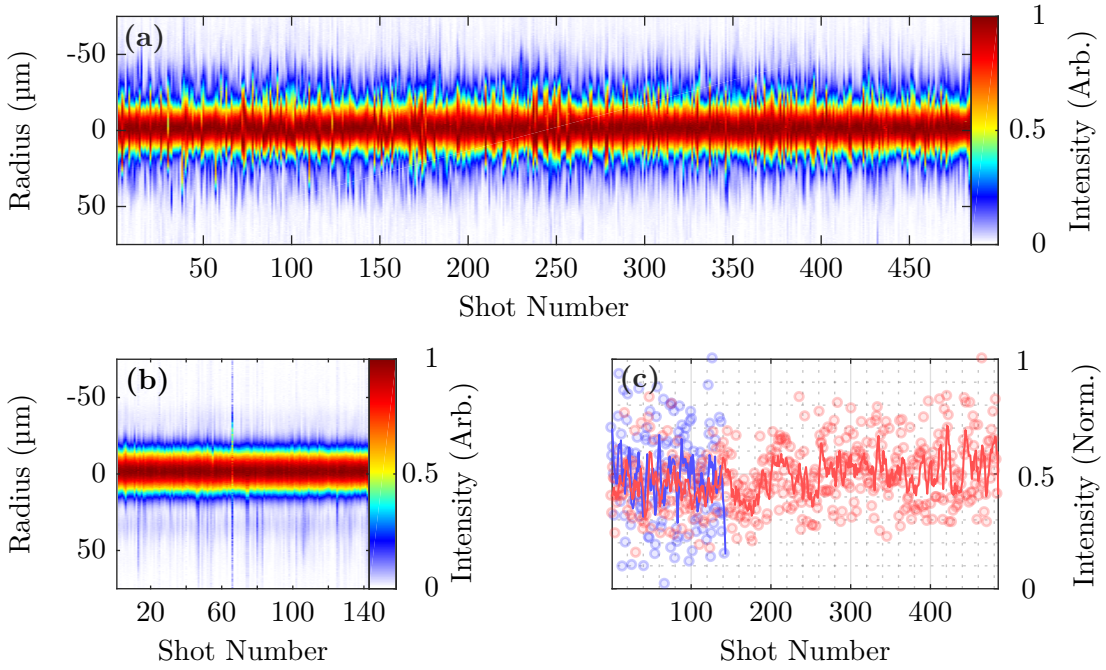

Figure 5.29: Comparison of guiding stability runs taken with both a high- and low-intensity guided beam. The waterfall data presented in panel (a) and (b) is the same as that presented in figure 5.20 and 5.25 respectively, but in this case the data has been presented with each vertical lineout normalized to its value on-axis to remove the effect of shot-to-shot variations in the guided intensity. Panel (c) shows the peak value of intensity to which each lineout was normalized (blue for the low-intensity run and red for the high-intensity run) to give a visual representation of the shot-to-shot variation in peak intensity. Both panel (a) and panel (b) have their x-axes on the same scale.

5.9 Modification of the Plasma Channel by the Guided Beam

The guiding results indicate that the axicon-formed HOFI plasma channels in these experiments might be modified by passage of the guided beam. Modification of the plasma channel can occur due to further ionization by the guided beam as it propagates through the channel. This further ionization can either occur in the center of the channel, if the plasma is not fully ionized, or in the region of neutral gas surrounding the plasma channel in the case of a high-intensity guided pulse. Thus analysis of the plasma channels before and after passage of

the guided beam can provide information on the ionization state of the plasma and on guiding dynamics at high-intensity.

5.9.1 Ionization State of the Initial Plasma Column

The axicon beam, having a peak intensity of approximately $5 \times 10^{15}\,\mathrm{W\,cm^{-2}}$ would be expected to fully ionize hydrogen (ionization threshold $\sim 4 \times 10^{14}\,\mathrm{W\,cm^{-2}}$). However, there are two issues which may prevent the full ionization. Firstly the axial intensity may be significantly different to that calculated by the pixel summation method due to chromatic aberrations in the axicon[§] or indeed other spatio-temporal couplings present in the beam. Secondly the critical density for grazing-incident rays is substantially lower than for normal incidence (section 2.5.2). Thus reflection from a local critical density surface may lead to a global ionization state lower than two (the fully ionized state of H_2).

To investigate the ionization state of the plasma column, longitudinal interferometry was used to inspect the plasma waveguide before and after passage of the high-intensity guided beam as shown in figure 5.30. Immediately obvious is the extra ionization outside the region of the original plasma channel with passage of the guided beam, confirming the conclusions made in the previous sections that the high-intensity beam is ionizing a region outside of the plasma waveguide; these results will be discussed in more detail in the next section.

Due to fringe bifurcations in the interferograms taken after passage of the high-intensity beam, it was not possible to convert the fringe pattern directly into transverse phase and electron density profiles. Instead single fringe tracking was employed. In this analysis a fringe passing through the plasma structure was tracked and compared with the same fringe in a reference shot to determine the amount of phase shift incurred at the center of the plasma channel. This method was performed by hand, and while slow, it was capable of producing phase shifts similar to those garnered from the usual Fourier based fringe analysis methods for the case of phase maps without fringe bifurcations. Figure 5.30 gives a visual representation of the tracking procedure; the red line represents the path of the fringe without plasma. The fringe deviation from the red line indicates a local phase shift.

Using this technique several sets of interferograms before and after the passage of the

[§]The axicon used in these experiments, being a refractive optic, was highly susceptible to chromatic aberrations.

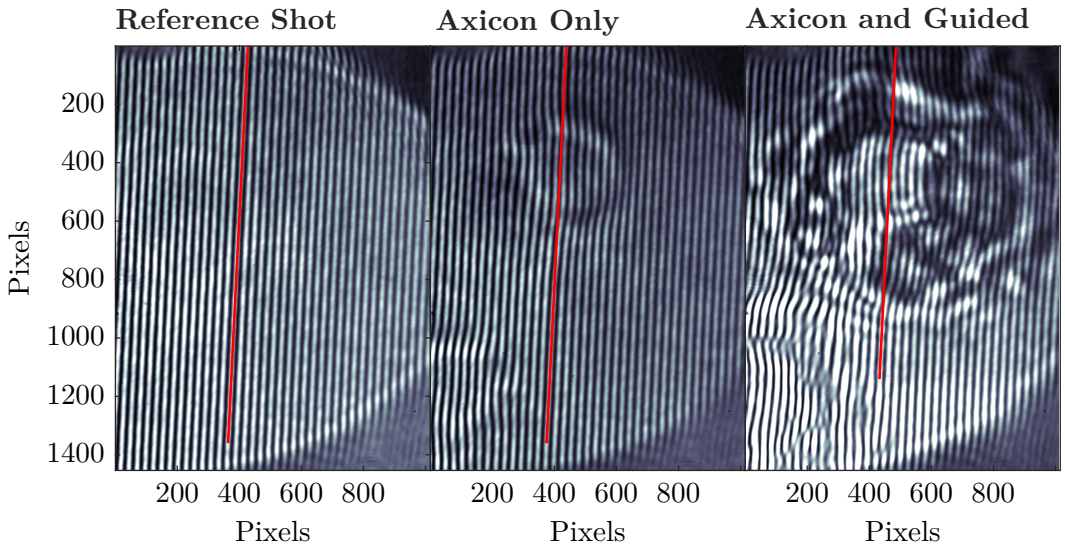

Figure 5.30: Interferograms showing the extra ionization introduced by passage of the guided beam through the HOFI plasma channel. The red line indicates the path of a fringe in the absence of plasma; by tracking the path of the fringe and measuring its deviation from the red line, phase shifts can be extracted.

high-intensity guided beam, were analyzed and the fringe shifts compared. It was found that typically the fringe shift at the center of plasma channel increased with passage of the guided beam, suggesting that the plasma channel might not be fully ionized. An ionization state of $Z = 1.6$ was extracted from the calculations which would imply that approximately 60 % of the H_2 was fully ionized while 40 % was singly ionized. It would be expected that any remaining singly ionized hydrogen would be fully ionized by the leading edge of the guided pulse. This would cause the on-axis density of the plasma channels to increase by 25 %.

It should be noted that this measurement does not take into account any effects of a gas ramp on the way in to, and out of, the gas cell. Gas ramps increase the complexity of the problem and require careful treatment. As the gas pressure drops in the ramp, critical density effects for axicon plasma formation, which may be present in the bulk of the cell, would be mitigated. Thus the ionization state in the ramps may be different to that in the bulk of the cell. If the plasma is fully ionized in the ramp but partially ionized in the bulk of the cell, this method would provide an overestimate of the ionization state.

If it were not for the asymmetry in the plasma structure, the transverse interferometer may have been able to provide a better estimate of the on-axis density before and after the

passage of the high-intensity guided beam, and thus the ionization state of the plasma. Further analysis of the current experimental data, both longitudinal and transverse, will be required to fully determine the ionization state although it was not possible to perform these analyses on the timescale of submission of this thesis.

5.9.2 Plasma Waveguide Enhancement

Figure 5.31 shows phase maps recorded as the guided beam passes the field of view of the transverse interferometer, which was close to the front pinhole of the gas cell. In these the beam is traveling from right to left and the leading edge of the guided beam is approximately half way across the panel. The top-left panel shows the guided beam alone with no channel-forming beam, and thus no HOFI channel, while the bottom-left panel shows the phase measured when both the guided and channel-forming beam were present. The channel-forming beam was fired 1.5 ns before the guided beam and thus it is possible to see the HOFI channel extending out in front of the guided beam.

As can clearly be seen in the lower panel, there is significant ionization outside the waveguide due to leakage fields, this a direct observation of what had been postulated in section 5.8.

This transverse interferometry, together with the observed improvement in guiding at high-intensity can be explained by the model illustrated schematically on the right of figure 5.31. For simplicity, let us suppose that the initial plasma column generated by the channel-forming beam is fully ionized. The top-right panel depicts this situation; a thin column of hydrogen plasma (blue shaded region), with an electron density equal to twice the initial neutral H_2 fill density is ionized. Outside the channel, neutral hydrogen (gray shaded region) remains at the fill density.

After a sufficient amount of time, say 1.5 ns, this column of hot plasma has expanded radially outwards into the cold surrounding gas, driving a shockwave and creating a HOFI plasma channel as can be seen in the middle panel. In the process of channel formation, the neutral hydrogen surrounding the channel has been driven outwards by the hydrodynamic pressure of the shock expansion. In the schematic, the neutral hydrogen remains at the fill pressure, although it may also rise slightly due to compression as the plasma shocks outwards. It is at this point that the high-intensity guiding beam (red shaded region) is injected.

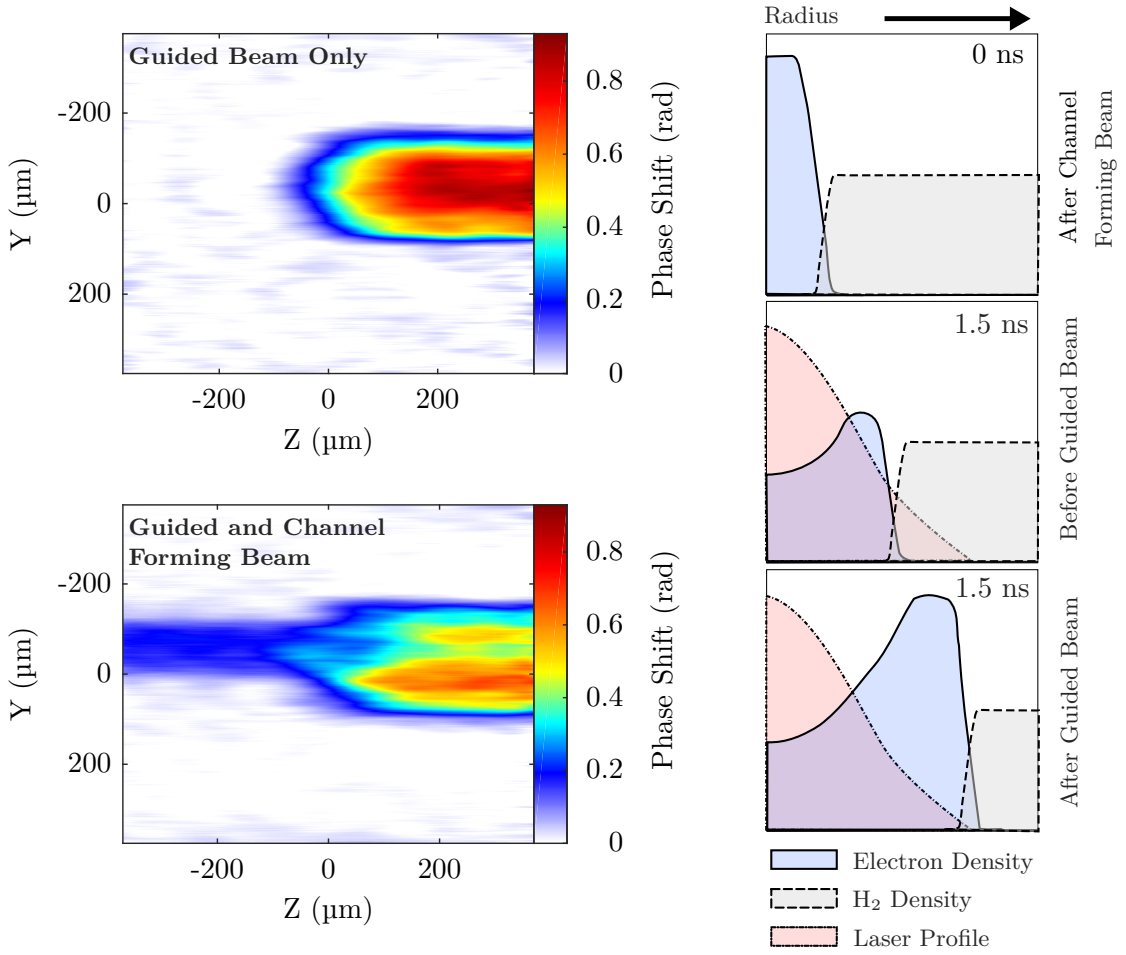

Figure 5.31: Left: Phase maps taken with the transverse interferometer as the guided beam passes the field of view. In the top panel, the guided beam is seen passing through the neutral hydrogen alone, while in the bottom panel the guided beam is propagating within a HOFI plasma channel ionized 1.5 ns in advance of the arrival of the guided beam. The three panels on the right represent a hypothesis to explain the improved guiding at high intensity, based upon the experimental data shown on the left.

When the guided beam is introduced, leakage of the guided mode through the wall of the channel can lead to ionization of an annulus of surrounding neutral gas. This can have two effects; (i) an increase in thickness of the walls of the channel, leading to reduced loss; and (ii) an increase in the wall height, leading to a reduction in the matched spot size. This situation is depicted in the bottom-right pane.

As this is a simple hypothesis, further experimental and computational tests will need to be performed to confirm the HOFI channel enhancement by the high-intensity guiding pulse. This would however explain the guiding properties observed in sections 5.7 and 5.8, namely,

the improved throughput and the reduction in optimum cell pressure for guiding; the extra ionization and waveguide enhancement could easily change the matched spot size of the HOFI channel in addition to increasing the attenuation length.

If the hypothesis does prove to be true, then there is ample opportunity for experiments in which a HOFI channel is first formed by an axicon and subsequently deepened by a pre-pulse to the main high-intensity guided beam. This extra degree of control could be highly beneficial to the generation of low-density gradient-index plasma waveguides; other groups working with gradient-index plasma waveguides have noted that control over the depth of the channel can be difficult to achieve[177]. For the case of capillary discharge waveguides, one method of overcoming this leakage is to guide a long ns heater pulse to heat the plasma waveguides and deepen the channel[178]. With HOFI channels the opposite approach could be taken, rather than trying to deepen the plasma channel to increase the attenuation length, the HOFI channels, which can already be formed with low-on axis densities suitable for high-energy LPAs, could simply have the wall of the channel thickened and raised to provide the necessary increase in attenuation length.

5.10 Conclusions & Further Work

In this chapter the implementation of the experiment and the measurement of key experimental parameters have been described. In addition, a detailed description of the plasma channel probing diagnostics and the gas cell used were given. Results were presented demonstrating for the first time, axicon-formed HOFI plasma channels. Further, the first results pertaining to high-repetition rate, high-intensity guiding in axicon-formed HOFI plasma channels were presented.

HOFI plasma channels up to 16 mm in length were formed in hydrogen. On-axis densities, measured for short channels, fell as low as $2 \times 10^{17}\,\mathrm{cm}^{-3}$ with delays between the channel-forming and guided beams of up to 2.5 ns. Matched spot sizes varied between 20 µm and 60 µm. Plasma channel formation was efficient, requiring laser pulse energies of only $0.5\,\mathrm{mJ\,mm}^{-1}$ to $0.84\,\mathrm{mJ\,mm}^{-1}$, more than an order of magnitude less than was found in chapter 4 for lens formed HOFI channels.

The data suggests that the plasma may not have been fully ionized, with an estimate of $Z = 1.6$ extracted from analysis of longitudinal interferograms taken before and after passage of the high-intensity guided beam. However, there was no significant degradation observed in guided beam quality due to full ionization of a partially ionized plasma channel. More analysis, and potentially more experimental investigation will be required to fully determine the ionization state of the axicon-formed HOFI plasma channels.

As expected, probing the plasma channels transversely was challenging. While the transverse diagnostic proved capable of measuring milliradian level phase shifts, extracting density information from the transverse interferograms by straightforward application of an Abel transform was complicated by the initial plasma column being azimuthally asymmetric. This asymmetry was confirmed by longitudinal probing. The asymmetry was thought to arise from an asymmetric near field profile in the channel-forming beam.

Both high- and low-intensity guiding was observed in the 16 mm HOFI plasma channels, representing guiding over approximately $14.5 z_R$. Guiding stability scans were performed for both the high- and low-intensity beams with stable repeatable guiding observed for both intensity regimes; improved throughput up to a maximum of ~ 60 % was seen at high intensity, while superior stability including reduced transverse spatial jitter and reduced variation in the measured spot size were observed at low-intensity.

By combining the guiding results together with interferometry results, it was possible to form a hypothesis as to the reason for increased throughput at high-intensity. It was postulated that the high-intensity beam enhanced the plasma waveguide by ionizing the neutral gas outside with waveguide. This is thought to increase the thickness and density of the walls of the waveguide thus increasing its ability to confine light. Further work is required to understand the guiding dynamics at high-intensity and the observed modification to the plasma channel.

In this work, the length of the plasma channel was limited by the gas cell design. An attempt was made to produce longer plasma channels, but ultimately it was unsuccessful due to the interaction of the channel-forming beam with the thin window of the long gas cell. More work will be required to develop new plasma sources capable of facilitating long HOFI plasma channel formation at high-repetition rates for extended periods, but the work presented in this chapter is a very promising starting point.

Chapter 6

Conclusions

In this thesis the concept of a low-density hydrodynamic optical-field-ionized or HOFI plasma waveguide has been introduced and experimentally developed. The key findings are reviewed here together with prospects for future work.

6.1 Summary and Conclusions

In the introduction, plasma waveguides for the next generation of LPAs were discussed, with four desirable properties being identified; **(i)** the possibility for extended duration operation at high-repetition rate without damage to the waveguide structure; **(ii)** the capability to operate at low plasma densities of order 10^{17} cm^{-3}; **(iii)** the capability of guiding high-intensity laser pulses over 100s of millimeters; and **(iv)** compatibility with wakefield acceleration in the quasilinear regime.

HOFI plasma channels were introduced in chapters 1 and 2 as a waveguide capable of meeting these challenging requirements. HOFI plasma channels are a form of hydrodynamic plasma waveguide in which the ionization and heating of plasma electrons is performed by optical-field-ionization. Once ionized, this hot column of plasma expands outwards driving a radial shockwave as it does so. After a sufficient amount of time, the high-density plasma in the shock, together with the low-density plasma on-axis act as a gradient-index plasma waveguide.

This technique differs from other hydrodynamic plasma waveguides in that it makes use

of optical-field-ionization and heating rather than collisional ionization and heating. Optical-field-ionization, an atomic process, is capable of heating plasma electrons independent of the plasma density and so can form low-density plasma columns which can subsequently expand into low-density plasma channels. This is in contrast to collisional ionization and heating, upon which hydrodynamic plasma waveguides typically rely, in which an initially high plasma density is necessary to facilitate the the heating process.

HOFI plasma channels differ from capillary-based plasma waveguides in that they can be formed without the need for an external structure. This is particularly advantageous for the operation of high-energy LPAs at high-repetition rates. If a HOFI waveguide gets destroyed or damaged due to excess energy in the plasma or due to a mis-fired shot, it can simply be reformed on the next shot without sustaining lasting damage.

In chapter 2 the theory of both grazing-incidence and gradient-refractive index plasma waveguides were discussed. HOFI waveguides were introduced, and a discussion of the ionization and heating mechanism and expansion dynamics followed. A beam propagation code used to simulate the probing of plasma channels was developed by the author and also discussed in this chapter. The generation of long HOFI plasma channels requires the use of an optic capable of forming a line focus, such as an axicon. Thus theory pertaining to axicons and plasma formation by axicons was presented. Finally experimental methods, including focal spot characterization and interferometry were reviewed.

In chapter 3, the first proof of concept experimental demonstration of low-density HOFI plasma channels was presented. This experiment was performed using the Oxford TW laser in early 2017. In this experiment, short (2 mm to 4 mm long) fully-ionized HOFI plasma channels were formed in hydrogen using a spherical lens. The channels expanded over the course of a few nanoseconds and their expansion dynamics were well described by Sedov-Taylor blast wave theory. Channels with on-axis densities as low as $1.6 \times 10^{17}\,\mathrm{cm}^{-3}$ were observed and a computational and analytic investigation into the guiding properties of the measured electron density profiles showed matched spot sizes in the range 30 µm to 60 µm and $1/e$ attenuation lengths of order 100 mm.

This work constituted the first experimental verification that the production of low-density ($\sim 10^{17}\ \mathrm{cm}^{-3}$) plasma channels was possible by the hydrodynamic expansion of a laser-heated

plasma. The on-axis densities in this experiment were almost an order of magnitude lower than had been previously demonstrated in a hydrodynamic plasma channel. Further, the experimental results helped to benchmark simulation work which up to that point had been difficult to rely on due to a variety of bugs encountered in the codes. The results were published and successfully used to help bolster an application for beamtime at the Central Laser Facility, UK, to attempt an experiment which formed the basis of chapters 4 and 5.

Following on from the success of the Oxford experiments, it was desired to further develop the concept of HOFI plasma waveguides. In this context, an experiment was designed to demonstrate the formation of long, low-density HOFI waveguides formed by an axicon. Further, it was desired that high-intensity guiding in such HOFI waveguides be demonstrated at the highest available repetition-rate. The use of an axicon presented several challenges to the experimental design which were reviewed in chapter 4. Chapter 4 also detailed the experimental design process undertaken, including; design of the focusing geometry and gas cell. The experimental layout implemented was also discussed in detail.

Chapter 5 detailed the implementation of the experiment, which took place in 2018 at Astra-Gemini TA2. Measurements of the key parameters were presented along with the experimental results and discussion. In this work, 16 mm long axicon-formed HOFI plasma waveguides were generated with as little as 0.5 mJ of laser energy required per millimeter of channel formed. High-intensity guiding was demonstrated at 5 Hz over the full length of these waveguides, constituting high-intensity guiding over ~ 14.5 Rayleigh ranges. The channels were probed both longitudinally and transversely. Longitudinal measurements showed on-axis densities as low as $2 \times 10^{17}\,\mathrm{cm}^{-3}$ and matched spot sizes of 20 µm to 60 µm. An asymmetry was observed in both the longitudinal and transverse phase profiles which was attributed to the near-field profile of the Astra-Gemini beam and made extracting density information from the transverse interferometry difficult. The data suggests that the plasma may not have been fully ionized, with an estimate for the ionization state giving $Z = 1.6$. However, any additional on-axis ionization did not appear to hamper the ability of these plasma channels to act as waveguides for high-intensity laser pulses.

Repeatable guiding was observed at both low-and high-intensity. At high-intensity there was increased energy throughput up to approximately 60 % accompanied by a reduction in

the stability of the guided beam, when compared to the low-intensity guiding results. It was hypothesized that the improved throughput arose from modifications to the plasma waveguide structure by leakage fields of the guided pulse. This was observed experimentally using the transverse interferometry diagnostic.

These results constitute the first demonstration of axicon-formed HOFI plasma channels and the first demonstration of high-intensity guiding in a hydrodynamic plasma channel heated by optical-field-ionization. Thus, they represent an important step forward in the development of HOFI plasma channels as waveguides for the next generation of high-energy LPAs.

6.2 Future Work

While excellent progress has been made in the development of HOFI plasma waveguides, there is still work to be done to demonstrate that HOFI waveguides can provide a viable alternative to current guiding technology. In this section, future work is discussed which, in the author's opinion, is required to help further develop HOFI plasma waveguides.

Ionization and heating of the plasma, are key steps in the formation of a HOFI waveguide. As such, it is important to understand the experimentally measured or inferred parameters relating to these steps in the context of the theory. In chapter 3, there was a discrepancy between the electron temperature inferred from experiments and that calculated theoretically. Additionally, in chapter 5 it was noted that the axicon-formed plasma waveguides may not have been fully ionized. While neither one of these matters were an issue for the experiments presented in this thesis, further analysis, investigation and more detailed measurements of the initial plasma column are required to identify the ionization state and to understand the heating process in more detail.

In this thesis, HOFI waveguides were formed solely in hydrogen with 800 nm channel-forming pulses. Future experiments should aim to investigate the variation in waveguide formation with other species and other driver wavelengths. Heavier elements, while more difficult to fully ionize, can produce far hotter electrons and thus should produce stronger shocks which could aid waveguide formation. As was shown for axicon plasmas in chapter 4, the plasma energy per unit length of channel also scales linearly with driver wavelength.

Formation of plasma channels with far-infra red pulses, with wavelengths of a few microns, could therefore be highly beneficial.

Measuring the electron density profile of low-density lens- and axicon-formed HOFI waveguides presents a challenge for current diagnostic techniques. As such, the development of new and more sensitive methods of characterizing such profiles would aid in the continued advancement of these waveguides.

As was seen in chapter 5, the passage of the high-intensity guided beam modified the channel structure favourably to increase energy throughput. A hypothesis was presented to explain the observed phenomenon, however, further experimental and simulation work will be required to determine if this hypothesis is correct and to fully understand the dynamics at play.

The development of a long plasma source suitable for HOFI plasma channel operation at high-repetition rates was discussed in chapters 4 and 5. As was noted, more work is needed to further develop this concept and this remains an active area of research within the Oxford group. Indeed this development would be highly beneficial to the acceleration of electrons in HOFI plasma waveguides, which of course is next logical step forward for demonstrating the viability of HOFI plasma channels as waveguides for the next generation of LPAs. This will be the subject of future work.

The development of HOFI waveguides is in its infancy when compared with alternative plasma waveguiding techniques. As such there are numerous studies, such as those suggested above, which could be undertaken, and indeed should to undertaken, to develop this technique into a viable alternative to current guiding technology. However, as has been demonstrated in this thesis, HOFI plasma channels already show great promise as plasma waveguides for the next generation of plasma based particle accelerators.

References

[1] A. P. Chernyaev and S. M. Varzar. *Phys. At. Nucl.* **77**, 10, pp. 1203–1215 (2014). (Cited on p. 1)
"Particle accelerators in modern world"
DOI: 10.1134/S1063778814100032.

[2] *Accelerators for America's Future*, United States Department of Energy, (2010) (Cited on pp. 1, 2)
URL: https://science.energy.gov/$\sim$/media/hep/pdf/accelerator-rd-stewardship/Report.pdf

[3] The CMS Collaboration. *Phys. Lett. Sect. B* **716**, 1, pp. 30–61 (2012). (Cited on p. 1)
"Observation of a new boson at a mass of 125 GeV with the CMS experiment at the LHC"
DOI: 10.1016/j.physletb.2012.08.021.

[4] The ATLAS Collaboration. *Phys. Lett. Sect. B* **716**, 1, pp. 1–29 (2012). (Cited on p. 1)
"Observation of a new particle in the search for the Standard Model Higgs boson with the ATLAS detector at the LHC"
DOI: 10.1016/j.physletb.2012.08.020.

[5] J. R. Stewart. *IEEE Trans. Nucl. Sci.* **26**, 3, pp. 4086–4088 (1979). (Cited on p. 1)
"Particle Accelerators In Cancer Therapy"
DOI: 10.1109/TNS.1979.4329916.

[6] U. Amaldi. *Nucl. Phys. A* **654** (1999). (Cited on p. 1)
"Cancer therapy with particle accelerators"
DOI: 10.1016/S0375-9474(99)00264-X.

[7] J. M. Cole et al. *Proc. Natl. Acad. Sci.* P. 201802314 (2018). (Cited on pp. 1, 18)
"High-resolution μCT of a mouse embryo using a compact laser-driven X-ray betatron source"
DOI: 10.1073/pnas.1802314115.

[8] H. Chirinos et al. *Nucl. Instruments Methods Phys. Res. Sect. B* **208**, 1-4, pp. 256–259 (2003). (Cited on p. 1)
"Radiation vulcanization of natural rubber latex using 250 keV electron beam machine"
DOI: 10.1016/S0168-583X(03)01114-5.

[9] I. S. Arvanitoyannis. Academic Press, (2010), p. 24 (Cited on p. 1)
Irradiation of Food Commodities, 1st Edition
ISBN: 978-0-12-374718-1

[10] H. E Martz et al. CRC Press, (2017), p. 160 (Cited on p. 1)
X-Ray Imaging: Fundamentals, Industrial Techniques and Applications, 1st Edition
ISBN: 978-0-8493-9772-1

[11] R. W. Lutz. *IEEE Trans. Broadcast Telev. Receiv.* **19**, 2, pp. 99–105 (1973). (Cited on p. 1)
"The Impact of Ion Implantation on Consumer Electronics"
DOI: 10.1109/TBTR1.1973.299726.

[12] M. Sugitani. *Rev. Sci. Instrum.* **85**, 2, pp. 1–4 (2014). (Cited on p. 1)
"Ion implantation technology and ion sources"
DOI: 10.1063/1.4854155.

[13] *Diamond Light Source Ltd Report 2016/17*, (2017) (Cited on p. 2)
URL: http://diamond.ac.uk

[14] J. Kawai. *X-Ray Spectrom.* **43**, 1, pp. 2–12 (2014). (Cited on p. 2)
"Forensic analysis of arsenic poisoning in Japan by synchrotron radiation X-ray fluorescence"
DOI: 10.1002/xrs.2462.

[15] J. Simonsen. *Proc. R. Inst. Gt. Britain, Vol. 35*, p. 251 (1951). (Cited on p. 2)
"The Mechanics of Metal Crystals - Weekly Evening Meeting"

[16] M. Omet et al. *Phys. Rev. Spec. Top. - Accel. Beams* **17**, 7, pp. 1–7 (2014). (Cited on p. 3)
"High-gradient near-quench-limit operation of superconducting Tesla-type cavities in scope of the International Linear Collider"
DOI: 10.1103/PhysRevSTAB.17.072003.

[17] H. S. Padamsee. *Annu. Rev. Nucl. Part. Sci.* **64**, 1, pp. 175–196 (2014). (Cited on p. 3)
"Superconducting Radio-Frequency Cavities"
DOI: 10.1146/annurev-nucl-102313-025612.

[18] W. P. Leemans et al. *Phys. Rev. Lett.* **113**, 24, pp. 1–5 (2014). (Cited on pp. 3, 5)
"Multi-Gev electron beams from capillary-discharge-guided subpetawatt laser pulses in the self-trapping regime"
DOI: 10.1103/PhysRevLett.113.245002.

[19] P. A. Walker. PhD thesis. Unversity of Oxford, 2012, pp. 75–81. (Cited on p. 3)
"Laser Wakefield Acceleration of Electrons to GeV Energies and Temporal Laser Pulse Compression Characterization in a Capillary Discharge Waveguide"
URL: https://ora.ox.ac.uk/objects/ora:7482

[20] V. I. Veksler. *Cern Symp. High Energy Accel. Pion Phys.* **1**, p. 80 (1956). (Cited on p. 4)
"Coherent principle of acceleration of charged particles"
DOI: 10.5170/CERN-1956-025.80.

[21] Y. B. Fainberg. *Sov. Phys. Uspekhi* **10**, p. 750 (1968). (Cited on p. 4)
"Acceleration of charged particles in a Plasma"
DOI: 10.1029/JA091iA09p09973.

[22] T. Tajima and J. M. Dawson. *Phys. Rev. Lett.* **43**, 4, pp. 267–270 (1979). (Cited on pp. 4, 5)
"Laser electron accelerator"
DOI: 10.1103/PhysRevLett.43.267.

[23] W. L. Kruer. Westview Press, (2003), pp. 60–61 (Cited on p. 4)
The Physics of Laser Plasma Interactions Edition
ISBN: 0813340837

[24] J. M. Dawson. *Phys. Rev.* **113**, 2, pp. 383–387 (1959). (Cited on p. 5)
"Nonlinear electron oscillations in a cold plasma"
DOI: 10.1103/PhysRev.113.383.

[25] E. Esarey et al. *Rev. Mod. Phys.* **81**, 3, pp. 1229–1285 (2009). (Cited on pp. 5, 13)
"Physics of laser-driven plasma-based electron accelerators"
DOI: 10.1103/RevModPhys.81.1229.

[26] S. M. Hooker. *Nat. Photonics* **7**, 10, pp. 775–782 (2013). (Cited on p. 5)
"Developments in laser-driven plasma accelerators"
DOI: 10.1038/nphoton.2013.234.

[27] S. M. Hooker et al. *J. Phys. B At. Mol. Opt. Phys.* **47** (2014). (Cited on pp. 5, 7)
"Multi-pulse laser wakefield acceleration: a new route to efficient , high-repetition-rate plasma accelerators and high flux radiation sources"
DOI: 10.1088/0953-4075/47/23/234003.

[28] J. Cowley et al. *Phys. Rev. Lett.* **119**, 4, pp. 044802–044807 (2017). (Cited on pp. 5, 16)
"Excitation and Control of Plasma Wakefields by Multiple Laser Pulses"
DOI: 10.1103/PhysRevLett.119.044802.

[29] D. Strickland and G. Mourou. *Opt. Commun.* **56**, 3, pp. 219–221 (1985). (Cited on p. 5)
"Compression of amplified chirped optical pulses"
DOI: 10.1016/0030-4018(85)90120-8.

[30] L. M. Gorbunov and V. I. Kirsanov. *Sov. Phys. JETP* **66**, 2, pp. 290–294 (1987). (Cited on p. 5)
"Excitation of plasma waves by an electromagnetic wave packet"
DOI: 10.1103/PhysRevLett.61.2759.

[31] P. Sprangle et al. *Appl. Phys. Lett.* **53**, 22, pp. 2146–2148 (1988). (Cited on p. 5)
"Laser wakefield acceleration and relativistic optical guiding"
DOI: 10.1063/1.100300.

[32] S. P. D. Mangles et al. *Nature* **431**, 7008, pp. 535–538 (2004). (Cited on pp. 5, 8)
"Monoenergetic beams of relativistic electrons from intense laser-plasma interactions"
DOI: 10.1038/nature02939.

[33] C. G. R. Geddes et al. *Nature* **431**, 7008, pp. 538–541 (2004). (Cited on pp. 5, 8, 13)
"High-quality electron beams from a laser wakefield accelarator using plasma-channel guiding"
DOI: 10.1038/nature02900.

[34] J. Faure et al. **431**, pp. 541–544 (2004). (Cited on pp. 5, 8)
"A laser–plasma accelerator producing monoenergetic electron beams"
DOI: 10.1038/nature02963.

[35] W. P. Leemans et al. *Nat. Phys.* **2**, 10, pp. 696–699 (2006). (Cited on p. 5)
"GeV electron beams from a centimeter-scale accelerator"
DOI: 10.1038/nphys418.

[36] K. Nakamura et al. *Phys. Plasmas* **14**, 5 (2007). (Cited on p. 5)
"GeV electron beams from a centimeter-scale channel guided laser wakefield accelerator"
DOI: 10.1063/1.2718524.

[37] W. P. Leemans. *Eur. Adv. Accel. Concepts Work.* (2017). (Cited on p. 5)
"Progress on Petawatt level experiments at BELLA Center for electron and ion acceleration"

[38] S. Steinke et al. *Nature* **530**, 7589, pp. 190–3 (2016). (Cited on p. 6)
"Multistage coupling of independent laser-plasma accelerators."
DOI: 10.1038/nature16525.

[39] W. Rittershofer et al. *Phys. Plasmas* **17**, 6 (2010). (Cited on p. 7)
"Tapered plasma channels to phase-lock accelerating and focusing forces in laser-plasma accelerators"
DOI: 10.1063/1.3430638.

[40] W. P. Leemans et al. *Proc. PAC*, pp. 1097–1100 (2013). (Cited on p. 7)
"BELLA Laser and Operations"

[41] J. Ferri et al. *Sci. Rep.* **6**, June, pp. 1–10 (2016). (Cited on p. 7)
"Effect of experimental laser imperfections on laser wakefield acceleration and betatron source"
DOI: 10.1038/srep27846.

[42] *Laser Technology for k-BELLA and Beyond*, (2017) (Cited on p. 7)
URL: http://www2.lbl.gov/LBL-Programs/atap/Report_Workshop_k-BELLA_laser_tech_final.pdf

[43] C. Schroeder et al. *Phys. Rev. Spec. Top. - Accel. Beams* **13**, 10, pp. 1–11 (2010). (Cited on pp. 7–9, 82)
"Physics considerations for laser-plasma linear colliders"
DOI: 10.1103/PhysRevSTAB.13.101301.

[44] W. Lu et al. *Phys. Rev. Spec. Top. - Accel. Beams* **10**, 6, pp. 1–12 (2007). (Cited on pp. 9, 17)
"Generating multi-GeV electron bunches using single stage laser wakefield acceleration in a 3D nonlinear regime"
DOI: 10.1103/PhysRevSTAB.10.061301.

[45] S. Bulanov et al. *Phys. Rev. E* **58**, 5, R5257–R5260 (1998). (Cited on p. 9)
"Particle injection into the wave acceleration phase due to nonlinear wake wave breaking"
DOI: 10.1103/PhysRevE.58.R5257.

[46] C. G. R. Geddes et al. *Phys. Rev. Lett.* **100**, 21, pp. 1–4 (2008). (Cited on p. 9)
"Plasma-density-gradient injection of low absolute-momentum-spread electron bunches"
DOI: 10.1103/PhysRevLett.100.215004.

[47] T. P. Rowlands-Rees et al. *Phys. Rev. Lett.* **100**, 10, pp. 1–4 (2008). (Cited on p. 9)
"Laser-driven acceleration of electrons in a partially ionized plasma channel"
DOI: 10.1103/PhysRevLett.100.105005.

[48] A. Pak et al. *Phys. Rev. Lett.* **104**, 2, pp. 1–4 (2010). (Cited on p. 9)
"Injection and trapping of tunnel-ionized electrons into laser-produced wakes"
DOI: 10.1103/PhysRevLett.104.025003.

[49] N. Bourgeois et al. *Phys. Rev. Lett.* **111**, 15, pp. 1–5 (2013). (Cited on p. 9)
"Two-pulse ionization injection into quasilinear laser wakefields"
DOI: 10.1103/PhysRevLett.111.155004.

[50] J. Faure et al. *Nature* **444**, 7120, pp. 737–739 (2006). (Cited on p. 9)
"Controlled injection and acceleration of electrons in plasma wakefields by colliding laser pulses"
DOI: 10.1038/nature05393.

[51] C. Rechatin et al. *New J. Phys.* **11** (2009). (Cited on p. 9)
"Quasi-monoenergetic electron beams produced by colliding cross-polarized laser pulses in underdense plasmas"
DOI: 10.1088/1367-2630/11/1/013011.

[52] F. Amiranoff et al. *Phys. Rev. Lett.* **81**, 5, pp. 995–998 (1998). (Cited on p. 9)
"Observation of Laser Wakefield Acceleration of Electrons"
DOI: 10.1103/PhysRevLett.81.995.

[53] T. H. Tschentscher et al. *Synchrotron Radiat. News* **19**, 6, pp. 13–19 (2006). (Cited on p. 10)
"Technical Report: The European X-ray Free-Electron Laser Facility: A New Infrastructure for Research Using Ultrashort, Coherent X-ray Pulses of Extreme Brightness"
DOI: 10.1080/08940880601064968.

[54] P. A. Walker. *J. Phys. Conf. Ser.* **874**, p. 012029 (2017). (Cited on p. 10)
"HORIZON 2020 EuPRAXIA Design Study"
DOI: 10.1088/1742-6596/874/1/012029.

[55] Z. Qin et al. *Phys. Plasmas* **25**, 2 (2018). (Cited on p. 10)
"Ultralow-emittance measurement of high-quality electron beams from a laser wakefield accelerator"
DOI: 10.1063/1.5019987.

[56] C. Christou et al. *Proc. LINAC 2004*, pp. 84–86 (2004). (Cited on p. 10)
"The Pre-Injector Linac for the Diamond Light Source"

[57] V.C. Kempson et al. *Proc. EPAC*, pp. 3344–3346 (2006). (Cited on p. 10)
"Commisionning of the booster synchrotron for the Diamond Light Source"

[58] A.R. Maier et al. *Opt. InfoBase Conf. Pap.* **Part F43-C**, pp. 3–4 (2017)
. "Integration of the ANGUS 200 TW Laser-System into the Accelerator Infrastructure at DESY"
DOI: 10.1364/CLEO_AT.2017.Tu3L.4.

[59] J. P. Couperus et al. *Nat. Commun.* **8**, 1, pp. 1–7 (2017). (Cited on p. 10)
"Demonstration of a beam loaded nanocoulomb-class laser wakefield accelerator"
DOI: 10.1038/s41467-017-00592-7.

[60] Marie Emmanuelle Couprie. *Nucl. Instrum. Methods Phys. Res. A*, February (2018). (Cited on pp. 10, 11)
"Towards compact Free Electron-Laser based on laser plasma accelerators"
DOI: 10.1016/j.nima.2018.02.090.

[61] Y. P. Wu et al. *Proc. Int. Part. Accel. Conf.* Pp. 1258–1260 (2017). (Cited on p. 11)
"Experimental Demonstration of Energy-Chirp Reduction by a Plasma Dechirper"
DOI: 10.18429/JACoW-IPAC2017-TUOBB1.

[62] L. C. Steinhauer and H. G. Ahlstrom. *Phys. Fluids* **14**, 6, pp. 1109–1114 (1971). (Cited on p. 12)
"Propagation of coherent radiation in a cylindrical plasma column"
DOI: 10.1063/1.1693572.

[63] C. G. Durfee and H. M. Milchberg. *Phys. Rev. Lett.* **71**, 15, pp. 2409–2412 (1993). (Cited on p. 12)
"Light Pipe for High Intensity Laser Pulses"
DOI: 10.1103/PhysRevLett.71.2409.

[64] J. Lynch C. Durfree and H. Milchberg. *Phys. Rev. E* **51**, 3, pp. 2368–2387 (1995). (Cited on pp. 12, 13, 107)
"Development of a plasma waveguide for high intensity laser pulses"
DOI: 10.1103/PhysRevE.51.2368.

[65] H. M. Milchberg et al. *Phys. Plasmas* **3**, 5 pt 2, pp. 2149–2155 (1996). (Cited on p. 12)
"Development and applications of a plasma waveguide for intense laser pulses"
DOI: 10.1063/1.871668.

[66] P. Volfbeyn et al. *Phys. Plasmas* **6**, 5, pp. 2269–2277 (1998). (Cited on pp. 13, 107)
"Guiding of laser pulses in plasma channels created by the ignitor-heater technique"
DOI: 10.1063/1.873503.

[67] Y. F. Xiao et al. *Phys. Plasmas* **11**, 5 PART 1, pp. 20–24 (2004). (Cited on p. 13)
"Efficient generation of extended plasma waveguides with the axicon ignitor-heater scheme"
DOI: 10.1063/1.1695354.

[68] E. W. Gaul et al. *Appl. Phys. Lett.* **77**, 25, pp. 4112–4114 (2000). (Cited on pp. 13, 107)
"Production and characterization of a fully ionized He plasma channel"
DOI: 10.1063/1.1329323.

[69] V. Kumarappan et al. *Phys. Rev. Lett.* **94**, 20, pp. 18–21 (2005). (Cited on pp. 13, 14, 93, 107)
"Guiding of intense laser pulses in plasma waveguides produced from efficient, femtosecond end-pumped heating of clustered gases"
DOI: 10.1103/PhysRevLett.94.205004.

[70] N. Lemos et al. *Phys. Plasmas* **20**, 6, pp. 1–9 (2013). (Cited on pp. 14, 34, 91, 107)
"Plasma expansion into a waveguide created by a linearly polarized femtosecond laser pulse"
DOI: 10.1063/1.4810797.

[71] N. Lemos et al. *Phys. Plasmas* **20**, 10, pp. 16–21 (2013). (Cited on p. 14)
"Effects of laser polarization in the expansion of plasma waveguides"
DOI: 10.1063/1.4825228.

[72] N. Lemos et al. *Sci. Rep.* **8**, 1, pp. 1–9 (2018). (Cited on pp. 14, 82, 91, 129)
"Guiding of laser pulses in plasma waveguides created by linearly-polarized femtosecond laser pulses"
DOI: 10.1038/s41598-018-21392-z.

[73] S. Jackel et al. *Opt. Lett.* **20**, 10, pp. 1086–1088 (1995). (Cited on p. 15)
"Channeling of terawatt laser pulses by use of hollow waveguides"
DOI: 10.1364/OL.20.001086.

[74] M. Borghesi et al. *Phys. Rev. E* **57**, 5, pp. 4899–4902 (1998). (Cited on p. 15)
"Guiding of a 10-TW picosecond laser pulse through hollow capillary tubes"
DOI: 10.1103/PhysRevE.57.R4899.

[75] F. Dorchies et al. *Phys. Rev. Lett.* **82**, 23, pp. 4655–4658 (1999). (Cited on pp. 15, 24)
"Monomode guiding of 1016W/cm2laser pulses over 100 rayleigh lengths in hollow capillary dielectric tubes"
DOI: 10.1103/PhysRevLett.82.4655.

[76] C. Courtois et al. *J. Opt. Soc. Am. B* **17**, 5, pp. 864–867 (2000). (Cited on p. 15)
"Experimental study of short high-intensity laser-pulse monomode propagation in centimeter-long capillary tubes"
DOI: 10.1364/JOSAB.17.000864.

[77] C. Courtois et al. *Phys. Plasmas* **8**, 7, pp. 3445–3456 (2001). (Cited on p. 15)
"Propagation of intense ultrashort laser pulses in a plasma filled capillary tube: Simulations and experiments"
DOI: 10.1063/1.1378327.

[78] B. Cros et al. *IEEE Trans. Plasma Sci.* **28**, 4, pp. 1071–1077 (2000). (Cited on p. 15)
"Extending plasma accelerators: Guiding with Capillary Tubes"
DOI: 10.1109/27.893291.

[79] G. Genoud et al. *Appl. Phys. B Lasers Opt.* **105**, 2, pp. 309–316 (2011). (Cited on p. 15)
"Laser-plasma electron acceleration in dielectric capillary tubes"
DOI: 10.1007/s00340-011-4639-4.

[80] A. Zigler et al. *J. Opt. Soc. Am. B* **13**, 1, p. 68 (1996). (Cited on p. 15)
"Optical guiding of high-intensity laser pulses in a long plasma channel formed by a slow capillary discharge"
DOI: 10.1364/JOSAB.13.000068.

[81] Y. Ehrlich et al. *Phys. Rev. Lett.* **77**, 20, pp. 4186–4189 (1996). (Cited on p. 15)
"Guiding of high intensity laser pulses in straight and curved plasma channel experiments"
DOI: 10.1103/PhysRevLett.77.4186.

[82] Y. Ehrlich et al. *J. Opt. Soc. Am. B* **15**, 9, p. 2416 (1998). (Cited on p. 15)
"Guiding and damping of high-intensity laser pulses in long plasma channels"
DOI: 10.1364/JOSAB.15.002416.

[83] S. M. Hooker et al. *J. Opt. Soc. Am. B* **17**, 1, p. 90 (2000). (Cited on p. 15)
"Guiding of high-intensity picosecond laser pulses in a discharge-ablated capillary waveguide"
DOI: 10.1364/JOSAB.17.000090.

[84] D. J. Spence and S. M. Hooker. *Phys. Rev. E* **63**, 015401, pp. 1–4 (2000). (Cited on pp. 15, 16)
"Investigation of a hydrogen plasma waveguide"
DOI: 10.1103/PhysRevE.63.015401.

[85] A. Butler et al. *J. Phys. B At. Mol. Opt. Phys.* **89**, 18, p. 185003 (2002). (Cited on p. 15)
"First demonstration of guiding of high-intensity laser pulses in a hydrogen-filled capillary discharge waveguide"
DOI: 10.1103/PhysRevLett.89.185003.

[86] P. A. Walker et al. *New J. Phys.* **15** (2013). (Cited on p. 16)
"Investigation of GeV-scale electron acceleration in a gas-filled capillary discharge waveguide"
DOI: 10.1088/1367-2630/15/4/045024.

[87] A. J. Gonsalves et al. *J. Appl. Phys.* **119**, 3 (2016). (Cited on p. 16)
"Demonstration of a high repetition rate capillary discharge waveguide"
DOI: 10.1063/1.4940121.

[88] G Sun et al. *Phys. Fluids* **30**, 2, p. 526 (1987). (Cited on p. 17)
"Self-focusing of short intense pulses in plasmas"
DOI: 10.1063/1.866349.

[89] S. Y. Chen et al. *Phys. Rev. Lett.* **80**, 12, pp. 2610–2613 (1998). (Cited on p. 17)
"Evolution of a plasma waveguide created during relativistic-ponderomotive self-channeling of an intense laser pulse"
DOI: 10.1103/PhysRevLett.80.2610.

[90] E. Esarey et al. *IEEE J. Quantum Electron.* **33**, 11, pp. 1879–1914 (1997). (Cited on p. 17)
"Self-focusing and guiding of short laser pulses in ionizing gases and plasmas"
DOI: 10.1109/3.641305.

[91] P. Sprangle et al. *Phys. Rev. Lett.* **64**, 17, pp. 2011–2014 (1990). (Cited on p. 17)
"Nonlinear theory of intense laser-plasma interactions"
DOI: 10.1103/PhysRevLett.64.2011.

[92] C. D. Decker et al. *Phys. Plasmas* **3**, 5, pp. 2047–2056 (1996). (Cited on p. 17)
"The evolution of ultra-intense, short-pulse lasers in underdense plasmas"
DOI: 10.1063/1.872001.

[93] G. Sarri et al. *Nat. Commun.* **6**, pp. 1–8 (2015). (Cited on p. 18)
"Generation of neutral and high-density electron-positron pair plasmas in the laboratory"
DOI: 10.1038/ncomms7747.

[94] G. J. Williams et al. *Phys. Plasmas* **22**, 093115, pp. 1–8 (2015). (Cited on p. 18)
"Positron generation using laser-wakefield electron sources"
DOI: 10.1063/1.4931044.

[95] F. Albert and A.G. R. Thomas. *Plasma Phys. Control. Fusion* **58**, 10, p. 103001 (2016). (Cited on p. 18)
"Applications of laser wakefield accelerator-based light sources"
DOI: 10.1088/0741-3335/58/10/103001.

[96] M. J. V. Streeter et al. *Appl. Phys. Lett.* **112**, 24 (2018). (Cited on p. 18)
"Temporal feedback control of high-intensity laser pulses to optimize ultrafast heating of atomic clusters"
DOI: 10.1063/1.5027297.

[97] F. Salehi et al. *Opt. Lett.* **42**, 2, pp. 215–218 (2017). (Cited on p. 18)
"MeV electron volt electron acceleration at 1 kHz with $<$ 10 mJ laser pulses"
DOI: 10.1364/OL.42.000215.

[98] D. Guénot et al. *Nat. Photonics* **11**, 5, pp. 293–296 (2017). (Cited on p. 18)
"Relativistic electron beams driven by kHz single-cycle light pulses"
DOI: 10.1038/nphoton.2017.46.

[99] D. Gustas et al. *Phys. Rev. Accel. Beams* **21**, 1, pp. 1–7 (2018). (Cited on p. 18)
"High-charge relativistic electron bunches from a kHz laser-plasma accelerator"
DOI: 10.1103/PhysRevAccelBeams.21.013401.

[100] S. Feister et al. **25**, 16, pp. 531–536 (2015). (Cited on p. 18)
"Relativistic electron acceleration by mJ-class kHz lasers normally incident on liquid targets"
DOI: 10.1364/OE.25.018736.

[101] The EuPRAXIA Project. *Milestone Rep. M 3.1* (2017). (Cited on p. 19)
"Design for an electron injector and a laser plasma stage proposed"

[102] W. P. Leemans et al. *AIP Conf. Proc.* **1299**, pp. 3–11 (2010). (Cited on p. 19)
"The Berkeley Lab Laser Accelerator (BELLA): A 10 GeV laser plasma accelerator"
DOI: 10.1063/1.3520352.

[103] E. Hecht. Addison Wesley, (2002), p. 595 (Cited on p. 22)
Optics, 4th Edition
ISBN: 0805385665

[104] B. Cros et al. *Phys. Rev. E* **65**, 2, pp. 1–7 (2002). (Cited on pp. 23, 24)
"Eigenmodes for capillary tubes with dielectric walls and ultraintense laser pulse guiding"
DOI: 10.1103/PhysRevE.65.026405.

[105] P. Gibbon. Imperial College Press, (2007), pp. 24–25 (Cited on p. 25)
Short Pulse Laser Interactions with Matter, 1st Edition
ISBN: 1-86094-135-4

[106] C. G. Durfee III et al. *Opt. Lett.* **19**, 23, pp. 1937–1939 (1994). (Cited on pp. 25, 26)
"Mode properties of a plasma waveguide for intense laser pulses"
DOI: 10.1364/OL.19.001937.

[107] C. G. Durfee III et al. *J. Opt. Soc. Am. B* **13**, 1, pp. 59–67 (1996). (Cited on pp. 25, 28)
"Mode control in a two-pulse-excited plasma waveguide"
DOI: 10.1364/JOSAB.13.000059.

[108] E. Esarey and W. P. Leemans. *Phys. Rev. E* **59**, 1, pp. 1082–1095 (1999). (Cited on p. 25)
"Nonparaxial propagation of ultrashort laser pulses in plasma channels"
DOI: 10.1103/PhysRevE.59.1082.

[109] T. R. Clark and H. M. Milchberg. *Phys. Rev. E* **61**, 2, pp. 1954–1965 (2000). (Cited on pp. 25, 26, 28, 80, 91)
"Optical mode structure of the plasma waveguide"
DOI: 10.1103/PhysRevE.61.1954.

[110] A. J. Gonsalves et al. *AIP Conf. Proc.* **1299**, 2010, pp. 150–155 (2010). (Cited on p. 28)
"Plasma channel diagnostic based on laser centroid oscillations"
DOI: 10.1063/1.3520304.

[111] *National Institute of Standards and Technology Atomic Spectra Database* (Cited on p. 30)
URL: https://physics.nist.gov/PhysRefData/ASD/levels_form.html (visited on 01/28/2018)

[112] D. N. Fittinghoff. PhD thesis. University of California Davis & Lawrence Livermore National Laboratory, 1993. (Cited on pp. 30, 31)
"Optical Field Ionization of Atoms and Ions Using Ultrashort Laser Pulses"
URL: https://inis.iaea.org/search/search.aspx?orig_q=RN:25038227

[113] L. V. Keldysh. *Sov. Phys. JETP* **20**, 5, pp. 1307–1314 (1965). (Cited on p. 31)
"Ionization in the field of a strong electromagnetic wave"
DOI: 10.1234/12345678.

[114] P. B. Corkum et al. *Phys. Rev. Lett.* **62**, 11, pp. 1259–1262 (1989). (Cited on pp. 31, 33)
"Above-threshold ionization in the long-wavelength limit"
DOI: 10.1103/PhysRevLett.62.1259.

[115] S. Augst et al. *Phys. Rev. Lett.* **63**, 20, pp. 2212–2215 (1989). (Cited on pp. 31, 32)
"Tunneling ionization of noble gases in a high-intensity laser field"
DOI: 10.1103/PhysRevLett.63.2212.

[116] R. R. Freeman and P. H. Bucksbaum. *J. Phys. B At. Mol. Opt. Phys.* **24**, 2, pp. 325–347 (1991). (Cited on p. 31)
"Investigations of above-threshold ionization using subpicosecond laser pulses"
DOI: 10.1088/0953-4075/24/2/004.

[117] E. Mevel et al. *Phys. Rev. Lett.* **70**, 4, pp. 406–409 (1993). (Cited on p. 31)
"Atoms in strong optical fields: Evolution from multiphoton to tunnel ionization"
DOI: 10.1103/PhysRevLett.70.406.

[118] G. Gibson et al. *Phys. Rev. A* **41**, 9, pp. 5049–5052 (1990). (Cited on p. 31)
"Tunneling ionization in the multiphoton regime"
DOI: 10.1103/PhysRevA.41.5049.

[119] A. Rudenko et al. *J. Phys. B At. Mol. Opt. Phys.* **37**, 24 (2004). (Cited on p. 31)
"Resonant structures in the low-energy electron continuum for single ionization of atoms in the tunnelling regime"
DOI: 10.1088/0953-4075/37/24/L03.

[120] M. V. Ammosov et al. *Sov. Phys. JETP* **64**, December 1986, pp. 1191–1194 (1986). (Cited on pp. 31, 84, 88)
"Tunnel ionization of complex atoms and of atomic ions in an alternating electromagnetic field"
DOI: 10.1117/12.938695.

[121] N. B. Delone and Vladimir P. Krainov. *Physics-Uspekhi* **41**, 5, pp. 469–485 (1998). (Cited on pp. 32, 94)
"Tunneling and barrier-suppression ionization of atoms and ions in a laser radiation field"
DOI: 10.1070/PU1998v041n05ABEH000393.

[122] J. H. Posthumus et al. *Conf. Ser. - Inst. Phys.* **154**, pp. 298–307 (1997). (Cited on pp. 32, 84, 88)
"Molecular dissociative ionization using a classical over-the-barrier approach"

[123] T. D. Arber et al. *Plasma Phys. Control. Fusion* **57**, 11 (2015). (Cited on pp. 32, 84)
"Contemporary particle-in-cell approach to laser-plasma modelling"
DOI: 10.1088/0741-3335/57/11/113001.

[124] A. Lawrence-Douglas. PhD thesis. University of Warwick, 2013, p. 65. (Cited on pp. 32, 84, 88)
"Ionisation Effects for Laser-Plasma Interactions by Particle-in-Cell Code"
URL: http://wrap.warwick.ac.uk/57465/1/WRAP_THESIS_Lawrence-Douglas_2013.pdf

[125] P. H. Bucksbaum et al. *Phys. Rev. Lett.* **56**, 24, pp. 2590–2593 (1986). (Cited on p. 33)
"Suppression of multiphoton ionization with circularly polarized coherent light"
DOI: 10.1103/PhysRevLett.56.2590.

[126] V. P. Krainov. *J. Opt. Soc. Am. B* **14**, 2, p. 425 (1997). (Cited on p. 33)
"Ionization rates and energy and angular distributions at the barrier-suppression ionization of complex atoms and atomic ions"
DOI: 10.1364/JOSAB.14.000425.

[127] L. I. Sedov. *Prikl. Mat. Mekh.* **10**, pp. 241–250 (1946). (Cited on p. 33)
"Propagation of Strong Shock Waves"

[128] G. Taylor. *Proc. R. Soc. A Math. Phys. Eng. Sci.* **201**, 1065, pp. 175–186 (1950). (Cited on p. 33)
"The Formation of a Blast Wave by a Very Intense Explosion. II. The Atomic Explosion of 1945"
DOI: 10.1098/rspa.1950.0050.

[129] US Department of Energy. *DOE/NV–209-Rev 15*, July 1945, p. 170 (2000). (Cited on p. 33)
"United States Nuclear Tests: July 1945 through September 1992"

[130] G. J. Hutchens. *J. Appl. Phys.* **88**, 6, pp. 3654–3658 (2000). (Cited on pp. 33, 82)
"Approximate near-field blast theory : A generalized approach"
DOI: 10.1063/1.1288785.

[131] T. R. Clark and H. M. Milchberg. *Phys. Rev. Lett.* **78**, 12, pp. 2373–2376 (1996). (Cited on pp. 34, 107)
"Time- and space-resolved density evolution of the plasma waveguide"
DOI: 10.1103/PhysRevLett.78.2373.

[132] John H. McLeod. *J. Opt. Soc. Am.* **44**, 8, p. 592 (1954). (Cited on p. 37)
"The Axicon: A New Type of Optical Element"
DOI: 10.1364/JOSA.44.000592.

[133] S. J. Gessner. PhD thesis. Stanford University, 2016, pp. 65–66. (Cited on p. 38)
"Demonstration of the hollow channel plasma wakefield accelerator"
URL: http://www.slac.stanford.edu/pubs/slacreports/reports19/slac-r-1073.pdf

[134] O. Brzobohatý et al. *Opt. Express* **16**, 17, pp. 12688–12700 (2008). (Cited on p. 38)
"High quality quasi-Bessel beam generated by round-tip axicon"
DOI: 10.1364/OE.16.012688.

[135] F. F. Chen. Plenum Publishing Corporation, (1984), pp. 115–116 (Cited on p. 40)
Introduction to Plasma Physics and Controlled Fusion, 2nd Edition
ISBN: 8181288025

[136] J. Fan et al. *Phys. Rev. E - Stat. Nonlinear, Soft Matter Phys.* **65**, 5, pp. 1–12 (2002). (Cited on pp. 41, 94)
"Resonant self-trapping of high intensity Bessel beams in underdense plasmas"
DOI: 10.1103/PhysRevE.65.056408.

[137] H. Sheng et al. *Phys. Rev. E - Stat. Nonlinear, Soft Matter Phys.* **72**, 3, pp. 1–8 (2005). (Cited on pp. 41, 82, 94, 107)
"Plasma waveguides efficiently generated by Bessel beams in elongated cluster gas jets"
DOI: 10.1103/PhysRevE.72.036411.

[138] *ISO 11146-2: Lasers and laser-related equipment - Test methods for laser beam widths, divergence angles and beam propagation ratios - Part 2: General astigmatic beams* (Cited on pp. 44, 69)
URL: https://www.iso.org/obp/ui/#iso:std:iso:11146:-2:ed-1:v1:en (visited on 10/13/2017)

[139] M. Takeda et al. *J. Opt. Soc. Am.* **72**, 1, p. 156 (1982). (Cited on p. 50)
"Fourier-transform method of fringe-pattern analysis for computer-based topography and interferometry"
DOI: 10.1364/JOSA.72.000156.

[140] R. M. Goldstien et al. *Radio Sci.* **23**, 4, pp. 713–720 (1988). (Cited on p. 55)
"Satellite radar interferometry: Two-dimensional phase unwrapping"
DOI: 10.1029/RS023i004p00713.

[141] *2D phase unwrapping algorithms* (Cited on p. 55)
URL: https://uk.mathworks.com/matlabcentral/fileexchange/22504-2d-phase-unwrapping-algorithms (visited on 09/18/2018)

[142] M. A. Herráez et al. *Appl. Opt.* **41**, 35, p. 7437 (2002). (Cited on p. 55)
"Fast two-dimensional phase-unwrapping algorithm based on sorting by reliability following a noncontinuous path"
DOI: 10.1364/AO.41.007437.

[143] *scikit-image: image processing in Python* (Cited on p. 55). 2014
DOI: 10.7717/peerj.453

. [144] R. N. Bracewell. McGraw-Hill, (2000), pp. 351–356 (Cited on p. 57)
The Fourier Transform and its Applications, 3rd Edition
ISBN: 0-07-116043-4

[145] *PyAbel (v0.7): A Python Package for Abel Transforms* (Cited on p. 58). 2016
DOI: 10.5281/zenodo.47423

. [146] E. W. Hansen and P. Law. *J. Opt. Soc. Am. A* **2**, 4, p. 510 (1985). (Cited on p. 58)
"Recursive methods for computing the Abel transform and its inverse"
DOI: 10.1364/JOSAA.2.000510.

[147] J. M. Cole. PhD thesis. Imperial College London, 2016, pp. 74–75. (Cited on p. 59)
"Diagnosis and Application of Laser Wakefield Accelerators"
URL: http://hdl.handle.net/10044/1/42222

[148] L. Spitzer. Interscience Publishers, (1967) (Cited on pp. 62, 86)
Physics of Fully Ionized Gases, 2nd Edition
ISBN: 0486449823

[149] H. H. Chu et al. *Appl. Phys. B* **79**, 2, pp. 193–201 (2004). (Cited on p. 66)
"A versatile 10-TW laser system with robust passive controls to achieve high stability and spatiotemporal quality"
DOI: 10.1007/s00340-004-1533-3.

[150] S. Ito et al. *Appl. Phys. B* **76**, 5, pp. 497–503 (2003). (Cited on p. 66)
"Seven-terawatt Ti:sapphire laser system operating at 50 Hz with high beam quality for laser Compton femtosecond X-ray generation"
DOI: 10.1007/s00340-003-1144-4.

[151] B. Hammer and J. K. Norskov. *Nature* **376**, 6537, pp. 238–240 (1995). (Cited on p. 66)
"Why gold is the noblest of all the metals"
DOI: 10.1038/376238a0.

[152] S. Akturk et al. *J. Opt.* **12**, 9, p. 093001 (2010). (Cited on p. 69)
"Spatio-temporal couplings in ultrashort laser pulses"
DOI: 10.1088/2040-8978/12/9/093001.

[153] M. Raghuramaiah et al. *Opt. Commun.* **223**, 1-3, pp. 163–168 (2003). (Cited on p. 70)
"Simultaneous measurement of pulse-front tilt and pulse duration of a femtosecond laser beam"
DOI: 10.1016/S0030-4018(03)01638-9.

[154] S. Keppler et al. *Laser Photonics Rev.* **10**, 2, pp. 264–277 (2016). (Cited on p. 71)
"The generation of amplified spontaneous emission in high-power CPA laser systems"
DOI: 10.1002/lpor.201500186.

[155] W. Rittershofer. PhD thesis. University of Oxford, 2014. (Cited on pp. 76, 77)
"Laser wakefield acceleration in tapered plasma channels - Theory, simulation and experiment"
URL: https://ora.ox.ac.uk/objects/uuid:be45ca7d-790c-496c-9e52-160ce4fe277d

[156] C. R. Thornton. PhD thesis. University of Oxford, 2017. (Cited on pp. 76, 77)
"Experimental aspects of plasma wakefields driven in the linear regime"
URL: https://ora.ox.ac.uk/objects/uuid:f8087db1-fdb9-4cff-9fcc-859fde95b052

[157] J. D. Huba. *Off. Nav. Res.* (2013). (Cited on p. 82)
"NRL Plasma Formulary"

[158] M. Y. Jaffrin and R. F. Probstein. *Phys. Fluids* **7**, 10, p. 1658 (1964). (Cited on p. 82)
"Structure of a Plasma Shock Wave"
DOI: 10.1063/1.1711072.

[159] H. K. Sen. *Phys. Rev. Lett.* **102**, 1, pp. 5–11 (1956). (Cited on p. 82)
"Structure of a Magnetohydrodynamic Shock Wave in a Plasma of Infinite Conductivity"
DOI: 10.1103/PhysRev.102.5.

[160] C. Arran. PhD thesis. University of Oxford, 2018. (Cited on pp. 84, 85, 88, 98)
"Techniques for High Repetition Rate Laser Wakefield Acceleration"

. [161] Wolfgang Lotz. *Zeitschrift für Phys.* **216**, 3, pp. 241–247 (1968). (Cited on p. 87)
"Electron-Impact Ionization Cross-Sections and Ionization Rate Coefficients for Atoms and Ions from Hydrogen to Calcium"

[162] M. A. Biondi and S. C. Brown. *Phys. Rev.* **75**, 11, pp. 1700–1705 (1949). (Cited on p. 87)
"Measurements of Ambipolar Diffusion in Helium"
DOI: 10.1103/PhysRev.75.1700.

[163] A. Giusti-Suzor et al. *Phys. Rev. Lett.* **64**, 5, pp. 515–518 (1990). (Cited on p. 88)
"Above-threshold dissociation of H2+ in intense laser fields"
DOI: 10.1103/PhysRevLett.64.515.

[164] J. H. Posthumus. *Reports Prog. Phys.* **67**, 5, pp. 623–665 (2004). (Cited on p. 88)
"The dynamics of small molecules in intense laser fields"
DOI: 10.1088/0034-4885/67/5/R01.

[165] M. R. Thompson et al. *J. Phys. B At. Mol. Opt. Phys.* **30**, 24, pp. 5755–5772 (1997). (Cited on p. 89)
"One and two-colour studies of the dissociative ionization and Coulomb explosion of with intense Ti:sapphire laser pulses"
DOI: 10.1088/0953-4075/30/24/014.

[166] P. B. Corkum. *Phys. Rev. Lett.* **71**, 13, pp. 1994–1997 (1993). (Cited on p. 89)
"Plasma perspective on strong field multiphoton ionization"
DOI: 10.1103/PhysRevLett.71.1994.

[167] A. S. Alnaser et al. *Phys. Rev. Lett.* **91**, 16, p. 163002 (2003). (Cited on p. 89)
"Rescattering Double Ionization of D2 and H2 by Intense Laser Pulses"
DOI: 10.1103/PhysRevLett.91.163002.

[168] J. P. Palastro et al. *Phys. Rev. A* **033835**, December 2017, pp. 1–9 (2018). (Cited on p. 107)
"Ionization waves of arbitrary velocity driven by a flying focus"
DOI: 10.1103/PhysRevA.97.033835.

[169] H. M. Milchberg et al. *Philos. Trans. A. Math. Phys. Eng. Sci.* **364**, 1840, pp. 647–61 (2006). (Cited on p. 107)
"Clustered gases as a medium for efficient plasma waveguide generation"
DOI: 10.1098/rsta.2005.1729.

[170] K. Poder et al. *Plasma Phys. Control. Fusion* **60**, 1 (2018). (Cited on p. 108)
"Measurements of self-guiding of ultrashort laser pulses over long distances"
DOI: 10.1088/1361-6587/aa8f0e.

[171] C. Iaconis and I. A. Walmsley. *Opt. Lett.* **23**, 10, p. 792 (1998). (Cited on p. 126)
"Spectral phase interferometry for direct electric-field reconstruction of ultrashort optical pulses"
DOI: 10.1364/OL.23.000792.

[172] P. Tournois. *Opt. Commun.* **140**, 4-6, pp. 245–249 (1997). (Cited on p. 126)
"Compensation of group delay time dispersion in laser systems"
DOI: 10.1016/S0030-4018(97)00153-3.

[173] R. J. Shalloo et al. *Phys. Rev. E* **97**, 5, pp. 1–8 (2018). (Cited on p. 129)
"Hydrodynamic optical-field-ionized plasma channels"
DOI: 10.1103/PhysRevE.97.053203.

[174] S. P. Nikitin et al. *Opt. Lett.* **22**, 23, pp. 1787–1789 (1996). (Cited on p. 152)
"Guiding of intense femtosecond pulses in preformed plasma channels"
DOI: 10.1364/OL.22.001787.

[175] S. P. Nikitin et al. *Phys. Rev. E* **59**, 4, R3839–R3842 (1999). (Cited on p. 152)
"High efficiency coupling and guiding of intense femtosecond laser pulses in preformed plasma channels in an elongated gas jet"
DOI: 10.1103/PhysRevE.59.R3839.

[176] E. Hecht. Addison Wesley, (2002), p. 115 (Cited on p. 153)
Optics, 4th Edition
ISBN: 0805385665

[177] J. Daniels et al. *Proc. SPIE 10240, Laser Accel. Electrons, Protons, Ions* **IV**, May, 102400N (2017). (Cited on p. 162)
"Laser-assisted capillary discharge for enhanced guiding of tightly focused laser pulses at low densities"
DOI: 10.1117/12.2267432.

[178] J. Daniels. PhD thesis. Eindhoven University of Technology, 2017. (Cited on p. 162)
"Measuring and modifying plasma density profiles to confine high power lasers"
URL: https://pure.tue.nl/ws/files/87364377/20171204_Daniels.pdf